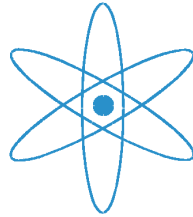


PHYSIK-DEPARTMENT



Cosmic Background Discrimination
for the Rare Neutrino Event Search
in BOREXINO and LENA

Dissertation
von

Michael Wurm



TECHNISCHE UNIVERSITÄT
MÜNCHEN

Technische Universität München

Physik Department
Lehrstuhl für Experimentalphysik-Astroteilchenphysik E15
Univ.-Prof. Dr. Franz von Feilitzsch

**Cosmic Background Discrimination for the
Rare Neutrino Event Search in BOREXINO and LENA**

Michael Wurm

Vollständiger Abdruck der von der Fakultät für Physik der Technischen Universität
München zur Erlangung des akademischen Grades eines

Doktors der Naturwissenschaften (Dr. rer. nat.)

genehmigten Dissertation.

Vorsitzender: Univ.-Prof. Dr. Alejandro Ibarra

Prüfer der Dissertation: 1. Univ.-Prof. Dr. Lothar Oberauer

2. Jun.-Prof. Dr. Laura Fabbietti

Die Dissertation wurde am 18.05.2009 bei der Technischen Universität München
eingereicht und durch die Fakultät für Physik am 19.06.2009 angenommen.

Abstract

The level of cosmogenic background is of great importance for the search for very rare neutrino events in a liquid-scintillator detector: Exact knowledge of the cosmic muon, cosmogenic neutron and radioisotope background is essential for solar neutrino detection in BOREXINO; it also has considerable impact on the design of the next-generation LENA experiment.

In the present work, the performance of the muon identification tags applied in BOREXINO was evaluated to precisely determine the residual muon rate contaminating the neutrino data sample. While the veto efficiency for cosmic muons is more than sufficient for solar neutrino analysis, the muon-induced in-situ production of radionuclides inside the detection volume presents a challenging background. Especially regarding the search for CNO and pep neutrinos, the rate of cosmogenic ^{11}C β decays exceeds the expected neutrino signal by at least one order of magnitude. A measurement by BOREXINO of these up to now undetermined branches of solar neutrino production will only succeed if the subtraction of the ^{11}C events becomes possible on an event-by-event basis. The muon track reconstruction devised in this thesis is mandatory for this task: The spacial information on the track is on the one hand basis for the threefold coincidence veto used in the direct tagging of ^{11}C decay events. On the other hand, muon reconstruction is a prerequisite for the study of the characteristics of muon-induced neutron showers that are generating ^{11}C at a larger distance from the track. The results on muon track resolution and on the multiplicity and lateral extension of neutron showers are used to derive optimal values for ^{11}C rejection.

Due to their superior background-discrimination power, liquid-scintillator detectors offer distinctive advantages in the search for the Diffuse Supernova Neutrino Background (DSNB) which has not yet been observed. Only a detector as large as LENA can hope to detect the extremely low DSNB flux. Based on an analysis of the relevant neutrino and cosmogenic backgrounds presented in this work a basically background-free observation window reaching from about 10 to 30 MeV can be determined. Current DSNB models predict a rate of about 10 $\bar{\nu}_e$ events per year in LENA. A dedicated Monte Carlo study indicates that the spectroscopy of the DSNB events acquired over several years of measurement will allow to set constraints on the underlying supernova neutrino spectrum; the premise is a rather accurate knowledge of the cosmic supernova rate from optical observations.

Related to this phenomenological work, the optical scattering lengths of candidate scintillators for LENA have been measured in a laboratory experiment. Scattering and attenuation length determine the optical transparency of the scintillator. Their impact on the detector performance, especially on the energy and time resolution, has been evaluated in a Monte Carlo simulation.

Zusammenfassung

Der kosmogene Untergrund hat großen Einfluss auf die Suche nach seltenen Neutrinoereignissen in Flüssigszintillationsdetektoren: Die genaue Bestimmung des durch kosmische Myonen, kosmogene Neutronen und Radioisotopen erzeugten Untergrunds ist essenziell für den Nachweis solarer Neutrinos in Borexino. Er hat aber auch Auswirkungen auf das Design des zukünftigen LENA Experiments.

In der vorliegenden Arbeit wurde die Effizienz der in Borexino zur Myonidentifikation benutzten Kriterien ausgewertet, um die verbleibende Kontamination des zur Neutrino-Analyse verwendeten Datensatzes mit Myon-Ereignissen zu bestimmen. Während die Unterdrückung kosmischer Myonen für den Nachweis solarer Neutrinos die Anforderungen übertrifft, stellt die Erkennung der von Myonen im Detektionsvolumen produzierten Radionuklide eine Herausforderung dar. Speziell im Fall der solaren CNO und pep Neutrinos dominiert die Rate von kosmogenen ^{11}C Beta-Zerfällen das erwartete Neutrinosignal um mindestens eine Größenordnung. Eine Messung dieser bisher unbestimmten Beiträge zum solaren Neutrinospektrum in Borexino ist daher nur möglich, falls die Identifikation eines Großteils der einzelnen ^{11}C Ereignisse gelingt. Die in dieser Arbeit erstellte Myonspurrekonstruktion ist dafür eine zwingende Voraussetzung: Die Ortsinformation der Myonspur ist einerseits grundlegend für das Dreifachkoinzidenzveto, das für die direkte Erkennung von ^{11}C Zerfällen benutzt wird. Andererseits ist die Myonrekonstruktion eine Grundvoraussetzung für die Untersuchung von den durch Myonen verursachten Neutronenschauern, die ^{11}C im größeren Abstand zur Myonspur erzeugen können. Die Ergebnisse zur Ortsauflösung der Rekonstruktion und zur Multiplizität und lateralen Ausdehnung von Neutronenschauern erlauben es, optimale Parameter für die Reduktion des ^{11}C -Untergrunds zu bestimmen.

Aufgrund ihrer ausgezeichneten Untergrunddiskrimination bietet sich für Flüssigszintillationsdetektoren auch die Chance auf einen erstmaligen Nachweis des Diffusen Supernova-Neutrino hintergrunds (DSNB). Es ist jedoch ein Experiment von der Größenordnung von LENA notwendig, um diesen extrem niedrigen Neutrinofluss nachzuweisen. Basierend auf der in dieser Arbeit vorgestellten Analyse zu kosmogenen und Neutrino-Untergrundquellen kann ein nahezu untergrundfreies Beobachtungsfenster bestimmt werden, das von 10 bis 30 MeV reicht. Aktuelle Modelle für den DSNB sagen für LENA eine Rate von etwa 10 Antineutrinoereignissen pro Jahr voraus. Die Ergebnisse einer Monte Carlo-Simulation deuten darauf hin, dass es durch Spektroskopie der Messdaten einiger Jahre möglich sein wird, Rückschlüsse auf das zugrundeliegende Supernova-Neutrinospektrum zu ziehen; Voraussetzung sind allerdings präzise Kenntnis der kosmischen Supernova-Rate durch optische Beobachtungen.

Neben dieser phänomenologischen Arbeit wurden in einem Laborexperiment die optischen Streulängen möglicher Szintillatorkandidaten für LENA bestimmt. Streu- und Abschwächlänge beschreiben die optische Transparenz eines Szintillators. Ihr Einfluss auf die Energie- und Zeitauflösung des zukünftigen Detektors wurde in einer Monte Carlo-Simulation ermittelt.

Contents

1	Low-Energetic Neutrinos	1
1.1	Neutrinos as Particles	2
1.1.1	Neutrinos in the Standard Model	2
1.1.2	Vacuum Oscillations	3
1.1.3	The MSW-Effect	5
1.2	Neutrinos as Messengers	7
1.2.1	Solar Neutrinos	9
1.2.2	Supernova Neutrinos	10
1.2.3	The Diffuse Supernova Neutrino Background	12
1.2.4	Geoneutrinos	14
1.2.5	Dark Matter Annihilation	16
2	Real-Time Neutrino Detection	17
2.1	Detection Technique	18
2.1.1	Water-Čerenkov Detectors	18
2.1.2	Liquid-Scintillator Detectors	19
2.2	Detection Reactions	21
2.2.1	Elastic Scattering	21
2.2.2	Inverse Beta Decay	23
2.2.3	Reactions on Carbon	23
2.3	Background Sources	24
2.3.1	Intrinsic Radioactive Contaminants	24
2.3.2	Cosmic Muons	26
2.3.3	Cosmogenic Radio-Isotopes	27
2.3.4	Fast Neutrons	31
3	The BOREXINO Experiment	33
3.1	Physics Program	33
3.1.1	Solar ${}^7\text{Be}$ Neutrinos	34
3.1.2	Solar ${}^8\text{B}$ Neutrinos	34
3.1.3	<i>CNO</i> , <i>pep</i> , and <i>pp</i> Neutrinos	36
3.1.4	Geoneutrinos	37

3.1.5	Supernova Neutrinos	38
3.1.6	The CNGS neutrino beam	39
3.2	Detector Design	39
3.2.1	Inner Detector	39
3.2.2	Outer Detector	41
3.2.3	Current Status	42
3.3	Data Acquisition System	42
3.4	<i>Echidna</i> Analysis Software	44
4	Muon Identification in BOREXINO	49
4.1	Muon Identification Criteria	49
4.1.1	Outer Detector Flags	50
4.1.2	Inner Detector Flags (IDF)	51
4.2	Flagging Efficiencies	54
4.2.1	Direct Efficiency Determination	54
4.2.2	Relative Efficiencies	56
4.2.3	The Deutsch parameter	58
4.3	Muon Tagging Time Stability	59
4.3.1	Data Screening	59
4.3.2	Problematic Runs	60
4.3.3	Run Validation	61
4.3.4	Long-Term Stability	62
5	BOREXINO Muon Tracking	65
5.1	Outer Detector Tracking	66
5.1.1	Candidate Clusters	66
5.1.2	Cluster Splitting	69
5.1.3	Entry and Exit Point	69
5.1.4	MC Simulations	71
5.2	Inner Detector Tracking	72
5.2.1	Entry Point	73
5.2.2	Track Orientation	73
5.2.3	Impact Parameter	76
5.2.4	Impact Point	78
5.3	Global Fit	80
6	Cosmic Background in BOREXINO	83
6.1	Cosmic Muons	83
6.1.1	Muon Rate and Flux	84
6.1.2	Muon Veto Efficiency	85
6.1.3	Tracking Efficiency	87

6.1.4	Angular Distributions	87
6.1.5	Tracking Angular Resolution	91
6.2	Cosmogenic Neutrons	93
6.2.1	Neutron DAQ	94
6.2.2	Neutron Capture Energy	95
6.2.3	Neutron Capture Time	97
6.2.4	Neutron Rate	98
6.2.5	Neutron Multiplicity	100
6.2.6	Veto of Cosmogenic ^{11}C	100
6.2.7	Distance to Parent Muon	103
7	The LENA Project	109
7.1	Physics Program	109
7.1.1	Solar Neutrinos	110
7.1.2	Supernova Neutrinos	111
7.1.3	Geoneutrinos	112
7.1.4	Dark Matter Annihilation Neutrinos	113
7.1.5	Nucleon Decay	113
7.1.6	Neutrino Parameters	114
7.2	Detector Design	115
7.2.1	Detector Layout	115
7.2.2	Background Levels	117
7.2.3	The LAGUNA Detector Site Study	117
8	Scattering Length Experiment	119
8.1	Light Propagation in a Medium	119
8.1.1	Absorption/Re-Emission	120
8.1.2	Rayleigh Scattering	121
8.1.3	Mie Scattering	122
8.2	Investigated Scintillators	123
8.2.1	Solvents	123
8.2.2	Wavelength Shifters	126
8.3	Experimental Setup	127
8.3.1	General Layout	127
8.3.2	Optical Components	128
8.3.3	Electronics and DAQ Components	130
8.4	Data Analysis	131
8.5	Systematic Uncertainties	134
8.5.1	Measured Intensity Ratio	134
8.5.2	Background Correction	135

8.5.3	Photomultiplier-Induced Uncertainties	136
8.5.4	Reflective Correction	136
8.5.5	Transmission of Greyfilters and Polarizer	137
8.5.6	LED emission waveband	138
8.5.7	Solid Angle Ω	138
8.6	Results	142
8.6.1	First series: Screening Materials	142
8.6.2	Second Series: Testing Wavelength Dependence	143
8.6.3	Implications for LENA	144
9	Detection of the DSNB in LENA	151
9.1	$\bar{\nu}_e$ Signal	152
9.2	Antineutrino Backgrounds	155
9.2.1	Reactor Antineutrinos	155
9.2.2	Atmospheric Antineutrinos	159
9.3	Cosmogenic Background	160
9.3.1	${}^9\text{Li}$ In-Situ Production	160
9.3.2	Fast Neutrons	161
9.4	Detection Potential	163
9.4.1	Energy Window	163
9.4.2	Event Rates	165
9.4.3	Spectral Analysis	166
10	Conclusions	171
10.1	BOREXINO	171
10.2	LENA	173
10.3	Outlook	174
	Bibliography	176
	Acknowledgments	184

Chapter 1

Low-Energetic Neutrinos

In 1930, the neutrino was first introduced by Wolfgang Pauli in order to conserve energy and spin in the β decay of radioactive nuclei [1]. Since then, the exotic properties of this particle have baffled physicists more than once: The most prominent case was presumably the unexpectedly low rate of solar neutrinos measured in terrestrial neutrino detectors [2, 3, 4], commonly known as the Solar Neutrino Problem [5]. But even after the discovery of neutrino oscillations, a significant number of open questions remain: The absolute mass scale of the neutrino mass eigenstates, their hierarchy, the size of the small mixing angle θ_{13} , and the size of the CP violating phase δ in the neutrino mixing matrix are up to now undetermined. Most fundamentally, the nature of the neutrino as a Dirac or Majorana particle is still unknown [6, 7].

However, our knowledge of neutrino properties is now precise enough to finally exploit neutrinos for the investigation of their emission sources [8]. While the minuscule interaction of neutrinos with matter is cumbersome for detection, it offers an important advantage in the observation of astrophysical objects: Unlike the charged particles of cosmic radiation, neutrinos are not deflected by galactic and intergalactic magnetic fields, pointing back at their source. In this respect, neutrinos can be used analogously to photons in conventional astronomy. Especially for high-energetic neutrinos, this has inspired the installation of large-volume neutrino telescopes in natural water reservoirs: presently, ANTARES in the Mediterranean [9] and ICECUBE in the antarctic ice crust [10] are the most prominent examples, the latter aiming to reach a detection volume of one cubic kilometer [11].

In general, neutrinos are not affected by matter surrounding their source or located in the line of sight to a terrestrial detector. This is a crucial difference to the observation of light: Photons reaching an optical telescope are mostly emitted at the surface of stellar objects and have a spectrally dependent probability to be absorbed by intermediary gas and dust clouds or by the Earth's atmosphere. Neutrinos on the other hand are presently a unique way to directly observe fusion processes in the center of the Sun, the formation of a proto-neutron star hidden inside a stellar envelope, or the production of thermal heat in the deep layers of the Earth [8].

The neutrinos created in these processes are of rather low energies: Due to their origin in nuclear interactions, the energy scale is reaching from 100 keV to at most 50 MeV. The detection thresholds of neutrino telescopes like ICECUBE are far too high in energy to be sensitive to these neutrinos. The experiments dedicated to low-energy neutrino

search are usually lower in volume and at the same time more densely instrumented with light detectors. Both the running solar-neutrino experiment BOREXINO [12] and the future neutrino observatory LENA [13] are liquid-scintillator detectors aiming for the observation of low-energy astrophysical neutrinos.

The present work encompasses experimental works, data analysis, and phenomenology on both BOREXINO and LENA. Their basic detection techniques will be described in Chap. 2, while their experimental setup and physics program will be outlined in Chaps. 3 and 7. The main focus of the work on BOREXINO is on the identification and investigation of cosmic muons and cosmogenic radionuclides, which pose the main background for solar CNO/pep neutrino search. While the efficiency of the BOREXINO muon veto is determined in Chap. 4, the muon track reconstruction algorithms devised as part of this thesis are introduced in Chap. 5. The muon tracking is utilized in the following analysis of cosmic muons, in-situ produced neutrons, aiming at the rejection of cosmogenic ^{11}C background events. The results are presented in Chap. 6. As a second focus of this thesis, the technical feasibility and physics potential of LENA is investigated: A laboratory experiment determining the optical scattering length of an assortment of scintillator solvents has been performed at the TUM. The experiment and the implications of the results for light yield and timing capabilities of LENA are presented in Chap. 8. Moreover, the large volume and excellent background rejection of the LENA detector will allow the detection of the Diffuse Supernova Neutrino Background (DSNB). An overview of the background sources and the gain of a spectroscopic measurement in LENA are given in Chap. 9.

In the present chapter, Sect. 1.1 is intended to give a short account of presently known neutrino properties in the context of the Standard Model (SM) of particle physics, and the aspects in which neutrinos demand an expansion of this model. Sect. 1.2 is an overview of neutrino production at low energies, encompassing both astrophysical and terrestrial sources.

1.1 Neutrinos as Particles

In the late 20th century, neutrino physics gave first indications of new physics beyond the SM [14]: The main conflict arises from the observation of neutrino oscillations in several experiments [15, 16, 17, 18], which establishes the concept of non-zero neutrino mass terms instead of the massless SM neutrinos. Nevertheless, this section will start from the SM to describe neutrino properties before concentrating on neutrino oscillations, both in vacuum and matter. For a more thorough discussion of the present status of neutrino physics and its future perspectives, see for example [7, 19].

1.1.1 Neutrinos in the Standard Model

The SM [14, 20] describes the neutrinos as massless and electrically neutral partners of the charged leptons. The neutrino counterparts of electron, muon, and tauon are commonly denoted as ν_e , ν_μ , and ν_τ , the index describing the so-called family or flavor of the particle: In weak charged current (CC) reactions, charged leptons are converted into their neutrino-partners of the same flavor and vice versa. The exchange particles

Fermions	Doublets	Singlets
Quarks	$\begin{pmatrix} d_L \\ u_L \end{pmatrix}, \begin{pmatrix} s_L \\ c_L \end{pmatrix}, \begin{pmatrix} b_L \\ t_L \end{pmatrix}$	$(d_R), (u_R), (s_R), (c_R), (b_R), (t_R)$
Leptons	$\begin{pmatrix} e_L \\ \nu_{e,L} \end{pmatrix}, \begin{pmatrix} \mu_L \\ \nu_{\mu,L} \end{pmatrix}, \begin{pmatrix} \tau_L \\ \nu_{\tau,L} \end{pmatrix}$	$(e_R), (\mu_R), (\tau_R)$

Currents	Boson
Charged (CC)	W^\pm
Neutral (NC)	Z^0

Table 1.1: Quarks and leptons in the scope of weak interaction. Only left-handed neutrinos are part of the SM and can be associated to their charged lepton partners. Weak currents are described by the exchange of massive vector bosons [14].

of weak interactions, the W^\pm and Z^0 vector bosons, couple only to left-handed (LH) particles (or right-handed (RH) antiparticles). Therefore, LH charged leptons and their neutrino partners form doublet states of weak interaction, while RH charged leptons are described by singlet states. RH states of the neutrino are assumed not to exist, as neutrinos are generated exclusively LH and – as they are massless – their helicity is a conserved quantity. According to CP symmetry, weak vector bosons couple only to RH antiparticles, while LH antiparticles remain inactive. Antineutrinos are therefore exclusively right-handed. The situation in the quark sector can be described in similar fashion, allowing to arrange the particles taking part in weak interactions as depicted in Tab. 1.1.

While the coupling strengths of W^\pm and Z^0 bosons to the weak charge of fermions is comparable to electromagnetic interactions, the fact that the weak exchange bosons are massive ($m_W = 80 \text{ GeV}$, $m_Z = 92 \text{ GeV}$) significantly decreases the effective reach and observable strength of the force at low energies. In this regime, neutrino interactions can therefore be described as point-like, the way weak interactions were first introduced by E. Fermi [20, 21]. The Fermi coupling constant $G_F \cong 90 \text{ eV fm}^3$ that enters neutrino scattering cross sections quadratically is a rather small quantity: Typical cross sections are therefore of the order of 10^{-43} to 10^{-44} cm^2 (Sect. 2.2). Usually, CC reactions between particles provide larger cross sections than neutral currents (NC).

1.1.2 Vacuum Oscillations

The SM assumes the neutrino to be massless, thereby forbidding a mixture of mass and flavor eigenstates as it is present in the quark sector. Assuming a non-zero neutrino rest mass and a mass splitting between the eigenstates, a similar mixing of mass eigenstates $|\nu_i\rangle$ and weak eigenstates $|\nu_\alpha\rangle$ can be introduced [7, 20]:

$$|\nu_i\rangle = U_{\alpha i} |\nu_\alpha\rangle \quad (1.1)$$

The PMNS¹ matrix U is usually parameterized by three rotation angles θ_{ij} and a CP violating phase δ which is written alongside the still unknown mixing angle θ_{13} :

$$U = \begin{pmatrix} 1 & 0 & 0 \\ 0 & c_{23} & s_{23} \\ 0 & -s_{23} & c_{23} \end{pmatrix} \begin{pmatrix} c_{13} & 0 & s_{13}e^{-i\delta} \\ 0 & 1 & 0 \\ -s_{13}e^{-i\delta} & 0 & c_{13} \end{pmatrix} \begin{pmatrix} c_{12} & s_{12} & 0 \\ -s_{12} & c_{12} & 0 \\ 0 & 0 & 1 \end{pmatrix} \quad (1.2)$$

Here, c_{ij} and s_{ij} are used as abbreviations of $\cos\theta_{ij}$ and $\sin\theta_{ij}$, respectively. Three neutrino families are assumed, as the number of active neutrino flavors can be determined from the Z^0 decay width at LEP [22]. Two additional CP violating phases can be introduced if the neutrino is a Majorana rather than a Dirac particle [7].

The discrepancy of mass and flavor eigenstates leads to flavor oscillations of neutrinos along their trajectory [7, 20]: The probability $P_{\alpha\rightarrow\beta}$ that a neutrino produced in flavor α is detected as a neutrino of flavor β in an experiment depends on the ratio ℓ/E of the distance ℓ the neutrino has travelled and its energy E . The oscillations are caused by the phase difference in the propagation of the underlying neutrino mass eigenstates; in the most general case, the probability is

$$P_{\alpha\rightarrow\beta} = |\langle\nu_\beta|\nu_\alpha(\ell)\rangle|^2 = \left| \sum_i U_{\alpha i}^* U_{\beta i} e^{-\frac{m_i^2 \ell}{2E}} \right|^2. \quad (1.3)$$

In experiments, the ratio of distance to neutrino energy ℓ/E that is governing the oscillations is often at a scale that allows to choose a simplified two-flavor approach: In this case, the PMNS matrix is reduced to a 2×2 rotation matrix of a single mixing angle θ , and the oscillation probability P can be written as

$$P = \sin^2 2\theta \sin^2 \left(\frac{\Delta m^2 \ell}{4E} \right) = \sin^2 2\theta \sin^2(\ell/\ell_{\text{osc}}). \quad (1.4)$$

The oscillation length $\ell_{\text{osc}} = \frac{4E}{\Delta m^2}$ can be introduced as a typical length scale for the oscillation. $\Delta m^2 = m_1^2 - m_2^2$ is the mass squared difference of the two participating neutrino eigenstates.

The knowledge of the mixing angles and quadratic mass splittings was gained in a series of experiments: While the value of the solar mixing angle $\theta_{12} \cong 35^\circ$ is mainly fixed by the ^8B neutrino measurements performed by the SNO and SUPER-KAMIOKANDE experiments [23, 24], the mass difference $\Delta m_{12}^2 \cong 8\times 10^{-5} \text{eV}^2$ is determined by the results of the KAMLAND reactor experiment [25]. SUPER-KAMIOKANDE has measured the atmospheric mixing angle $\theta_{23} \cong 43^\circ$ to a high precision [26]. However, it is still unknown whether it is truly maximal. The best value for $\Delta m_{23}^2 \cong \pm 2.5\times 10^{-3} \text{eV}^2$ is currently given by the MINOS experiment [27]. Different from the solar case, the sign of the mass difference is not known yet, allowing both for normal and inverted hierarchy of the neutrino mass eigenstates. As the solar splitting is much smaller, the approximation $\Delta m_{13}^2 \approx \Delta m_{23}^2$ is common. Finally, the best direct limit on the reactor mixing angle $\theta_{13} \leq 13^\circ$ is determined by the CHOOZ experiment [28]. Tab. 1.2 summarizes the results of a global analysis on all available oscillation data performed in 2008 [29, 30]. Although the best fit value for $\theta_{13} \neq 0$, it is still compatible to fully suppressed mixing.

¹Named after Pontecorvo, Maki, Nakagawa, and Sakata who introduced the formalism for ν flavor mixing.

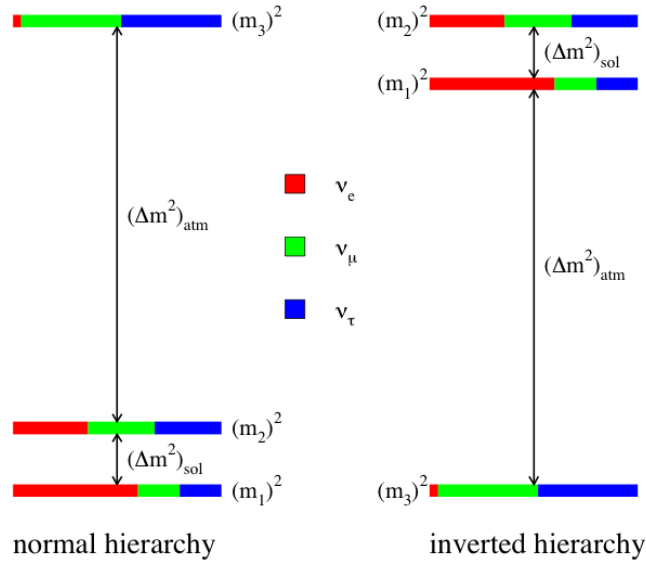


Figure 1.1: Ordering of the neutrino mass eigenstates, for normal (left) and for inverted (right) hierarchy. The colors depict the contribution of electron (red), muon (blue), and tau (green) flavor eigenstates to each mass eigenstate.

Parameter	Best Fit $\pm 1\sigma$	3σ Interval
$\Delta m_{12}^2 [10^{-5} \text{ eV}^2]$	$7.67^{+0.22}_{-0.21}$	$7.07 - 8.34$
$\Delta m_{13}^2 [10^{-3} \text{ eV}^2]$	-2.39 ± 0.12 $+2.49 \pm 0.12$	$-(2.02 - 2.79)$ $+(2.13 - 2.88)$
$\sin^2 \theta_{12}$	$0.321^{+0.023}_{-0.022}$	$0.26 - 0.40$
$\sin^2 \theta_{23}$	$0.47^{+0.07}_{-0.06}$	$0.33 - 0.64$
$\sin^2 \theta_{13}$	0.003 ± 0.015	≤ 0.049

Table 1.2: Neutrino quadratic mass splittings and mixing angles from a global analysis of all oscillation data available in 2008 [29, 30].

While the measurements of oscillations demand that at least two of the neutrinos are massive, the absolute scale of neutrino masses still remains undetermined. The currently best direct limit $m_{\nu_e} \leq 2.2 \text{ eV}$ has been achieved by the MAINZ and TROITSK experiments by measuring the endpoint of the Tritium β decay spectrum [31, 32]. More stringent but indirect limits can be set by cosmology and neutrinoless double beta decay [33, 34]. Moreover, the hierarchy of the neutrino mass eigenstate is still open as vacuum neutrino oscillations are not sensitive to the sign of the Δm^2 's [7]. However, the relative order of the masses of ν_1 and ν_2 is determined by the observation of the MSW-effect in solar neutrinos. Fig. 1.1 illustrates the remaining ambiguity by showing the two possibilities for the ordering of the three mass eigenstates and their individual flavor contributions.

1.1.3 The MSW-Effect

When traversing matter, neutrinos undergo coherent forward-scattering on the weak potential generated by electrons and nucleons [7, 20]. Normally, the effect is negligible.

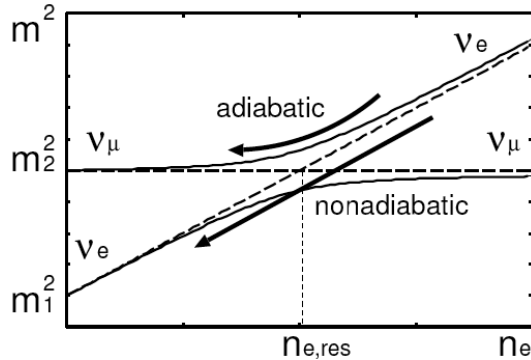


Figure 1.2: An illustration of the impact of the matter potential inside the Sun on the survival probabilities of ν_e created at the center of the Sun (right), and propagating through a decreasing matter potential to vacuum. If the adiabaticity condition is fulfilled, ν_e will leave the sun in the mass eigenstate ν_2 which contains mainly ν_μ [20].

But the density of celestial bodies like stars or even planets like the Earth is large enough to generate an observable effect. Named as the Mikheyev-Smirnov-Wolfenstein effect after its discoverers, it has been grandly confirmed by the energy-dependent oscillation probability observed in solar neutrinos [35].

At low energies, all neutrino flavors interact via NC with the electrons and neutrons of the medium. But only ν_e 's are able to scatter on electrons in CC reactions, enlarging their scattering amplitude with respect to NC reactions by a factor

$$A = 2\sqrt{2}G_F N_e p, \quad (1.5)$$

where N_e is the electron density in the medium and p the neutrino momentum. It is possible to interpret the potential terms of both NC and CC scattering as additions to the mass terms of the eigenstates in the Hamiltonian. As only differences in the mass terms drive the oscillations, the equal shift of all neutrino masses by the NC interactions can be neglected. The CC interaction term A on the other hand only affects the ν_e flavor proportion of the mass eigenstates. If large enough, the matter potential A can therefore significantly change the effective Δm_m^2 in matter. This also affects the oscillation probabilities described by $\sin^2 \theta_m$. In general, the mass eigenstate ν_1 is affected the most as its proportion of the flavor ν_e is the largest; at very high electron densities, like it is the case for the solar center or the inner envelope of a SN progenitor star, the lightest eigenstate in vacuum, ν_1 , can even become heavier than ν_2 .

The MSW resonance effect describes the impact of a slowly varying matter potential on neutrino oscillation probabilities: Fig. 1.2 illustrates the situation for solar neutrinos generated at the center of the Sun. Again, the simplified approach of a two-neutrino picture is sufficient [20]. Therefore, the effective matter oscillation amplitude $\sin^2 2\theta_m$ and the vacuum parameters θ and Δm^2 can be set in the relation [20]

$$\sin^2 2\theta_m = \frac{\sin^2 2\theta}{\left(\frac{A}{\Delta m^2} - \cos 2\theta\right)^2 + \sin^2 2\theta}. \quad (1.6)$$

There is a critical matter density ρ_c for which the equation $A = \Delta m^2 \cos 2\theta$ is fulfilled and the oscillation probability becomes maximal while Δm_m^2 of the eigenstates gets

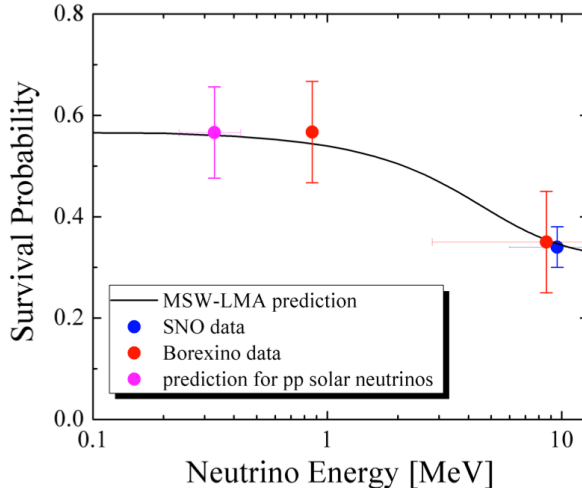


Figure 1.3: The survival probability of solar ν_e neutrinos. At low energies, the prediction for pp neutrinos is shown in pink, while the SNO ${}^8\text{B}-\nu$ data is included in blue at high energies. BOREXINO is able to provide the input on both ${}^7\text{Be}$ and low-energetic ${}^8\text{B}-\nu$'s [37].

minimal. At the higher densities of the solar core, the oscillation amplitude decreases to very small values, while at the same time the proportion of ν_2 to ν_e rises. A ν_e produced in a fusion reaction in the solar center is produced in the mass eigenstate $\nu_{2,m}$ only, and no oscillations occur. Approaching the critical density, the neutrinos will remain in the mass eigenstate $\nu_{2,m}$ if the gradient in density is small in comparison to the matter oscillation length $\ell_m = \ell \sin 2\theta / \sin 2\theta_m$. In the case of such an adiabatic conversion, mostly ν_μ will remain when the neutrino reaches the vacuum: The flavor contributions to ν_2 will have changed because now the vacuum PMNS matrix applies. The MSW survival probability of

$$P_{ee} = \sin^2 2\theta_{12} \cong 30\% \quad (1.7)$$

reflects the chance of the neutrinos to be detected as ν_e in a terrestrial detector.

As the potential A is a function of both the electron density N_e and the neutrino momentum p , only part of the solar neutrino spectrum is undergoing this effect. While both pp and ${}^7\text{Be}-\nu$'s are too low in energy to be affected and undergo only vacuum oscillations, the high-energetic part of the ${}^8\text{B}-\nu$ spectrum is subject to the MSW-effect. This energy-dependence of the survival probability P_{ee} of solar ν_e is depicted in Fig. 1.3 (compare Sect. 1.2.1). For a more detailed treatment of the matter effects, see also [20, 36].

1.2 Neutrinos as Messengers

Based on the current understanding of neutrinos (Sect. 1.1), low energetic neutrinos can be used as probes to investigate the physics processes underlying their production and propagation, at the same time learning about the composition of their sources [8].

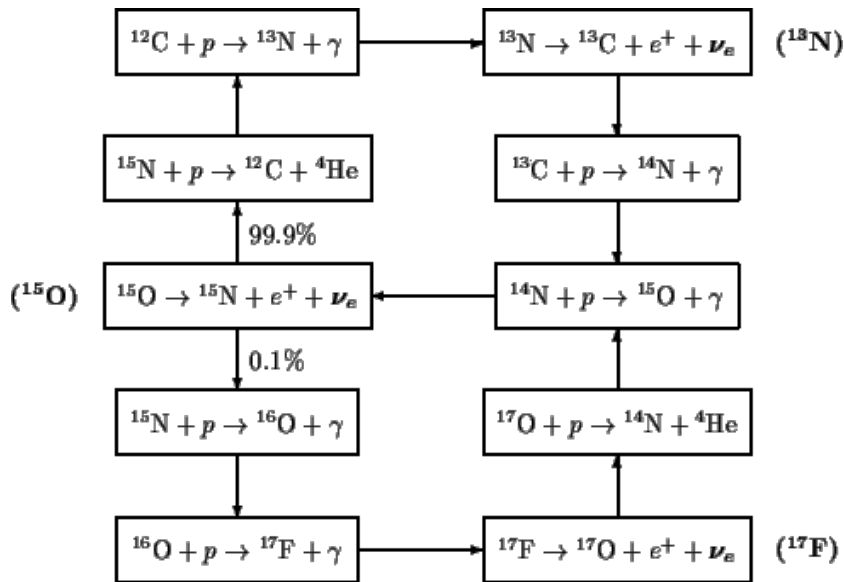
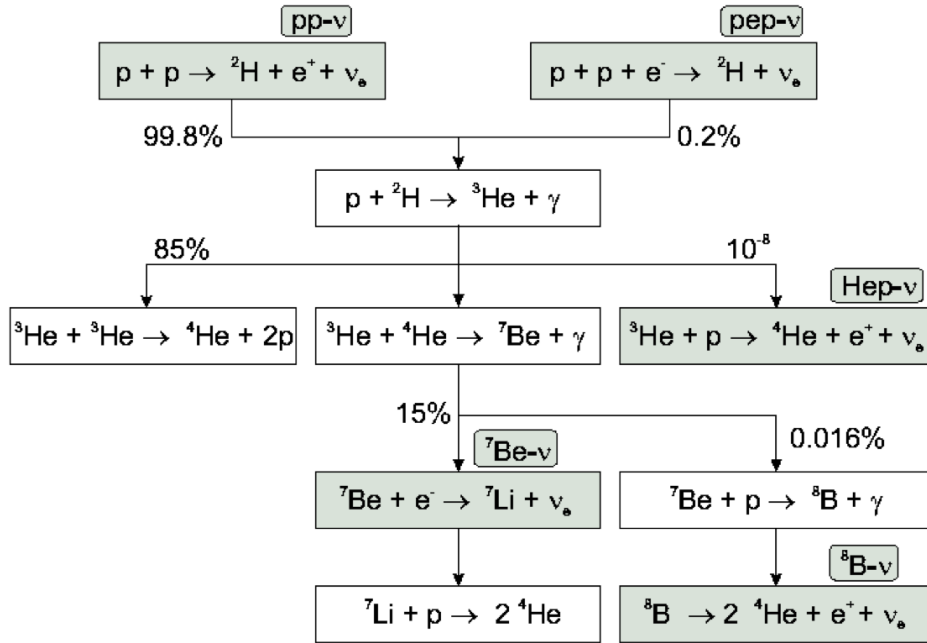


Figure 1.4: *Top:* The reactions of the solar pp chain that describes the fusion to ${}^4\text{He}$ and that is responsible for 99% of the solar ν flux. The sub-ratios of the different branches are included. *Bottom:* Hydrogen fusion by the CNO cycle which uses the eponymous elements as catalysts. Two alternative sub-cycles are possible, the upper one is, however, dominant in the Sun.

Source	Energy [MeV]	Neutrino Flux [see caption]		
		BPS08(GS)	BPS08(AGS)	Difference
pp	≤ 0.420	5.97 (0.6 %)	6.04 (0.5 %)	1.2 %
pep	1.442	1.41 (1.1 %)	1.45 (1.0 %)	2.8 %
hep	≤ 18.773	7.90 (15 %)	8.22 (15 %)	4.1 %
${}^7\text{Be I}$	0.384	0.51 (6 %)	0.46 (6 %)	10 %
${}^7\text{Be II}$	0.862	4.56 (6 %)	4.11 (6 %)	10 %
${}^8\text{B}$	≤ 14.6	5.94 (11 %)	4.72 (11 %)	21 %
${}^{13}\text{N}$	≤ 1.199	2.88 (15 %)	1.89 (${}^{+14\%}_{-13\%}$)	34 %
${}^{15}\text{O}$	≤ 1.732	2.15 (${}^{+17\%}_{-16\%}$)	1.34 (${}^{+16\%}_{-15\%}$)	31 %
${}^{17}\text{F}$	≤ 1.740	5.82 (${}^{+19\%}_{-17\%}$)	3.25 (${}^{+16\%}_{-14\%}$)	44 %

Table 1.3: Energy and predicted flux for the solar neutrinos produced along the pp chain and the CNO cycle. The fluxes are derived assuming high (GS) and low (AGS) solar metallicity. Relative uncertainties are given in brackets. The last column shows the relative difference in flux predictions. The fluxes are presented in units of 10^{10} (pp), 10^9 (${}^7\text{Be}$), 10^8 (pep , ${}^{13}\text{N}$, ${}^{15}\text{O}$), 10^6 (${}^8\text{B}$, ${}^{17}\text{F}$), 10^3 (hep) $\text{cm}^{-2}\text{s}^{-1}$ [38].

1.2.1 Solar Neutrinos

Solar energy production relies on the binding energy released by the fusion of protons to Helium. The fusion of charged nuclei is impeded by the Coulomb forces between protons. However, the quantum mechanical tunnel effect allows protons to fuse even at the relatively low temperature of the solar core of $\sim 10^7$ K.

In the 1930's, two processes have been discovered by which the fusion of four protons to one ${}^4\text{He}$ nucleus is possible [39, 40]: The first one, accounting for $\sim 99\%$ of the solar energy production, is the pp chain. The basic step of the chain is the fusion of two protons to a deuterium nucleus after which the chain is named. Fig. 1.4 depicts (on the top) the full chain that splits into three branches. The net reaction is in any case

$$4p \rightarrow {}^4\text{He} + 2e^+ + 2\nu_e + 26.7 \text{ MeV}. \quad (1.8)$$

Independently of the pp sub-branch, two ν_e have to be produced in every fusion to ${}^4\text{He}$. The neutrino energy is strongly dependent on the nuclear reaction it originates from: While the pp neutrinos of the first reaction in the chain are with a spectral endpoint of 0.42 MeV rather low in energy, the maximum energy of hep neutrinos is 18.8 MeV. The abundances of these neutrinos are proportional to the probability at which the production processes occur: Tab. 1.3 lists ν energies and fluxes as predicted by the most recent model calculations [38], while the spectra are shown in Fig. 1.5.

The second possibility for the fusion to ${}^4\text{He}$ is via the CNO cycle. The cosmologically youngest Population I stars including our Sun are enriched in metallicity Z to a level of 2%. Metals include all elements heavier than Hydrogen and Helium, which make up 75% and 23% of the solar mass M_\odot , respectively. There are two reaction cycles using solar Carbon, Nitrogen, and Oxygen as catalysts to fuse protons to ${}^4\text{He}$. Once again, two ν_e are produced in one full cycle. In the present status of the Sun, the solar core temperature is too low to allow for a large contribution of the CNO cycle to the energy budget, and therefore the CNO - ν flux is small. However, model calculations

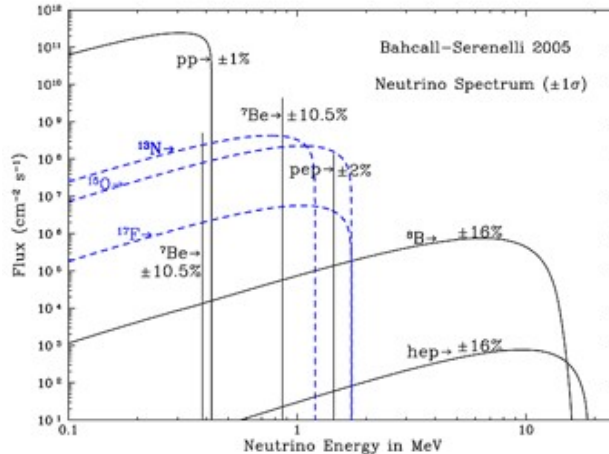


Figure 1.5: Solar neutrino spectrum based on the Standard Solar Model by Bahcall and Serenelli in 2005 [41].

predict a rise in core temperature with the progress of Hydrogen burning, and therefore an increase of the *CNO* contribution to the solar energy budget to a 30 % level during the Sun’s life time.

The solar model calculations necessary to derive the neutrino fluxes were originally done by J. Bahcall [41], and were later continued by M. Pinsonneault and A. Serenelli (BPS) [38]. The value of Z is one of the input parameters to the calculations. Tab. 1.3 shows the predicted fluxes both for *pp* and *CNO* neutrinos based on two different analyses of the elemental abundances: Both use the Fraunhofer lines in the solar electromagnetic spectrum as a fingerprint of the elements contained in the solar photosphere. The more recent analysis performed by M. Asplund, N. Grevesse, and A. J. Sauval (AGS) indicates a lower Z value [42]. While the self-consistency of the results for different indicator molecules is better, the predicted sound speeds in the solar matter are now in conflict with the measurements done by helioseismology. This was not the case for the earlier analysis by Grevesse and Sauval (GS) [43]. It has been proposed that solar neutrinos could be used to solve this dilemma as especially ${}^7\text{Be}$, ${}^8\text{B}$ and naturally the *CNO* ν flux predictions are sensitive to Z .

1.2.2 Supernova Neutrinos

At the end of Fe burning, a star more massive than $8 M_{\odot}$ becomes unstable against its own gravitation. The Fermi-pressure of the electrons in the innermost iron-core fails to balance the gravitational pressure, and the core collapses to a neutron star. This collapse comes to a sudden halt when the core reaches nuclear density; further material bounces off the ultra-dense core and forms an outwards-running shock front that disrupts the stellar envelope. These events are optically very bright and are classified as Supernovae (SNe) Type IIa [44] by astronomers.

During the collapse, large numbers of ν_e ’s are released by the conversion of protons into neutrons inside the core region, the so-called neutronisation burst. As about 3×10^{53} erg of gravitational binding energy are released, the proto-neutron star is heat-

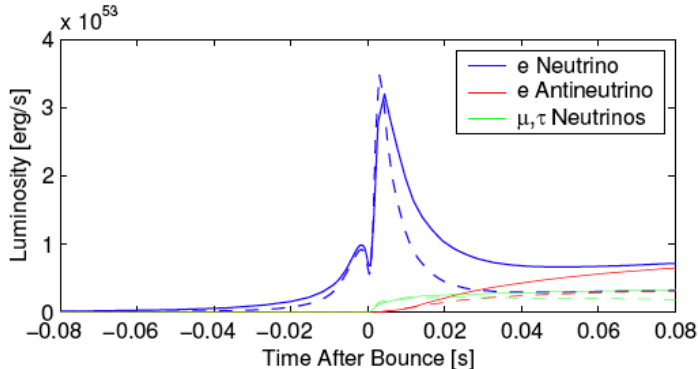


Figure 1.6: Development of the fluxes of the individual ν flavors around the time of a SN core-collapse. The neutronisation burst is clearly visible in the ν_e flux. Later on, the cooling of the proto neutron star by $\nu\bar{\nu}$ pair production leads to an increase in the fluxes of all flavors [45].

ing up considerably. However, this ultra-dense core is opaque to all kinds of radiation but neutrinos; it cools down by the emission of $\nu\bar{\nu}$ pairs of all flavors, releasing 99% of binding energy in the form of ν 's. Contemporary SN models assume a ν -induced heating in the dense regions of the stellar envelope behind the shock front nurturing the explosion that would otherwise stall. Fig. 1.6 shows the neutrino flux of the different flavors relative to the time scale of the core collapse: the neutronisation burst and the onset of the neutrino cooling can be clearly distinguished [45].

There have been several Monte Carlo calculations by different groups predicting the ν spectra of a SN explosion. Only the simulations done at the Lawrence-Livermore National Laboratory were continued far enough to observe an explosion [46]. On the other hand, the more recent calculations performed by Thompson, Burrows, and Pinto (TBP) [47] and by Keil, Raffelt, and Janka (KRJ) [48] are considering the neutrino transport in more detail. The neutrinos are emitted in different layers (the so-called neutrino-spheres) of the core as their interaction possibilities with matter vary with their flavor. In first approximation, the energy spectra can be assumed to follow the Fermi distribution. The MC spectra for the individual flavors can be parameterized in the form

$$\frac{dN_\nu}{dE_\nu} = \frac{(1 + \beta_\nu)^{1+\beta_\nu} L_\nu}{\Gamma(1 + \beta_\nu) \langle E_\nu \rangle^2} \left(\frac{E_\nu}{\langle E_\nu \rangle} \right)^{\beta_\nu} e^{-(1+\beta_\nu)E_\nu/\langle E_\nu \rangle} \quad (1.9)$$

where N_ν is the number of neutrinos, E_ν the neutrino energy, and L_ν the expected luminosity of the individual flavor [49]. In general, equipartition of the total binding energy to all L_{ν_i} is assumed as the neutrinos originate from pair production. The parameters describing the spectral shape are the mean energy $\langle E_\nu \rangle$ and a shape or pinching factor β_ν which represents the impact of the spatial extension of the neutrinosphere. The results of the MC simulations for ν_e , $\bar{\nu}_e$ and $\nu_x = \{\nu_\mu, \bar{\nu}_\mu, \nu_\tau, \bar{\nu}_\tau\}$ are presented in Tab. 1.4. The (mixed) fluxes of $\bar{\nu}_e$ and $\bar{\nu}_x$ provide the main signal in a liquid-scintillator detector via the inverse beta decay (Sect. 2.2.2).

In 1987, terrestrial neutrino detectors observed for the first time neutrinos emitted by a SN explosion in the Great Magellanic Cloud, the famous SN1987A. At a distance of 50 kpc, a total of 19 $\bar{\nu}_e$ events was observed in two large-volume water Čerenkov

Model	Mass [M_\odot]	$\langle E_{\nu_e} \rangle$ [MeV]	$\langle E_{\bar{\nu}_e} \rangle$ [MeV]	$\langle E_{\nu_x} \rangle$ [MeV]	$\beta_{\bar{\nu}_e}$	β_{ν_x}
LL [46]	20	12.0	15.4	21.6	3.8	1.8
TBP [47]	11	10.0	11.4	14.1	3.7	2.2
	15	10.0	11.4	14.1	3.7	2.2
	20	10.0	11.9	14.4	3.6	2.2
KRJ [48]	—	13.0	15.4	15.7	4.2	2.5

Table 1.4: MC simulations of a core-collapse SN predict different shapes for the emitted neutrino spectra. The mean energies \bar{E} and pinching factors β of ν_e , $\bar{\nu}_e$, and $\nu_x = \nu_\mu, \bar{\nu}_\mu, \nu_\tau, \bar{\nu}_\tau$ are here reported for 5 different scenarios and progenitor masses. The simulations were done by three different groups. The parameterization (Eq. 1.9) and fit values were taken from [49].

detectors (WCDs), the IMB and KAMIOKANDE experiments [50, 51]. This number is in rough agreement with theoretical expectations, while the measured mean energy was rather low. The predicted SN rate in our galaxy is about 1 to 3 per century [44]; a detector with a life time of 30 years would therefore stand a good chance to observe ν 's from at least one galactic SN.

It has been shown that the matter potential of the stellar envelope and the propagation of the shock front through the star leave imprints in the observed neutrino spectra [44]. Recently, the self-interaction of the dense neutrino field emitted in the core collapse has moved into focus of theoretical research, predicting a coherence effect that leads to collective neutrino oscillations [52]. For a more extensive overview of the processes during the core-collapse and the forming of the neutrino spectra, read [44].

1.2.3 The Diffuse Supernova Neutrino Background

SNe throughout the universe contribute to a cosmic background of neutrinos released in the core-collapse [49, 53]. This diffuse SN neutrino background (DSNB) flux is of the order of $10^2 \text{ cm}^{-2} \text{ s}^{-1}$ and therefore far less abundant than for instance solar neutrinos. The energy of the neutrinos from more remote SNe are in addition red-shifted by cosmic expansion. Present neutrino detectors are not sensitive enough to detect the DSNB. The best limit is set by the SUPER-KAMIOKANDE experiment, imposing an upper bound for the $\bar{\nu}_e$ flux of $1.2 \text{ cm}^{-2} \text{ s}^{-1}$ above 19.3 MeV [54]. This is already close to the theoretical predictions. The expected flux and energy spectrum of the neutrinos can be obtained by combining a MC simulated SN neutrino spectrum with the red-shift dependent Supernova rate (R_{SN}).

The *Supernova neutrino spectrum* can be derived from the simulations by LL [46], TBP [47], and KRJ [48] that are discussed in Sect. 1.2.2. Both WCDs and liquid-scintillator detectors (LSDs) are most sensitive to the flux of $\bar{\nu}_e$ via the inverse beta decay (Sect. 2.2.2) [49]. To obtain the spectrum in a terrestrial detector, the mixing of $\bar{\nu}_e$ and $\bar{\nu}_x$ and the impact of the matter potential caused by the core and the surrounding progenitor star on oscillation probabilities has to be considered [44, 49]. As the neutrinos pass from the core which is above the critical density ρ_c (Sect. 1.1.3) through the stellar matter to vacuum, the change of the mixing parameters in the PMNS matrix leads to a partial conversion of $\bar{\nu}_e$ to $\bar{\nu}_x$ and vice versa. This hardens the $\bar{\nu}_e$ spectrum as the $\bar{\nu}_x$ are

initially higher in energy. Moreover, there is a resonance in the neutrino sector which efficiently converts ν_e and ν_x due to the mixing angle θ_{12} . A similar conversion at higher matter densities due to the mixing angle θ_{13} is in principle possible if the angle is larger than $\sim 1^\circ$ and adiabatic conversion is therefore possible. While for normal neutrino mass hierarchy this effect will again apply for the neutrino sector only, it is observable in the $\bar{\nu}_e$ signal if the hierarchy is inverted: As the survival probability P_{ee} is determined by the smallness of θ_{13} (compare Eq. 1.7), the conversion of $\bar{\nu}_e$ and $\bar{\nu}_x$ will be almost complete. Especially for the LL model this leads to a significant hardening of the spectrum [49].

The *Supernova rate* $R_{\text{SN}}(z)$ can be determined by combining optical information on the star formation rate $R_*(z)$ and the initial mass function (IMF) of the forming stars [49]. Stars that end in a SN explosion are rather heavy ($m > 8 M_\odot$) and therefore short-lived. On the cosmic time scale of both R_* and R_{SN} , the maximum life cycle of several million years is a negligible aberration. There is an uncertainty on the proportion of heavy SN-progenitor stars as the value of the IMF at low masses is known at limited precision. Using the standard Salpeter IMF of $\phi(m) \propto m^{-2.35}$, the relation between R_* and R_{SN} is [49]:

$$R_{\text{SN}}(z) = 0.0122 M_\odot^{-1} R_*(z). \quad (1.10)$$

However, modified models of the IMF return -25 % to +8 % relative to the result of Eq. (1.10) [55, 56]. A possible parameterization of the cosmic R_* is given in [49], which results in a R_{SN} of

$$R_{\text{SN}}(z) = 3.9 \times 10^{-4} f_{\text{SN}} h_{70} \frac{e^{3.4z}}{e^{3.8z} + 45} \frac{\sqrt{\Omega_m(1+z)^3 + \Omega_\Lambda}}{(1+z)^{3/2}} \text{yr}^{-1} \text{Mpc}^{-3}. \quad (1.11)$$

Here, $h_{70}=1$ for a Hubble constant of $H=70 \frac{\text{km}}{\text{sMpc}}$; $\Omega_m=0.3$ and $\Omega_\Lambda=0.7$ are the cosmological density parameters of matter and dark energy, respectively. The overall uncertainty in normalization of the R_{SN} is parameterized by the parameter f_{SN} . Fig. 1.7 shows $\dot{\rho}_{\text{SN}}(z)$ for $f_{\text{SN}}=1$ in comparison to data points of optical R_{SN} observations at $z < 0.9$ [57, 58, 55], which are in good agreement. However, R_{SN} data on larger red-shifts is not available and one has to rely on the observations of star formation regions in the UV [59, 60, 61] and far infrared (FIR) [62, 63] band. Due to the uncertainties introduced by dust absorption, a rather large span for f_{SN} reaching from 0.7 to 4.1 is chosen in [49]. In the last years, considerable progress has been made in a closer determination of f_{SN} : Combining the upper bound derived from the SUPER-KAMIOKANDE measurements with limits from the cosmic γ ray background, a concordance model of the star formation rate could be derived in [64]: It favors a value of $f_{\text{SN}}=2.5$. In addition, the consideration of more recent UV and FIR observations point towards some changes in the z -dependence of the R_* compared to Eq. (1.11) at large red shifts [56]. However, these modifications are still well contained in the original limits given by [49].

Combining both R_{SN} and the SN neutrino spectra from the different models, S. Ando and K. Sato computed the expected $\bar{\nu}_e$ spectrum that reaches a neutrino detector at Earth [49]. Fig. 1.8 shows on the left the DSN spectra based on the three models mentioned before. For the LL model, an additional spectrum is added that assumes the resonant conversion of $\bar{\nu}$ flavors that significantly hardens the $\bar{\nu}_e$ spectrum. The effect is smaller for TBP and insignificant for the KRJ model because $\bar{E}_{\nu_e} \approx \bar{E}_{\nu_x}$. As the spectral contributions of SN at higher z values are red-shifted in energy, their contributions will

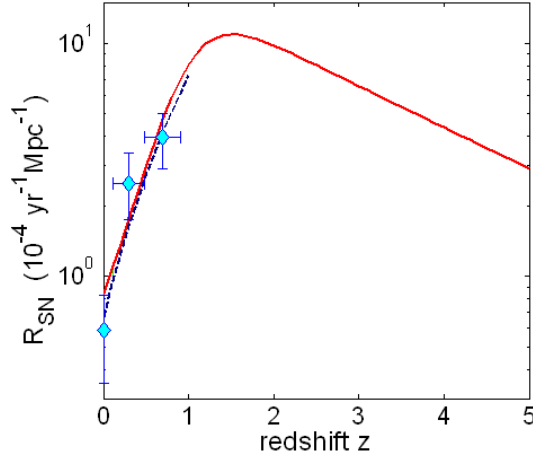


Figure 1.7: The red-shift dependent Supernova rate (R_{SN}). The drawn line follows the parameterization of Eq. (1.11)[49], while the data points mark optical observations of the R_{SN} for $z < 1$ [57, 58, 55].

be towards the lower end of the spectrum. Fig. 1.8 breaks the total simulated LL flux down into the spectra originating from different redshift regimes up to $z = 5$ [49].

1.2.4 Geoneutrinos

The energy released in the radioactive decays of nuclei along the natural Uranium and Thorium chains contributes significantly to the terrestrial heat flow of about 40 TW. Present-day models assume that at least 50% of the flow is produced by the elements embedded in the Earth's crust and mantle. The rest of the heat flow is provided by the crystallization of the liquid outer core and potentially by a natural georeactor in the Earth's core [65]. Apart from the charged α 's and electrons, the β^- decays also create a flux of $\bar{\nu}_e$'s. Fig. 1.9 shows on the left a sum spectrum of these geoneutrinos, including the contribution of the β^- decay of ^{40}K . The spectrum extends as far as 3.3 MeV which is below the threshold of WCDs, but measurable in LSDs via the inverse beta decay (Sect. 2.2.2). However, the endpoint of ^{40}K at 1.4 MeV lies below the reaction threshold and therefore presently not detectable.

The first measurement of the geoneutrino flux from the $^{238}\text{U}/^{232}\text{Th}$ chains was published by the KAMLAND collaboration in 2005 [66]. The right plot of Fig. 1.9 shows the $\bar{\nu}_e$ spectrum in the relevant energy region that was released in 2008 [25]. Included in the lower panel are backgrounds from reactor $\bar{\nu}_e$ (white area), accidentals (red) and αn -reactions on the natural ^{13}C content of the scintillator (green). The remaining counts (bluely shaded) are due to the geoneutrino signal. In the upper panel, the data points are compared to the reference model for geoneutrinos described in [67]. Both the energy spectrum and the total flux of $(4.4 \pm 1.6) \times 10^6 \text{ cm}^{-2}\text{s}^{-1}$ are in good agreement with theoretical expectations.

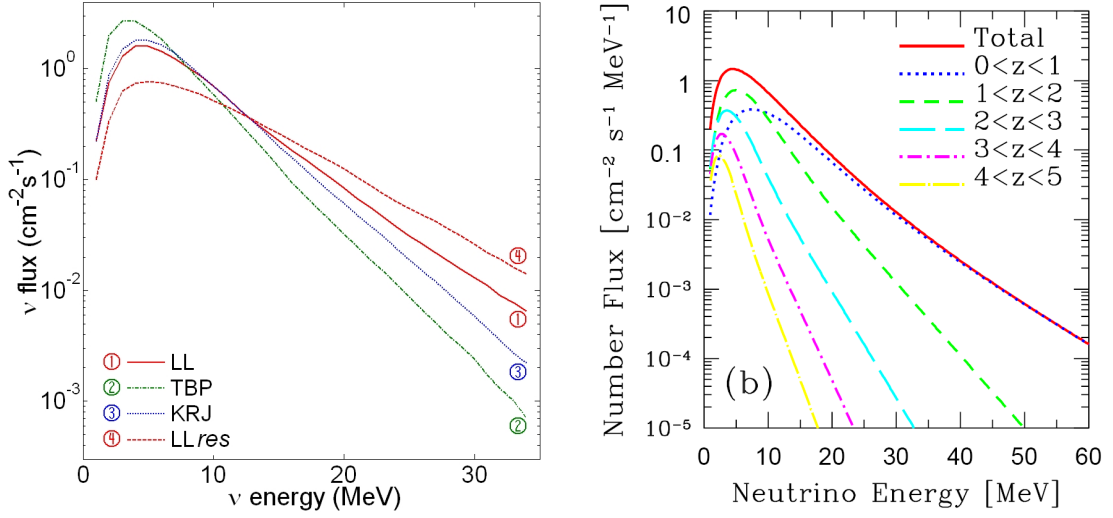


Figure 1.8: *Left*: Model spectra of the $\bar{\nu}_e$ proportion of the DSNB calculated by Ando and Sato [49] using parameters from the SN simulations performed by the LL, TBP, and KRJ groups presented in Sect.1.2.2. For the LL model, also the spectrum in case of resonant $\bar{\nu}_e \leftrightarrow \bar{\nu}_x$ conversion LLres is shown. *Right*: Contributions of different red-shift regions to the $\bar{\nu}_e$ spectrum [49]. Neutrinos from higher z values are shifted by cosmic expansion.

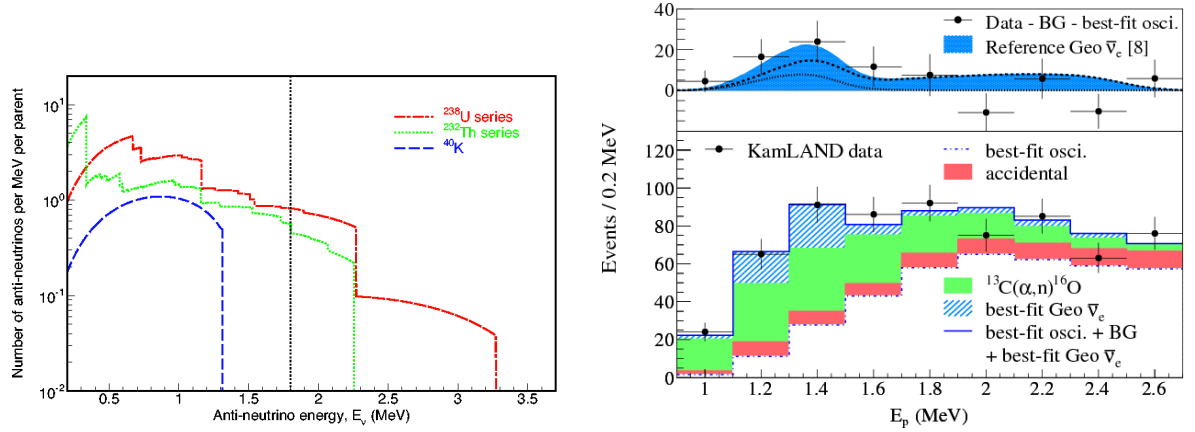


Figure 1.9: *Left*: Expected spectrum of $\bar{\nu}_e$ spectrum emitted by radioactive elements embedded in the Earth's crust and mantle. The contribution of ^{40}K and of the $^{238}\text{U}/^{232}\text{Th}$ chains are shown separately [66]. *Right*: The geoneutrino spectrum as measured by the KAMLAND experiment, showing the $\bar{\nu}_e$ -induced positron spectrum and background contributions from various sources in the lower panel [25]. In the upper panel, the measured spectrum is compared to the reference model in [67].

1.2.5 Dark Matter Annihilation

Evidence from galactic rotation curves, gravitational lensing, large-scale structure, and the cosmic microwave background (CMB) point towards a contribution of $\sim 23\%$ of cold dark matter (CDM) to the total energy content of the universe [68]. Currently, the WIMP (weakly interacting massive particle) is the most promising candidate to constitute the CDM. Direct DM search utilizes the scattering of WIMPs on nucleons in a cryogenic calorimeters or a liquid noble gas detector. The WIMP is often identified as the lightest and therefore stable supersymmetric particle (LSSP).

The interaction cross sections of WIMPs and nuclei are either comparable or below the ones of standard weak interactions. The expected mass range is of the order of 10 GeV to 1 TeV. There are, however, models assorting lower masses to these particles. It is possible that the nature of the neutral particles is Majorana instead of Dirac, allowing for pair annihilation. Both γ and cosmic radiation telescopes therefore look for deviations from the usual cosmic rays spectrum. This approach to the search has lately attracted renewed interest: Both the PAMELA [69] and ATIC [70] experiments report to observe an excess in positron flux which could be explained by DM annihilation [71]. In the same line of reasoning, large gravitational potential wells are supposed to trap DM particles, enhancing the collision probability. Therefore, even relatively close celestial bodies like the Sun or even the Earth should be sources of DM annihilation radiation. The $\nu\bar{\nu}$ pairs produced in this way would not be affected by solar or terrestrial matter and could therefore be detected by neutrino observatories [72]. While high-energy neutrino telescopes are most attractive for the expected WIMP mass range, more exotic scenarios of relatively light DM favour low-energy neutrino experiments for detection (Sect. 7.1.4).

Chapter 2

Real-Time Neutrino Detection

From the discovery of the neutrino in the 1950s [73] to the present day, detectors for low-energetic neutrinos in the MeV-region have played an important role in neutrino physics. Water-Čerenkov Detectors (WCD) and Liquid-Scintillator Detectors (LSD) define the state-of-the-art. However, these real-time detectors lacked for a long time the sensitivity for the detection of astrophysical neutrinos.

The first solar neutrino experiments were radiochemical detectors: The Homestake Chlorine experiment [74, 2] was followed by the Gallium-based GALLEX [3], SAGE [75], and GNO [4] detectors which discovered and confirmed, respectively, the deficit in the detected solar ν_e flux compared to the predictions. To the present day, the Gallium detectors provide the only measurements of low-energetic solar neutrinos that include part of the pp neutrino spectrum.

In the further exploration of the so-called Solar Neutrino Problem, real-time WCDs replaced the time- and energy-integrating radiochemical experiments. WCDs allow both the spectroscopy and the identification of solar neutrinos due to the energy-dependence and directionality of the Čerenkov light emission. At the same time, liquid-scintillator experiments were used in a series of reactor $\bar{\nu}_e$ -disappearance experiments benefiting from their high energy resolution and low threshold. The search culminated in the discovery of atmospheric, solar, and reactor neutrino oscillations by the SUPER-KAMIOKANDE, SNO and KAMLAND experiments [15, 16, 17, 18].

The full potential of the WCDs and especially of the LSDs has not yet been tapped, a fact that was magnificently illustrated by the first detection of solar ${}^7\text{Be}$ neutrinos by BOREXINO in 2007 [76]. As shown in Chap. 7, a large-volume detector like LENA could address a number of fundamental questions outreaching the field of astroparticle physics.

Sect. 2.1 gives a short overview over the two real-time detection techniques, WCDs and LSDs; the focus is, however, on the liquid scintillator, as it is central to both the BOREXINO and LENA experiments. The reaction channels and signatures for the real-time detection of astrophysical neutrinos are listed in Sect. 2.2. The chapter closes with Sect. 2.3 that describes the background sources and discrimination capabilities of a LSD.

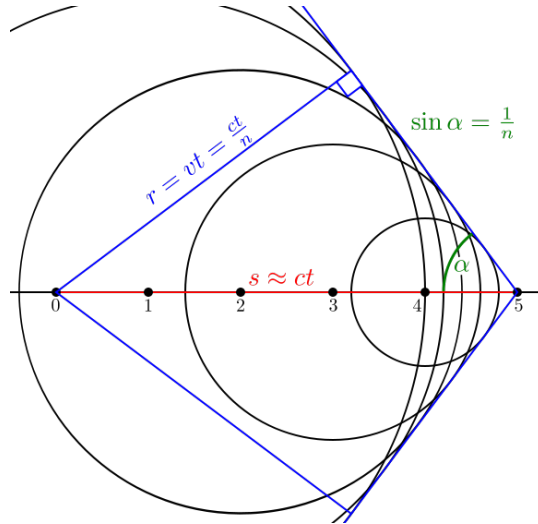


Figure 2.1: Čerenkov light emission of a particle traveling at superluminal speed through a medium. The characteristic conical shape of the light front is caused by the interference of the spherical light waves emitted along the track [77]. Eq. (2.1) describes the opening angle α as function of the refractive index n of the medium.

2.1 Detection Technique

Čerenkov and scintillation detectors allow the real-time spectroscopy of neutrinos: In both cases, neutrinos transfer energy to charged particles in the detector which leads to light emission. Information on energy and interaction time of the incident particles is available by measuring the amount of light and the photon arrival times at photomultiplier (PM) tubes covering the walls of the detector. Due to the low cross sections of weak interaction (Sect. 2.2), the target mass must be at least of the order of tons. For weak neutrino sources as the diffuse supernova neutrinos (Chap. 9), the necessary mass is considerably larger, reaching tens of kilotons. This need can be partially compensated by exposure times of several years. It requires on the other hand sufficient time-stability of both the detector target and the electronic read-out of the signals.

A further aspect common to all neutrino detectors is the need for extensive passive shielding from cosmic rays. Usually, overburdens of several 1000 meters of water equivalent (mwe) are necessary to achieve a sufficiently low level of atmospheric muons, neutrons and cosmogenic radioisotopes. The relevant background levels are described in Sect. 2.3.

A short description of WCDs is included as the Outer Muon Veto of BOREXINO is based on this technique (Chap. 3). LSDs are more thoroughly described in the second part.

2.1.1 Water-Čerenkov Detectors

The light generated by charged particles traveling at superluminal speed through a medium is known as Čerenkov radiation [77]. Caused by the polarization of molecular dipoles in the material, the interference of spherical waves emitted successively along the particle track generates a light front of conical shape, resembling a supersonic Mach

cone (Fig.2.4). The opening angle α_c is both related to the velocity $\beta = v/c$ of the particle and the refractive index n of the medium [77],

$$\cos \alpha_c = \frac{1}{\beta n}. \quad (2.1)$$

For particles at nearly the vacuum speed of light c , the angle converges towards the minimum value defined by $\alpha_{\max} = \arccos(1/n)$. A particle must reach a minimum velocity of $\beta_{\min} = c/n$ to be visible in a Čerenkov detector. This translates to a threshold energy

$$E_{\text{thr}} = \gamma m_0 = \frac{1}{\sqrt{1 - \frac{1}{n^2}}} m_0. \quad (2.2)$$

In water, this means $\alpha_{w,\max} = 41.4^\circ$ and $E_{w,\text{thr}} = 1.52 m_0$. The kinetic energy therefore has to be at least half of the rest mass m_0 . The typical Čerenkov light yield is of the order of 200 photons per MeV which are mostly generated in the UV and blue part of the optical spectrum.

Water has been used often and very successfully as Čerenkov medium in neutrino experiments [15, 17]. It is possible to sustain a large target volume at low costs, the main expense arising from the large number of PMs necessary. It is easy to handle in terms of flammability and toxicity. Purification by common techniques like deionization enables high optical transparency in the UV. From the point of view of a neutrino detector, the two elements contained in water, Hydrogen and Oxygen, offer a similar variety of detection channels as a liquid scintillator.

The orientation of the Čerenkov cone can be utilized to determine the direction of the light-emitting particle. In the case of neutrino-electron scattering, the correlation between the direction of the incident neutrino and the backscattered electron is stricter at higher energies. Already at the energies of ^8B neutrinos, directionality can be efficiently used as means of background suppression, as was illustrated by the Super-Kamiokande detector [78]. The high-energetic electrons and muons caused by atmospheric neutrino interactions generate tracks extending over several meters. Thus, an event fully contained in the detection volume produces a ring-like activation profile of the PMs on the detector walls. When a particle traverses the detector wall, the PM activation is of disk-like shape. The signals created by cosmic muons in the Outer Muon Veto of BOREXINO feature this shape if the muons also cross the Inner Detector. This is exploited in the muon track reconstruction (Chap. 5).

2.1.2 Liquid-Scintillator Detectors

LSDs are the state-of-the-art of astrophysical neutrino detectors. The detection relies on the emission of light intrinsic to organic solvents: they are used both as target and as active detector. The molecules usually feature one or two benzene rings: Charged particles decelerating in the material excite or ionize the weakly bound electrons in the π -orbitals of the rings. Their de-excitation releases photons in the near UV which are emitted isotropically with a decay time constant of a few nanoseconds. The energy range of the photons is broadened by vibrational modes of the molecules, resulting in absorption and emission bands of several tens of nanometers in width. Although there is a Stoke's shift of the same order between the two bands, they heavily overlap.

The reason for the addition of solutes to the liquid is the necessity of shifting the light to longer wavelength, allowing it to pass through the detector volume without re-absorption by the solvent material. This can be achieved by adding small concentrations of a solute featuring a large Stoke's shift (usually few grams per liter). The absorption band has to be chosen according to the emission band of the solvent, while the (shifted) emission band is preferably far from the absorption bands of solvent and wavelength shifter. Ultimately, it is necessary to shift the light to the blue regime of the visible spectrum. This is a compromise, as the transparency of the solvent steeply increases in the green and red (Sect. 8.1). On the other hand, common photomultipliers are most efficient in the region from 400 to 430 nm; moreover, none of the regular wavelength shifters significantly exceeds wavelengths of 430 nm in its emission band.

Due to the efficient light production of an organic scintillator of roughly 10^4 photons per 1 MeV of deposited energy, large volume detectors with a yield of several hundreds of registered photoelectrons per MeV are feasible. This corresponds to an energy resolution of a few percent even in the low energetic energy regime of solar neutrinos, surpassing by far the resolution power of a WCD. It also allows a low instrumental threshold for the neutrino detection: A few hundreds of keV are possible, depending on the intrinsic radioactive background (see below). As the light is isotropically emitted, the position of the event vertex inside the detection volume can be reconstructed using the photon arrival time and hit patterns of the PMs.

In any neutrino detector, the expected low event rate must be faced by a low rate of background events. In underground laboratories, the internal radioactivity of the detector components, radioactive noble gases emanating from the walls, and the cosmogenic background induced by muons are the main background sources (Sect. 2.3). The use of standard techniques like distillation, water extraction, nitrogen purging, and column chromatography for an efficient purification of the liquid scintillator allows to achieve extremely low concentrations in radioimpurities. The same techniques are utilized to increase the transparency of the liquid to scintillation light by removing organic impurities. The self-shielding by the outer layers of liquid allows the definition of a fiducial volume. Events within this volume are selected by spacial reconstruction.

Moreover, a liquid scintillator provides several means to discriminate signal from background events: Prominent examples are the coincidence signals of inverse beta decay (Sect. 2.2.2), the proton decay into $K^+\bar{\nu}$ and the subsequent Kaon decay (Sect. 7.1.5), or the fast sequence of ^{214}Bi β and ^{214}Po α decay. Towards short time gaps between events, the fast decay time constant of the scintillation light signal sets a limit of a few nanoseconds. For long time spans, the combination with spatial information allows to extend the time gate, like in the threefold coincidence of muons, neutrons and ^{11}C decay (Sect. 2.3.3). In addition, pulse shape discrimination is often used as a powerful tool to distinguish signals generated by protons and alpha-particles from beta-decays and γ/ν electron recoils. The difference in the pulse shape is caused by the ionization densities of the incident particles. According to the Bethe-Bloch law, heavier particles will deposit their energy over a shorter distance [79]. For the same reason, the energy-to-light conversion is less efficient for the comparatively heavy protons and α 's: As the ratio of light emission centers to ionization density is smaller, the light yield decreases. The amount of generated scintillation light is usually parameterized by the semi-empirical Birk's formula [79]. In the case of α 's, this "quenching" can reach more than a factor

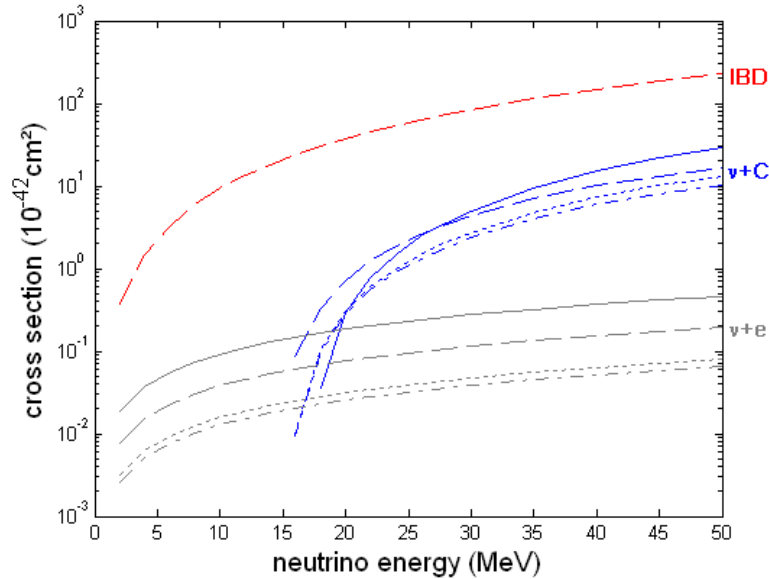


Figure 2.2: Reaction cross sections for low-energetic neutrinos in a liquid-scintillator detector. The inverse beta decay (in red, see Sect.2.2.2) is the main detection channel for $\bar{\nu}_e$. The reactions on ^{12}C are depicted in blue (Sect.2.2.3), the elastic scattering on electrons in grey (Sect.2.2.1): solid - ν_e , dashed - $\bar{\nu}_e$, dotted - $\nu_{\mu,\tau}$, dashes and dots - $\bar{\nu}_{\mu,\tau}$.

10 in common scintillator liquids as PC or PXE [80, 81].

Compared to WCDs, the loss of information on directionality is a drawback. Only high-energetic events like cosmic muons or atmospheric neutrinos will cause a track long enough to detect the deviation from sphericity in light emission [82]. Moreover, some of the organic liquids in use are easily flammable or poisonous to the environment. Special care has therefore to be applied when handling large amounts of those liquids in underground laboratories.

2.2 Detection Reactions

The solvents of liquid scintillators are based on hydrocarbons: The target therefore offers electrons, the free protons of Hydrogen, and the bound protons and neutrons of Carbon nuclei as interaction partners for neutrinos. Both neutral and charged current reactions can be observed. Water provides the same detection reactions as LSDs, with the exception of the Carbon processes; the corresponding reactions on Oxygen are however very similar (not listed below).

2.2.1 Elastic Scattering

The elastic *neutrino-electron-scattering* is the main detection channel of several solar neutrino experiments (including BOREXINO). The reaction resembles the Compton effect of γ rays. All neutrino flavors take part in the scattering by NC. However, the cross section of electron neutrino scattering is significantly enhanced, as a charged current reaction to the same final state is possible. Cross sections are presented in Tab.2.1 and

Reaction	Current	Threshold [MeV]	Cross section [10^{-44} cm 2]
$e^-(\nu_e, \nu_e) e^-$	NC/CC	-	$0.92 E_\nu$
$e^-(\bar{\nu}_e, \bar{\nu}_e) e^-$	NC	-	$0.38 E_\nu$
$e^-(\nu_x, \nu_x) e^-$	NC	-	$0.16 E_\nu$
$e^-(\bar{\nu}_x, \bar{\nu}_x) e^-$	NC	-	$0.13 E_\nu$
$p(\nu_\mu, \nu_\mu) p$	NC		$0.32 E_\nu^2$
$p(\bar{\nu}_e, e^+) n$ $\rightarrow p(n, \gamma) d$ (250 μ s)	CC	1.8	$9.5 (E_\nu - 1.29)^2$
$^{12}\text{C}(\nu_e, e^-)^{12}\text{N}$ $\rightarrow ^{12}\text{N} : \beta^+, \tau = 11.0$ ms	CC	17.34	28.7 @ 20 MeV
$^{12}\text{C}(\bar{\nu}_e, e^+)^{12}\text{B}$ $\rightarrow ^{12}\text{B} : \beta^-, \tau = 20.2$ ms	CC	13.37	71.1 @ 20 MeV
$^{12}\text{C}(\nu, \nu)^{12}\text{C}^*$ $^{12}\text{C}(\bar{\nu}, \bar{\nu})^{12}\text{C}^*$ $\rightarrow ^{12}\text{C}^* : \gamma$	NC NC	15.11	30.2 27.9 @ 20 MeV
$^{13}\text{C}(\nu_e, e^-)^{13}\text{N}$ $\rightarrow ^{13}\text{N} : \beta^+, \tau = 862$ s	CC	2.22	85.7 @ $\langle E_{sB} \rangle$
$^{13}\text{C}(\nu, \nu)^{13}\text{C}^*$ $\rightarrow ^{13}\text{C}^* : \gamma$	NC	3.68	11.5 @ $\langle E_{sB} \rangle$

Table 2.1: Detection reactions along with the applying weak current, threshold, the energy-dependent cross section (energy in MeV), and the subsequent reactions. For a more detailed description see Sect. 2.2. The nomenclature $\nu_x, \bar{\nu}_x$ is used to summarize the μ and τ flavors of ν and $\bar{\nu}$. Values are cited from [36, 83, 84].

Fig. 2.2.

As the particles in initial and final state are the same, the reaction has no intrinsic energy threshold; the detection at low energies is therefore impeded solely by instrumental limitations and the radioactive background (e.g. ^{14}C) because there is no intrinsic mean to discriminate neutrino signals from beta decay events (Sect. 2.3).

At energies of several MeV, the electron is mostly scattered in forward direction, the tracks will however be short due to ionization losses and electron scattering. While this bears no meaning for LSDs, in a WCD the Čerenkov ring of the scattered electron can be used to identify the ν direction, as in the case of solar ^8B neutrinos in Super-Kamiokande [78].

Similarly, elastic ν scattering is possible on protons. Due to the larger proton mass and due to the quenching of the scintillation light caused by the recoil proton (Sect. 2.1.2), neutrinos of the same energy will create a much smaller visible signal by scattering of protons than by scattering of electrons. Therefore, a relatively low instrumental threshold for νe -scattering in the order of hundreds of keV corresponds to several MeV for proton recoils. However, this channel offers interesting possibilities for the detection of high-energetic SN neutrinos, as the more energetic ν_x are expected to create most of the signal. Therefore, proton scattering allows a spectroscopic measurement of ν_x fluxes, while electron scattering provides mostly information on the ν_e contribution.

2.2.2 Inverse Beta Decay

The capture of a $\bar{\nu}_e$ on a proton is the primary channel of a LSD for $\bar{\nu}_e$ detection. It has the largest cross section at low energies (Tab. 2.1), and it provides a clear event signature: A first signal is due to the positron that carries away most of the kinetic energy transferred from the neutrino. In a LSD, this prompt signal caused by the ionization and annihilation of the positron provides energy and time information. A second signal is generated about 250 μs later when the generated free neutron is captured on a free proton of the scintillator, thereby releasing the deuteron binding energy of 2.2 MeV in a gamma quantum. The delayed coincidence can be used for an efficient background discrimination.

As the gamma emitted by the deuteron is below the instrumental thresholds of state-of-the-art WCDs, these detectors would either have to lower their thresholds or to add a neutron-catcher creating a more discernible signal [85, 86]. The most prominent example is Gadolinium which creates a 8 MeV gamma cascade in case of a neutron capture. It is also used in LSDs like the DOUBLECHOOZ experiment [87] for the enhancement of the event signature.

As the forward scattering of the recoil positron is favored, the inverse beta decay in principle includes directional information. While this can be quite easily exploited by WCDs, LSDs have to rely on the relative displacement of positron annihilation and neutron capture to each other. Due to the random thermalization path of the neutron, there is no way for an event-by-event analysis; only a mean displacement can be determined (see [88, 89] for more details).

2.2.3 Reactions on Carbon

^{12}C offers three possible reaction channels to neutrinos, two charged current and one neutral current reaction with thresholds around 15 MeV (Tab. 2.1). While the thresholds are too high and the cross sections too low for most applications (Chap. 1), SN neutrino observation significantly benefits from these channels.

The charged current reactions both provide a very similar delayed coincidence. The incoming $\nu_e/\bar{\nu}_e$ interacts with the nucleus, thereby creating an e^-/e^+ and an instable isotope. The signal due to the e^\pm is then followed 10 ms/20 ms later by the re-decay of the $^{12}\text{N}/^{12}\text{B}$ under emission of an e^+/e^- . Once again, this delayed coincidence can be used as event signature. It must however be stated that – as the subsequent β^\pm -decays feature similar endpoints, and the half-life is very similar – it is experimentally challenging to discriminate on an event-by-event basis ν_e from $\bar{\nu}_e$ events. The third channel, inelastic scattering exciting the Carbon nucleus, is possible for all neutrino flavors. As there is no prompt signal, the only event signature is the de-excitation gamma of 15.11 MeV. Apart from its threshold, the reaction bears no spectroscopic and no flavor information of the incident neutrino.

As the natural isotopic abundance of ^{13}C is 1.1 %, a LSD can also exploit neutrino reactions on this isotope. Albeit event rates are low due to the reduced number of target nuclei, both the CC reaction of ν_e and the NC inelastic scattering are interesting as their thresholds are low, 2.2 and 3.7 MeV, respectively. Especially the delayed coincidence signal of the CC reaction could be utilised in the detection of solar ^8B and SN ν_e

(Chaps. 3, 7) [84].

2.3 Background Sources

Background events to neutrino detection in a LSD originate from two main sources: One is residual radioactivity in the detection volume, in the tank containing the scintillator, in the phototubes mounted to it, and in the surroundings of the detector. This background is central at very low energies but plays almost no role above a few MeV. The second component is caused by cosmic radiation. As most neutrino detectors are deep underground, only muons generated by air showers in the atmosphere can reach the detector cavern. Apart from the signals that are caused by the muons themselves, they create radionuclides by spallation. Some of them are long-lived enough to make the correlation with the parent muon challenging. Moreover, muons passing nearby the detector give rise to a background of fast neutrons that can enter the detector unnoticed and mimic the signature of an inverse beta decay.

2.3.1 Intrinsic Radioactive Contaminants

As the basic solvents of liquid scintillators are hydrocarbons, an ideal scintillator will only suffer from the natural abundance of unstable isotopes of Hydrogen and Carbon bound in its molecules. The unique isotope featuring a half-life long enough to be considered is ^{14}C . However, ^{14}C produced in the Earth's atmosphere is integrated only in living material in typical concentrations of parts per trillion. As the formation of petroleum from biomass is a long process in comparison to the ^{14}C half-life of 5150 years, the concentration in the solvent, which is a petroleum derivate, will be substantially lower. Nevertheless, due to the large scintillator mass, the ^{14}C β decay will effectively block neutrino detection for energies below the endpoint of the β spectrum at 156 keV [90].

Moreover, radioactive contaminants can be dissolved in the liquid. While the original solvent produced in distillation plants is usually rather pure, the surface contamination of transport and experimental containers in contact may later be dissolved in the liquid. Diffusion and above all convection transport these impurities to the detector bulk. Even specially treated surfaces of stainless steel normally bear a certain amount of metallic impurities that are potentially radioactive. The possibilities range from the heavy mother nuclides of the Uranium and Thorium chains, ^{238}U and ^{232}Th with half-lives in the order of billions of years, down the decay chain to the relatively long-lived ^{210}Pb and ^{210}Po . Tab. 2.2 lists the most relevant of these nuclei including their half-lives and energies.

Even if radionuclides are solved in the scintillator, there are still possibilities to reject the decay events: The first is pulse shape discrimination, as many of the daughter nuclei in both U and Th chains are α -emitters and can therefore be distinguished from β -like neutrino events. Moreover, α particles are emitted at one (or several) fixed energies for a given unstable nucleus. These lines are distinguishable in the energy spectrum. Even in the case of β -emitters, their association to a decay chain can be often used to tag them via a temporal and spacial coincidence. The most famous example is the fast ^{214}Bi - ^{214}Po -coincidence in which the short half-life of ^{214}Po allows an easy allocation to

Isotope	$T_{1/2}$ [s]	Decay Mode	E_{\max} [keV]
^{14}C	5730 a	β^-	157
^{40}K	1.3 Ga	β^- (89%)	1311
		β^+ (11%)	1505
^{85}Kr	10.8 a	β^-	687
^{222}Rn	3.8 d	α	5590
^{210}Pb	22.3 a	β^-	64
^{210}Bi	5.0 d	β^-	1162
^{210}Po	138.4 d	α	5408
^{208}Tl	3.1 m	β^-	5001
^{212}Bi	60.6 m	β^- (64%)	2254
		α (36%)	6207
^{212}Po	0.3 μs	α	8954
^{214}Pb	26.8 m	β^-	1024
^{214}Bi	19.9 m	β^-	3272
^{214}Po	164.3 μs	α	7833

Table 2.2: Overview of prominent radioactive contaminants in a liquid scintillator that are not cosmogenic. Half-lives, primary decay modes, and line or endpoint energies are presented [90].

the subsequent α decay of known energy. While this energy is usually in the range of several MeV, quenching in the scintillator will shift these lines down to energy regimes relevant for neutrino detection. There are also cases where the β decay is to an excited state of the daughter nucleus, providing a coincidence between the β and the subsequent γ quantum originating from the de-excitation of the nucleus.

Apart from surface contaminations that can also occur during transport of the scintillator to the experimental site or during the filling of the detector, radioactive noble gases like Radon or Krypton are able to diffuse into the liquid. As scintillators are for this reason often sealed from the surrounding air and half-filled tanks are buffered by a layer of nitrogen, contamination will mostly occur in case of an air-leak or due to impurities in the nitrogen. Radon nuclei are part of the U/Th decay chains. After dissolution in the scintillator they will quickly decay to Po, Bi, and Pb nuclei which are usually more stable. In the case of ^{85}Kr , which is an important background to solar neutrino detection in BOREXINO, the only way to determine the concentration in the scintillator from the data is looking for a fast $\beta\gamma$ -decay at low energies. However, this decay channel features only a low branching ratio of $\Gamma = 0.43\%$.

Finally, radioactive nuclides must not necessarily be solved in the bulk of the liquid in order to interfere there with neutrino detection. Different from α and β radiation, γ rays as uncharged particles can travel for several meters before interacting in the scintillator, undergoing a number of Compton scattering events and eventually being absorbed via the photo-effect. Especially the glass of the photomultiplier tubes is usually rich in ^{40}K . Even external γ radiation from outside the detector walls may reach the scintillator. Only extensive shielding by high Z-materials or by thick layers of water or of organic solvents is able to reduce this background.

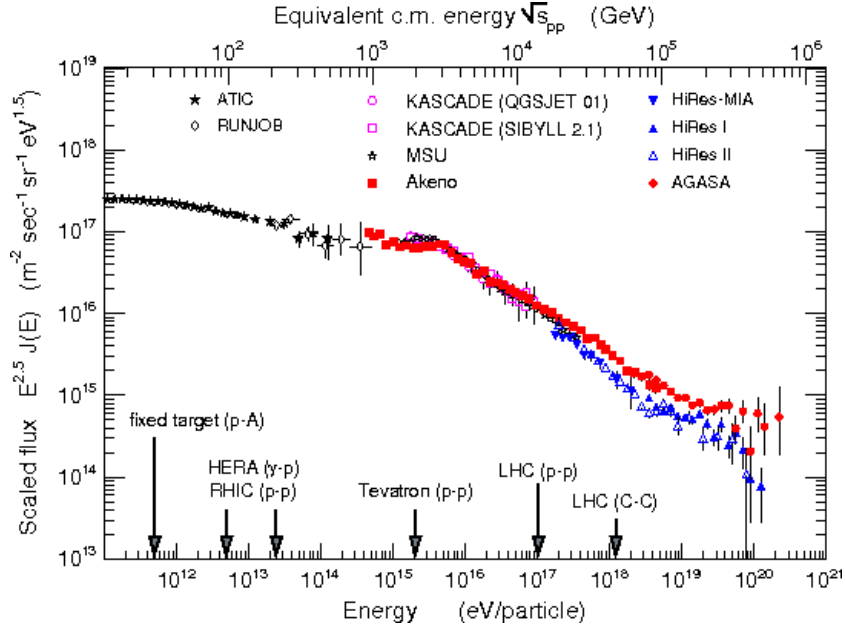


Figure 2.3: Cosmic ray spectrum as it was measured by several experiments. The kinetic energy released in the interactions in the atmosphere are compared to the center of mass energies accessible at particle colliders.

2.3.2 Cosmic Muons

Various experiments have measured the energy spectrum dN/dE_0 of the primary cosmic rays (Fig. 2.3). Protons are the main component with a proportion of 90%. Their dependence on energy is polynomial,

$$\frac{dN}{dE_0} \propto E_0^{-(\gamma+1)}. \quad (2.3)$$

Above energies of 10 GeV, the slope $\gamma \approx 1.7$ remains constant over six orders of magnitude. After the transition region of the “knee” at roughly 1 PeV, the spectrum becomes even more steep, $\gamma \approx 2.0$. At very high energies of the “ankle” region at $\sim 10^{20}$ eV, the effects of the GZK cut-off become visible; however, the exact behavior of the spectrum in and above this energy region is the subject of current-day research [91].

Cosmic muons are secondary particles produced by the interaction of the primary cosmic rays in the atmosphere. At a typical height of 15 km, protons will create a hadronic shower that – depending on the incident energy – can reach down to the Earth’s surface and stretch over an area of several km^2 . Such a shower consists to a large extent of unstable mesons. The charged variants of the lightest of these mesons, pions and kaons, will mostly decay into muons via $\pi^\pm, K^\pm \rightarrow \mu^\pm(\bar{\nu}_\mu)$. At ground level, the flux of these atmospheric muons is roughly $(180 \pm 20) \text{ m}^{-2} \text{ s}^{-1}$ [92]. The spectrum follows a similar polynomial as described by Eq. (2.3) as the maximum energy of the muons is depending on the energy of the parent particle. The LVD experiment has determined the spectral exponent to $\gamma_\mu = 1.76 \pm 0.05$ [93].

Even a few meters of solid matter are enough to stop the hadronic and electromagnetic components of cosmic radiation. Deep underground, the only particles prevailing are muons. Their long range in solid matter is due to their small ionisation power:

As can be derived from the basic Bethe-Bloch formula [79], muons lose only $\sim(2\rho)$ MeV traversing 1 cm of matter of density ρ (in g/cm^3). On the other hand, the rest mass of the muon is substantially larger than the one of the electron. Therefore, discrete radiation processes like pair production, bremsstrahlung, or even production of hadrons are subdominant to normal ionization loss below a critical energy of $\epsilon = 500$ GeV [79, 94]. Monte Carlo simulations show that even in a depth of 10 000 meters water equivalent (mwe), there is a residual flux of high energetic muons [95]. The depth-dependent muon rate in a spherical detector volume with a diameter of 5.4 m, corresponding to ~ 100 tons of liquid scintillator of density 1, is depicted in Fig. 2.4.

The energy spectrum of the muons is dependent on the amount of rock shielding: Due to the linearity of the energy loss below the critical energy ϵ , low energetic muons will be absorbed at a more shallow depth. The initial spectrum of the muons is a polynomial decreasing with energy. Therefore, the resulting average energy of the muons will rise steadily with the depth as long as it is substantially lower than the critical energy. As stated above, muons of energies larger than ϵ undergo radiative processes that increase the energy loss per unit length, depopulating the high-energetic tail of the muon spectrum. The mean energy will therefore approach asymptotically the value of the critical energy of $\epsilon = 500$ GeV at large depth [94].

Due to the high mean energy, most of the cosmic muons reaching an underground muon detector will simply pass through it. It can be shown that only 1-2 % of the muons are stopped in a detector the size of BOREXINO [96]. In any case, a muon deposits a considerable amount of energy when passing the scintillator, ~ 2 MeV/cm. The visible output will even increase if a hadronic shower is generated. Apart from the very large prompt signal that momentarily blinds the detector, a muon is able to create additional background by spallation processes in its wake.

The angular distribution of the muons in an underground laboratory heavily depends on the surface topology. In case of a laboratory that lies deep under a relatively flat surface, most of the muon flux is vertical, following the shortest path through the rock. This scenario would apply to LENA in the Pyhäsalmi mine in Finland: there, a flux of $(1.1 \pm 0.1) \times 10^{-4} \text{ m}^{-2} \text{ s}^{-1}$ has been measured at 3 960 mwe (Chap. 7) [92]. The situation changes significantly in the case of BOREXINO: The Laboratori Nazionali del Gran Sasso (LNGS) are placed next to a motorway tunnel crossing the mountain massive. While the coverage from above is corresponding to 3 600 mwe, the additional flux for larger zenith angles contributes substantially to the flux. Measurements done by LVD and MACRO reflect the shape of the surrounding mountains in the azimuthal dependence of the muon flux [97], as well as the increased flux of $1.16 / \text{m}^2 \text{ h}$ and mean energy of (320 ± 12) GeV [98]. In Fig. 2.4, the situation at the LNGS is reflected by the empty circles, while the solid lines show the dependence on depth for a flat surface geometry.

2.3.3 Cosmogenic Radio-Isotopes

The background generated by muons traversing the detector is not limited to the direct signal itself. More dangerously, a muon may create unstable nuclei in the detector by spallation processes that knock-out one or several of the nucleons of a target nucleus. In a liquid scintillator, Carbon and especially ^{12}C is the most abundant nucleus. The production rate of a radioisotope R is therefore depending on the energy-dependent

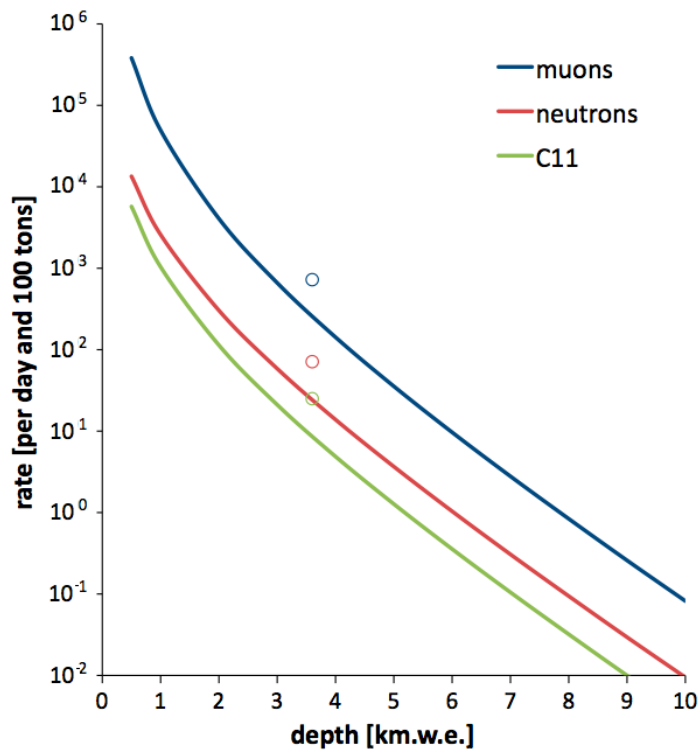


Figure 2.4: The expected background rates of cosmic muons, muon-induced neutrons, and of cosmogenic ^{11}C depending on the depth of the laboratory (in kilometers water equivalent) [95]. The rates are normalized to a sphere corresponding to 100 tons of liquid scintillator at density 1. A flat surface geometry is assumed. The empty circles show the situation of BOREXINO at 3600 mwe: All rates are increased due to the geometry of the mountain. Values were derived from [95].

Isotope	$T_{1/2}$	Decay Mode	E_{\max} [MeV]	Rate [/d 100t]	α
^7Be	53.3 d	β^+	0.48	0.34 ± 0.04	0.93 ± 0.23
^{10}C	19.3 s	$\beta^+ \gamma$	$2.9 + 0.72$	2.0 ± 0.2	0.62 ± 0.22
^{11}Be	13.8 s	β^-	11.5	< 0.034	
^{11}C	20.4 m	β^+	1.98	14.5 ± 1.5	0.70 ± 0.16
^8He	0.12 s	$\beta^- n$	< 7.4 (10.7)	0.034 ± 0.007	
^9Li	0.18 s	$\beta^- n$	11.2 (13.6)		

Table 2.3: Radioisotopes produced by interaction of cosmic muons with the scintillator. Half-life, relevant decay mode and the maximum deposited energy are listed. The production rate was calculated for the BOREXINO detector at the Laboratori Nazionali del Gran Sasso, a mountain site with 3 600 mwe shielding. In addition, the exponent α of the energy-dependence of the production rate is given (compare Eq. 2.4) which allows to extrapolate the rates for other underground sites [99].

cross-section $\sigma(E)$, the muon flux Φ_μ , the number of ^{12}C atoms N_C contained in the detector, and the energy of the muons E_μ which can be approximated by their mean energy \bar{E}_μ [95]. As shown in Sect. 2.3.2, both Φ_μ and \bar{E}_μ are a function of the depth d of the experiment. The depth-dependent production rate $R(d)$ is therefore:

$$R(d) = \Phi_\mu(d) N_C \sigma(\bar{E}_\mu(d)) = \Phi_\mu(d) N_C \sigma_0 \bar{E}_\mu(d)^\alpha \quad (2.4)$$

During the R&D phase of BOREXINO, the experiment NA54 was performed at a muon beam in CERN to determine the production cross sections of different radioisotopes in liquid-scintillator [99]. The experiment was done at two different beam energies to allow investigation of the energy dependence. As indicated in the last part of Eq. (2.4), this dependence can be assumed to be polynomial, following the exponent α while σ_0 is a constant. A list of the investigated radionuclides is presented in Tab. 2.3. Half-life, decay mode and the maximum (visible) energy depositon are given. The production rates have been calculated in [99] for the case of the BOREXINO detector at the LNGS, a mountain site with 3 600 mwe of rock shielding (Chap. 3). To obtain the same rates for LENA at Pyhäsalmi (Chap. 7), the values have to be divided by a factor of 3. The most interfering with neutrino detection are the long-lived β^+ -emitters ^{10}C and ^{11}C , or high energetic βn -emitters as ^8He and ^9Li .

Cosmogenic Carbon Isotopes

Unstable Carbon isotopes are generated by the knock-out of neutrons from ^{12}C nuclei in the scintillator. The only Carbon isotopes long-lived enough to pose a relevant background for neutrino detection are ^{10}C and ^{11}C . Moreover, the production cross section are the largest of all radioisotopes investigated in the NA54 experiment. Spectral fits of the BOREXINO data imply that their production rate is maybe twice as high as expected (Chap. 3). Both isotopes are β^+ emitters, adding the annihilation energy of the positron to the energy deposition. ^{11}C covers therefore the range from 1 to 2 MeV of visible energy. It is the main background for the detection of pep and CNO-neutrinos. The energy deposited by a ^{10}C nucleus is at least 1.7 MeV and stretches as far as 3.6 MeV, as two annihilation γ 's and one deexcitation γ add to the signal. It interferes with the detection of the low-energetic part of the ^8B spectrum (Sect. 3).

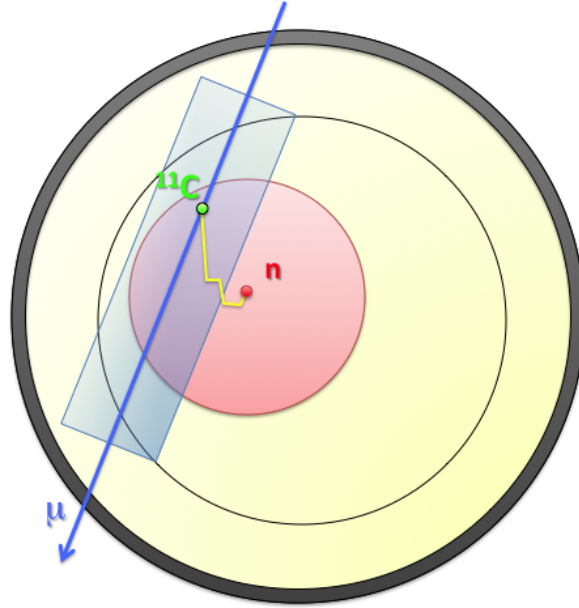


Figure 2.5: Conceptual drawing of the Threefold Coincidence (TFC) Veto used for the identification of cosmogenic ^{10}C and ^{11}C [100]. The minimum sub-volume that has to be blinded out for several half-lives of the isotope can be found by the intersection of a cylinder around the muon track and a sphere around the neutron capture vertex.

An indication for the production of these nuclides delivers the capture of the knock-out neutrons on Hydrogen in the trail of the muon event. The capture time of $\sim 250\ \mu\text{s}$ in liquid scintillator (Sect. 6.2.3) is rather short in comparison to the muon rate: The association to the parent muon is therefore unambiguous. A viable way of tagging both ^{10}C and ^{11}C on an event-by-event base is the so-called Threefold Coincidence Technique [100], using spacial and temporal information on cosmic muon, knock-out neutron(s), and Carbon β^+ decay: Neglecting the secondary production of radioisotopes in particle showers and convection in the scintillator, the radioactive Carbon isotope is created and also remains on the muon track. The knock-out neutron travels a short distance from its origin and is then captured. The Carbon isotope should therefore be located in a cylindrical volume around the reconstructed muon track (that allows for tracking uncertainties) as well as a sphere centered on the neutron vertex. The radius of the latter is mainly determined by the free mean path of the neutron. As shown in Fig. 2.5, the loss of exposure due to a TFC veto can be significantly reduced by vetoing only the intersection of the two volumes for a time span corresponding to several half-lives of the radionuclide. The appropriate radii for both volumes are investigated in Sect. 6.2.7.

βn -Emitters

Spallation processes create neutron-rich elements by knocking out several of the protons of a ^{12}C nucleus. These nuclei are β^- emitters with large endpoint energies. In the case of neutron-rich nuclei like ^8He and ^9Li , it is possible that the decay to an excited state of the daughter nucleus is followed by the emission of a neutron. As the second decay is due to strong interactions, it is instantaneous for the concerns of a liquid scintillator. As the neutron is low in energy, it thermalizes and will only show itself when it is captured by

a Hydrogen nucleus, emitting a 2.2 MeV γ quantum. The signal is therefore mimicking the one of the inverse beta decay, as a prompt β signal is followed by a neutron capture about 250 μ s later.

It should be noted that in case of a subsequent neutron, the β endpoint energy is effectively lowered as the decay is to an excited state of the daughter nucleus. In Tab. 2.3, this reduced value is given, followed by the real endpoint in brackets. For an analysis of $\bar{\nu}_e$ events, this background could be in principle excluded by vetoing a fixed period of ~ 1 s after each muon corresponding to several half-lives of the two isotopes. The detector dead time induced by this can be rather large if the muon rate is of the order of 1/min or more. Therefore, the veto can be combined with a spatial cut around the muon track to increase the live exposure (Chap. 9).

2.3.4 Fast Neutrons

The high-energetic cosmic muons passing an underground laboratory are able to transfer a considerable amount of their kinetic energy to knock-out neutrons. Different from thermal or low-energetic neutrons that can be easily absorbed by low-Z material, high-energetic, or fast, neutrons can travel distances of several meters through materials before interacting. Fig. 2.6 shows the initial spectrum of the neutrons on the left, while the distance distribution relative to the muon track is presented on the right. The measured data of the LVD experiment (blue empty circles) [101] is reproduced by the simulations done in [95] (red full circles).

For both BOREXINO and LENA, fast neutrons pose a serious background: If created in the rock just outside a neutrino detector, the parent muon is not recognized by the surrounding muon veto. Although the production of neutrons is often accompanied by a more extent hadronic shower, and in some cases the neutron itself will produce visible particles by crossing the water, there is a remaining probability that a neutron enters the detector without activating the muon veto. It is possible that the deposition of the kinetic energy of the neutron via elastic scattering on one or several protons in the scintillator volume is mistaken for the prompt signal of an inverse beta decay (Sect. 2.2.2). Once thermalized, the capture on Hydrogen will release a delayed 2.2 MeV signal. Fast neutrons are therefore able to mimic $\bar{\nu}_e$ events at various energies.

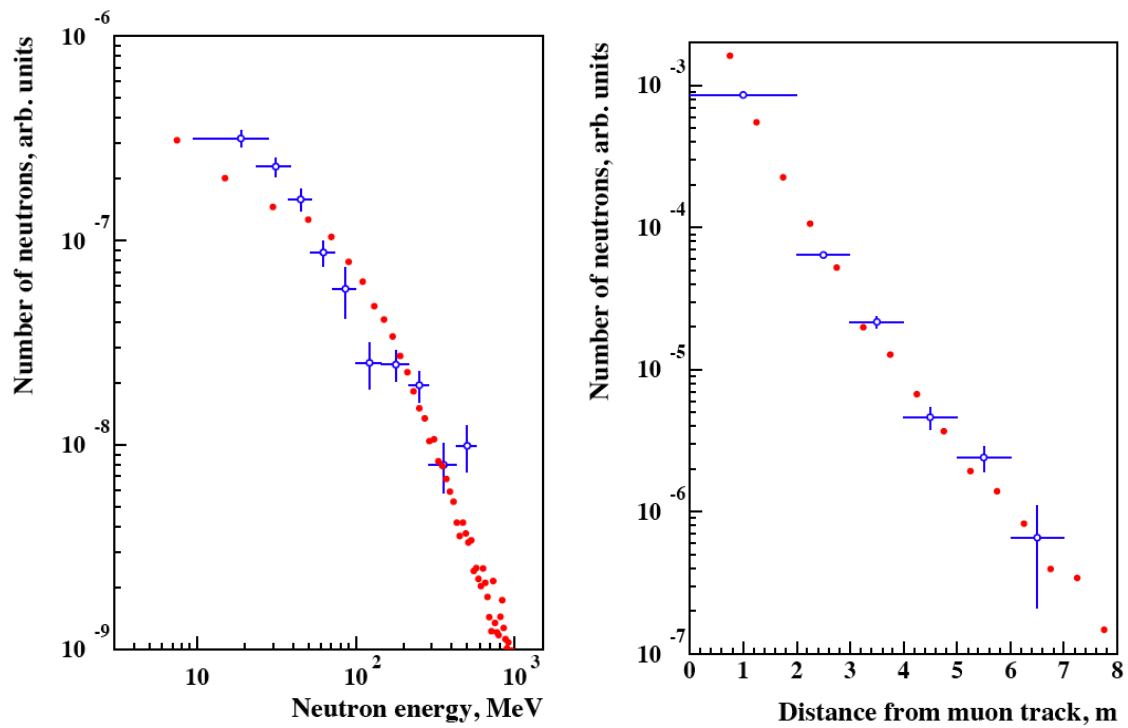


Figure 2.6: Cosmogenic neutron energy spectrum (left) and their distance to the muon track (right) as found in the LVD experiment [101]. The blue empty circles represent the data, while the red filled ones are based on Monte Carlo studies performed in [95].

Chapter 3

The BOREXINO Experiment

The central intention of the BOREXINO experiment is the real-time measurement of low-energy solar neutrinos. Almost 20 years have past from the first proposal of the project in the late 80s [102] to the start of solar data taking in May 2007. This time span was needed to reach the extremely high level of radiopurity that allows for the low energy threshold necessary. Finally, the primary goal of the experiment, the measurement of the solar ${}^7\text{Be}$ neutrinos, has been achieved [76, 81].

Nevertheless, the full potential of the detector has not yet been tapped: Presently, the most promising possibility seems the detection of solar *CNO* and *pep* neutrinos. The development of the software analysis tools that are needed for this task is integral to this thesis: Reliable identification criteria for muons (Chap. 4) and the development of a muon track reconstruction (Chap. 5) are prerequisites to an efficient veto of cosmogenic ${}^{11}\text{C}$ that forms the main background for *CNO/pep- ν* detection. The three-fold coincidence (TFC) veto [100] used in this context is described in Sect. 3.1.3 and later on in Chap. 6.

The first part of the present chapter (Sect. 3.1) is meant to give both an overview on the published data and an outlook on possible future measurements. Sect. 3.2 describes the general detector layout, with an emphasis on the subsystems in focus of this thesis (see [12] for further details). The DAQ system and the offline analysis software framework *echidna* are described in the last Sects. 3.3 and 3.4. The later is intended as a reference for the following chapters.

3.1 Physics Program

The main focus of the BOREXINO experiment lies on the detection of low-energy solar neutrinos. Before the start of BOREXINO, real-time measurements of solar ν 's were limited to the energy regime above 5 MeV. The low background levels in the detector allow for an analysis of electron recoil events above a threshold of ~ 200 keV, in principle including all ν 's from the *pp* fusion chain and the *CNO* cycle (Sect. 1.2.1).

The experiment also offers the possibility for a spectroscopic measurement of geoneutrinos (Sect. 1.2.4). Conditions in BOREXINO are favorable as the distinctive signature of the inverse beta decay in a liquid-scintillator detector (LSD) significantly reduces the background. The high radiopurity of the scintillator and the low reactor $\bar{\nu}_e$ background

flux favor geoneutrino detection in comparison to KAMLAND [25]. In case of a galactic Supernova (SN) explosion, BOREXINO could provide valuable data that is partially complementary to the measurements of water Čerenkov detectors (WCDs) (Sect. 1.2.2). Moreover, BOREXINO will join the SN Early Warning System SNEWS in the course of 2009.

3.1.1 Solar ${}^7\text{Be}$ Neutrinos

In liquid scintillator, low-energetic ν 's are detected via the Compton-like electron recoils of νe -scattering (Sect. 2.2.1). As ${}^7\text{Be}$ - ν 's are monoenergetic, the spectrum features a distinctive "shoulder" at the maximum recoil energy of 660 keV. From the very beginning of data-taking in BOREXINO, background levels in the "neutrino window" (NW) from 200 to 800 keV were low enough that this shoulder was clearly visible in the spectrum.

The most recent BOREXINO analysis of the ${}^7\text{Be}$ - ν event rate was published in May 2008, based on 192 days of solar data. Fig. 3.1 shows on the left the electron recoil spectrum of all recorded events inside the NW (black line). About 500 photoelectrons (pe) correspond to 1 MeV of energy. The rejection of background muons (Chap. 4) and the application of a fiducial volume (FV) cut that limits the data to the innermost 100 tons of the Inner Vessel (IV) remove the two main sources of background, muons and external γ rays. After an additional veto of fast ${}^{214}\text{Bi}/\text{Po}$ -coincidences, the blue spectrum of Fig. 3.1 remains. In this spectrum, the ${}^{210}\text{Po}$ α -peak at ~ 200 pe (that is quenched from 5.3 MeV to ~ 450 keV of visible energy) is very prominent. The subtraction of these events by α/β -discrimination results in the red curve.

All further backgrounds, mainly ${}^{85}\text{Kr}$ and ${}^{210}\text{Bi}$ are β^- emitters for which a rejection is impossible. However, as their decay spectra are known, they were included in a fit of the event rates in the NW that also includes the expected shape of the ${}^7\text{Be}$ - ν recoil spectrum. The result is shown in Fig. 3.1. The light yield is left as a free parameter of the fit and is mainly determined by the shape of the ${}^{14}\text{C}$ β decay spectrum. The analysis was done in parallel by the American and European analysis groups: Both approaches return a value of $49 \pm 3_{\text{stat}} \pm 4_{\text{syst}}$ cpd/100 tons. The fit results for the rates of ${}^{85}\text{Kr}$ and ${}^{210}\text{Bi}$ imply a signal to background (S/B) ratio of 1:1. The systematic error of the ${}^7\text{Be}$ result is determined by the uncertainty in the detector response function and in the target mass defined by the fiducial volume. A calibration campaign to reduce these errors was performed in the beginning of 2009, aiming at an overall uncertainty on the ${}^7\text{Be}$ flux measurement of less than 5%.

3.1.2 Solar ${}^8\text{B}$ Neutrinos

The solar neutrino spectrum above 5 MeV has been determined in real-time measurements by both SNO and SUPER-KAMIOKANDE [23, 24]. BOREXINO cannot hope to significantly improve the preceding results as its target mass is comparatively small. On the other hand, the higher light yield of the LSD allows for a lower neutrino energy threshold: A first BOREXINO analysis measuring the ${}^8\text{B}$ - ν spectrum down to 2.8 MeV was presented in August 2008 [37]. The necessary background reduction is for the most parts very similar to the one presented in Sect. 3.1.1: After the application of FV, fast coincidence, and muon cuts the main background source are short-lived cosmogenics

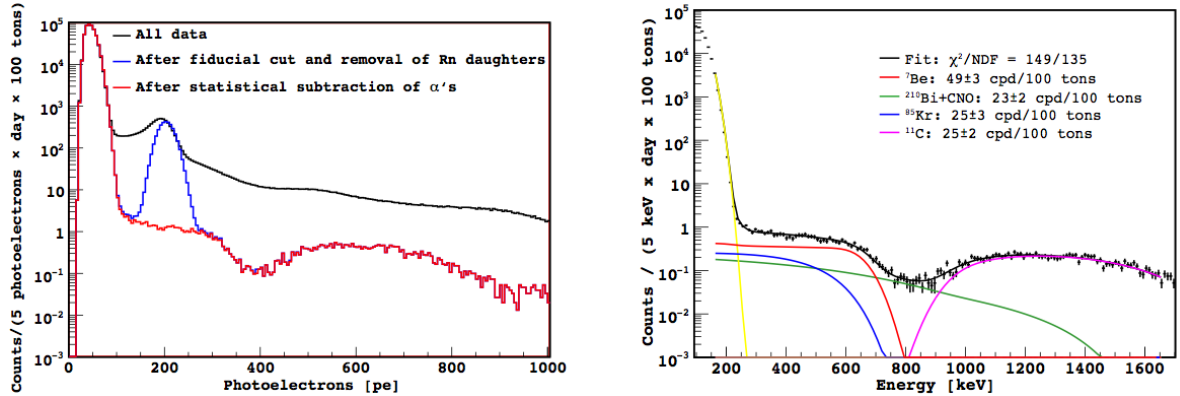


Figure 3.1: Recoil energy spectra in the ${}^7\text{Be}$ region after 192 days of BOREXINO data-taking. While the left photoelectron spectrum shows the effect of different cuts on the selected event sample, the right plot illustrates the fit to the data including both ${}^7\text{Be}-\nu$ and background spectra [81].

featuring high β endpoint energies that can be removed by a 5 sec veto of the whole FV after each muon. In addition, radioactive ${}^{208}\text{Tl}$ in the detector bulk poses a significant background: Its $\beta\gamma$ -decay produces a visible light output between 2.8 and 5 MeV (Sect. 2.3.1). These events can be subtracted statistically using the measured rate of ${}^{212}\text{Bi}/\text{Po}$ -coincidences and scaling by the branching ratios of the ${}^{212}\text{Bi}$ α and β decay channels. However, the lower bound for this analysis is set by the 2.8 MeV γ rays from ${}^{208}\text{Tl}$ decays outside the IV as the abundance of external ${}^{208}\text{Tl}$ cannot be determined analogously.

Based on a detector live time of 246 days, the measured ${}^8\text{B}$ neutrino rate is $0.26 \pm 0.04_{\text{stat}} \pm 0.02_{\text{syst}}$ cpd/100 tons. The ${}^8\text{B}-\nu$ energy spectrum derived from the measured recoil energy spectrum is shown on the left side of Fig. 3.2. Especially the low energy bins are sensitive to spectral deformation caused by the MSW effect: In the energy regime below 5 MeV, the transition of matter to vacuum-dominated oscillations implies a change in ν_e survival probability P_{ee} (Sect. 1.1.3). Unfortunately, the statistical uncertainty in this energy regime is still relatively large. The measured spectrum is well reproduced by the SSM MSW-LMA solution (solid blue line in Fig. 3.2). The no oscillation solution (dotted blue line) is excluded at a 4σ level.

For the first time, BOREXINO allows to test the energy dependence of P_{ee} using the ${}^7\text{Be}$ and ${}^8\text{B}-\nu$ flux measurements of a single detector. Fig. 3.2 shows on the right side P_{ee} as a function of ν energy as predicted by the MSW-LMA solution (solid black line). The two data points of BOREXINO (red) test P_{ee} below and above the transition region; for the second point, the mean of the ${}^8\text{B}$ measurement is used. Survival probabilities were calculated relative to a *high-Z* SSM [37]. BOREXINO on its own confirms the predicted difference in P_{ee} on a 1.8σ level. Lower uncertainties on both ${}^7\text{Be}$ and ${}^8\text{B}$ flux measurements as well as the potential measurement of *pep*- ν 's will improve this result in the future.

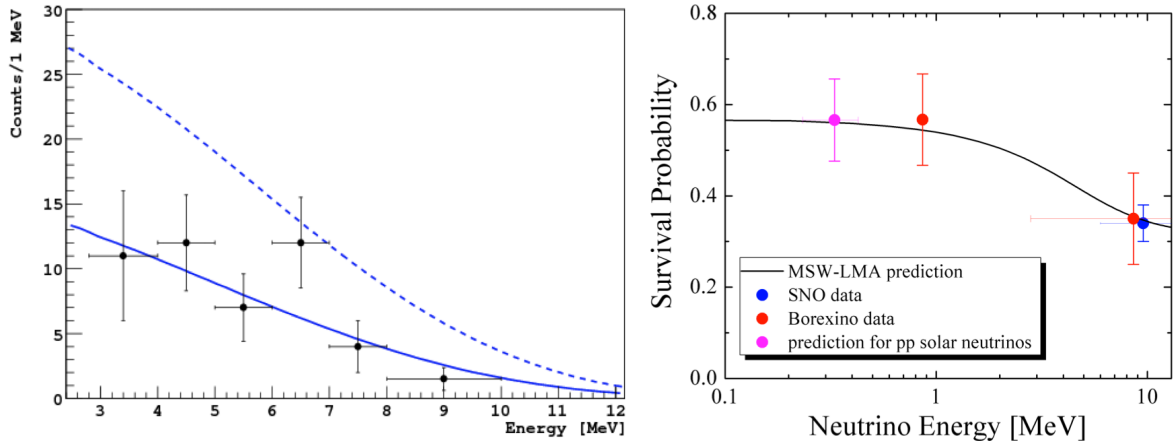


Figure 3.2: *Left*: ${}^8\text{B}-\nu$ energy spectrum from 3 to 12 MeV [37]. The black data points are derived from the BOREXINO experiment. Especially the two bins below 5 MeV as these contain new information compared to WCDs. The solid blue line representing the MSW-LMA oscillation solution reproduces the data well, while the dotted line without oscillations is excluded at 4σ level. *Right*: The survival probabilities derived for ${}^7\text{Be}$ and ${}^8\text{B}-\nu$'s in BOREXINO (red points) are well in agreement with the SSM MSW-LMA prediction (black line) [37].

SSM prediction	w.o. LC	with LC
f_{pp} (1σ)	$1.04^{+0.13}_{-0.18}$	$1.005^{+0.018}_{-0.020}$
f_{CNO} (90% C.L.)	< 6.27	< 3.80

Table 3.1: Determination of the $pp-\nu$ flux and upper limit on the $\text{CNO}-\nu$ flux combining the data of radiochemical, water and scintillator solar experiments [81]. While in the left column no further assumptions were made, the results in the right column also use the solar luminosity constraint. Values are given relative to the current *high-Z* SSM predictions (Sect. 1.2.1, [38]).

3.1.3 CNO , pep , and pp Neutrinos

The best current limits on both pp and $\text{CNO}-\nu$ fluxes can be derived subtracting the realtime data of SNO, SUPER-KAMIOKANDE, and now BOREXINO on ${}^7\text{Be}$ and ${}^8\text{B}-\nu$ fluxes from the integral flux obtained by radiochemical experiments. The results are presented in [81], and are quoted in Tab. 3.1: Both limits with and without the solar luminosity constraint (which is set by measurements of the optical solar constant) are shown.

The BOREXINO collaboration intends to measure the pp , CNO , and $pep-\nu$ spectral contributions in real-time. Fig. 3.3 shows the BOREXINO energy spectrum from 0.2 to 2.2 MeV [103]. FV, muon, and fast coincidence cuts have been already applied. The colored lines represent the fit of the individual signal and background contributions to the overall event rate. Currently, solar ν fluxes (except ${}^7\text{Be}$) enter as fixed parameters because they cannot be determined by the fit. The predicted event rate of pep (*pink line*) and CNO neutrinos (*red*) in BOREXINO is of the order of 1 cpd/100 t in the detection window from 1 to 1.5 MeV. Below this threshold, the flux of ${}^7\text{Be}-\nu$'s (*blue*) as well as the background events of ${}^{85}\text{Kr}$ (*turquoise*) and ${}^{210}\text{Bi}$ (included in *red*) conceal the signal. But even inside the window, spectral fits (Fig. 3.1 *right*) show that cosmogenic ${}^{11}\text{C}$

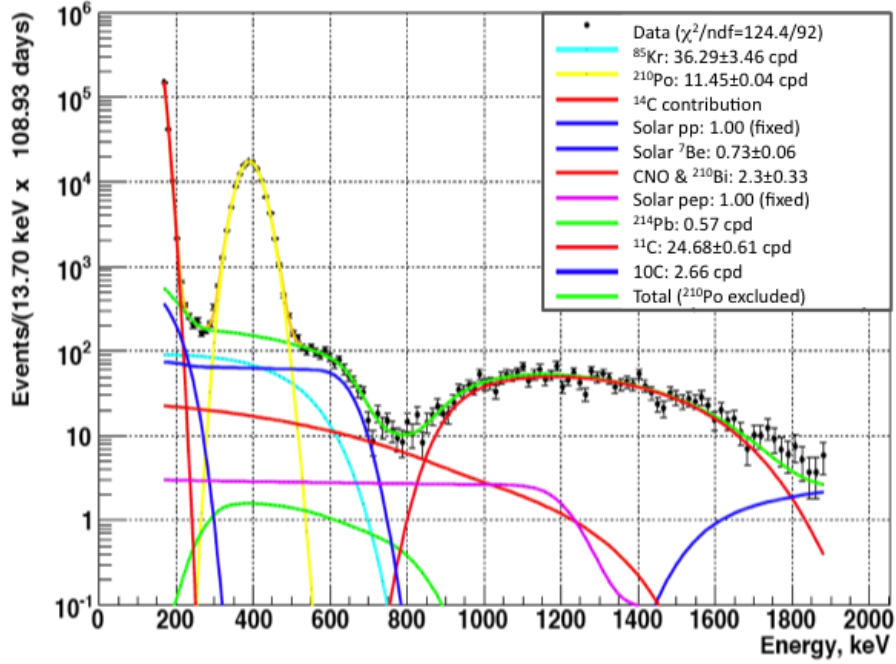


Figure 3.3: BOREXINO event spectrum after 300 days of measurement (black data points). FV, muon, and fast coincidence cut have been applied. The colored graphs indicate the composition of the signal due to individual signal and background sources. pp , pep , and CNO rates are given as fixed input parameters [103].

(red) exceeds with ~ 25 decays per day and 100t the signal by more than one order of magnitude (Sect. 2.3.3). Investigations of tagging this relatively long-lived cosmogenic background ($T_{1/2} \approx 20$ min) via its production process are on-going; an account of the so-called three-fold coincidence (TFC) veto using both the muon track and a radial cut around the ^{12}C knock-out neutron is described in Sect. 2.3.3.

It is still dubious if the detection of pp - ν 's (blue) will be possible in BOREXINO. The on first glance substantial pp event rate of 140 ν -interactions per day is surpassed by the vast count rate of ^{14}C β decays (red) by several orders of magnitude. Only a negligible portion of the electron recoil spectrum exceeds the ^{14}C β endpoint of 157 keV; due to the relatively low energy resolution in this regime ($\sim 10\%$ at 1σ), the ^{14}C spectrum is effectively smeared out to 200 keV. Nevertheless, an increase of knowledge on the detector response function in consequence of the calibration runs might in the future allow to disentangle the endpoints of the ^{14}C decay and pp electron recoil spectra.

3.1.4 Geoneutrinos

As a LSD, BOREXINO is very sensitive to $\bar{\nu}_e$'s and therefore for the detection of geoneutrinos (Sect. 1.2.4). The predicted flux at the LNGS of $\Phi_{geo-\bar{\nu}_e} = 4.2 \times 10^6 \text{ cm}^{-2}\text{s}^{-1}$ is comparatively large as the site is surrounded by continental crust [104]. A rate of ~ 6 inverse beta decay events per year is expected for the whole IV: The FV can be expanded as external γ rays do not play a role for this detection channel (Sect. 2.2.2). Background conditions are favorable: One of the main intrinsic backgrounds in KAMLAND is the reaction $^{13}\text{C}(\alpha, n)^{16}\text{O}$, in which α 's emitted by ^{210}Po are captured on the natural ^{13}C

Channel	Rate
(1) $\bar{\nu}_e + p \rightarrow n + e^+$	45–85
(2) $\bar{\nu}_e + {}^{12}\text{C} \rightarrow {}^{12}\text{B} + e^+$	0.9–3.7
(3) $\nu_e + {}^{12}\text{C} \rightarrow {}^{12}\text{N} + e^-$	1.2–4.2
(4) $\nu_e + {}^{13}\text{C} \rightarrow {}^{13}\text{N} + e^-$	~ 0.06
(5) $\nu + {}^{12}\text{C} \rightarrow {}^{12}\text{C}^* + \nu$	4.2–13
(6) $\nu + e^- \rightarrow e^- + \nu$	4.2
(7) $\nu + p \rightarrow p + \nu$	9.2–35
(8) $\nu + {}^{13}\text{C} \rightarrow {}^{13}\text{C}^* + \nu$	~ 0.06

Table 3.2: Overview of the detection channels for SN neutrinos available in BOREXINO. The rates are scaled from [107] and depend on the assumed SN explosion model. Total event rates vary from 60 to 100 events for the standard SN scenario ($8 M_{\odot}$ progenitor in 10 kpc distance).

in the scintillator [25]. The following emission of a neutron mimics the signature of the inverse beta decay. However, the ${}^{210}\text{Po}$ decay rate in BOREXINO is two orders of magnitude below the KAMLAND level. Scaling from [25], the expected rate of αn -events is ~ 0.1 events per year. The also present reactor $\bar{\nu}_e$ background is about 1/10 of the one in KAMLAND as Italy has no active nuclear power plants. The expected rate of 12 events per year can be scaled from [105]. Nevertheless, the relatively low target mass of 270 t requires a detector live time of at least 3 years to obtain a geoneutrino flux measurement relevant for the discussion of geophysical models [104].

3.1.5 Supernova Neutrinos

Including the whole IV, BOREXINO will detect about 60 to 100 events in case of a core-collapse Supernova (SN) at the center of our galaxy. Tab. 3.2 shows the expected event ranges. The exact values depend on the assumed SN ν spectrum (Sect. 1.2.2). The main contribution of the signal is from $\bar{\nu}_e$ detection via the inverse beta decay (1). But also the NC reaction on ${}^{12}\text{C}$ and the νp -scattering will provide significant signals; both channels are mainly sensitive to $\nu_x = \nu_{\mu}, \nu_{\tau}, \bar{\nu}_{\mu}, \bar{\nu}_{\tau}$ (Sect. 2.2).

The BOREXINO collaboration has decided on joining the SN Early Warning System SNEWS [106]: As the SN neutrino signal is supposed to arrive on Earth several hours before the light of the visible explosion, neutrino detectors can call the attention of optical astronomers to the imminence of a core collapse which would allow for the observation of the early SN light curve. In the best case, a directionally sensitive neutrino detector provides in addition the SN position in the sky. This could also be reached by evaluating the delay time of detectors at different locations on Earth. Currently, only SUPER-KAMIOKANDE and ICECUBE are connected to the SNEWS alarm network. Both BOREXINO and KAMLAND plan to reach the compulsively low rate of false alarms during 2009 and will then join the network.

3.1.6 The CNGS neutrino beam

The CNGS (CERN Neutrinos to Gran Sasso) project is a long-baseline neutrino oscillation experiment. Since 2007, the neutrino beam is generated at the SPS accelerator at CERN: Charged pions and kaons are produced by a proton beam on Berillium target. The mesons are directed into a decay line that is aimed at the LNGS. The resulting decay ν_μ and $\bar{\nu}_\mu$ feature a mean energy of 17 GeV due to the Lorentz boost of the incident proton. Due to the ratio of the beam energy to the 730 km long baseline, the LNGS is located in the first oscillation maximum of $\nu_\mu \rightarrow \nu_\tau$ conversion: The OPERA experiment (which is located in Hall C next to the BOREXINO detector) aims at the direct detection of ν_τ appearance by CC interactions [108].

The intended beam intensity of 4.5×10^{19} pot (protons on target) per year corresponds to 2900 ν_μ CC reactions per kton and year at the LNGS site. As a result, high-energetic muons are created in μ_ν CC reactions either inside the BOREXINO detector or in the rock mass in front of the experiment. Similar to cosmic muons, these muons are high enough in energy to create tracks crossing both ID and OD. A large fraction of these tracks should be orientated along the beam axis. The total number of beam events is noticeable by a significant increase of the muon rate during beam times (Sect. 6.1.1). As the ν_μ beam is pulsed and the proton injection time of each spill is available, the beam events can be tagged and rejected in the solar neutrino analysis. On the other hand, the CNGS muons allow a test of the muon veto efficiency (Sect. 4.2.1). The data of the OPERA high-precision tracker [109] would provide a further calibration source for the BOREXINO track reconstruction, based on the fraction of muon tracks crossing both detectors.

3.2 Detector Design

The BOREXINO detector is located in the Hall C of the Laboratori Nazionali del Gran Sasso (LNGS) that it shares with the OPERA detector. The laboratory is accessible by a 10 km highway tunnel crossing the Gran Sasso mountain massive. An exact value for the shielding from cosmic radiation is hard to specify due to the irregular shape of the mountains; effective values range from 3200 to 3800 mwe (meters water equivalent).

The BOREXINO hardware is optimized for the search of rare neutrino events. The onion-like structure of the detector is chosen to shield the central target region effectively from external backgrounds, while at the same time the radiopurity of the used materials increases towards the center (Fig. 3.4). BOREXINO is divided into two subdetectors, the scintillator-filled Inner Detector (ID) and the water-filled Outer Detector (OD). The intersection is done by a stainless steel sphere (SSS) of 13.7 m diameter, while the OD is contained in a steel dome of 18 m diameter and 16.9 m height. A very detailed account is given in [12]. Therefore, only a short overview is presented here.

3.2.1 Inner Detector

Fig. 3.4 (*right*) shows on a view of the BOREXINO Inner Detector: The centerpiece of the ID are 280 tons of liquid scintillator, contained in a spherical nylon vessel of 8.5 m diameter. The scintillator is based on the organic solvent Pseudocumene (PC), with an



Figure 3.4: *Left:* Layout of the BOREXINO detector. *Right:* View of the Inner Detector before filling. The two spherical nylon vessels are surrounded by the stainless steel sphere to which the PMs are mounted.

addition of $\sim 1.5 \text{ g/l}$ PPO (Sect.8.2). The resulting light yield is about 10^4 photons per MeV of deposited energy (ph/MeV). The light attenuation length is $\lambda_{\text{att}} \approx 8 \text{ m}$ (Sect. 8.1), the fast decay component of the signal $\sim 3 \text{ ns}$. To provide the necessary radiopurity, the scintillator was distilled once again on-site before filling. The contents of $^{232}\text{Th}/^{238}\text{U}$ has been determined to be $(6.8 \pm 1.5) \times 10^{-18} / (1.6 \pm 0.1) \times 10^{-17} \text{ g/g}$ scintillator. Equal care was given during the manufacture of the surrounding Inner Vessel (IV): The $125 \mu\text{m}$ thick nylon membrane was constructed off-site under clean room conditions. It is attached by nylon strings to the south pole of the SSS to compensate the small density difference between scintillator and buffer.

This innermost active detection region is surrounded by a buffer layer of 2.4 m thickness, filling the space between the IV and the SSS. A mass of 1040 tons of PC is needed. This inactive zone is meant to shield the IV from external γ radiation. In order to obtain an acceptable trigger rate, the light output of buffer events is quenched by about a factor 20 by the addition of dimethylphthalate (DMP). It is dissolved at a concentration of $\sim 5 \text{ g/l}$. Moreover, a second nylon sphere, the Outer Vessel (OV), divides the buffer at a radius of 5.5 m; it acts as a diffusion barrier to the radioactive noble gas ^{222}Rn emanating from the glass of the PMs mounted to the SSS.

The stainless steel sphere itself is holding 2212 inward-facing photomultipliers. The 8" ETL 9351 would in principle correspond to a light-sensitive surface coverage of $\sim 15 \%$. However, reflective Winston cones have been attached around the photocathode of all but 384 PMs. These light concentrators increase the effective optical coverage for IV events to 30%, at the same time limiting the field of view of the PMs regarding buffer events. The photocathode quantum efficiency of the used PMs is 21%; without optical losses due to light propagation in the scintillator, the expected photoelectron yield is therefore 630 pe/MeV. The observed value (scaled to the full number of PMs) is $\sim 550 \text{ pe/MeV}$. At the moment of writing, about 1950 channels are still working. This value can be determined by the monitoring of laser test pulses that are fed to the PMs

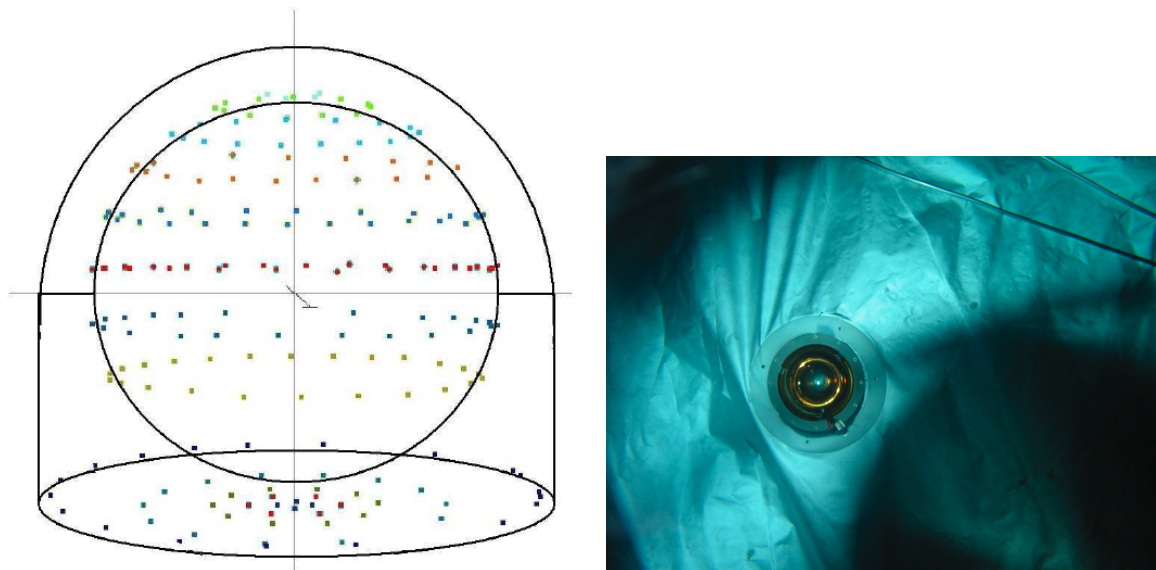


Figure 3.5: Left: Distribution of photomultipliers of the OD muon veto. Right: View of an encapsulated PM in the OD, photograph taken after filling. The PM is surrounded by reflective Tyvek foil.

via optical fibers.

The photograph on the right of Fig. 3.4 has been taken by one of the optical cameras attached to the SSS wall. These cameras are used to monitor the shape of the nylon vessels and to optically determine the position of calibration sources inserted into the detector.

3.2.2 Outer Detector

The Outer Detector contains 2.1 kt of deionized water which serve as additional shielding against external radioactivity. It is equipped with 208 PMs that act as a water Čerenkov muon veto. The PMs are of the same fabrication type as the ID ones; in addition, they are fully encapsulated to be protected from the water of the OD. 154 of the PMs are distributed in 8 horizontal circles on the upper 3/4 of the SSS, while the lower 1/4 of the sphere is left unequipped. The remaining 54 PM are distributed in 5 circles on the OD floor. Monte Carlo simulations have shown this configuration to be most effective in the identification of cosmic muons. Similar to the ID PMs, the OD PMs are equipped with optical fibers through which LED calibration pulses can be fed.

Most of the OD surfaces is covered with highly reflective Tyvek foil to increase the muon detection efficiency by redirecting the light of the muon Čerenkov cones. While this efficiency enhancement is actually reached, the reflected light interferes with the muon track reconstruction, as will be demonstrated in Chap. 5. Moreover, the OD is divided by Tyvek foils at the SSS equator. The two subregions are not fully optically decoupled, as only 2/3 of the interspace between SSS and steel dome are blocked. Fig. 3.5 shows on the right an encapsulated PM surrounded by Tyvek foil. The photograph was taken by one of the six cameras installed in the OD to monitor water quality and the state of the foils.

3.2.3 Current Status

Since the beginning of data taking in 2007, several adjustments have been done to maintain the spherical shape of the IV. By extraction of small quantities of the Outer Buffer (OB) the pressures of the three subvolumes inside the SSS were adjusted. In the end of 2007, a haze of condensed water formed at the south pole of the IV, caused by the large temperature gradient present in the detector (several °C from bottom to top). A permanent water loop heating the lower half of the OD was put into operation. It successfully removed the condensed water.

In autumn 2008, a leakage of liquid scintillator from the IV into the Inner Buffer (IB) was discovered. Analyzing the data from ID cameras and regular DAQ, a total leakage of 6 tons over a period of half a year starting from March or April 2008 could be determined. The cause of this leak with an estimated diameter of 1-2mm remains unknown. Possible explanations are the start of the water loop mentioned before, or the warming of Hall C due to the air-cooling of the OPERA deflecting magnet which resumed operation in spring 2008.

The leak had shown itself in a significant deformation of the IV. As a countermeasure, about 3 tons of PC and PC+PPO were introduced into the IV in late autumn 2008 which restored it to a more spherical shape. In order to anticipate an irreparable deflation of the IV due to an enlargement of the leak, a calibration campaign using radioactive sources was started in the end of the year. The calibration sources were introduced through the tubing at the north pole of the SSS where a dedicated clean room is maintained. Calibration was done in two phases: A first on-axis phase in which sources were let down in the IV on a rope; and a second off-axis phase in which the source was fastened to the end of two rods of variable length linked by a joint. The evaluation of the calibration data is still ongoing. In the meantime, the purification of the IB liquid in loop mode has begun, removing both PPO and DMP from the buffer. The later is done to reduce the buoyancy force acting at the IV. Up to now, the leak rate remains unchanged, allowing for a stable operation of the detector.

3.3 Data Acquisition System

A very detailed description of the DAQ hardware can be found in [96, 12]. This section can provide only basic information, highlighting systems necessary for the understanding of the offline analysis software presented in Sect. 3.4.

The PMs of the BOREXINO detector are read out by several DAQ subsystems. Both HV and signals are led by coaxial underwater cables of 55 m length from the electronics room (ER) in front of the detector to the PMs inside (and vice versa). Once arrived in the ER, the signal is separated from the HV by means of voltage decouplers that are part of each input channel of an electronic front-end board (FEB). From here, the signals are fed to the different DAQ subsystems. Block diagrams of both ID and OD electronics are shown in Figs. 3.6 and 3.7.

- **Main DAQ (Laben):** The ID read-out electronics and especially the ADCs were built in collaboration with the Laben company¹, and are commonly referred to as

¹Laben S.p.A., Milan (I)

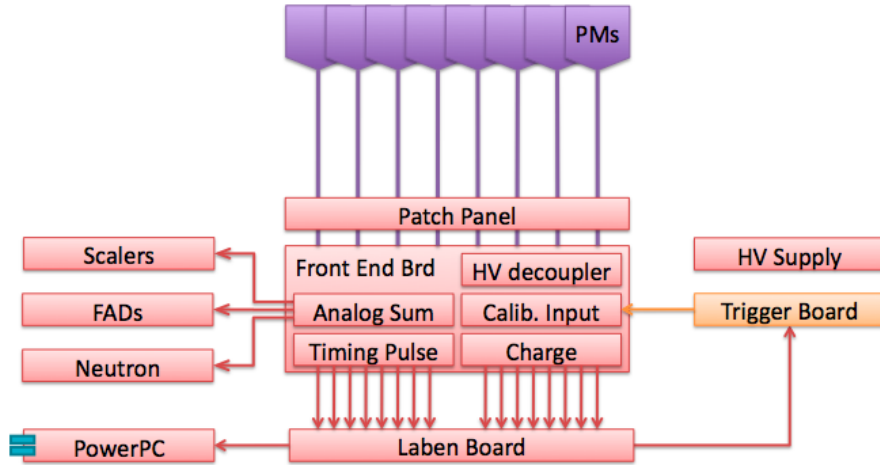


Figure 3.6: Block diagram of the ID electronics.

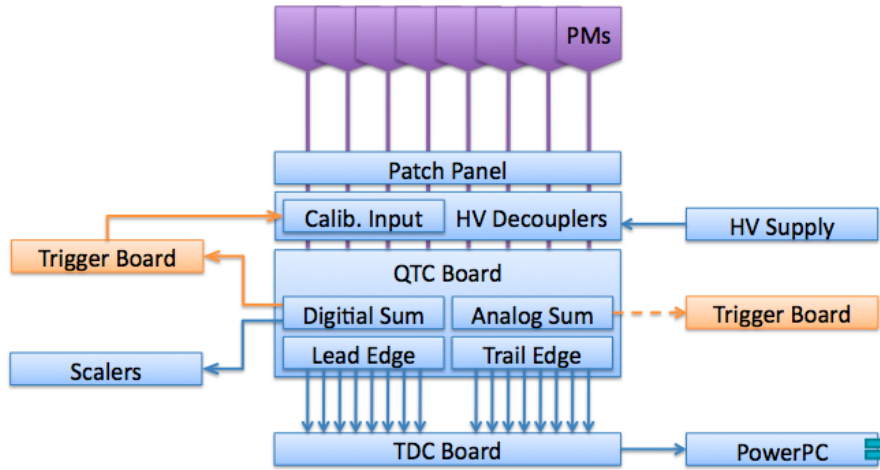


Figure 3.7: Block diagram of the OD electronics.

the *Laben* system. The ID electronics are arrayed in 14 racks of 158 channels each, corresponding to 2212 ID PMs. These channels are in turn distributed on 20 FEBs of eight channels each. For the main DAQ, the FEBs provide both a fast amplified signal used for timing and an integrated signal. The integration gate is 80 ns wide and the output corresponds to the signal charge. If several photons arrive inside the same integration gate, their combined charge will be measured. Both time and charge information are forwarded to *Laben* ADC boards that are housed in a VME crate (20/crate). The *Laben* boards digitize the data with a time resolution of 200 ps relative to a common clock and provide the data to the Power PC (PPC) of the VME crate. It is connected to the LAN and sends the data in case of a trigger to the central PC (*BxBuild*) that gathers all the information belonging to an individual trigger event.

- **Muon DAQ:** The DAQ chain of the OD differs in several points from the ID one: Signal and HV from the 208 OD PMs are decoupled in nine separated modules of 24 channels each. The signals are forwarded to 16 charge-to-time converter (QTC) boards in a VME crate. The primary output of the boards is a logic pulse

of variable length: The leading edge corresponds to the rising flank of the PM signal, while the difference of the time stamps of trailing edge and leading edge is proportional to the charge of the signal (plus a fixed pedestal). Again, the integration gate is roughly 80 ns wide. The logic pulse is forwarded to two time-to-digital converter (TDC) boards that in turn are connected to the LAN via a PPC.

- **FADC/Neutron system:** Both systems are meant to provide full pulse shape information of the PM signals to complement the information of the main DAQ. In case of the *FADC* system, the signal of 24 PMs are superimposed by the Analog Sum modules integrated into the FEBs and fed to one input channel of the FADCs. While in this way full time information on the signal is available, the possibilities for spacial reconstruction are fairly limited. The motivation for the operation of this system is the high event rate in case of a galactic SN explosion (Sect. 3.1.5) that would surpass the possibilities of the main DAQ. An additional FADC system (*Neutron*) was introduced in summer 2008 in order to investigate the neutron detection efficiency of the Main DAQ, and to provide additional information on the events following in the wake of a muon.
- **Trigger:** The *Borexino Trigger Board* (BTB) plays a central role in evaluating the information sent by the *Laben* and *Muon* subsystem and to feed a read-out signal to all DAQ systems if the trigger condition is fulfilled. In addition, the BTB issues service triggers which are used for the monitoring and calibration of the detector. For the *Laben* system, a trigger occurs if 25 PM hits are registered by the *Laben* boards in a time window of 60 ns. This number of hits corresponds to an ID event of a visible energy of 50 keV and lies therefore well inside the ^{14}C β decay spectrum. The trigger condition of the outer *Muon* system is 6 PM hits in a time gate of 150 ns. This is the typical time scale of a muon Čerenkov event (including light reflections). The total trigger rate of the DAQ is presently ~ 35 Hz. If one of the two subdetectors triggers, both are read out for a time gate of about 16 μs . The baseline in front of the event is chosen to be relatively short, positioning the hits of the triggering event in the very beginning of the gate. This allows for the detection of fast coincidence signals inside a single gate. In the case of a cosmic muon crossing both detectors (and therefore triggering both), a second acquisition gate is opened immediately after the one of the muon to guarantee a high neutron detection efficiency (Sect. 6.2.1).

3.4 *Echidna* Analysis Software

All European institutes that are part of BOREXINO collaborate in a common analysis group, while a second group is formed by the American universities. Both groups have been developing software codes that prepare the raw data provided by the DAQ to a level that allows a physics analysis. Since 2004, earlier versions of software tools based on the programming languages Fortran, C, and C++ have been bundled in the common *echidna* framework which is now used as a standard for the European analysis [96]. The equivalent American software package goes by the name *Mach4*. At the beginning of the data taking in spring 2007, most of the software necessary for ^7Be neutrino analysis

was completed. However, the processing of OD PMT data was still at a relatively low level. The finding and refinement of applicable muon identification markers (Chap. 4) as well as the introduction of a muon track reconstruction using the information available both from ID and OD (Chap. 5) constitutes one of the main topics of the present work.

Presently, the typical duration of a DAQ run is six hours. The raw data is contained in binary files, encoding the information on the trigger, and the data of ID and OD PMs. These files are read by the *echidna* reconstruction program; basis are C++ and the physics data analysis framework ROOT [110].

Following the object-orientated approach, both raw data and higher analysis information are stored in classes: These contain variables in which the data is stored and at the same time basic *getter* functions necessary to evaluate these variables. The defined output of these *getters* allows a high modularity of the code and provides the possibility that several persons work in parallel on improvements of individual classes without interference; while the contents of a class may change, its interface to other classes remains the same. In this way, the information on physics provided by different detectors subsystems can be easily accessed by all users. At the same time, the data itself is protected from direct access or writing to preserve its integrity.

ROOT has been developed for the analysis of CERN experimental data and provides a basic framework of data-processing objects for this task. Most of the high-level analysis is performed using the ROOT interpreter that allows to run short macros or enter single command line inputs without the need of code compilation. To ease the access to the data, the *echidna* output files are organized by a customized ROOT tree (*BxTree*), basically a list of all the trigger events of a given DAQ run. The physics information belonging to each individual trigger is stored alongside in a defined set of classes (*BxEvent*). As displayed in Fig. 3.8, each subsystem of the DAQ is represented by a class: While general information on trigger time and type are contained in the class *trigger*, the data retrieved from the ID is stored in the three classes *laben* (the main DAQ), *fadc*, and *neutron*, representing the three electronic subsystems described in Sect. 3.3. The data collected by OD PMs is stored in the class *muon*. As part of this thesis, the class *track* was introduced which contains the data on the muon tracking obtained by a global fit to ID and OD muon data.

Tab. 3.3 and 3.4 order all the variables used in Chaps. 4-6 according to their classes and shortly describe their physical meaning. Where it is necessary, more detailed descriptions will be given in the following chapters.

The *echidna* framework contains about fifty modules: Low-level modules write the data to the output root-file, check the stability of the detector systems using the service triggers and identify problematic channels. They also provide the connection to a common BOREXINO SQL database that contains information on detector geometry and preceding calibration runs. Higher-level modules identify PM hits associated to physical events inside the detector and determine energy, position, start time and pulse shape. At the end of this chain, data files combining DAQ runs of an entire week are created. The events contained in these DST² files are flagged according to low-level analysis filters that identify for instance muons, alpha-particles, or coincidence signals.

²DST = Data Storage Tape

Class	Description
<i>event</i>	data object comprising all data acquired due to a trigger of the DAQ system
<i>trigger</i>	class containing trigger information
<i>trigger.trgtype</i>	denotes the trigger condition: 1 - ID event (overrides 2) 2 - OD event 128 - neutron event (issued after ID muon)
<i>trigger.btb_inputs</i>	additional information on the trigger condition: 0 - ID trigger only 4 - OD trigger is present <i>note: a muon crossing both ID and OD features trgtype = 1 and btb_inputs = 4</i>
<i>trigger.gps_times</i> []	array encoding the GPS time in [0] seconds and [1] nanoseconds
<i>laben</i>	class containing the main DAQ data
<i>laben.n_decoded_hits</i>	number of all hits acquired in the time gate
<i>laben.trigger_time</i>	time relative to the internal clock
<i>laben.empty_boards</i>	number of laben boards containing no hits
<i>laben.clusters</i> []	class comprising the information of a single physical scintillation event; one <i>event</i> may contain several <i>clusters</i>
<i>laben.clusters</i> [][<i>start_time</i>]	start of the cluster relative to the clock
<i>laben.clusters</i> [][<i>nhits</i>]	number of hits associated to the cluster
<i>laben.clusters</i> [][<i>nhits_conc</i>]	hits in PMs with light concentrator only
<i>laben.clusters</i> [][<i>charge</i>]	sum charge of all hits associated to the cluster
<i>laben.clusters</i> [][<i>position_mi</i>]	reconstructed position of the (point-like) event contains variables <i>x, y, z</i> and getter <i>GetR()</i>
<i>laben.track</i>	class containing the output of ID tracking
<i>laben.track.x1, y1, z1, dx1, ...</i>	coordinates of ID track entry point
<i>laben.track.x2, y2, z2, dz2, ...</i>	coordinates of the impact point
<i>muon</i>	class comprising OD data
<i>muon.start_time_sss</i>	time of the first clustered hit on the SSS
<i>muon.start_time_floor</i>	time of the first clustered hit on floor
<i>muon.n_clusters</i>	number of clusters found by the algorithm
<i>muon.clusters</i> []	class containing the information of an entry/exit point candidate (Chap. 5) a single muon will generate several <i>clusters</i>
<i>muon.clusters</i> [][<i>start_time</i>]	time relative to <i>start_time_sss</i>
<i>muon.clusters</i> [][<i>charge</i>]	sum charge of all clustered hits
<i>muon.clusters</i> [][<i>x, y, z</i>]	coordinates of the cluster barycenter
<i>muon.is_tracked</i>	boolean, <i>true</i> if track is found
<i>muon.track</i>	class containing the OD track
<i>muon.track.x1, y1, z1, dx1, ...</i>	coordinates of OD track entry point
<i>muon.track.x2, y2, z2, dz2, ...</i>	coordinates of OD exit point

Table 3.3: *Echidna* classes and variables used in this work

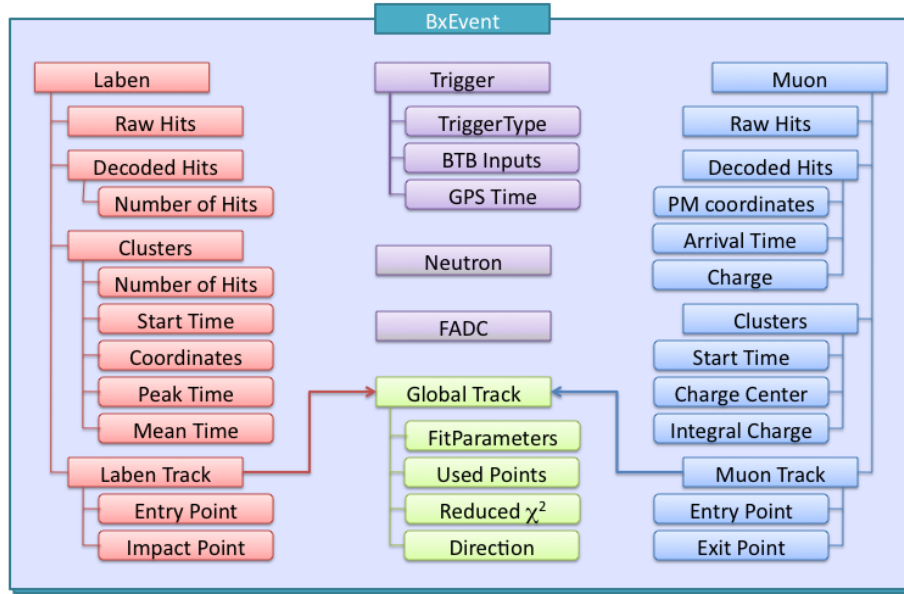


Figure 3.8: Data Structure of the *echidna* reconstruction code: The data gathered by all detector subsystems after a trigger is stored in the *BxEvent* class. The information of each of the subsystems is stored in an individual class. Inside these containers, data is saved in several levels of processing and complexity. The variables most relevant for the following analyses are indicated.

Class	Description
<i>track</i>	global track combining ID/OD data
<i>track.alpha</i> , <i>alpha_error</i> <i>track.beta</i> , <i>beta_error</i> <i>track.gamma</i> , <i>gamma_error</i> <i>track.delta</i> , <i>delta_error</i>	parameters and uncertainties of the 3D track fitted to ID/OD track points: $y = \alpha + \beta \cdot x$ $z = \gamma + \delta \cdot x$
<i>track.downward</i>	boolean - indicates track direction
<i>track.chi2</i>	reduced χ^2 value of the fit
<i>track.npoints</i>	number of points used in the fit
<i>track.GetTheta()</i> <i>track.GetPhi()</i>	zenith (θ) and azimuth (φ) angle describing the orientation of the track pointing towards the muon source
<i>track.GetImpact()</i>	distance of the muon track to the detector center

Table 3.4: *Echidna* classes and variables used in this work

Chapter 4

Muon Identification in BOREXINO

A prominent source of background for the detection of solar neutrinos is the residual flux of cosmic muons present in the *Laboratori Nazionali del Gran Sasso* (LNGS). While the rock overburden of ~ 3600 mwe reduces the surface flux of $\sim 6.5 \times 10^5 \text{ m}^{-2} \text{ h}^{-1}$ by several orders of magnitude, a residual flux of $1.2 \text{ m}^{-2} \text{ h}^{-1}$ remains at the depth of the underground laboratory [92, 93, 98].

Due to the need of vetoing these muons and to reject muon-induced spallation products in the detection volume (Chap. 6), the detector was designed to allow an efficient identification of muon events. 208 photomultiplier (PM) tubes cover both sphere and ground of the outer water tank, detecting the Čerenkov light cones emitted by the through-going muons. Moreover, the Inner Detector (ID) system is able to discern "track-like" and "point-like" scintillation events¹ by pulse shape analysis.

The *echidna* analysis package adds a flag² to all events that are identified as a muon by either one of the above mentioned criteria. In the following Sect. 4.1, both the signature of muon events and the possibilities for the flagging of muons in Inner and Outer Detector (OD) will be discussed. Further on, the efficiencies of the muon flags currently used in the *echidna* [12, 96] analysis software will be evaluated in Sect. 4.2, using mutual comparison of the flags as well as the few pure muon samples that are available. The potential of using the photomultipliers without Winston cones [12] in the ID for muon identification is shortly addressed. A study of the time stability of the muon flags currently in use and their combined muon identification efficiency will close the chapter (Sect. 4.3).

4.1 Muon Identification Criteria

With increasing depth, the percentage of low energetic muons in the overall cosmic muon flux decreases as they are absorbed by the shielding rock. The mean energy of the cosmic muons reaching the underground laboratory is therefore 320 GeV (compared to about 1 GeV at the surface) [98]. In water and scintillator, materials of density $\sim 1 \text{ g/cm}^3$,

¹In the following section, track-like, muon-like, and muon events will be used synonymously. The same is true for neutrino-like, point-like or neutrino events which will also include (if not stated otherwise) α , β , and γ decays as background events.

²A flag is a software marker.

muon energy loss is about 2 MeV/cm at ionization minimum. As a consequence, most of the muons entering the detector (usually from above) will not be stopped by the materials inside and leave without any significant loss of energy. On their way, they will traverse the water tank, and in many cases also the buffer liquid and the liquid scintillator.

4.1.1 Outer Detector Flags

Cosmic muons crossing the OD Water Tank create Čerenkov light as the energy is far above the muon Čerenkov threshold in water of 160 MeV ($\simeq 1.5 m_\mu$). This light will be detected by the 208 phototubes that are distributed on the upper 3/4 of the surface of the Stainless Steel Sphere (SSS) and the floor of the Outer Detector (Fig. 3.5). The Čerenkov light is not emitted uniformly but on a cone of 41° half opening angle that is centered around the track (Sect. 2.1.1). Moreover, a highly relativistic muon will be travelling faster than the Čerenkov light it produces as light speed is lowered by the medium. When a muon crosses a surface covered by phototubes, the group of PMs near to the penetration point will return a large and almost synchronous signal. As a result of the Čerenkov cone, this point will be circularly surrounded by less intense PM hits that are delayed in time (Fig. 5.1). This distinctive hit pattern is the fundament of the tracking algorithm (Chap. 5).

Muon Trigger Board (MTB)

The OD muon tags are both searching for an increase in OD PM activity above usual dark noise fluctuations. They operate at two different stages of data processing: The first one is the hardware trigger of the Outer Detector which is issued by the Muon Trigger Board. The trigger condition is given by a significant increase in number of hits in a time span comparable to the transit time of a muon. At the moment, a threshold of 6 hits in a timegate of 150 ns is set. This threshold is high enough to prevent dark noise triggers but it is sometimes fooled by light entering through leaks in the outer water tank (Sect. 4.3).

In its current state, only the logical information of the discriminator of each channel is used, i.e. the sum of the issued square pulses has to surpass the trigger threshold set by the MTB³. The actual pulse height of the signal in each of the PMs is therefore irrelevant as long as it surpasses the ADC threshold. An alternative design using the analog sum of the channels was foreseen in the original design; this analog trigger is sensitive to intense hits in only very few PMs and will become important if the number of broken PMs substantially increases. It is, however, currently not in use as the performance of the digital trigger is satisfactory.

Muon Clustering (MCR)

The Muon Clustering algorithm is a downstream software trigger based on the acquired OD data. Its trigger condition is a slight refinement of the MTB triggering condition:

³The Secondary Output of each QTC board returns the sum of the logical pulses of each of its channels, which is passed on to the MTB (Chap. 3 and [96]).

The software module *bx_muon_findcluster* is dedicated to search for groups of almost simultaneous hits in neighbouring PMs which are in a later reconstruction step used for the muon tracking (Chap.5). In a first step, two subsets of PMs are defined, distinguishing between hits at PMs mounted on the stainless steel sphere and PMs mounted on the floor. The trigger condition is met if four phototubes or either subset are firing within 150 ns. In this case, a software flag is set and the event will be treated as a muon in analysis.

As will be seen, the efficiencies of both OD tags are comparable. This redundancy is useful as MTB and MCR are for several reasons not available for the whole data set (Sect. 4.3). Therefore, both flags are in use for muon identification.

4.1.2 Inner Detector Flags (IDF)

Muons passing through the scintillator of the Inner Vessel create a very large light output as they depose hundreds of MeV of ionization energy. In this case, the limitations of both the phototubes and the electronics cause a distortion of the energy information. Still, the visible energy of these signals is comparable to point-like events with an energy of several tens of MeVs. As this energy is far above the ${}^7\text{Be}$ shoulder or even the endpoint of the ${}^8\text{B}$ recoil energy spectrum these signals do not pose a serious background for neutrino observation.

The situation changes for muons crossing the ID buffer without touching the Inner Vessel. In this case, the generated light output will be partly due to the Čerenkov effect, and partly due to residual scintillation of the buffer liquid; the energy deposition of a muon is large enough to create some scintillation despite of the quencher dissolved in the liquid⁴. These situations are dangerous, as the light output of a muon crossing only the buffer is low enough to mimic a neutrino signal. The amount of produced light depends almost linearly on the length of the muon trajectory in the buffer. The muon signals cover therefore the whole range of solar neutrino recoil energies, depending on the length of the trajectory in the buffer.

However, in this case the light source is off-center and widespread both in space and time. This can be utilised in two general approaches: Typical muon pulses feature longer rise and decay times than neutrino-like scintillation events of comparable energy. In the later case the whole energy is deposited almost instantly in one space point, the spread of photon arrival times mainly due to geometry and the scintillation decay constants (the fastest component being of the order of a few nanoseconds). On the other hand, a muon crossing the buffer will need depending on the track length up to 45 ns to depose all of its ionisation energy. Pulse shape discrimination (PSD) is therefore a valuable tool for the identification of muons.

Pulse Shape Analysis

A number of variables are available in *echidna* that are sensitive to either rise or decay time of the acquired pulses. The leading edge of the signal is described by the *peak time* variable that contains the time difference between on-set and peak of the pulse. The

⁴In addition, there will be absorption-reemission processes of Čerenkov light both in buffer and scintillator which further complicates the light arrival pattern.

nhits range	μ parameter range
100-900	peak time >40 ns
900-5000	peak time >30 ns
>5000	mean time >100 ns

Table 4.1: The ID pulse shape discrimination of point-like and track-like events relies on their peak and mean time parameters. The cuts are chosen dependent of the number of hits as the distribution of muon-like events is varying with energy.

mean time, which is defined as the average of the time differences between the onset of the pulse and the individual hits in the pulse. This parameter is therefore sensitive to the overall signal duration.

In current *echidna* data-analysis, a combination of these two parameters is the only Inner Detector Flag (IDF) in use for muons. Fig. 4.1 shows the overlaying *mean time* vs. *peak time* distribution of ID neutrino and muon events for three visible energy sub-ranges⁵: Low (100–900 hits) in red, medium (900–5 000 hits) in green, and high (>5 000 hits) in blue. Muons are assumed to feature large *peak* and *mean times*, their distributions spreading over the upper and right half of the scatter plot, while neutrinos are concentrated at the lower left. In the low and medium energy range, the *peak time* is the more efficient discrimination parameter. The respective discrimination thresholds of 40 ns for the low range and 30 ns for the medium one are denoted as red and green lines in the scatter plot. For high energies, PM after-pulses begin to contribute significantly to the signal, increasing especially the *mean time* of the events. In this range, a *mean time* cut at 100 ns is applied. In general, the limits were chosen conservatively to avoid the false identification of point-like events as muons, minimizing potential overefficiencies of the muon flagging. The values are summarized in Tab. 4.1.

For completeness, it should be mentioned that α/β -discrimination methods can be extended to the identification of muons, as these techniques rely on the difference in the decay times of α - and β -like events. In the *echidna*-analysis, both the *Gatti-parameter* and the *tail-to-total-ratio* of the pulse area are used for this task. Tests done in [112] show that these parameters are useful for muon identification, as the decay of muon signals is on average even slower than the one of α -events. However, the methods are correlated to the *mean time/peak time* cuts already implemented in *echidna*, and therefore not used in this analysis.

The Deutsch parameter

The BOREXINO ID phototubes are in their majority equipped with Winston cones (Chap. 3) [12]. The shape of these aluminium mirrors was chosen to enhance the photon collection for scintillation events located at the center of the detector. On the other hand, the cones limit the field of view of the PMs to the radius of the Inner Vessel. However, 384 of the 2212 photomultipliers were installed without light concentrators. In consequence, these photomultipliers will collect less scintillation light but be more sensitive to light-emitting events in the buffer, i.e. muons. The ratio of hits in the

⁵Pulse shape analysis becomes increasingly ineffective with the decrease of registered photons; a lower threshold was therefore chosen at 100 hits.

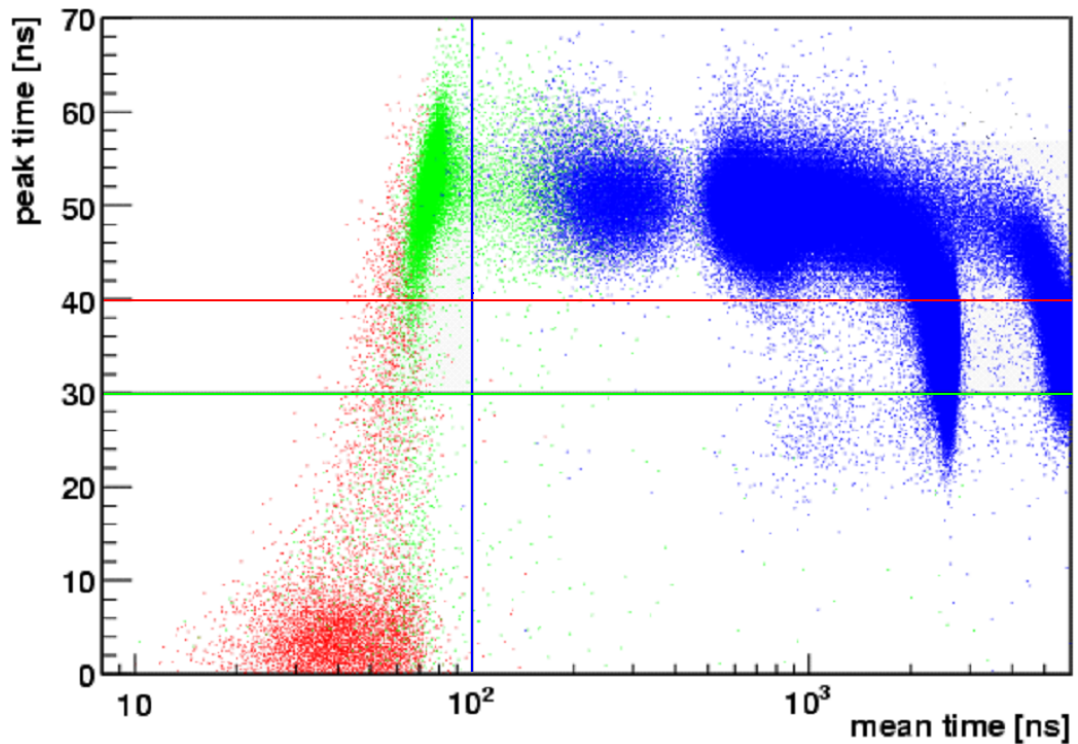


Figure 4.1: The distribution of Inner Detector events in a *mean time vs. peak-time* scatter plot. Colors code events with visible energies of 100 – 900 (red), 900 – 5 000 (green) and above 5 000 hits (blue). While neutrino-like events are concentrated at low mean and peak time regions, muons feature larger *peak times*, and, especially above 5 000 hits, by far larger *mean times*. Muon discrimination limits (depicted as lines of colors corresponding to their energy ranges) were chosen accordingly (Tab. 4.1) [111].

photomultiplier subsets with and without the Winston cones can therefore be used as a discrimination parameter for neutrino-like (IV) and muon-like (buffer) events. In the following, it will be referred to as the *Deutsch-parameter* after Martin Deutsch who suggested the technique [76].

4.2 Flagging Efficiencies

As part of this thesis, the efficiencies of the available muon tags were investigated in order to provide reliable values for muon identification and for the rejection capability of the muon veto. Two general methods were chosen: Samples of selected muon events were used to find directly the identification efficiencies of the flags. For these studies, limitations arise from the quantity of events and impurities of the samples. In a second step, a high-statistic study of all neutrino data was carried out, using the mutual comparison of the ID and OD muon flags [112]. The result of these tests is limited by the non-ideal performance of the testing flag itself. However, this method is able to provide reliable lower limits for the flagging efficiencies and can be regarded as a cross-check of the absolute methods.

Only muons crossing the Inner Detector are considered. For the present analysis, all regular neutrino runs from May '07 (the start of data-taking) to June '08 are included. Moreover, the data undergo a screening process, the run validation described later in Sect. 4.3.3. Data-acquisition runs not passing the validation criteria are either cut or fully excluded from analysis. The remaining data set corresponds to an exposure of ~ 215 days. For the CNGS⁶ events that present an almost pure sample of muons for the IDF efficiency study, a special subset of distilled data files is used. The contained events are selected by their GPS time stamps that are compared to the individual spill times of the CNGS beam.

The study includes both MTB and MCR flags for the Outer Detector, and pulse shape discrimination in the Inner Detector. For the latter, a combined cut on peak time and mean time parameters is discussed. Also the Deutsch parameter is shortly addressed.

4.2.1 Direct Efficiency Determination

Ideally, the discrimination efficiencies of the different methods is determined by comparing pure samples of muon and point-like events. As the efficiency of the flags will be both dependent on the visible energy of the events and, in case of the muons, on the direction and extension of the track, the samples would have also to reflect this variety. In reality, such an ideal sample is not immediately available for both types of events. However, high-energetic Inner Detector events present in normal neutrino runs are an appropriate muon sample for the Outer Detector. The same is true for the muons induced by the CNGS neutrino beam in the Inner Detector (Sect. 3.1.6).

⁶CERN neutrinos to Gran Sasso, Sect. 3.1.6.

High-Energetic ID events

At high visible energies, scintillation events in the Inner Detector will predominantly be caused by cosmic muons that are crossing the Inner Vessel creating large amounts of light. In Fig. 4.2, the Inner Detector energy spectra of events flagged ("muons", *blue*) or not flagged ("neutrinos", *red*) by the OD MTB tag are shown. The contribution of unflagged events at high energies is very low, of the order of 0.5%.

The following study was limited to events with more than 5 000 hits in the first cluster of an ID event⁷. This threshold of 5000 PM hits is equivalent to an integral charge of at least 10 000 – 15 000 photoelectrons. In case of a point-like event, this would correspond to an energy deposition of roughly 20 – 30 MeV. This energy is higher than the endpoint of the most energetic solar neutrinos, the *hep- ν* , and far above the maximum energies of the radioactive decays in the U/Th chains (Sect. 2.3.1). However, a small background contribution due to the spallation products of muons, especially of fast neutrons, cannot be excluded. In this sense, efficiencies obtained using this sample will always present a lower limit, as a small contamination of the sample with non-muon events cannot be avoided.

The resulting efficiencies of $\varepsilon_{\text{MTB}} > 0.9951(10)$ for MTB and of $\varepsilon_{\text{MCR}} > 0.9970(10)$ for MCR are comparable (see last column of Tab. 4.2). It is important to note that the efficiencies of the OD flags are independent of the visible energy detected in the Inner Detector: The PM coverage of the Outer Detector has (at the moment of writing) no large gaps, and all muons have – independently of the exact track geometry – to cross several meters of water before entering the steel sphere, thereby creating comparable amounts of Čerenkov light. The result of this study can therefore be assumed to be constant over the the whole energy range of ID events.

CNGS muon events

The CNGS neutrino beam provides a large abundance of muon events in BOREXINO which are created by ν_{μ} charged current reactions in the upstream rock or the detector materials itself. As these events can be easily assigned to the beam spills via their GPS time signature, it seems to be an ideal calibration source for the muon veto. However, the Outer Detector of BOREXINO is optimized for vetoing and tracking the mainly vertical tracks of cosmic muons. The CNGS neutrino beam, on the other hand, arrives at the detector at an angle of about 5° below the horizon, and will therefore generate mostly horizontal muon tracks. As a result, the distribution of the phototubes is inappropriate (especially for muons crossing the uninstrumented lower third of the sphere) which leads to a decreased veto efficiency. Moreover, the interaction vertices of the neutrinos will be distributed over rock, OD, and ID. For muons creating signals in both subdetectors, it is difficult to determine if the track is stopping in the ID or OD, originating from the ID or OD, or fully crossing both subdetectors, as the Tyvek foils sometimes create light reflections in the whole of the OD (Sect. 3.2.2). As these aspects introduce systematical uncertainties for the determination of a muon identification efficiency, the high-energetic ID events are more reliable for an OD efficiency study; therefore, no analysis based on

⁷As stated in Sect. 3.4, a cluster is an actual physical scintillation signal in an event which covers a time gate of several microseconds (and can therefore contain several clusters).

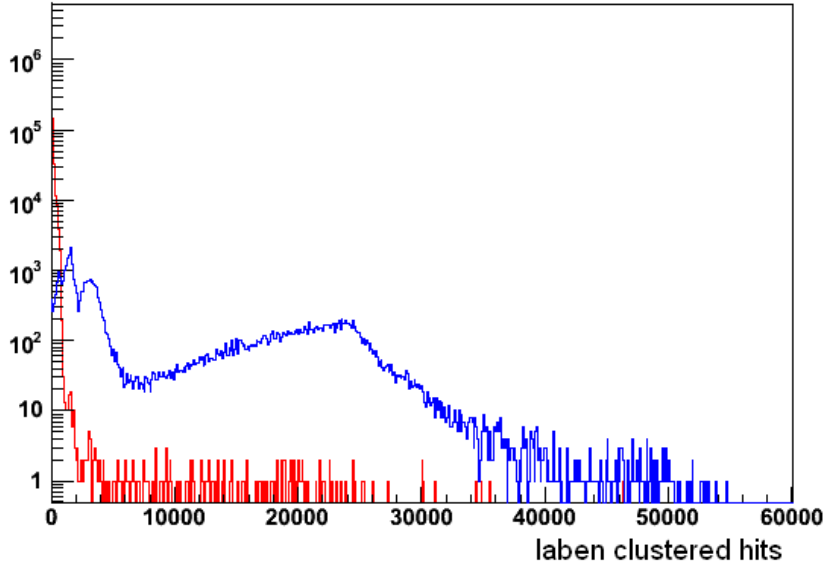


Figure 4.2: Number of hits spectra of neutrino-like (*red*) and muon-like (*blue*) events in the Inner Detector, the latter flagged by the muon trigger board (MTB). Above 5000 hits, only few events without a MTB flag are present. The ratio of unflagged of flagged events can be considered as the MTB inefficiency.

the CNGS was performed for MTB and MCR.

The situation is different for the Inner Detector; due to its spherical symmetry, its ability for muon flagging is in principle independent of the track direction. A small contamination of the sample arises from random coincidences of the 30 Hz of ^{14}C decay events with the time gate of 40 ms applied to each CNGS spill. After removal of these events by an energy cut at 100 hits, the CNGS events offer in principle an excellent possibility to test the IDF efficiency. Unfortunately, the available data sample for 2007 is rather low in statistics.

In a sample of 420 ID events denotes all events with a light output above threshold in the ID., the three energy regions and the discrimination cuts as defined in Sect. 4.1.2 and Tab. 4.1 were tested. The results are shown in the last column of Tab. 4.2. At low energies, $(77 \pm 9)\%$ of the events were correctly identified as muons. All events in the medium and high energy range were identified as muons according to the cuts; the arising lower efficiency limits are 93% and 92%, respectively. The general increase of efficiency with the (visible) energy is according to expectations as the larger number of registered PM hits improves the temporal pulse shape resolution. The global energy-independent efficiency was determined to $(95 \pm 5)\%$. In general, the uncertainties are relatively large as statistics are low.

4.2.2 Relative Efficiencies

As a cross-check, the efficiencies of the three tags can be derived by mutual comparison to each other. As regular neutrino runs can be used, the large available data sample is reducing the statistical uncertainties to a very low level. On the other hand, systematical uncertainties are introduced: As the test-sample is created applying a reference muon flag on both point-like and muon events, the sample itself will contain point-like events

due to overefficiencies of the reference flag. Moreover, it is essential for a relative test of two flags that their tagging methods are uncorrelated, which is not true for MCR and MTB. The test of IDF against the OD flags and vice versa is however valid.

Lower Limit on Efficiencies

In the following, the tested flag will be referred to as A , the reference flag as B . In lowest order, flag B is assumed to produce a pure sample of muons, containing N_B events. The relative efficiency of the flag A , $\varepsilon(A|B)$ can then be obtained by dividing the number of events flagged by both tags, $N_{A\wedge B}$, by N_B :

$$\varepsilon_0(A|B) = \frac{N_{A\wedge B}}{N_B - \Delta_B} \quad (4.1)$$

Δ_B is an unknown number of events wrongly flagged by B , caused by its overefficiency. Here, Δ_B is assumed to be 0. The resulting efficiencies shown in Tab. 4.2 are therefore lower limits, as Δ_B will reduce the denominator of Eq. (4.1). The results of the relative tests of MTB and MCR to each other should be handled with care as the flags are not truly uncorrelated. The tests versus IDF imply efficiencies of at least 99.6% for MTB and 99.7% for MCR. IDF on the other hand shows an overall performance of 98.5%, with a relatively poor discrimination efficiency at low visible energies of 68.7%. The values are in good agreement with the efficiencies derived in Sect. 4.2.1. This already indicates relatively low overefficiencies of the flags.

Over-Efficiencies

Large over-efficiencies, i.e. the unintended flagging of point-like events as muons, reduce the data available for neutrino analysis or, even worse, introduce a bias. This danger is larger for the IDF, as discrimination thresholds optimized for muon identification alone could quite easily flag also neutrino events because the distributions of both types of events in peak and mean time are overlapping. Both MTB and MCR are basically free of overefficiencies as long as there is no light connection between Inner and Outer Detector. However, light leaks in the external steel dome increase the rate of trigger type 2 events⁸ and can cause random coincidences with physical events in the ID. This can in principle cause an effective overefficiency.

To calculate the overefficiency, ω_A , the number of events that are flagged by flag A but not by the test flag B is compared to the expected number of neutrino events, i.e. the events not flagged by B :

$$\omega_A = \frac{N_{A\wedge\bar{B}}}{N_{\bar{B}}}$$

At least some of the events identified by flag A but not by flag B are caused by the inefficiency of B . In this sense, the results shown in Tab. 4.3 are overestimated and therefore an upper limit to the actual overefficiency. As one would expect, the upper bounds for the over-efficiencies for both MTB and MCR are relatively high: The test

⁸Trigger type 2 events are only triggering the Outer Detector (Sect. 3.3).

Flag	nhits	MTB	MCR	IDF	direct
MTB	> 75		0.9998(10)	0.9960(11)	0.9952(10)
MCR		0.9988(10)		0.9970(11)	0.9971(10)
IDF		0.9849(10)	0.9849(10)		0.95(5)
IDF	75-500	0.687(5)	0.687(5)		0.77(9)
	500-5000	0.9935(14)	0.9936(14)		1.00(7)
	> 5000	1.0000(17)	1.0000(17)		1.00(8)

Table 4.2: Relative efficiencies (columns IDF, MTB, and MCR) of the investigated muon flags (denoted in the 1st column). For comparison, the values obtained by the direct methods described in Sect.4.2.1 are shown in the last column. The first three rows show energy-independent global values (excluding the ^{14}C region). In the lower part, the IDF efficiency is split into subranges of visible energy. MTB and MCR are independent of ID visible energy. All values are lower bounds to the actual tagging efficiencies (Sect. 4.2).

Flag	MTB	MCR	IDF
MTB		$2.7(2) \times 10^{-5}$	$2.065(18) \times 10^{-3}$
MCR	$1.75(5) \times 10^{-4}$		$2.214(19) \times 10^{-3}$
IDF	$5.77(10) \times 10^{-4}$	$4.36(9) \times 10^{-4}$	

Table 4.3: Relative overefficiencies of the muon flags (listed in 1st column): The values were obtained by comparing the number of events flagged by the tested flag but not by the reference flag (columns MTB, MCR, IDF) to the overall number of events not flagged by the reference flag (Sect. 4.2.2). The given values are upper bounds.

against IDF returns 0.2%, caused by the contribution of the comparatively low efficiency of the IDF to $N_{A\wedge B}$. IDF overefficiency is determined to $\sim 0.06\%$ by both OD muon flags.

4.2.3 The Deutsch parameter

The Deutsch parameter is defined as the ratio of hits in phototubes without Winston cone to the total number of hits. The potential of the Deutsch parameter as tag for muon identification has been investigated using the data-set of regular neutrino runs. Using MTB flag to identify the events as neutrino-like or muon-like, a relative study of the efficiency can be performed. As a dependence on energy comparable to the one of the IDF is expected, the analysis is split into subranges from 100-900, 900-5000, and above 5000 hits.

The resulting distributions for roughly one month of data are shown in Fig. 4.3. The distributions have been normalized to 1. Although a difference in the mean values of the distributions is discernible in each energy subrange, the separation is not large enough to define an effective cut without accepting large overefficiencies. This is especially true for the energy range below 900 hits in which the contribution of the Deutsch parameter would be mainly needed to add to the comparatively weak IDF performance. At more than 900 hits, the discrimination power rises, the overlap in point-like and track-like distributions being partly due to the inefficiencies of the MTB.

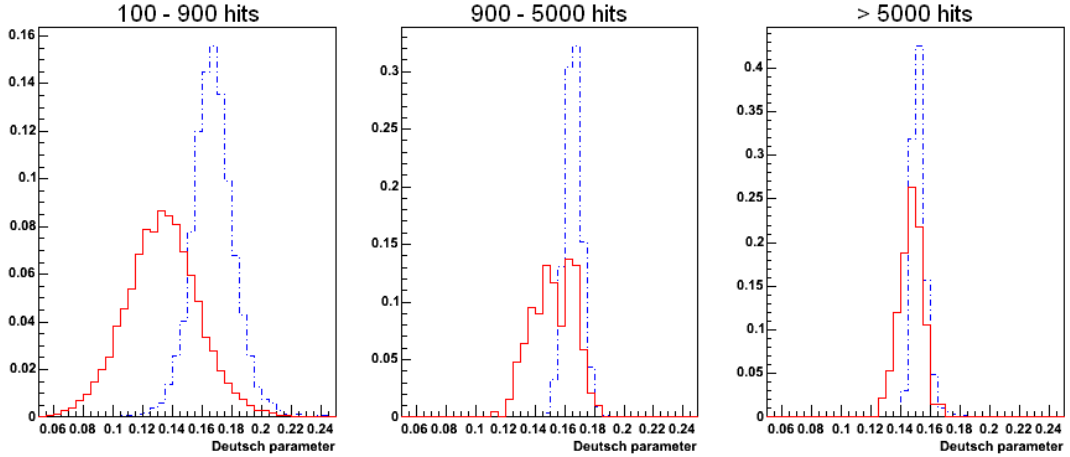


Figure 4.3: Normalized Deutsch-parameter distributions for point-like (red line) and track-like (blue dashes) events in three visible energy subranges. Track-like events were identified using the MTB flag. Especially in the first subrange (left), the distributions show a significant overlap, which will result in low efficiencies or large overefficiencies, depending on the chosen discrimination threshold. For medium energies (medium), the distribution of point-like events shows two peaks: The right one is due to the residual of muons not flagged by the MTB. For high energies (right), virtually no real point-like events are left; the red curve is mainly due to unidentified muons.

As it is conceivable from Fig. 4.3 that the impact of including the Deutsch parameter in the analysis would be rather small, no further-going studies were performed.

4.3 Muon Tagging Time Stability

As mentioned above, a careful selection of the data is necessary to obtain reliable numbers in the flagging efficiency studies. Maybe even more important, the screening of the data helps to identify several problems related to the muon flagging (and also tracking), which have an immediate impact on neutrino analysis.

4.3.1 Data Screening

For the identification of malfunctions of the muon flagging and data acquisition, several criteria are used, most of them based on stability tests of flagging efficiencies. An automated script looping over all runs and further tools for evaluation have been prepared for this screening. Only events of *trigger type 1* (i.e. point-like and track-like events of the ID) are considered; the rates of muons merely crossing the OD are not taken into account. As many of the identified problems appear in the course of a DAQ run, the runs are divided into ten time bins of equal length. The following criteria are used:

- MTB and Muon Crate are enabled.
- the muon rate of an individual flag is within expectations.
- the relative difference between the tagging rates of two muon flags is small.
- the flagging rates of each bin are within expectations.

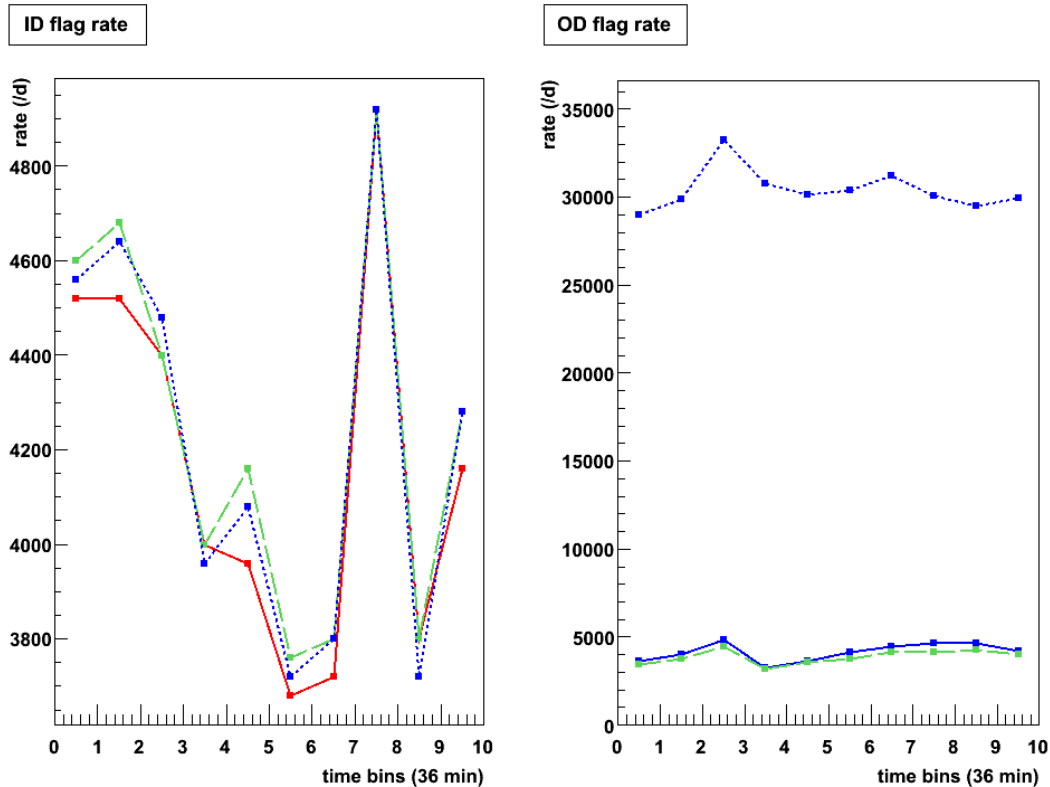


Figure 4.4: Scaled muon rates derived from the muon flags for both ID and OD data of a typical 6 hour run. The left plot shows rates for IDF (solid red line), MTB (blue dotted), and MCR (green dashed) for ten time bins of 36 minutes each. The right plot depicts MTB (blue solid) and MCR (green dashed) rates. OD regular MTB (blue dotted) rate is very large for this run, as light leaks are present in the outer water tank. However, applying a minimum threshold of 25 photomultiplier hits to the data reduces the rate to the expected ~ 4000 muons/day. The plot was taken from the Run Validation (Sect. 4.3.3).

The last step is not applied if runs last less than 1.5 hours. Fig. 4.4 shows the variation in tagging rates for a typical run. In this way, 965 out of 1353 runs have been identified as immediately usable for analysis, corresponding to a total of ~ 125 days of exposure.

4.3.2 Problematic Runs

However, 388 runs show non-standard behaviour. These runs have been screened very carefully to trace the problems back to their origins in the DAQ chain. Almost all of these runs can be assorted to one or more of the following categories:

85 runs are without MTB flag, as the MTB was installed only one month after data taking had begun in June '07.

168 runs are affected by the disabling of the muon QTC boards from the DAQ. Especially in the beginnings of BOREXINO data-taking, the muon DAQ was very unstable and frequently crashed midway a DAQ run. For muon tagging, this means the loss of the MCR flag for the rest of the run.

108 runs feature a disalignment of the OD hits to the corresponding trigger: The OD data is written together with the trigger and ID data of another event, being off by a small and constant number of events.

23 runs are affected by sudden outbreaks of noise in the ID, leading to an increased IDF rate while OD flags are stable.

18 runs with unusually high MTB rates for OD events (most likely due to an increase in light leakage) show also an increased number of ^{14}C -like events in ID that are random coincidence with an OD light event, therefore increasing the MTB muon rate for ID.

20 runs feature neither MTB, MCR, nor OD data as the HV of the OD phototubes is (unintentionally) disabled for the whole run.

4.3.3 Run Validation

Several steps have been taken to reduce the occurrence rate of these incidents. The *run controller*, a software module governing the data acquisition, was modified to stop the acquisition in the case of a failing DAQ crate, and to restart after re-activation of all crates. It was further modified to detect states of DAQ disalignment, and to restart the DAQ in this case. A software module for the realignment of OD data to the correct trigger event is in preparation. Moreover, runs with a disabled muon data acquisition will be flagged in order to be able to omit these in analyses relying on muon tracking. If both MTB and MCR are disabled in a run, it is lost for analysis.

In the course of this thesis, a software tool monitoring the performance of the OD data-taking was developed and integrated into a similar module for ID data screening that was already present. As part of these modules, several plots are created that allow the user to check the items listed below:

- muon flag stability in both subdetectors for 10 equally spaced time bins (Fig. 4.4)
- muon rate for both ID and OD in 10 minutes time bins
- mean pulse shape for neutrino, muon and calibration events
- number of hits spectra for muon events both for ID and OD
- dark noise levels of the OD photomultipliers depending on trigger type
- event size (number of hits) in the OD depending on run time and trigger type

The script also checks automatically the status of both MTB and Muon Crate and the presence of OD event disalignments.

This Run Validation tool is now part of the data processing done by the shifters present at the experimental site. In case of deviations from the norm, the shifter can decide either to invalidate the run partly or entirely, and to pass on information about unknown effects to the muon group.

4.3.4 Long-Term Stability

The results of the efficiency studies can be used to check the time stability of the individual flags. Apart from the known problems identified in Sect. 4.3.2, more subtle changes in efficiency could be discovered in the long-term monitoring of the muon event rates determined by the individual flags. Fig. 4.5 depicts the rates for MTB, MCR, IDF for all unproblematic runs from May 2007 to October 2008. The first phase of data taking is only available for MCR and IDF, as MTB was installed not earlier than Run 5265. Rates are given in muon events per day, while the typical run duration is about 6 hours. Within statistical errors, all three flags are reasonable stable. Fortunately, no systematic decrease of the efficiency with proceeding detector life time is visible. However, small variations are present in all of the three flags: The annual modulation of the cosmic muon flux on a 2% level is visible, as well as an increase in event rate towards the end of the period due to the CNGS neutrino beam (Sect. 6.1.1).

The deviations of the individual tagging rates relative to each other might as well reveal changes in efficiency. Fig. 4.6 displays a long-term study of the difference in muon event numbers tagged N by the three flags. The plot shows the the normalized difference D_{AB} of two individual flags A and B for the selected runs:

$$D = \frac{N_A - N_B}{N_{A \wedge B}} \quad (4.2)$$

In general, the results are in agreement with the expectations according to the efficiency studies of Sect. 4.2. The slight but continuous excess in MCR rate relative to MTB that is evident in the upper plot corresponds to the higher tagging efficiency of the MCR. No time dependence is visible. Similarly, the two lower plots comparing the IDF to the two OD flags reflect the lower efficiency of the IDF. However, here a time-dependence is evident: at later times, the event numbers rise and approach the ones of MTB and MCR. This trend is a result of the leakage of IV scintillator into the Inner Buffer (Sect. 3.2.3): β -like buffer events caused by radio-impurities and external γ 's feature distorted pulse shapes and therefore an increased probability to be falsely tagged as a muon by the IDF.

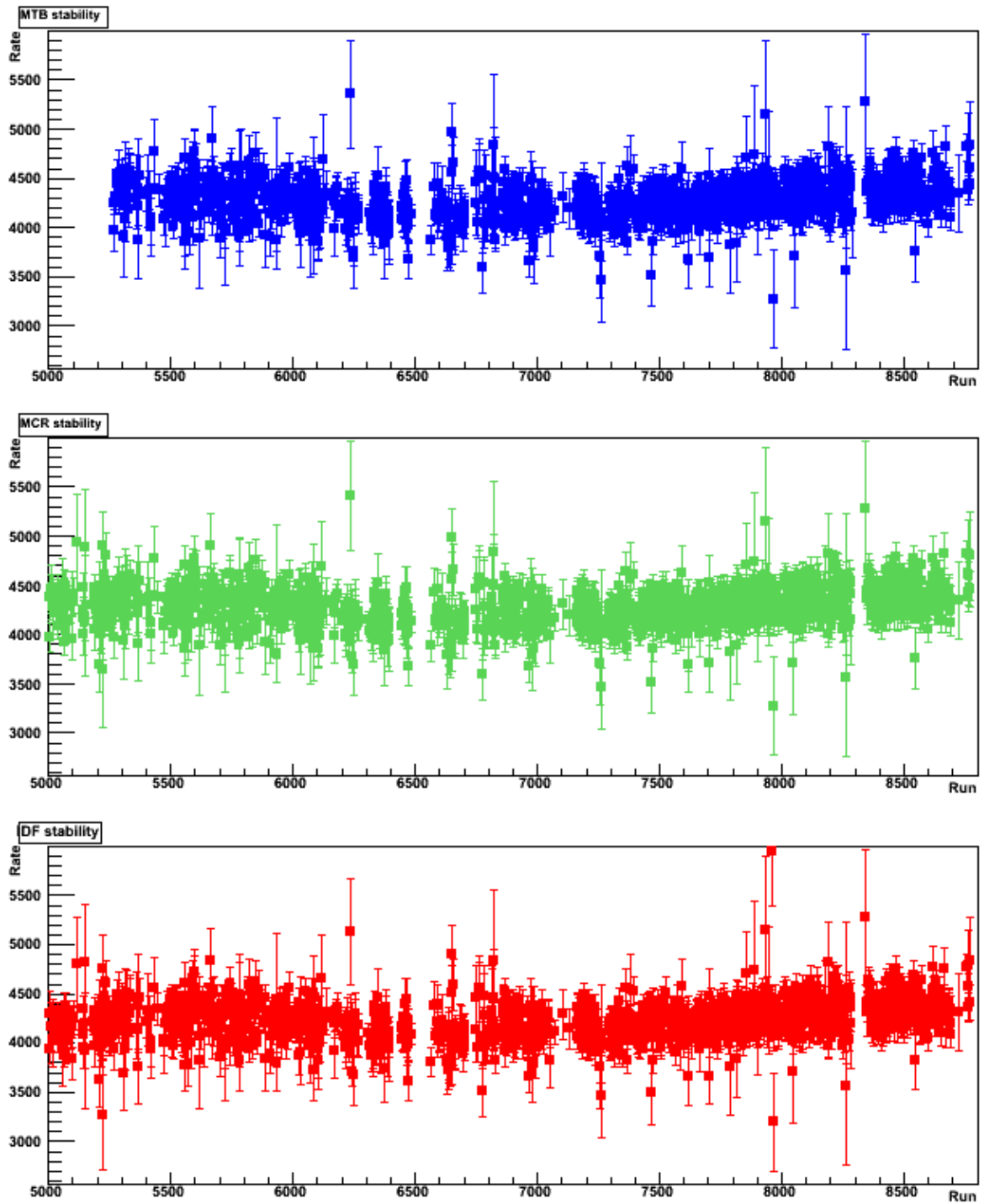


Figure 4.5: Inner Detector muon rate derived from the individual muon flags for runs from May 2007 to October 2008: All three flags (MTB, MCR, and IDF) show small variations due to the annual modulation of the cosmic muon rate and the CNGS beam (Sect. 3.1.6). No data is present for MTB before run 5265 when it was installed. The visible gaps in run numbers are caused by detector maintenance and calibration phases.

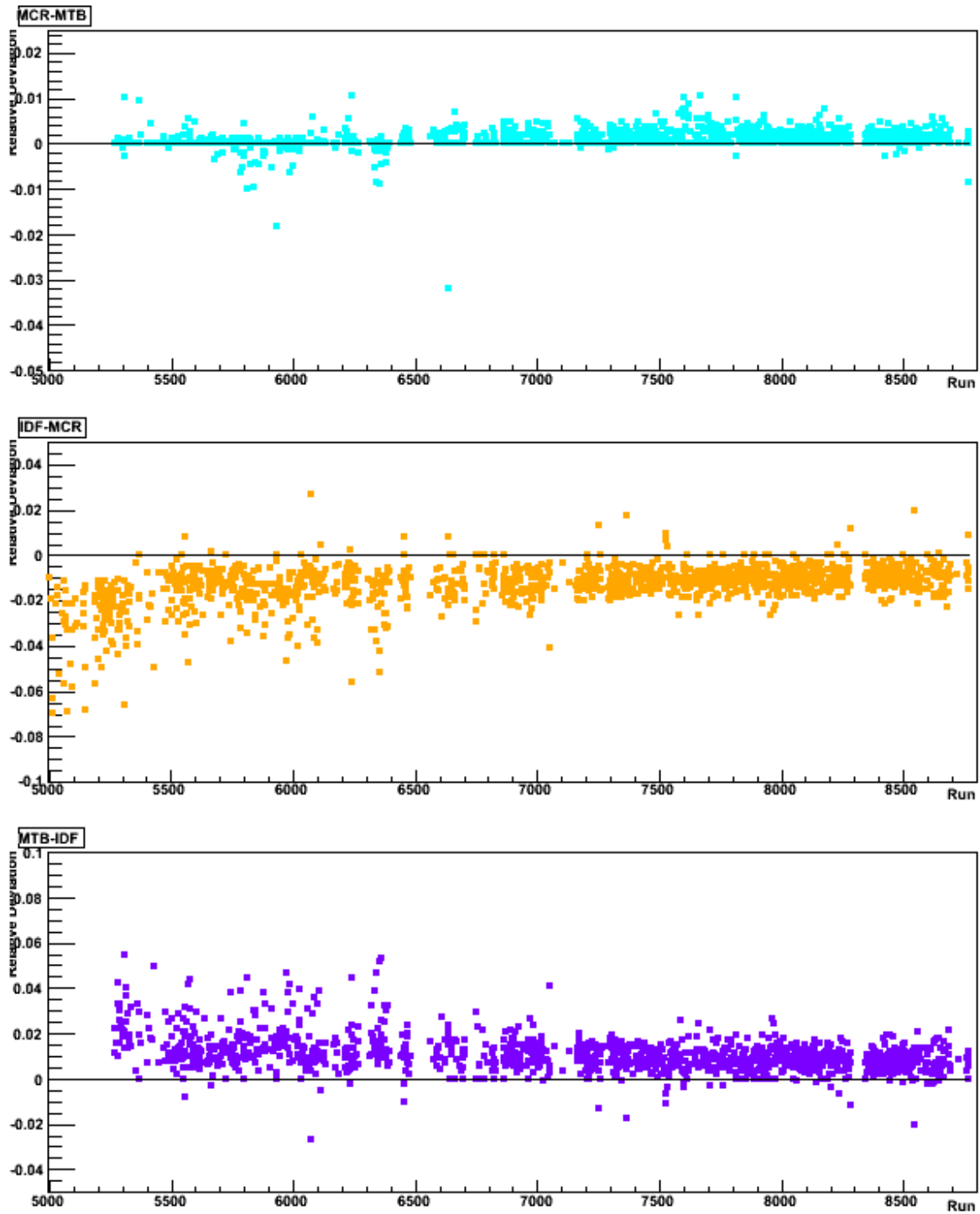


Figure 4.6: Deviation in ID muon event numbers tagged by the three muon flags IDF, MTB, and MCR. Each plot shows the difference in the event numbers tagged by two of the flags, normalized to the number of events tagged by both. The first plot (MCR-MTB) shows a continuous surplus of MCR-tagged events, in agreement with the efficiency evaluation in Sect. 4.2. Both lower plots illustrate a relative increase in the event rates tagged by IDF: Buffer events caused by the leak in the IV nylon sphere are identified as muons due to their distorted pulse shape (Sect.3.2.3).

Chapter 5

BOREXINO Muon Tracking

The residual cosmic muon flux present in the LNGS is one of the most important external backgrounds for the neutrino search in BOREXINO. The ${}^7\text{Be}-\nu$ analysis is strongly reliant on a highly efficient muon identification (Sect. 6.1.2) [81]. However, the introduced dead time is rather low: Cosmogenic neutrons, PM after pulses and electronics instabilities in the wake of the muon require a time veto of about 2 ms per event. Vetoing the whole of the Inner Vessel (IV) after each muon introduces a negligible loss of exposure on the level of $\sim 10^{-4}$. The same approach is still viable for the measurement of low-energetic ${}^8\text{B}-\nu$'s [37]: Short-lived cosmogenics can be rejected by a 5 s veto of the IV following each muon. As a consequence, the dead time increases to $\sim 22\%$ which is still tolerable. Nevertheless, the loss of exposure can be substantially decreased by using the track information of the muon: As cosmogenic radioisotopes are created close to the muon track, a rejection of all events inside a cylinder surrounding the muon track for a time span of 5 s is sufficient to remove the background. Following a more conservative approach, muons crossing only the buffer of the ID could be neglected for the veto. However, the introduction of muon tracking has the most significant impact on the search for CNO and *pep* neutrinos: The main background to this ν search is cosmogenic ${}^{11}\text{C}$ that features a half life of 20.38 min. Therefore, a complete veto of the FV over a time span of several half-lives is not applicable: The dead time ratio would be close to 100%. The only practicable approach is a combination of the spacial information available on muons and neutrons to define subvolumes of the detection region that can be vetoed for the order of 1 to 2 hours. This threefold coincidence technique is described in more detail in Sect. 2.3.3 [100].

In this chapter, the tracking algorithms are presented that have been introduced in the course of this thesis to the *echidna* analysis framework. This reconstruction is limited to muon tracks that are crossing both ID and OD (*trigger.trgtype=1*, *trigger.btb_inputs=4*, Sect. 3.4) and are therefore most relevant for neutrino analysis. The OD tracking is based on the entry and exit points generated by the Čerenkov cone of the muons (Sect. 5.1). In the ID, a combination of the entry point generated by the residual scintillation of the buffer and pulse shape analysis provides the necessary information for the definition of a track (Sect. 5.2). Finally, the combination of both ID and OD tracking results in a best-fit global track (Sect. 5.3). Tests of the reliability of the reconstructed tracks will be presented in the succeeding Chap. 6.

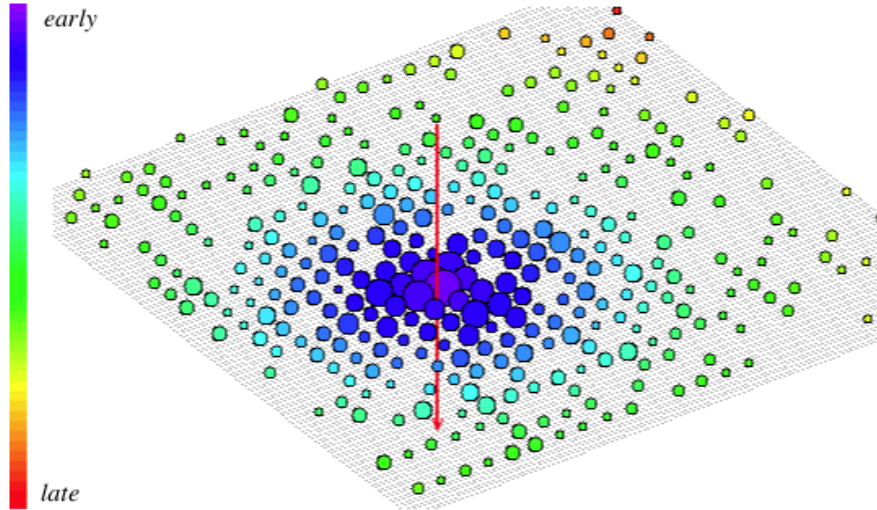


Figure 5.1: Activation profile created by the Čerenkov cone of a muon that is crossing a plain array of PMs: The size of the dots indicates the number of photons registered by a PM, while colors code the photon arrival time. The further a PM is from the penetration point, the less and the later he will detect light.

5.1 Outer Detector Tracking

An overview of the OD track reconstruction is given in Fig. 5.2: The algorithm is based on the identification of the disc-like activation profile of PMs that is generated by a muon crossing both ID and OD (Sect. 2.1.1): The Čerenkov cone around the track is registered by the PMs around the muon entry point (usually on the SSS) and a second time by PMs near the exit point (either on SSS or floor of the water tank). High-energetic cosmic muons are fully relativistic and their velocity is very close to the vacuum speed of light c . As the Čerenkov light is propagating at the light speed of the medium c/n ($0.75c$ in the case of water), the muon will arrive at the PM-equipped surface on top of its Čerenkov light cone. If the track is perpendicular to the surface, the first light is detected by the PMs nearby the penetration point: Light emitted on the last section of the track before crossing the surface will arrive at the PMs first. As light is emitted at a fixed Čerenkov angle $\alpha_c = 41^\circ$, the time profile of PM hits will follow circles or (depending on the track inclination) ellipses around the penetration point, from early hits in the center to the late hits at the periphery. The energy loss of the muon along its track through the detector is negligible. Therefore, a constant emission of light can be assumed along the track. As a consequence, the number of photons per detection area decreases with the distance to the penetration point, PMs near the penetration point detecting more photons than remote ones. Fig. 5.1 shows an idealized activation profile for a muon crossing a plain array of PMs: Time is coded by colors while the number of photoelectrons or *charge* is represented by the size of the balls.

5.1.1 Candidate Clusters

The *bx_muon_findcluster* module tries to identify candidates for entry and exit point of a given muon event: Clusters of hits closely related in their PM positions and arrival times. The 154 PMs distributed over the SSS surface and the 54 PMs on the floor of

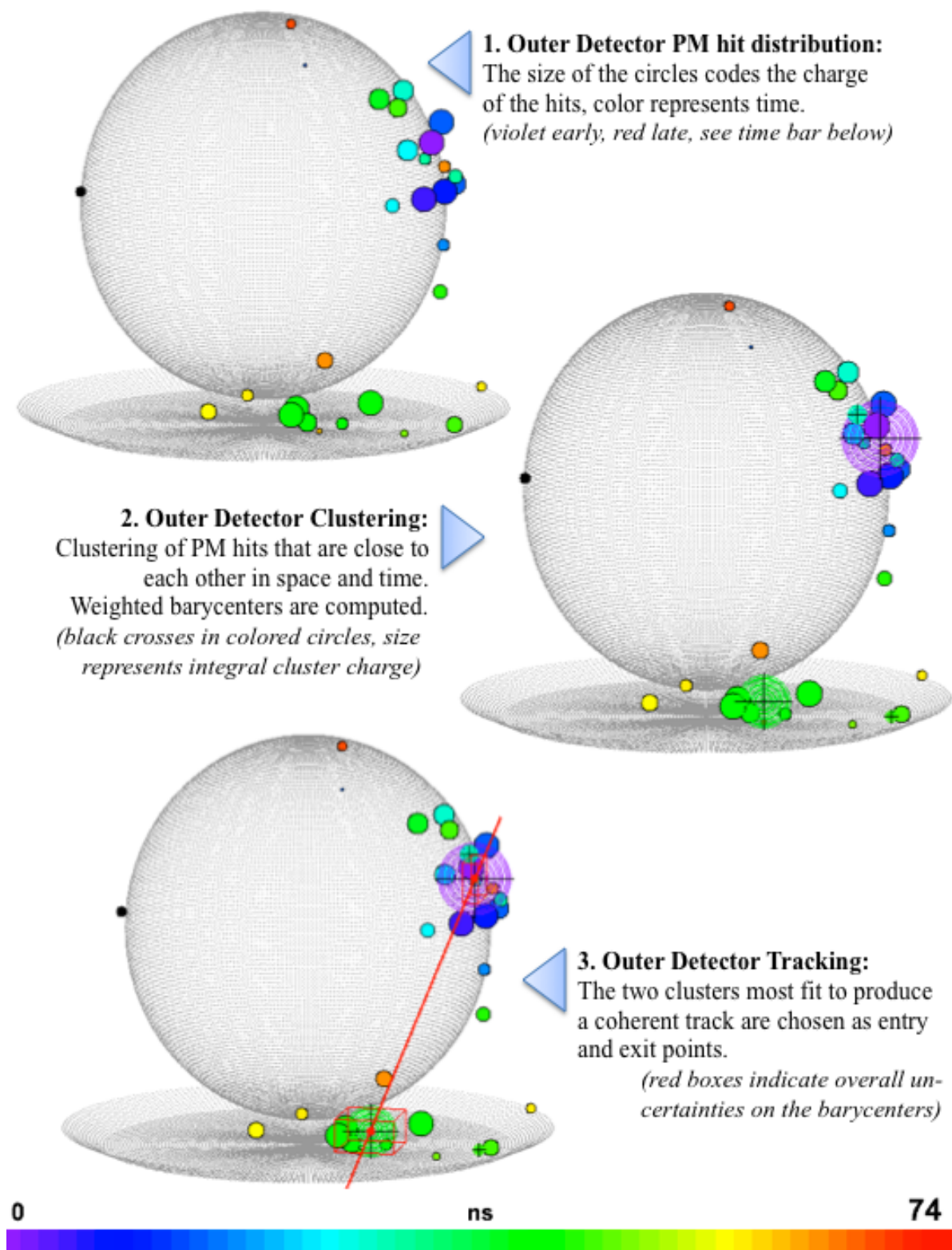


Figure 5.2: Strategy of the Outer Detector tracking.

the OD are treated separately as two subdetectors (Sect. 3.2.2). Not all the hits present in the OD are considered: A time gate around the physical event is defined in order to reject dark noise. The gate start is set if at least 4 PM either on the SSS or on the floor have fired in 48 ns. The gate closes as soon as the hit rate reaches again the regular dark noise level. In addition, hits caused by cross talk between electronic channels are rejected: A minimum charge threshold $q_i > 0.25$ pe (photoelectrons) is applied. The affiliation of the remaining hits to clusters is performed by relating each hit to all its possible neighbors on either SSS or floor: The spatial distance between two hits on the SSS (floor) has to be $\delta r \leq 3$ m (4 m) in order to affiliate the pair to the same cluster. This condition corresponds to about twice the mean distance between neighboring PMs, which is $\delta r_n = 1.7$ m (2.2 m). In addition, the time difference between these hits has to be $\delta t < 20$ ns. Every hit is affiliated to one cluster at most. To assure this, clusters are merged to one if a pair of hits is found that connects the two preceding clusters by fulfilling the requirements. While the radial cut limits the affiliation essentially to neighboring PMs, the time window is rather generous: The typical photon arrival time difference between neighboring PMs is

$$\delta t_n = \delta t(\delta r_n) = \left(n \sqrt{\frac{1 + \tan^2 \alpha_c}{\tan^2 \alpha_c}} - \frac{1}{\tan \alpha_c} \right) \frac{\delta r_n}{c} = 4.9 (6.3) \text{ ns.} \quad (5.1)$$

By elongating the allowed time difference, separate clustering of light reflected back at the original penetration point is suppressed. To reject clusters formed solely by reflected light a minimum integral charge ($Q = \sum_i q_i$) of the clusters is required; most of the light intensity will be concentrated in the clusters containing direct light. The applied charge threshold is $Q > 2$ pe.

The remaining clusters are written to file along with a number of parameters that are forwarded to the *bx_muon_tracker* module:

- Start time: *muon.cluster.start_time*
- Integral charge: *muon.cluster.charge*
- Charge barycenter coordinates including errors: *muon.cluster.x, y, z, dx, dy, dz*

The time of the clusters first hit t_0 is used as cluster start time. The barycenters \vec{R}_{cl} are computed to serve as future entry and exit points. The coordinates \vec{r}_i of the affiliated hits are weighted by w_i considering both charge q_i and time t_i :

$$\vec{R}_{bc} = \frac{\sum_i w_i \vec{r}_i}{\sum_i w_i} \text{ with } w_i(q_i, t_i) = q_i \cdot e^{-(t_i - t_0)/\tau} \quad (5.2)$$

with $\tau = 20$ ns. The barycenters are calculated in Euclidian coordinates. Due to the curvature of the surface, the SSS barycenters are constructed inside the sphere. This slightly falsifies the result, as the hit profile is originally an image of the Čerenkov cone on the SSS surface. Therefore, these barycenters are shifted radially to the surface of the sphere: $\vec{R}_{cl} = \frac{R_{pm}}{|\vec{R}_{bc}|} \vec{R}_{bc}$. The use of the radius $R_{pm} \approx 7.2$ m instead of the radius of the SSS takes into account that the Čerenkov light is detected at the PM photocathodes

protruding the SSS surface. The deviation of the weighted mean is used as statistical uncertainty $\Delta\vec{R}_{\text{cl}}$:

$$\Delta\vec{R}_{\text{stat}} = \sqrt{\frac{\sum_i w_i (\vec{r}_i - \vec{R}_{\text{cl}})^2}{(\sum_i w_i)^2}} \quad (5.3)$$

The weights have to be normalized to the maximum weight present in this cluster. This reflects that only one hit fully contributes to the weighted mean of Eq. (5.2) while all others are considered according to their relative weights.

5.1.2 Cluster Splitting

There is a chance that muons that pass the SSS tangentially on the very rim create a PM hit profile integrating both entry and exit point into a single SSS cluster. Therefore, for each muon event an attempt is made to split the cluster of the highest integral charge on the SSS in two sub-clusters. The choice relying on charge is the most sensible, as most of the muon light output is for sure centered on its penetration points.

The method `bx_muon_findcluster::m_split` decides if and how this cluster is split: It concentrates on the 33% of hits featuring the largest charge in the cluster. The first of these hits is selected as the preliminary entry point. Due to the height of ~ 30 cm of the PM cathode above the curved SSS surface, the track exit point must be at a minimum of 4 m distance from the entry point so that the track actually crosses the ID. Therefore, the splitting proceeds only if at least one of the selected hits is further than 3.5 m (or 2 mean PM distances) away. In this case, the barycenter of all hits is computed that are located outside a radius of 3.5 m from the entry point. The cut assures that the probability to include a hit actually belonging to the entry point is low. Finally, all the hits belonging to the original cluster are associated to either one of the penetration points by comparing the spatial distances to these points and choosing the nearer one. In this way, two new clusters are created that replace the original one.

There is a small risk that a cluster that actually contains only a single entry (or exit) point is split by this algorithm. This has only small influence on the accuracy of the barycenter that does not suffer significantly by the removal of later hits. As pointed out in Sect. 5.1.4, problems can arise if both of the sub-clusters feature larger charge values than the actual exit cluster and create a false tangential track along the sphere.

5.1.3 Entry and Exit Point

For an ideal track, only two clusters caused by the entry and exit point belonging to a single track are present, making no further selection necessary. Even if both entry and exit point are present, light reflected by the Tyvek foils creates in most cases additional fake clusters that have to be rejected. In addition, there are events where only the entry point can be identified: If the muon stops inside the ID, it will cause no exit point at all. Alternatively, if the track leaves the ID through the optically inactive lower hemisphere at a flat angle, it produces only a small amount of light that may be too faint to be detected. In these cases, it is vital to avoid the identification of a reflection light cluster as exit point.

The *bx_muon_tracker* module first evaluates all present clusters as candidates for the entry point by the means of a weighting function W_{en} : The following criteria are applied:

- The first cluster in the clustering time window is the most likely to contain the first light of the muon and therefore to be the entry cluster.
- The cluster charge Q should be large in comparison to clusters of reflected light as most of the light intensity is detected by the PMs close to the entry point.
- The cluster should be in causal correlation to the first ID cluster in order to allow a sensible track through OD and ID. The maximum deviation accepted is ± 200 ns/ -250 ns relative to the start time of the first *laben* cluster.

The weighting function reproduces these requirements:

$$W_{\text{en}}(Q, T) = Q \exp\left(-\frac{T - T_0}{\tau_0}\right) \exp\left(-\frac{(T - T_{\text{id}} + \Delta T_{\text{io}})^2}{2\tau_{\text{id}}^2}\right). \quad (5.4)$$

The charge Q is proportional to the number of detected photons and enters W_{En} linearly. In the first exponential, T is the start time of the cluster and T_0 is the start time of the first cluster. The weighting constant $\tau_0 = 2.5$ ns results in a steep decrease of W_{En} with time: Early cluster are therefore strongly favored. In the Gaussian, T_{id} indicates the start time of the first cluster in the ID, $\Delta T_{\text{io}} = 45$ ns the typical time offset of ID to OD, and $\tau_{\text{id}} = 10$ ns is the allowed variation of the ID and OD cluster start time. This last criterium is chosen to be relatively weak in comparison to the first two requirements. The cluster featuring the largest weight is chosen.

Now, candidate clusters for the exit point are identified. They have to fulfill the following requirements:

- They are inside the time gate defined above for the entry point candidates.
- The time difference to the entry point is more than $+10$ ns, mainly to avoid the effects of over-efficient splitting (Sect. 5.1.2).
- The track defined by the entry point and the candidate cluster crosses the sphere *in between* the two points. If that is not the case, the potential track does not belong to a muon crossing the ID and is therefore in conflict with the trigger type.

If no cluster remains as candidate, only the entry point is written to file. Otherwise, the remaining clusters are checked for their correct time alignment: The ideal time offset between entry and exit cluster ΔT_{tof} corresponds to the time of flight of the muon over the distance ΔR between the barycenters. As the muon is propagating nearly at light speed c , $\Delta T_{\text{tof}} \approx \Delta R/c$. The corresponding weight function is

$$W_{\text{ex}}(Q, \Delta T, \Delta R) = Q \exp\left(-\frac{(\Delta T - \Delta R/c)^2}{2\sigma_{\text{tof}}^2}\right). \quad (5.5)$$

Again, clusters of large charge Q are preferred. The testing deviation $\sigma_{\text{tof}} = 0.25 \Delta R/c$ is a function of the distance between the clusters ΔR . Currently, no lower limit for W_{En}

is applied. Further studies providing information on individual muon tracks will provide the necessary input (as indicated at the end of this chapter).

Entry and exit point are written to the *echidna* root file (*muon.track.x1,y1,z1,t1* and *x2,y2,z2,t2*). Start time and barycenter coordinates are copied from the corresponding clusters. The statistical uncertainties calculated for the clusters are added quadratically to the systematic uncertainties derived from Monte Carlo simulations: 0.3m for the entry and 1.0m for the exit point (Sect.5.1.4). The resulting values (*muon.track.dx1,dy1,dz1...*) are later on used in the global tracking.

5.1.4 MC Simulations

Within the *echidna* analysis group, a GEANT4-based simulation of the BOREXINO detector has been devised and constantly improved during the last years: The package *G4Bx* provides a very complete simulation of the experiment. It allows to simulate physical events inside the detector and includes realistic modeling of light production and propagation through scintillator and water. The output file provides for each individual PM the information on photon arrival times. In a next step, this data is processed by the electronics simulation program *bx_elec* that simulates the DAQ chain introducing corresponding uncertainties. It also transforms the MC data to the usual DAQ rawdata output format readable by *echidna*. While *bx_elec* is already fully available for the ID, the program is currently expanded to include the OD electronics.

Nevertheless, the OD track reconstruction code has been tested using the unprocessed output of *G4Bx*. The tests happened at a relatively early stage of the tracking development, when the reconstruction code was yet not implemented into *echidna* and therefore flexible enough to read the *G4Bx* output directly. Due to the high light output of muons, their simulation is very time-consuming. A relatively small sample of ~ 500 muon events was created according to the known energy and angular distribution of cosmic muons at the LNGS. The comparison of input and reconstructed muon track was used to adjust the parameters of the clustering (δt , δr , ...).

In a second step, the deviation of reconstructed to input MC tracks has been used to get a tentative estimate of the systematic uncertainties of the reconstruction. Fig. 5.3 shows a scatter plot of the distance of reconstructed entry and exit points to the input MC track versus the z -coordinate of the points. Entry points are shown in red at positive z -values: They do not feature any discernible dependence on z . The systematic uncertainty is small, the mean distance from point to track 0.3m. For the exit points (*blue*) the situation is more complex: Tracks leaving the OD by crossing the floor provide well-defined exit clusters ($z < -6$ m). The systematic uncertainty on the corresponding barycenter is rather low, the mean distance is 0.7 m (65 % of tracks). Tracks of larger inclination usually leave the SSS in the lower hemisphere but are not crossing the detector floor. The corresponding exit points ($-6 \text{ m} < z < 0 \text{ m}$, 25 %) are reconstructed using the Čerenkov that is light reflected back from the dome walls. These barycenters are worse defined and the mean deviation from the track is 1.3 m. Very flat tracks leaving the SSS on the upper hemisphere prove to be the most problematic: In general, the exit points ($z > 0 \text{ m}$, 10 %) seem to be reconstructed at a quality comparable to the lower hemisphere points. In some cases, however, a luminous entry cluster will be divided by the *split* module; if there is no further bright cluster available for $z < 0 \text{ m}$, the second cluster generated by the splitting is falsely identified as the exit point. Exit points of

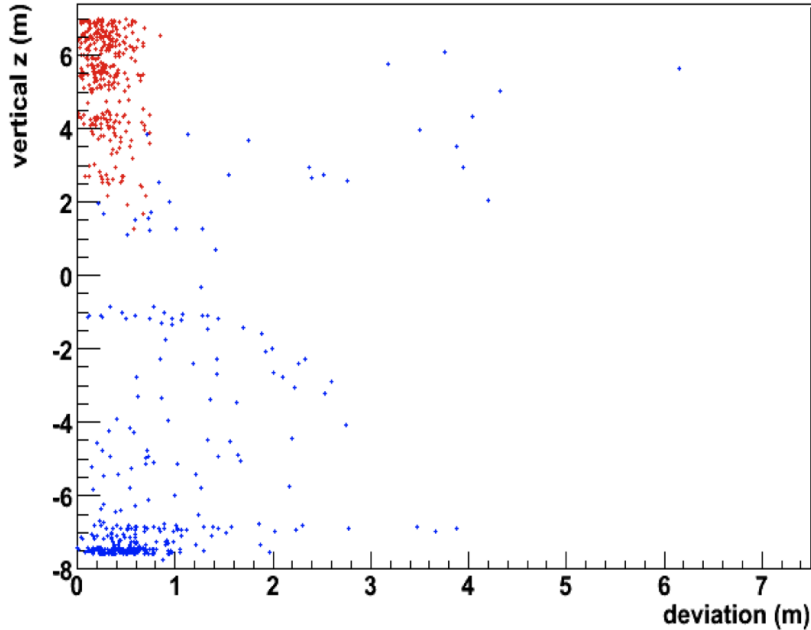


Figure 5.3: Monte Carlo test of the OD tracking: The distance of reconstructed entry points (*red*) and exit points (*blue*) to the input MC track are plotted versus the z -coordinate of the penetration points. Entry points are reconstructed rather well, the mean distance from the track is 0.3 m. The quality of exit points depends on its z -coordinate: Points on the detector floor provide the best results. The overall mean distance of the exit point to the track is 1.0 m.

this class can be found in the upper right corner of Fig. 5.3 where both z and deviation from the MC track are large.

The early version of the tracking algorithm used for the MC tests chose the most luminous cluster (of the largest charge) left after the selection of the entry point as the track exit point. Due to the results on the MC tracks, the selection rules for the OD tracking have been refined to the current state that is described in Sect. 5.1.3. These modifications mainly reduce the probability of selecting the wrong cluster as exit point; the systematic uncertainty in the determination of the penetration points using the cluster barycenter remains unchanged. Currently, the systematical uncertainties are set to be 0.3 m for the entry point and 1.0 m for the exit point in the reconstruction. These values are combined with the statistical uncertainties described in Sect. 5.1.3 and written to the *echidna* event.

5.2 Inner Detector Tracking

The ID tracking analyzes both the time patterns of the hits registered in the first 40 ns of the muon event and the information provided by muon light output and pulse shape. The entry point is identified by the first light generated by the muon in the ID: Similar to the OD, the quenched scintillation light of the buffer produces rings of isochronous PM hits centered on the entry point. Naively, one would expect that the exit point can be found in a very similar way. However, especially for tracks at large radii from the center this signature is very weak as effects caused by the general time development of the light front prevail. Therefore, several pieces of information have to be combined to

obtain a second point: Both the amount of created light and the duration of the PM signal are closely connected to the length of the track. Evaluating this information, the distance of the track to the detector center, the so-called impact parameter, can be obtained. Entry point and impact parameter on their own define only a cone that contains all possible muon tracks on its surface. The actual impact point can be found by analyzing the time distribution of hits surrounding the entry point: The light pattern corresponds to a projection of the track on the spherical surface of the ID. A graphical overview of the ID tracking is presented in Fig. 5.4.

5.2.1 Entry Point

The DMP added to the buffer suppresses the scintillation light output of the PC by about a factor of 50 (Sect. 3.2). Nevertheless, a muon at the ionization minimum deposits about 2 MeV/cm and generates a visible scintillation light output of about 400 photons/cm. The Čerenkov light output is of the same order of magnitude. From the data, a photoelectron yield of ~ 6 pe/cm can be found (Fig. 5.7). The light front generated by the superposition of the two luminiferous processes is depicted in Fig. 5.5 [113]: In the direction of flight, scintillation is creating a light front of the same opening angle as the light cone of the Čerenkov effect. In addition, a backward-running spherical light front is caused by the scintillation light only. The latter will reach the SSS first at the muon entry point, as the track section that is closest to the entry point emits the first light.

The reconstruction of the entry point is adopted from the OD clustering. The main difference lies in the definition of the hits contributing to the entry point cluster: For this, the hits of the first *laben* cluster which corresponds to the first physical event of the ID gate are selected¹. Only the hits detected in the first 5 ns relative to the cluster start time are considered, corresponding to the light of the first 70 cm of the track inside the ID, or more precisely inside the spherical surface defined by the Winston cones. Analogously to Eq. (5.2), the cluster barycenter is now determined from the selected hits. In fact, only the time information of the hits is used as most muon events saturate the PMs due to their enormous light output. The charge variable becomes therefore useless. However, the effect of weighting the hits with a time constant of $\tau=20$ ns is considering the short time window relatively weak. Statistical and systematic uncertainties are determined as in the case of the OD entry point.

5.2.2 Track Orientation

The geometrical construction of the impact point relies on the knowledge of the impact parameter R_I (distance of the muon track to the detector center) and an infinitesimal direction vector \vec{d} that indicates the orientation of the track relative to the entry point. This vector can be found by analyzing the time distribution of the early hits surrounding the entry point. Fig. 5.6 shows two idealized PM time profiles for illustration (the curvature of the sphere surface is neglected): The entry point is depicted by the violet region in the center of both figures. Circles or ovals of the same coloring indicate regions of synchronous hits, violet early, red late. The colored crosses symbolize the barycenters of isochronous regions. In the case of a muon entering the ID on a perpendicular track,

¹Usually, an ID muon event provides only a single cluster, as the muon afterpulses begin close enough to the prompt signal to be included in this cluster (see also Sect. 5.2.3).

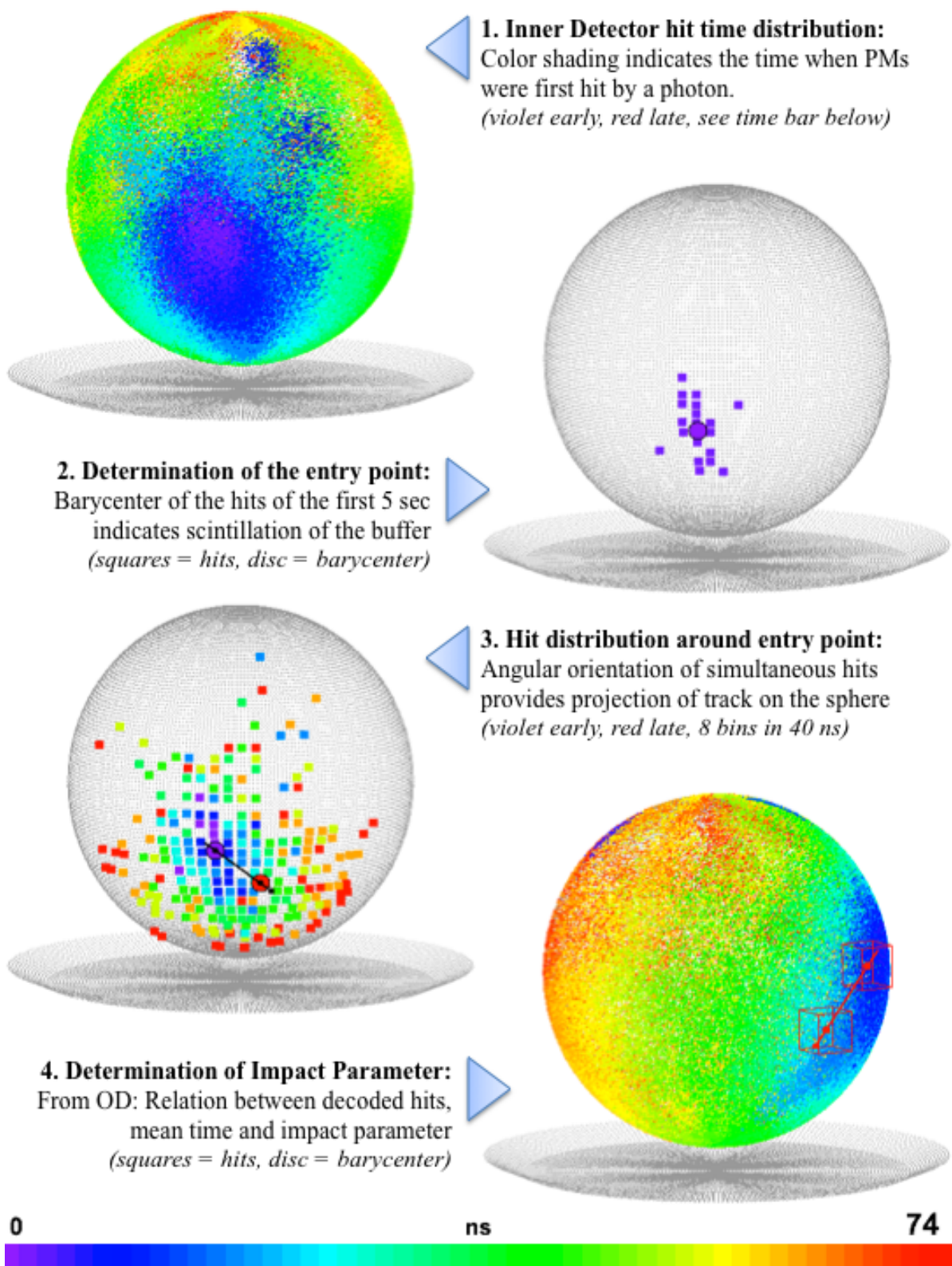


Figure 5.4: Strategy of the Inner Detector tracking.

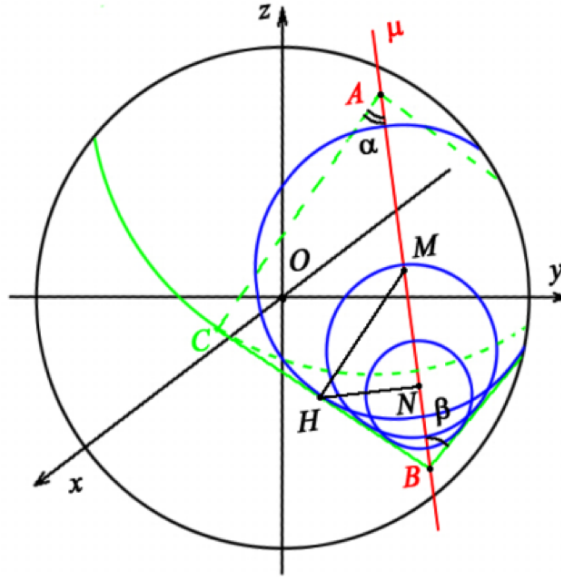


Figure 5.5: A muon traversing the ID will create light by (quenched) scintillation processes and the Čerenkov effect. The superposition of spherical waves along the track creates a light front (shown in *green*) similar to a normal Čerenkov cone. In addition, a spherical front propagating backwards is created by the Čerenkov effect [113].

all the barycenters coincide with the entry point (*left*). By contrast, the barycenters lie on a straight line originating from the entry point if the muon track features an inclination relative to the surface (*right*). The hit pattern therefore corresponds to a projection of the muon track on the sphere surface. Its orientation can be described by a vector \vec{d} that points from the entry point towards the later barycenters. However, \vec{d} is orientated along the (sphere) surface and carries no direct information of the inclination angle.

The tracking algorithm determines the barycenters of isochronous hit distributions with an uncertainty that is determined by the limited number of PM hits. A linear fit to these barycenters allows to obtain a reliable orientation for \vec{d} . The curvature of the sphere is not negligible as the size of the hit distributions is of the order of the SSS radius. This makes a switch to a polar coordinate system necessary to perform a geodetic fit to the barycenters. Therefore, the tracking algorithm is sorting the hits following the first 5 ns (that are used for the determination of the entry point) in bins of 5 ns. Depending on the available number of hits, the information of the first 3 to 8 bins (15-40 ns) is used. All PM coordinates associated to these hits are transformed to spherical coordinates described by the polar angle θ and azimuth angle φ . If the muon entry point is near to the SSS poles or close to the φ -discontinuity at 360° , a rotation is applied shifting the entry point to $\theta = 90^\circ$ and $\varphi = 180^\circ$. This allows the computation of the barycenters and their statistical uncertainties without further complications. The fit is performed assuming a linear function $\theta = m\varphi + t$. Near to the SSS equator, this is an acceptable approximation to a geodetic line. The fit result for the inclination is then transformed back to regular Euclidian coordinates and normalized to unity. The resulting vector \vec{d} is tangential to the sphere surface at the entry point.

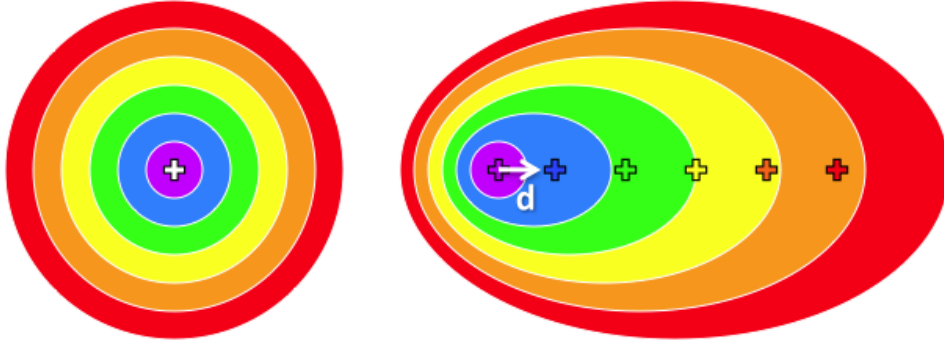


Figure 5.6: Idealized arrival time patterns of PM hits around the ID entry point of the muon track (*violet circle*). Regions of uniform color indicate synchronous hits (*blue: early, red: late*). *Left*: A muon penetrating the surface perpendicularly creates a circular light pattern of isochronous hits around the entry point. *Right*: Muons with an incline versus the surface produce a light pattern biased in their inclination direction (in this case to the right). The barycenters of isochronous hits are arrayed in a line originating from the entry point in direction \vec{d} . This coincides with a projection of the muon track on the sphere.

5.2.3 Impact Parameter

The impact parameter R_{I} is determined in two ways: Both the correlation with the visible light output of the muon and with the signal duration is utilized. The construction of the impact point uses the mean of the results provided by the two methods in order to increase the precision.

Visible Light Output

The number of photons produced by a muon in the ID strongly depends on its trajectory through buffer and IV. As long as the muon crosses only the buffer, its light output increases almost linearly with the path length through the ID; as soon as it traverses the scintillator of the IV, the light output increases dramatically and becomes dominated by the path length inside the IV.

Fig. 5.7 shows a scatter plot of the ID visible energy (*laben.n_decoded_hits*) of a large sample of cosmic muons versus the impact parameter that is determined by the OD tracking. In agreement with expectations, two main bands correlating the two parameters can be identified, intersected at the IV radius. The band created by buffer muons stretches from 0 to 5 000 hits, while the visibly curved band associated to IV muons stretches from 5 000 to 30 000 hits.

For the buffer band, the relation of impact and light output is at first glance nearly linear. This is surprising as the expected relation of path length L and impact R_{I} in a sphere of radius R is

$$L = 2\sqrt{R^2 - R_{\text{I}}^2} \quad (5.6)$$

and should increase steeply for $R \approx R_{\text{I}}$. However, the light generated by muons crossing the buffer tangentially is partially shadowed by the Winston cones. Also the Outer Vessel (OV) has an optical effect on the light output of the muons: There is an indication of line structures around 1 000, 2 000, and 3 500 hits. These are not artefacts of the OD tracking

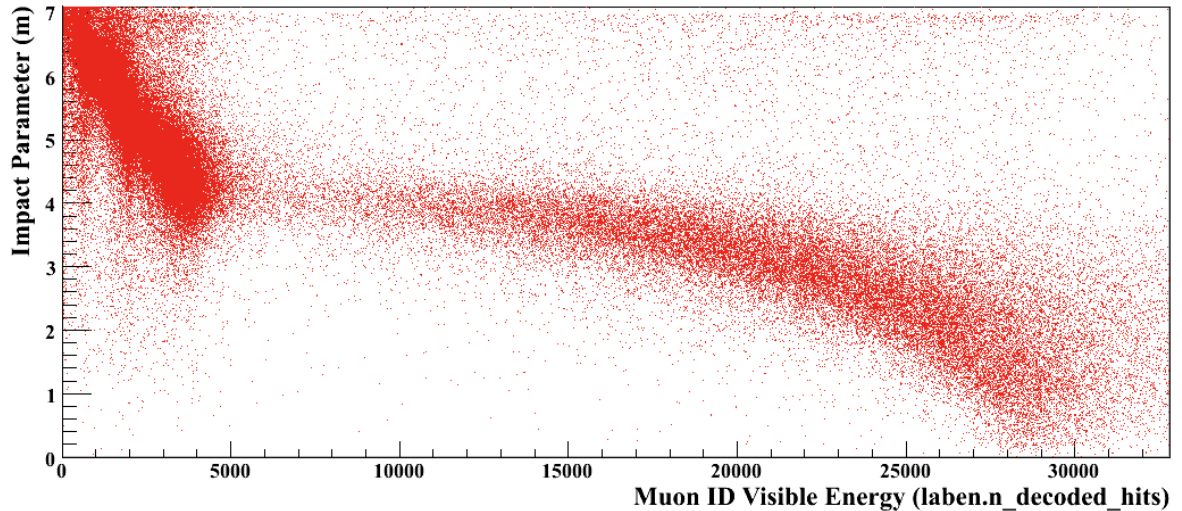


Figure 5.7: Number of *laben* decoded hits generated by a muon crossing the ID versus the impact parameter determined by OD tracking. Two main bands are visible in the regions below and above 5000 hits: They are caused by muons crossing only the buffer and muons crossing the IV, respectively. The IV band is strongly bent due to the relation of path length and impact.

as the peaks are also visible in the (blue) ID muon spectrum of Fig. 4.2. Toward 5 000 hits, the distribution of impact values reaches to 3.5 m which is 0.75 m smaller than the nominal IV radius. This can be attributed to the spacial resolution of the OD tracking and the aspherical deformation of the IV. The second band generated by IV muons starts out very flat from the radius of the IV of 4.25 m: Eq. 5.6 predicts a significant increase of the light output in this region. At smaller impacts, the band is bent and saturates at 30,000 hits. This agrees well with the expectations on the connection of light output and IV path length.

The ID tracking is utilizing the relations found in Fig. 5.7 as calibration curve for the determination of the impact parameter I_R . In principle, this procedure should provide a more precise value on I_R than the event-by-event-based OD tracking; the uncertainty should be significantly reduced by the high statistics available. A table containing 15 value pairs reproducing both the linear relation of the buffer band and the quadratic relation of the IV band is implemented in the code: Default numbers of decoded hits are paired with the mean of the distribution of I_R at this point. The values for intermediate hit numbers are interpolated. The uncertainty of I_R is set to 0.75 m, corresponding to the overlap of the buffer and IV bands visible in Fig. 5.7. This value is a very conservative estimate as the overlap is mainly due to the uncertainty of the OD tracking. Beyond the end of the IV band at 30 000 hits, a small amount of muons features visible energies of up to 120 000 decoded hits (not visible in Fig. 5.7). The OD tracking reconstructs their tracks mainly inside a radius of 3 m around the sphere center. The ID impact parameter is therefore chosen to be (1.5 ± 1.5) m.

Mean Time

Also the pulse duration of a muon event is strongly related to the impact parameter of a muon. The signal length is reproduced by the *mean time* variable that is defined as the

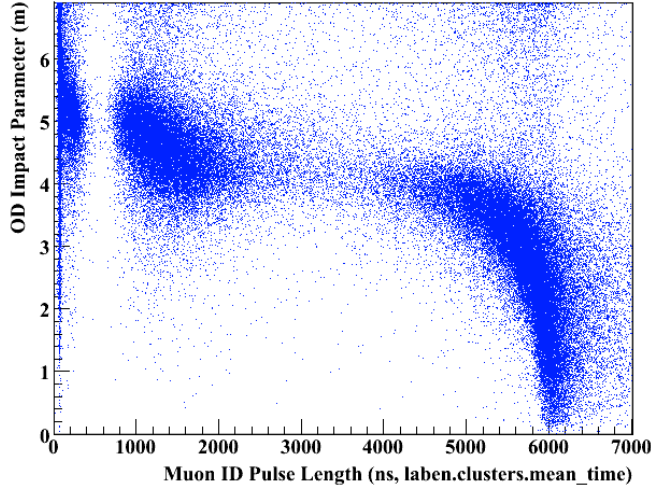


Figure 5.8: Cluster meantimes of muons crossing the ID versus the impact parameter determined by the OD tracking. Three bands of correlations are visible: While the first two related to buffer events are relatively steep, the third one can provide valuable information on muons crossing the IV. The mean time saturates at ~ 7000 ns due to the end of the DAQ gate.

average time difference of all the hits of a cluster relative to its start time. Fig. 5.8 shows a scatter plot of the `laben.cluster[0].mean_time` variable versus the impact parameter determined by the OD tracking. Three correlated bands are visible: In the first rather short band at small mean times, the decrease of the impact parameter with increasing mean time is fast and the slope therefore hard to discern in the plot. The gap in mean times between 300 and 1000 ns is an artefact of the clustering: The natural duration of a muon light pulse in the detector is on the scale of 100 nanoseconds. However, a luminous muon will cause after pulses in the PMs (Sect. 6.2.1). If these pulses significantly exceed the normal dark noise level, the clustering will include them in the cluster of the prompt signal. In this case, a cluster featuring a mean time of more than $1 \mu\text{s}$ is created. Another depleted region is visible from 2.5 to $4 \mu\text{s}$: This is caused by the dramatic increase in light output and after pulses of the muons crossing the periphery of the IV. The most valuable information is provided in the IV band where a clear correlation with the impact parameter is visible.

Similar to the case of the `laben` decoded hits, about 15 pairs of mean time and OD impact parameter are used as a calibration input for the ID tracking. Analogously to the impact determination by the visible energy, an uncertainty of 0.75 m is used up to mean times of $6 \mu\text{s}$. Above this region, a fixed value of (1.5 ± 1.5) m is introduced as a clear correlation is missing.

5.2.4 Impact Point

Impact parameter R_I and orientation vector \vec{d} are combined to obtain the coordinates of the impact point \vec{I} . Fig. 5.9 shows a sectional drawing of the ID: The cutting plane is defined by the muon track and the detector center. \vec{I} can be constructed by the sum of two vectors: The first one is the projection of \vec{I} on the coordinate vector pointing to the entry point \vec{E} . The length P_{IE} of this vector can be determined via the angle defined

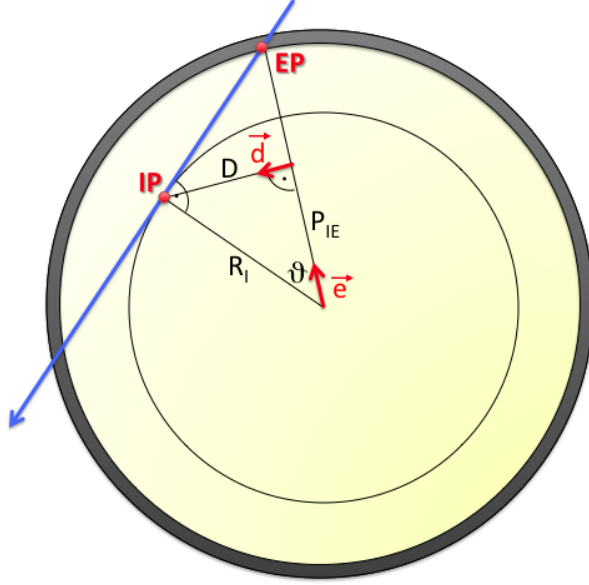


Figure 5.9: Construction of the muon impact point (IP): The ID section shows the plain defined by the muon track (*blue*) and the detector center. The coordinates of the entry point (EP), the impact parameter R_I and the track orientation vector \vec{d} are used to determine IP (see Sect. 5.2.4 for further details).

by \vec{I} and \vec{E} :

$$\frac{P_{IE}}{R_I} = \cos \vartheta = \frac{R_I}{R_E} \quad \Rightarrow \quad P_{IE} = \frac{R_I^2}{R_E} \quad (5.7)$$

R_E is the distance of the entry point to the detector center (which corresponds to the distance of the PM photocathodes from the center). The second vector is parallel to the directional vector \vec{d} . Its length is determined by the requirement that the sum of the two vectors must return the impact vector \vec{I} with the length R_I :

$$\vec{I} = \frac{P_{IE}}{R_E} \cdot \vec{E} + \sqrt{R_I^2 - P_{IE}^2} \cdot \vec{d}. \quad (5.8)$$

\vec{d} is already normalized (Sect. 5.2.2). Unfortunately, it is difficult to obtain a reasonable statistical error for \vec{I} that is applicable to Euclidian coordinates. It is more natural to give the uncertainties in a polar coordinate system, in which the error on the impact is radial and the uncertainty in \vec{d} a deviation in θ and φ . The resulting "allowed" region for the impact point corresponds to a blunt wedge. While it is possible (and also implemented in the ID tracking module) to obtain uncertainties in x , y , and z using Gaussian error propagation, the resulting "allowed" cuboid only poorly reproduces the actual circumstances. In practice, it proved to be insufficient for the global tracking. Until either the structure of the ID tracking variables or of the global fit is adjusted, the uncertainties of x , y , and z are set to 1 m. Compared to the uncertainties of the other track points, this is a rather conservative estimate.

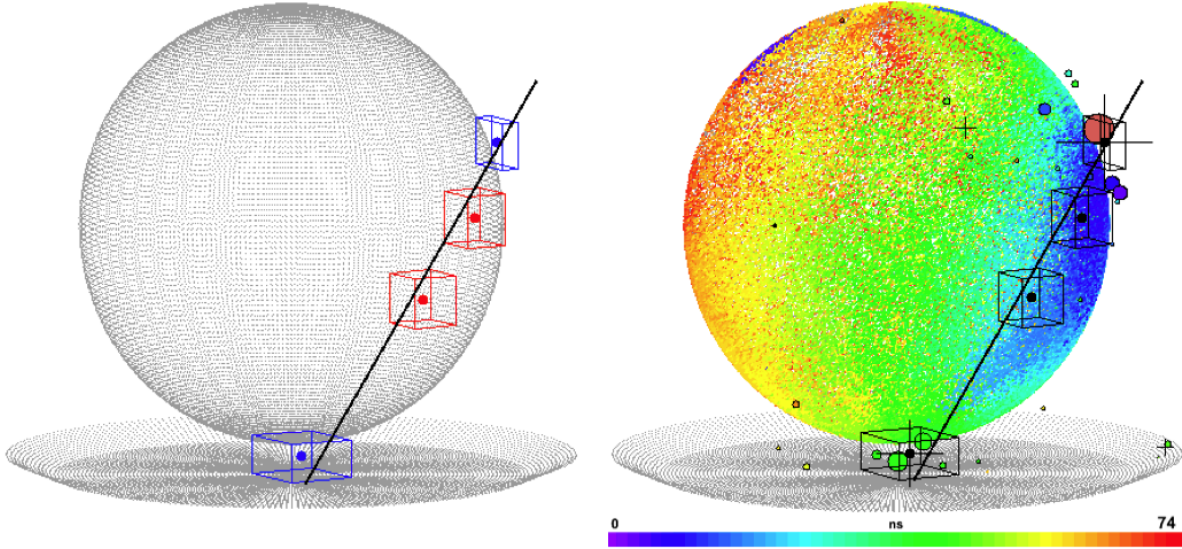


Figure 5.10: Graphical description of the global muon tracking. *Left:* The track points provided by the ID (*red*) and OD (*blue*) reconstruction are shown, the boxes indicating their uncertainties. The global tracking applies a fit based on Eq. (5.9). *Right:* The same muon event including information on the ID PM hit time distribution (*small colored dots*) and the OD hits (*colored circles*). The time scale is shown below.

5.3 Global Fit

To combine the information provided by OD and ID muon tracking, a global track can be defined representing the best fit to the up to 4 data points available for a single track. This task is performed by the module `bx_global_tracker`. Different from the other tracks, the information on the global track is not saved in form of two points but using 4 fit parameters: A three dimensional track $\vec{T}(x)$ can be parameterized in the form:

$$\vec{T}(x) = \begin{pmatrix} 0 \\ \alpha \\ \gamma \end{pmatrix} + x \begin{pmatrix} 1 \\ \beta \\ \delta \end{pmatrix}. \quad (5.9)$$

The reduced notation is $y(x) = \alpha + \beta x$, $z(x) = \gamma + \delta x$. As the latter equations already indicate, the 3D fit can be split into two independent 2D fits to projections of the track on the xy and xz coordinate planes. Fig. 5.10 shows the resulting track in a graphical representation: On the left, the four track points including their uncertainties (indicated by boxes) are shown along with the fitted track; on the right, all information provided by ID and OD is included.

There is a technical complication applying to tracks that are nearly parallel to the xz/xy -coordinate planes. These tracks feature a very steep correlation of y (or z) to x , causing the inclination parameters β and δ to diverge. While their chance to be infinite is negligibly small, the ROOT fitting package fails to return satisfactory results in this case. It is therefore necessary to perform a coordinate rotation by a relatively large angle (45°) around the z (or y) axis before fitting. The back-transformation of the resulting fit parameters to regular coordinates is possible via Eq. (5.9): Like the penetration point coordinates, the vector \vec{T} can be easily transformed by a regular 3D rotation matrix.

The track is described by two 2D fits or four variables which contain no information on the direction of motion of the muon along the track. Therefore, the introduction of a further variable (*track.downward*) indicating the orientation is necessary. The fit also provides a χ^2 value describing its quality. Although this value is not to be taken literally as for instance the coordinate uncertainties of the ID impact point are only preliminary values, the variable gives an indication of the alignment of the four points to each other. There are a number of cases in which 3 out of 4 points are reasonably aligned while a fourth point seems to be misreconstructed. If the reduced χ^2 value² is $\chi^2/ndf > 3$, the tracking algorithm performs four additional fits that each omit one of the track points. The fit ending up with the lowest value of χ^2/ndf is chosen for further use.

The fit parameters (*track.alpha, beta, gamma, delta*) as well as their uncertainties (*track.alpha_error, ...*) and the direction indicator (*track.downward*) are saved to the root-file in the *BxTrack* class (Sect. 3.4). In addition, the reduced χ^2 value (*track.chi2*) and the number of points used in the fit (*track.npoints*) is provided. *BxTrack* contains a number of getter functions that allow access to the data: *GetTheta()* and *GetPhi()* provide the direction of the track in polar coordinates; the two angles point back at the origin of the muon. *GetImpact()* returns the distance of the track to the detector center, while *GetDistance(pos)* returns the distance of a point-like event at position *pos* to the track. Similar getter functions are available for the ID and OD tracks individually.

An evaluation of both the efficiency and the accuracy of the tracking algorithms has been part of this thesis. However, the tests are in many cases closely linked to either the understanding of the BOREXINO detector or the physics of the cosmic/cosmogenic background sources. Therefore, the evaluation of the tracking using regular BOREXINO data is presented alongside the background analysis of Chap. 6.

In the not too far future, two additional methods will be available for testing the tracking that will amend the possibilities of Chap. 6: First, a full simulation of the OD physics and electronics will be available during the course of this year, allowing to identify systematic weaknesses in the algorithm (Sect. 5.1.4). Even more promising, the installation of an external muon tracker providing high spacial and directional resolution is planned in collaboration with the Universität Hamburg. Placing this module at different locations on the top of the BOREXINO steel dome, a sample of cosmic muons detected in coincidence by both detectors can be acquired. Based on the exact data on the muons provided by the external tracker, the BOREXINO reconstruction algorithms could be tested and further improved. Especially the opportunity to determine systematic errors using an independent detection system is highly desirable.

²The number of degrees of freedom *ndf* is 4 for 4 points (8 values of $y(x), z(x)$ minus 4 fit parameters).

Chapter 6

Cosmic Background in BOREXINO

The efficiencies for muon identification that have been determined in Chap. 4 and the muon track reconstruction developed in Chap. 5 are the starting point of cosmic and cosmogenic background discrimination in BOREXINO. This chapter is a compilation of cosmic background analyses that have been performed for several purposes: Naturally, this comprises the investigation of cosmic muons and induced neutrons as a background for neutrino detection in BOREXINO. Equally important, both muon flags and tracking offer the possibility to study the features of cosmic background in a more general approach: BOREXINO results on muon flux and especially on neutrons can be used as an input for background studies for other astroparticle experiments. Not least, cosmic backgrounds provide the largest sample of events available for testing the performance of the tracking algorithms: The combination of several tests allows to determine the spatial and angular resolution of the track reconstruction.

It is often the case that the analysis of a certain background feature returns results for more than one of the above mentioned aspects. This chapter is therefore structured in three units: Sect. 6.1 describes the analyses using only cosmic muons, while Sect. 6.2 encompasses the investigation of the induced neutrons. The results are summarized in Sect. 10.1 by putting them in the context of BOREXINO neutrino analysis, general background study, and muon tracking performance.

6.1 Cosmic Muons

Cosmic muons crossing the BOREXINO Inner Detector (ID) are a major source of background for neutrino search. This section starts out with an estimate of the mean muon rate in the ID (Sect. 6.1.1) and an investigation of its temporal variation. As a next step, the residual muon flux after application of the combined ID and OD (Outer Detector) muon veto is compared to the expected neutrino count rates (Sect. 6.1.2). The efficiency of the tracking algorithms to produce an output track is given in Sect. 6.1.3. Cosmic muons can also be used as a calibration source for the muon tracking: Sect. 6.1.4 is concerned with the impact and angular distributions of muons reconstructed by the three tracking algorithms: ID (*laben*), OD (*muon*), and global tracker. The comparison to the results of the MACRO experiment [97] allows to determine the angular resolution of the tracking (Sect. 6.1.5).

Flag	Event Rate [μ/d]	Efficiency	Corrected Rate [μ/d]	Flux [$\text{m}^{-2}\text{h}^{-1}$]
MTB	4287 ± 4	0.995 ± 0.001	$4309 \pm 4_{\text{stat}} \pm 4_{\text{syst}}$	1.218
MCR	4292 ± 4	0.997 ± 0.001	$4305 \pm 4_{\text{stat}} \pm 4_{\text{syst}}$	1.217
IDF	4243 ± 4	0.985 ± 0.001	$4308 \pm 4_{\text{stat}} \pm 4_{\text{syst}}$	1.218

Table 6.1: Cosmic muons crossing the ID are tagged by three different muon tags: MTB, MCR, and IDF (Sect. 4.1). Using the measured event rates and the flagging efficiencies, a corrected rate and the actual muon flux through the detector can be calculated separately.

6.1.1 Muon Rate and Flux

The number of events caused by cosmic muons crossing the BOREXINO ID can be determined by use of the three available muon flags: the muon trigger board (MTB), the muon clustering (MCR), and the Inner Detector flag (IDF) that is based on pulse shape analysis (Sect. 4.1). Tab. 6.1 shows the rates of tagged events for a live time of 287 days (6883 h)¹ in the first column. While the registered event numbers range from 4243 to 4292 events per day and diverge by less than 2%, the differences are very significant on the level of $\sim 0.1\%$. However, also the efficiency ε of a given muon tag has to be taken into account to obtain the muon rate. For this, the measured rate has to be divided by the efficiency of the flag, $R_\mu = R_{\text{exp}}/\varepsilon$. For MTB and MCR, the most reliable values for the efficiencies are obtained by the flagging of high-energetic ID events caused by cosmic muons (Sect. 4.2). The best value for IDF results from the tests relative to the OD tags. In all cases, an additional systematic error is introduced by the uncertainty on the efficiency. The resulting corrected rates show good agreement within their statistical and systematic uncertainties. The effective muon rate is $4307 \pm 4_{\text{stat}} \pm 4_{\text{syst}}$ events per day.

The corresponding flux can be computed dividing the rate by the cross-sectional area the ID offers to cosmic muons. Due to its spherical form, this cross section is virtually independent of the muon direction of motion: $A_{\text{ID}} = r_{\text{ID}}^2 \pi = 147 \text{ m}^2$, where $r_{\text{ID}} = 6.85 \text{ m}$ is the ID radius. Using this value, the measured rates correspond to a muon flux of $(1.22 \pm 0.04) \text{ m}^{-2}\text{h}^{-1}$. The result is marginally higher than the muon flux measured by the MACRO detector², $\Phi_{\text{MA}} = (1.16 \pm 0.03) \text{ m}^{-2}\text{h}^{-1}$ [98] which could be due to slight differences in rock coverage. The systematic uncertainty of the BOREXINO result is possibly larger than the ones introduced by statistics and the tagging efficiency only: The selected runs are distributed unevenly over the measurement period of 1.5 years which can in principle introduce an error of the order of 2% due to seasonal variations (see below). In addition, muons generated by the CNGS neutrino beam increase the rate on the same scale of uncertainty. To be conservative, the error on the flux is therefore assumed to be 3%. However, this error could be substantially reduced in the future using the time information of the CNGS pulses for the rejection of the associated events and choosing a seasonally balanced muon sample.

¹The data set corresponds to the validated DAQ runs from May '07 to Dec '08. The runs were selected from the DST-files of *echidna cycle 9*, according to the criteria described in Sect. 4.3.

²The objective of the MACRO (Monopole, Astrophysics, Cosmic Ray Observatory) experiment located at Hall B of the LNGS was the search for magnetic monopoles [98]. At the same time, the detection of $\sim 10^7$ cosmic muon events per year allowed a precise determination of the rate and angular distribution of these muons [97, 98, 114].



Figure 6.1: Temporal variation of the muon rate as measured by the MTB flag over the duration of 1.5 years in BOREXINO [115]. For the first year, the normal seasonal variation of $\pm 2\%$ is visible [114]. Later on, the muon events caused by the CNGS beam and the calibration phase of BOREXINO disturb the signal.

Fig. 6.1 shows the muon rate according to the MTB tag starting from mid of June '07 when the Muon Trigger Board (MTB) was connected to the main trigger. Each data point represents the muon rate averaged over 4 days. For the first measurement period stretching from July '07 to July '08, a sinusoidal modulation featuring a cycle duration of one year can be discerned; the rate maximum occurs in summer, the amplitude of the modulation is of the order of 2-3% of the mean value. This observation is in agreement with the data provided by the MACRO detector which reproduce this seasonal variation [114]. According to [114], the muon flux variation is caused by changes in atmospheric temperature and density that influence the height of cosmic ray interaction and muon production relative to ground level. Later than Jun '08, the CNGS beam comes into operation. The beam luminosity is sufficient to visibly enlarge the measured muon rate. The end of the CNGS beam time coincides with the BOREXINO on-axis calibration campaign which results in large gaps from September to November '08. Thereafter, a relatively low rate corresponding to the winter-induced muon flux minimum is again discernible.

6.1.2 Muon Veto Efficiency

The individual efficiencies of the muon tags MTB, MCR, and IDF are investigated in Sect. 4.2. All three of these tags are applied in combination for regular data analysis; usually, the tags are set in $\text{OR}(\vee)$ in order to maximize the efficiency in muon identification. Contrariwise, an analysis using the tags in $\text{AND}(\wedge)$ would be aiming on reducing overefficiencies of the muon tagging.

It is obvious that MTB and MCR are strongly correlated as they apply in principle the same identification criteria using OD data (Sect. 4.1). They can therefore be expected to identify virtually the same sample of events as muons, albeit the MCR flag does so with slightly higher efficiency ($\varepsilon_{\text{MCR}} \geq \varepsilon_{\text{MTB}}$). In most cases, the OD flagging efficiency ε_{ODF} will therefore correspond to ε_{MCR} in good approximation, while $\varepsilon_{\text{ODF}} = \varepsilon_{\text{MTB}}$ applies whenever muon DAQ is disabled³. On the other hand, the ID flag

³The Muon Trigger Board (MTB) is independent of the status of the TDC boards as it uses a dedicated secondary output of the QTC front end boards (Sect. 3.3) [96].

Laben NHits	Muon Veto Inefficiency ($1-E$)	
	$1-\varepsilon_{\text{IDF}\backslash\text{MTB}}$	$1-\varepsilon_{\text{IDF}\backslash\text{MCR}}$
75-500	$(1.5\pm 0.3)\times 10^{-3}$	$(9\pm 3)\times 10^{-4}$
500-5000	$(3.1\pm 0.9)\times 10^{-5}$	$(1.8\pm 0.8)\times 10^{-5}$
>5000	$<8.2\times 10^{-6}$	$<4.9\times 10^{-6}$
overall	$(7.2\pm 1.6)\times 10^{-5}$	$(4.3\pm 1.5)\times 10^{-5}$

Table 6.2: Veto efficiency E for the combination of the uncorrelated ID and OD tags. As the efficiency of the ID tag depends on the visible energy, three regions parameterized by the number of ID hits are presented along with an overall value. The performance of the combination of IDF\backslashMCR flags surpasses the one of IDF\backslashMTB (Sect. 4.1).

(IDF) can be regarded as fully independent of the OD flags. This allows to calculate the overall veto efficiency E by multiplication of the tagging inefficiencies:

$$E = 1 - (1 - \varepsilon_{\text{IDF}})(1 - \varepsilon_{\text{ODF}}), \quad (6.1)$$

with ε_{IDF} the ID flagging efficiency. Tab.6.2 shows the results for combinations of IDF\backslashMTB and IDF\backslashMCR. For readability, the results are displayed as veto inefficiencies ($1-E$). Like in Sect. 6.1.1, absolute values are used for MTB and MCR, while relative efficiency is adopted in case of IDF. As ε_{IDF} is a function of the ID visible energy, the combined efficiencies are quoted for three energy regimes that are defined by the number of PM hits associated to the ID event (*laben.n_clustered_hits*). In addition, an energy-independent value is presented that corresponds to the average value of veto efficiency. Following IDF, the veto is most efficient for high-energetic events: The overall inefficiency is of the order of 10^{-5} to 10^{-4} .

The grade of quality of the BOREXINO muon veto is determined by its background suppression in neutrino detection: A signal-to-background (S/B) ratio better than 1:1 is requested. Tab. 6.3 compares the residual muon rates for both IDF\backslashMTB and IDF\backslashMCR tagging to the expected ν signal. The energy windows (E_ν) cover the electron recoil spectra of ${}^7\text{Be}$ and ${}^8\text{B}-\nu$'s; the lower thresholds applied are in agreement with the analyses performed in [37, 81]. The residual muon rates can be calculated by multiplication of muon rate and veto inefficiency in the energy region. For the ${}^7\text{Be}-\nu$'s (200-900 keV), the resulting S/B ratio is very favorable: The more effective IDF\backslashMCR veto reduces the expected residual muon rate to 0.07 counts per day (cpd). In comparison to the ${}^7\text{Be}$ event rate of 35 cpd, a S/B ratio of ~ 500 is obtained. Also the somewhat less efficient IDF\backslashMTB tagging still provides an S/B ratio of 320. The contribution of unflagged muons to the event rate is therefore negligible. In case of ${}^8\text{B}-\nu$'s, the situation is less beneficial: The ν signal is with 0.25 cpd almost four orders of magnitude smaller than the muon rate of ~ 1600 cpd in the energy window from 2.8 to 15 MeV. However, the inefficiency of the combined muon veto is merely of the order of 10^{-5} : The resulting S/B ratios are therefore 9:1 for IDF\backslashMCR and 5:1 for IDF\backslashMTB, respectively. Currently, limited statistics as well as other uncertainty contributions overweigh the influence of the remaining muon-events on the ν count rate. For a future precision measurement, it will be necessary to subtract these muons to reach an uncertainty of better than 11% (20%) on the ${}^8\text{B}-\nu$ rate.

Neutrino Window	E_ν [MeV]	Laben NHits	ν Rate [d ⁻¹]	μ Rate [d ⁻¹]	Residual μ Rate [d ⁻¹]	
					IDFVMTB	IDFVMCR
⁷ Be- ν	0.2-0.9	75-350	~ 35	77	0.11 ± 0.02	0.07 ± 0.02
⁸ B- ν	2.8-15.0	900-3000	0.26 ± 0.05	1636	0.051 ± 0.15	0.029 ± 0.013
overall		>75	~ 37	4307	0.31 ± 0.07	0.19 ± 0.06

Table 6.3: Comparison of the expected ⁷Be/⁸B- ν signal rate to the background rate due to muons escaping the identification flags. The residual background rates were computed using the spectral shape of muon signals in BOREXINO and the overall veto efficiencies shown in Tab. 6.2. The visible energy windows were chosen to cover the actual detection regime of the ν 's that is used in analysis.

6.1.3 Tracking Efficiency

Cosmic muons are by far the largest muon sample available for the testing of tracking algorithms. As a first step, the efficiency of the tracking can be tested by evaluating the number of events that feature reconstructed tracks. The ratio of reconstructed to total event number represents the efficiency of the tracking module to produce an output track. However, it has no further implication concerning the track quality. For this study, a representative sample of runs acquired from beginning of March to mid of April '08 was used, applying the most recent version of *echidna* (cycle 11).

Tab. 6.4 presents an overview of the efficiencies for different reconstruction stages. Both for ID and OD, the prerequisite of the tracking is the existence of at least one cluster. If that is the case, the ID tracking reconstructs entry and impact point for $\sim 99.9\%$ of all events. In OD, the entry point is available in 99.5% of events, about 1% more often than the exit point. This difference coincides with the expectation value of muons stopped inside the ID, consequently producing no exit points [96]. However, this interpretation should be handled with care: It is probable that even for stopped muons light reflections will create additional light clusters in the OD which are in turn falsely identified as exit points by the OD tracking. If this was frequently the case, it would imply that the OD exit point efficiency is lower than quoted in Tab. 6.4. The ID tracking is not sensitive to this question, as it is able to reconstruct an impact point independently of the muon leaving the SSS.

The global tracking is initiated if at least two penetration points in either ID or OD are provided. This is the case in at least 99.9% of all cases (corresponding to the frequency of the ID impact point reconstruction). Therefore, the efficiency of the global tracking of 98.9% indicates that it succeeds to reconstruct a track in $\sim 99\%$ of the cases where the necessary input is provided. Of the tracks, 6% are reconstructed using less than the full set of four penetration points; 3.6% return $\chi^2/ndf > 3$. This means that even after retrying a fit neglecting one of the track points, the available points are still in conflict with a possible muon track.

6.1.4 Angular Distributions

The topology of the Gran Sasso mountain massive is imprinted on the angular distribution of the residual cosmic muon flux at the Laboratori Nazionali del Gran Sasso (LNGS). The LNGS was constructed right under the summit of Monte Aquila, which is

Tracking Stage	Frequency
OD clustered	99.84 %
Entry Point	99.50 %
Exit Point	98.45 %
ID clustered	99.97 %
Entry Point	99.94 %
Impact Point	99.89 %
Global Track	98.91 %
4 points provided	98.42 %
>2 points provided	99.94 %
4 points considered	93.13 %
<4 points considered	5.78 %
$\chi^2/\text{ndf} > 3$	3.58 %

Table 6.4: Efficiency of the reconstruction algorithms for producing a muon track output. For all three submodules, the frequencies at which different stages of the reconstruction are reached is shown relative to the number of events providing the necessary data. For the global tracking, also the number of points included in the fit and its quality is listed.

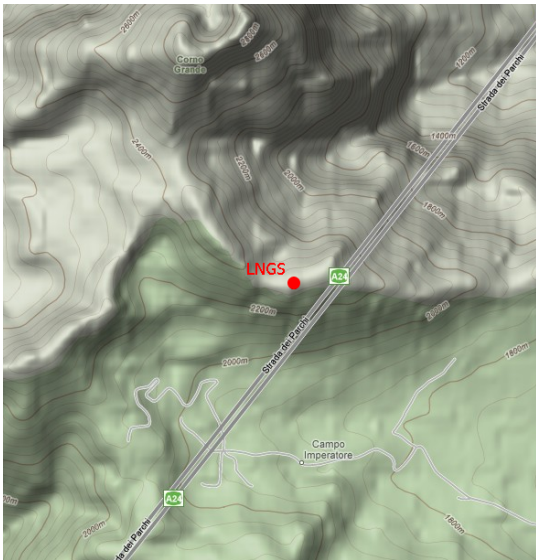


Figure 6.2: Topographic map of the surroundings of the LNGS site.

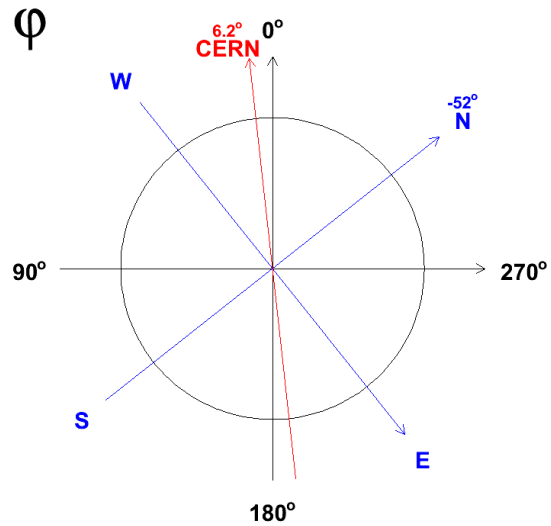


Figure 6.3: The BOREXINO coordinate system.

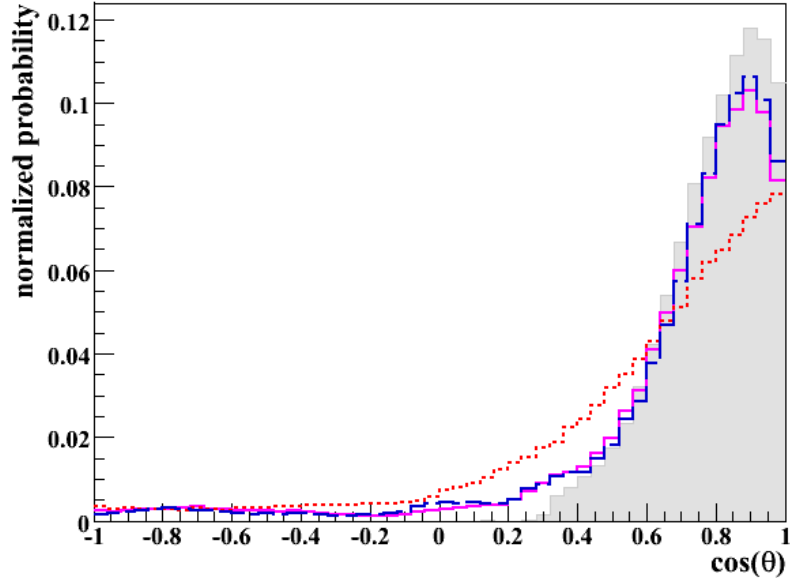


Figure 6.4: Zenith angle ($\cos \theta$) distribution for cosmic muon tracks detected at the LNGS. The colored curves indicate the result of the three BOREXINO tracking modules: ID (*dotted red*), OD (*dashed blue*), and global tracker (*solid pink line*). For comparison, the result of the MACRO detector is indicated as shaded grey region [97]. While OD and global tracking reproduce the MACRO result rather well, the ID angular resolution is low.

part of a small mountain ridge on the northern verge of Campo Imperatore, extending from West to East (Fig. 6.2). Unlike in deep underground mines in which most of the muons arrive from straight above ($\cos \theta=1$, θ being the zenith angle), the reduced shielding towards the mountain flanks causes additional contributions at lower values of $\cos \theta$. Most of the muons are expected to arrive from the South and North. In the coordinate system that is commonly used to define the geometry of the BOREXINO detector, this corresponds to an azimuth angle⁴ of $\varphi=130^\circ$ (S) and $\varphi=310^\circ$ (N), respectively.

Figs. 6.4 and 6.5 show the measured distributions for zenith angle θ and azimuth angle φ for muon tracks detected by BOREXINO. The statistics correspond to ~ 1 month of data or roughly 125 000 tracks. The CNGS beam was not operated in the corresponding period. For comparison, the angular distributions measured by the MACRO experiment is indicated as gray-shaded region [97].

At first glance, both $\cos \theta$ and φ distributions derived from the different BOREXINO tracking modules reproduce the general features of the MACRO measurement. Muons arrive mainly from above, centered around $\cos \theta=0.85$. The azimuth distributions peak around $\varphi=150^\circ$ (S) and $\varphi=280^\circ$ (N). In comparison to MACRO, the BOREXINO angular resolution seems to be inferior. Moreover, from the mutual comparison of ID and OD distributions it is obvious that the OD tracking provides more accurate results. The global track distributions are very close to the ones obtained by the OD tracking.

⁴BOREXINO coordinates impose the azimuth angle $\varphi = 0^\circ$ towards the back of Hall C which is almost exactly pointing towards North-West and the CNGS beam. Unlike the astronomical azimuth, φ is defined in the mathematically positive sense (Fig. 6.3).

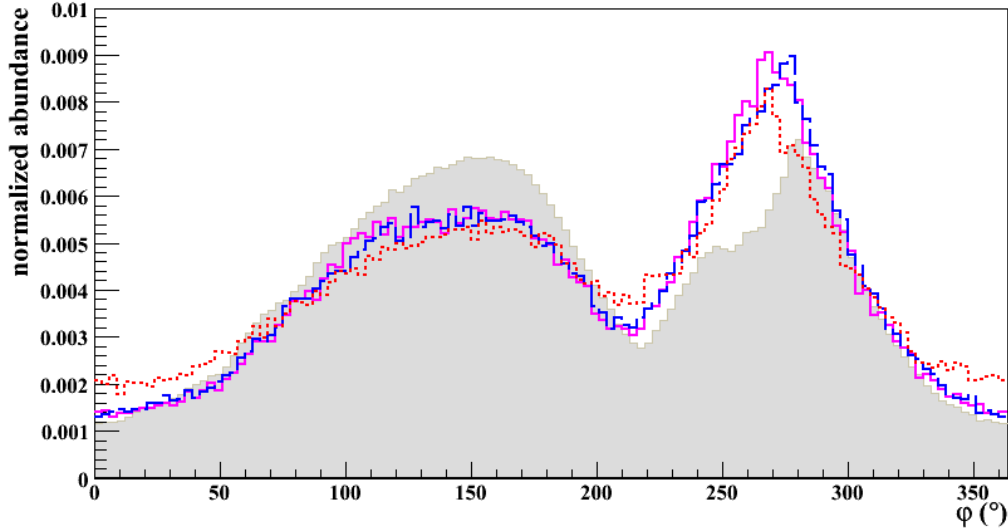


Figure 6.5: Azimuth angle φ distribution for cosmic muon tracks detected at the LNGS. The colored curves indicate the result of the three BOREXINO tracking modules: ID (*dotted red*), OD (*dashed blue*), and global tracker (*solid pink line*). For comparison, the result of the MACRO detector is indicated as shaded grey region [97]. The difference in the relative height of the two main peaks is conspicuous. As ID and OD return consistent results, the discrepancy is most likely due to minor differences in surface topology for the two experiments.

Azimuth Angle φ

For the azimuthal distributions (Fig. 6.5), it is evident that there is a difference in the relative amount of muons arriving from South and North in the two experiments: In comparison to MACRO, BOREXINO reconstructs more muon tracks to the North. In principle, this could indicate a systematical error of the BOREXINO tracking algorithms. On the other hand, both ID and OD tracking produce a concordant result, although they are fully independent. Therefore, the most likely explanation is based on the different positions of the detectors inside the underground lab. While MACRO was located in Hall B, the BOREXINO detector is operated in Hall C, about 100 m further to the North. This corresponds to a reduced rock overburden towards the North, while Southern shielding is increased. The relative shift in the directional distribution of muon tracks is therefore related to slight modifications of the surface topology.

Zenith Angle θ

Comparing MACRO and BOREXINO zenith angle distributions (Fig. 6.4), both global and OD tracking seem to reproduce the peak at $\cos\theta=0.85$ rather well, while the ID tracking is smeared out to lower values. For $\cos\theta<0.25$, no data for MACRO is present. Contrariwise, all three tracking algorithms of BOREXINO show a low but relatively constant amount of tracks in this regime. However, upward-going muons are supposed to be very rare as they are solely produced by atmospheric neutrinos; the tracks at $\cos\theta<0$ are by far too numerous and must be regarded to be to a large extent an artefact of the BOREXINO tracking. To understand this insufficiency, it is instructive to plot the muon zenith angle distribution in dependence of the muon impact parameter R_I . Fig. 6.6 shows the distributions that result from the global tracking for three different regimes of the

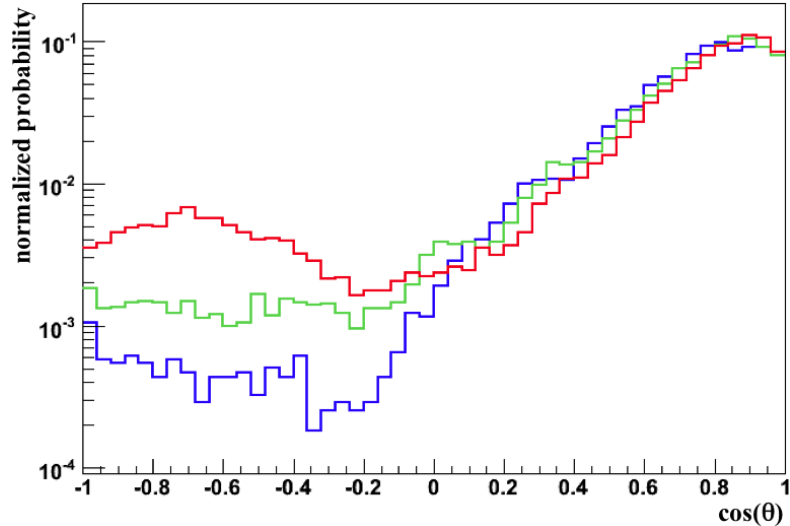


Figure 6.6: Normalized Zenith angle ($\cos\theta$) distribution as derived by the BOREXINO global tracker. The proportion of tracks falsely reconstructed as upward-going is investigated for different regimes of the impact parameter R_I : $R_I < 3$ m (*blue*), $3 \text{ m} < R_I < 5$ m (*green*), and $R_I > 5$ m (*red*). From comparison, the track reconstruction works most reliably for tracks crossing the IV.

R_I : $R_I < 3$ m (*blue*), $3 \text{ m} < R_I < 5$ m (*green*), and $R_I > 5$ m (*red*). The mutual comparison indicates that the smaller R_I , the smaller is the contribution of tracks reconstructed as upward-going. This can be understood if one regards the construction of the track from two points on the ID surface: A track touching the sphere only tangentially will produce both entry and exit (impact) point very close to each other. With increasing impact parameter, it is more likely that (within statistic and systematic errors) the direction of the reconstructed track is shifted by a large extent in comparison to the original. If the exit point is shifted above the entry point in z , the direction of a downward-going muon is in some cases changed to upward-going. However, this effect should have only small impact on neutrino analysis: Muon tracks crossing the IV are the most relevant for investigation of the distance to neutrons or cosmogenics. These track are reconstructed most reliably. The directional information becomes less important with increasing I_R : For a track on the periphery of the ID, the distance to an ID event is relatively independent of its perpendicular orientation.

6.1.5 Tracking Angular Resolution

The MACRO detector was devised as a high-resolution muon tracker [97]. Within the constraints that were pointed out in Sect. 6.1.4, its angular muon distributions are therefore well fit to determine the BOREXINO angular resolution by comparison. The zenith angle seems more adequate for this purpose because of the simpler structure of the distribution: Only a single peak around $\cos\theta=0.85$ ($\theta=32^\circ$) is present. It can be

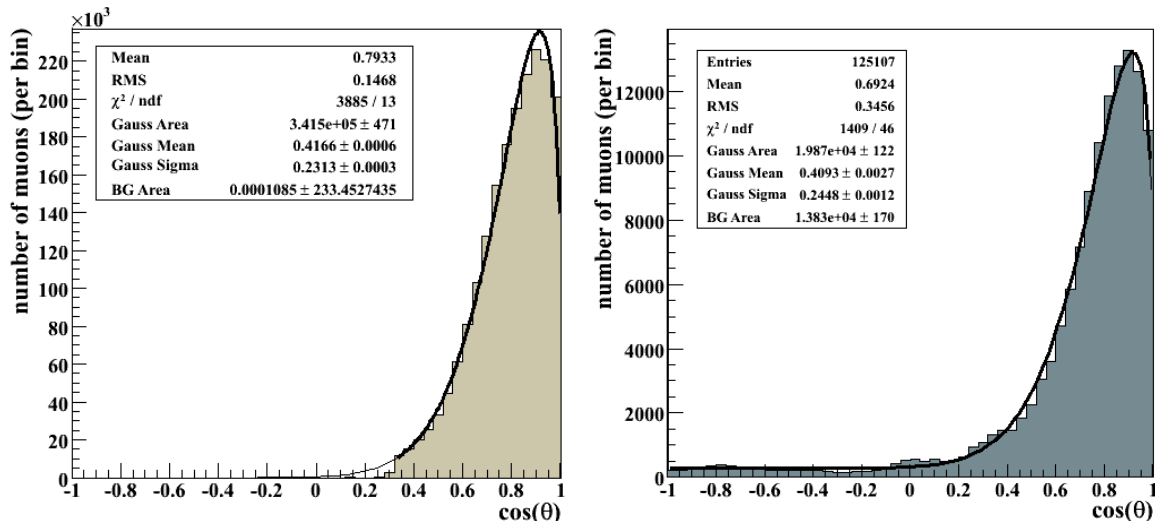


Figure 6.7: A comparison of the zenith angle ($\cos \theta$) distributions of cosmic muons measured in MACRO (*left*) and BOREXINO (*right*) can be used to determine the angular resolution of the BOREXINO tracking algorithms. The width σ of the measured distributions is determined by a Gaussian fit according to Eq. (6.2). The number of falsely reconstructed muons can be estimated by a constant fit to the muons featuring $\cos \theta < 0$.

roughly approximated by a Gaussian in θ ⁽⁵⁾:

$$f(\cos \theta) = \frac{A_{\text{gs}}}{\sqrt{2\pi}\sigma} \exp\left(-\frac{(\theta - \theta_0)^2}{2\sigma^2}\right) + \frac{A_{\text{bg}}}{N_{\text{bins}}}, \quad (6.2)$$

where A_{gs} is the area under the Gaussian, θ_0 its mean value and σ its width. The term $A_{\text{bg}}/N_{\text{bins}}$ allows for a constant contribution that can be used to obtain a rough estimate of the proportion of mis-reconstructed muons tracks (Sect. 6.1.4). Fig. 6.7 shows the experimental $\cos \theta$ distributions and the applied fits for the MACRO detector (*left*) and the BOREXINO OD tracking (*right*). The reduced χ^2 values are rather large, reflecting the imprecise approximation of the cosmic muon distribution by a Gaussian. However, general features (especially the width) are reproduced quite well.

Both the resolution of the tracking σ_{res} and the natural width of the muon angular distribution σ_{nat} contribute to the total width of the Gaussian σ of a detector measurement:

$$\sigma^2 = \sigma_{\text{res}}^2 + \sigma_{\text{nat}}^2. \quad (6.3)$$

The MACRO detector measured the muon angular distribution at an accuracy of $\sigma_{\text{res}} = 0.5^\circ$ [97]. In comparison to the cruder BOREXINO tracking, the distribution measured by MACRO can therefore be assumed to be very close to the natural one: $\sigma \approx \sigma_{\text{nat}}$. Based on this, the angular resolution of the BOREXINO tracking algorithms can be derived by subtracting the natural from the measured distribution width: $\sigma_{\text{res}} = \sqrt{\sigma^2 - \sigma_{\text{nat}}^2}$.

⁵The Gaussian distributions shown in Fig. 6.7 are distorted, as the function of the zenith angle θ is plotted against the cosine $\cos(\theta)$. The apparent truncation of the fit for $\cos \theta = 1$ ($\theta = 0^\circ$) is actually an effect of this deformation: A comparable plot for θ would show no entries for $\theta = 0^\circ$, and a roughly Gaussian shape of the muon distribution.

Tracking	σ [°]	σ_{res} [°]	σ_{nat} [°]	A_{bg}/A [%]
MACRO	13.3	0.5	13.2	0
Bx OD	14.0	4.7		11.2
Bx ID	20.9	16.2	13.2	14.0
Bx Global	13.7	3.7		11.2

Table 6.5: Best fit values for the approximation of the $\cos\theta$ distributions of cosmic muons as determined by MACRO and the three BOREXINO tracking modules. The parameter σ represents the width of the distribution according to Eq.(6.2), while A_{bg} parameterizes a constant contribution of falsely reconstructed muon tracks. Deriving the natural width σ_n of the muon distribution from the MACRO fit using the known angular resolution σ_{res} of the detector, the value of σ_{res} for BOREXINO can be derived as indicated in Eq. (6.3).

Tab.6.5 lists the values for σ , σ_{res} , and σ_{nat} as they are obtained by the fit to the data. As expected, the ID tracking features the worst angular resolution of 16° . OD and global tracking provide more accurate tracks, the resolution slightly better than 5° . Statistical uncertainties from the fit are $<1\%$. For sure, there is a larger systematic contribution introduced by the imprecise Gaussian approximation of the natural muon distribution. Nevertheless, the approximation of the resolution should be correct within one or two degrees.

The constant $A_{\text{bg}}/N_{\text{bins}}$ in Eq. (6.2) can be used to estimate the proportion of poorly reconstructed tracks. It is evident from Fig.6.7 that this is not reproducing specific features of the distribution for $\cos\theta < 0$ but corresponds to the mean of the bin content. Assuming that all tracks accounted for by A_{bg} are mis-reconstructed (even if $\cos\theta > 0$), about 12% of the muons are concerned. Tests of the tracking using the distance distribution of neutrons to their parent muons produce much lower results (Sect.6.2.7): As shown in Fig.6.6, most of the affected tracks are at high impact parameters, reducing the importance of directional information for the distance determination to IV events. From Fig.6.6 it is evident that the relative amount of mis-reconstructed track for muons crossing the IV is about a factor 5-10 smaller than the values quoted in Tab.6.5.

6.2 Cosmogenic Neutrons

Neutrons produced by the interaction of cosmic muons with the materials inside or around a detector are a dangerous background for many astroparticle experiments (Sect.2.3). The results of an investigation of the cosmogenic neutrons in BOREXINO are therefore as well valuable for other neutrino and dark matter experiments. Very luminous muons and high multiplicity neutron events are challenging for the BOREXINO DAQ. Sect.6.2.1 presents the trigger configuration introduced to study neutrons, while Sect.6.2.2 describes the corrections necessary to obtain reliable energy values. The determination of the neutron capture time in BOREXINO and the verification of the presence of neutron captures on Carbon are described in Sect.6.2.3. Using event energy and capture time profiles to select a clean neutron sample, production rate and neutron multiplicity are analyzed in Sects.6.2.4 and 6.2.5. ID neutrons are valuable for the veto of other and more long-lived cosmogenic background sources (Sect.6.2.6): They give an indication for the presence and location of cosmogenic radionuclides (es-

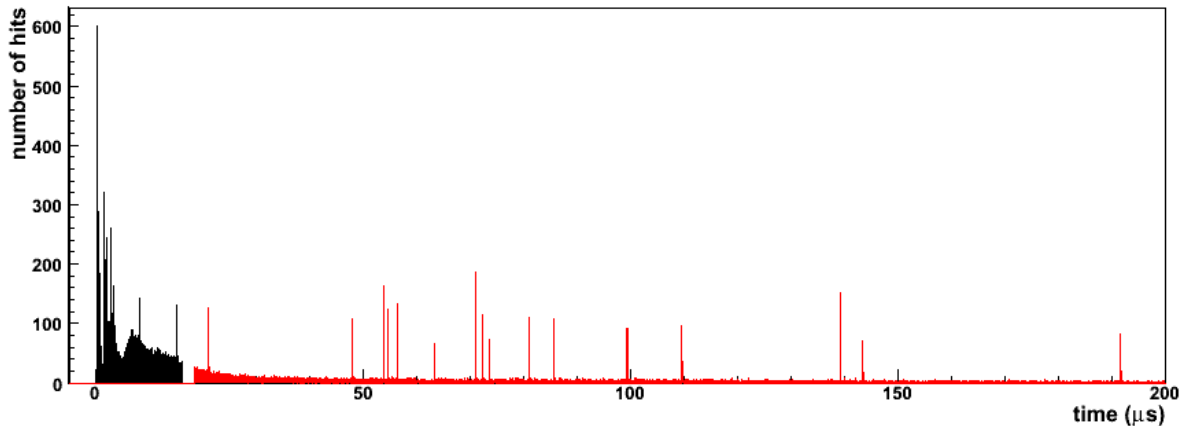


Figure 6.8: In case of a muon crossing the ID, a 1.6 ms neutron time gate (*red*) is opened immediately after the muon time gate (*black*) of 16 μs duration. The first 200 μs are displayed. The acquired pulse shape is shown as sum of PM hits per time bin. The highest peak in the muon time gate is the direct signal of the muon, the smaller peaks in the neutron gate correspond to neutrons. The continuous but exponentially decreasing contribution of PM afterpulses reaches several 100 μs into the neutron gate.

pecially ^{11}C), which are created when neutrons are knocked out of a Carbon nucleus, either directly by muons or by their shower secondaries. In Sect. 6.2.7, the mean free path of cosmic neutrons is investigated. It serves as input for the treatment of external neutron background and for the rejection of cosmogenic background by spatial cuts. At the same time, the distance of neutrons to their parent muons offers a handle on the determination of the lateral tracking accuracy.

For this analysis, the full sample of available data with the new neutron trigger setup from December '07 to February '08 is used, corresponding to 333 days of data. The version of *echidna* is cycle 11.

6.2.1 Neutron DAQ

In December '07, the BOREXINO DAQ was modified to maximize the detection efficiency for cosmogenic neutrons. Immediately in the wake of every event triggering both ID and OD (*trigger.trgtype=1 & trigger.btb_inputs=4*), a second acquisition gate is opened for 1.6 ms (the maximum duration provided by the electronics). The resulting hit distribution in the two gates for a very luminous muon is displayed in Fig. 6.8: The muon time gate in *black*, and the first 200 μs of the neutron gate in *red*.

It is imminently visible that the muon (the first peak) creates a signal extending far longer in duration as its physical crossing time of ~ 50 ns. These additional hits are due to photomultiplier (PM) afterpulses: They are created if the amplifying electron avalanche inside a PM ionizes rest gas contained in the vacuum between the dynodes. While normally on a sub-percent level, their rate increases dramatically with the large amount of light detected in a muon event. In some cases, the number of hits is so large that the size of the electronic storage reserved for each channel on the *Laben* VME boards is insufficient. Additional PM hits of such a channel that are registered after the storage is full are not written by the ADCs, significantly diminishing the pulse height of the neutrons. This effect is visible in Fig. 6.8, as the peaks in the neutron window are in

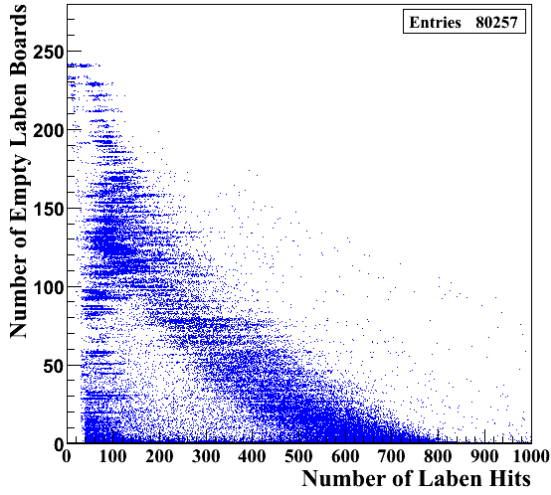


Figure 6.9: Scatter plot of the number of boards temporarily emitted from DAQ (*laben.empty_boards*) vs. the neutron visible energy (*laben.clusters.nhits*). The band of bulk neutron events stretches from ~ 150 on the empty boards axis to ~ 700 on the *laben* hits axis and ^{14}C decays are located to the lower left of this band.

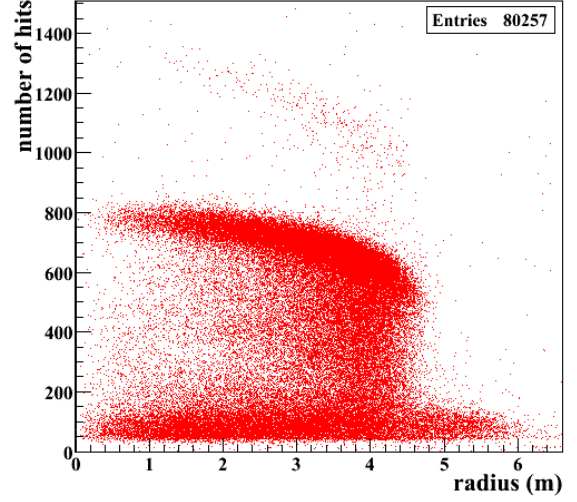


Figure 6.10: Scatter plot of neutron visible energy (*laben.clusters.nhits*) vs. the radius of vertex point reconstruction. The band of bulk neutron events at ~ 700 hits stretches to the IV radius. Neutron clusters affected by empty boards neutrons and ^{14}C are located at lower hit numbers. The vertical band at 4 m is due to neutron buffer events.

the depicted time gate not higher than 200 hits, while the visible energy of the 2.2 MeV neutron capture γ corresponds to ~ 700 hits⁶. Moreover, the charge information of the remaining hits is corrupted as all channels undergo baseline oscillations due to the huge muon light signal.

6.2.2 Neutron Capture Energy

Nevertheless, it is possible to correct for the adversities listed in Sect.6.2.1: Fig. 6.9 shows the number of hits of individual clusters inside the neutron gate N_{hits} (*laben.clusters.nhits*) versus the number of VME boards that featured a full storage in the beginning of the gate N_{eb} (*laben.empty_boards*)⁷. A dominant diagonal band reaches from 150 on the N_{eb} axis to 700 on the N_{hits} axis. This corresponds to neutron events in the bulk of the detector. The more boards provide no hits (are empty), the less hits contribute to the cluster of hits associated to the neutron. A large number of events is also located near the diagram origin: These clusters are low in N_{hits} although all the hits were acquired, and can be associated to ^{14}C decays.

It is instructive to do the comparison to Fig. 6.10 that displays the radial distance r

⁶The linear correlation between number of hits and energy (500 hits/MeV) is only valid for low energies as two hits of the same PM within 140 ns cannot be resolved without charge information. For larger hit numbers, multiple hits of a single channel become more common and Poissonian statistics have to be taken into account.

⁷The convention to refer to the boards with filled storage that consequently provide no hits in the given time gate (and are therefore "empty") is a bit unfortunate but established within the collaboration.

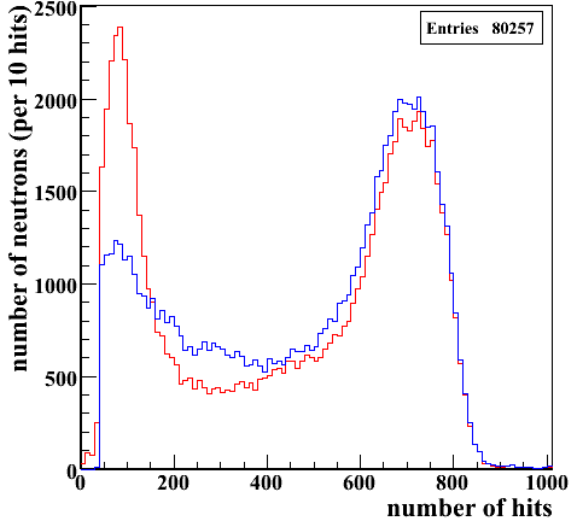


Figure 6.11: Neutron visible energy spectrum (number of hits). The main peak of neutron bulk events is at 700 hits. The spectrum is shown without (*red*) and applying (*blue*) a correction for dysfunctional *laben* boards. The remaining peak at low energies for the corrected curve is due to ^{14}C , the events in between the two peaks to buffer neutrons.

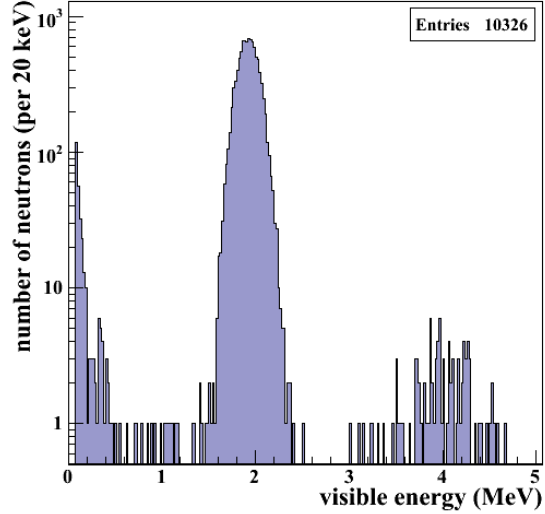


Figure 6.12: Neutron visible energy spectrum after application of a radial cut at 3.25 m and Poissonian energy corrections as indicated by Eq. 6.5. The Hydrogen capture peak at 2 MeV is clearly distinguishable, as well as events due to neutron capture on Carbon at 3-5 MeV.

of the clusters to the detector center versus N_{hits} . Here, the bulk neutrons are located in the horizontal band $N_{\text{hits}} \approx 700$ stretching from the detector center to the radius of the IV. The band is visibly curved, an effect that is partly caused by the radial disparity of the detector response and partly by the loss in visible energy if part of the γ signal "leaks" into the non-scintillating buffer. Near to the IV surface, the visible energy output drops very fast, resulting in the vertical band of "buffer events" centered around $r=4$ m. At very low hit numbers, ^{14}C creates a second band for $0 < r < 6$ m. Neutrons featuring $N_{\text{eb}} > 0$ are located either in the region enclosed by the bands or (for large values of N_{eb}) superimposed to ^{14}C .

The missing hits caused by the *empty boards* can be compensated by applying a correction term to the number of hits. Fig. 6.11 (*left*) shows in *red* the N_{hits} spectrum of neutron clusters. Again, bulk neutrons are located at $N_{\text{hits}}=700$. Using the total number of *laben* boards $N_{\text{b}}=280$ to correct for the missing boards N_{eb} , one obtains:

$$N_{\text{hits}}^* = \frac{N_{\text{b}}}{N_{\text{b}} - N_{\text{eb}}} N_{\text{hits}}. \quad (6.4)$$

The resulting spectrum is shown in *blue* in Fig. 6.12. As can be seen, many of the clusters formerly located at low values of N_{hits} are shifted to larger visible energies towards the peak at $N_{\text{hits}}=700$. Events lying in the region from 200 to 600 hits are mainly neutron buffer events (Fig. 6.10), while for $N_{\text{hits}} < 200$ residual ^{14}C remains.

Finally, a clean energy spectrum of the bulk events can be found by applying a radial cut at 3.25 m to reject neutron buffer events. The corrected visible energy value E_{vis} of

an individual cluster can be written as:

$$E_{\text{vis}} = -\ln\left(\frac{N_{\text{LPM}} - N_{\text{PM}}}{N_{\text{LPM}}}\right) \left(\frac{N_{\text{b}}}{N_{\text{b}} - N_{\text{eb}}}\right) \frac{1}{Y_{\text{ch}}}. \quad (6.5)$$

The first logarithmic term computes the number of hits by comparing the number of hit PMs N_{PM} to the total number of live PMs N_{LPM} : The proportion of PMs that did not register photons $P_0 = (N_{\text{LPM}} - N_{\text{PM}})/N_{\text{LPM}}$ is connected to the mean number of hits per PM, $\mu = -\ln(P_0)$, by Poissonian statistics. The second term corresponds to the empty board correction of Eq. (6.4). Finally, the photoelectron yield per channel $Y_{\text{ch}} = 0.25 \text{ pe/MeV}$ has to be applied.

The resulting visible energy spectrum is shown in Fig. 6.11: It features a very distinctive peak around 2 MeV that is caused by the capture of neutrons on Hydrogen. The slight shift in visible energy from 2.2 MeV is due to γ quenching (Sect. 2.1.2). The second distribution located around 4 MeV is caused by neutron capture on ^{12}C ; the binding energy is released in form of a 5.0 MeV γ quantum that is quenched in energy. The expected ratio of H/C neutron captures is about 125:1, as the cross sections for thermal neutron capture are $\sigma_{\text{H}}=332.6 \text{ mb}$ and $\sigma_{\text{C}}=3.5 \text{ mb}$, and the relative abundance of Hydrogen and Carbon in PC corresponds to 12:9. This agrees very well with the number of clusters contributing to the two peaks.

6.2.3 Neutron Capture Time

The affiliation of clusters to different types of physical scintillation events can be validated by the time difference to preceding muons. After generation by a muon, a cosmic neutron loses its kinetic energy by elastic scattering in the liquid scintillator on a short time scale. Subsequently to thermalization, the neutron is captured by either a Hydrogen or a Carbon nucleus with a time constant $\tau \approx 250 \mu\text{s}$ relative to the muon. Cosmogenic radioisotopes are correlated to muons, but can be distinguished either by their high decay endpoint energy (if short-lived) or a much longer decay time. Accidental coincidences with ^{14}C and other radioactive contaminations feature a constant time structure.

The exact value of the neutron capture time τ depends on the chemical composition of the solvent: τ is an effective value of the two competing processes of H and C capture. The time constant is clearly dominated by the first process as its cross section is two orders of magnitude larger. Measurements with an AmBe-source during the BOREXINO calibration campaign in early '09 imply a value of $\tau = 256 \mu\text{s}$ [115].

For background suppression, only clusters of a visible energy corresponding to 150 to 900 N_{hits}^* are selected for the time analysis (the correction for *empty boards* is applied, Fig. 6.11). The lower threshold rejects ^{14}C , the upper short-lived cosmogenics. Fig. 6.13 depicts the histogram of cluster start times relative to the muon signal (including a small offset of several μs). The fit to the distribution is according to the function:

$$f(t) = \frac{N_{\text{bg}}}{N_{\text{bins}}} + \frac{N_n}{W_{\text{bins}}\tau} \exp\left(-\frac{t}{\tau}\right), \quad (6.6)$$

where N_n is the number of neutrons and N_{bg} the number of background events. The normalization is done using bin number N_{bins} and bin width W_{bins} . The fit returns a

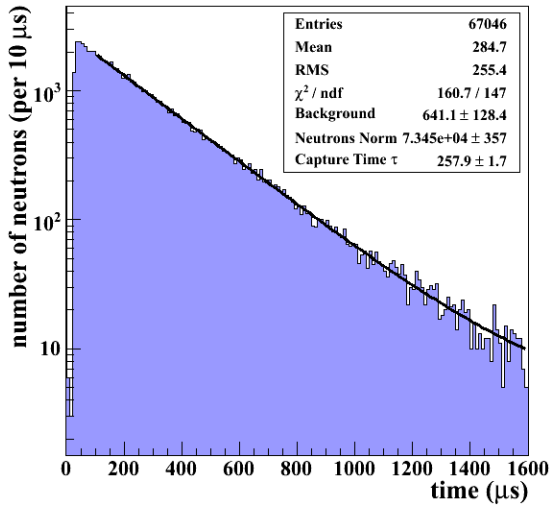


Figure 6.13: Time of neutron captures relative to gate start. A fit to the distribution using an exponential decay returns the neutron capture time τ . As indicated by Eq. (6.6), a constant contribution can be used to determine the amount of uncorrelated background.

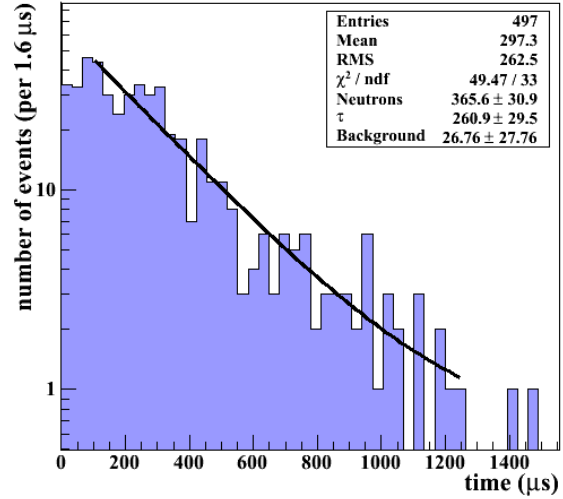


Figure 6.14: Neutron cluster start times relative to the gate start in the visible energy region associated to Carbon captures. Although statistics are low, the correct neutron capture time τ can be found by applying a fit according to Eq. (6.6).

neutron capture time $\tau = (257.9 \pm 1.7) \mu\text{s}$ which is in good agreement with the AmBe-source measurements. N_n is normalized to the integral $\int_0^\infty \frac{1}{\tau} \exp(-\frac{t}{\tau}) dt$ and therefore exceeds the total number of entries in the histogram. The fit result for N_{bg} corresponds to 0.3 % of the total number of clusters, indicating a very clean neutron sample.

The same time fit can be applied to validate the clusters populating the visible energy region from 3 to 5 MeV as neutron captures on Carbon. To obtain more statistics, the sample of Fig. 6.12 can be enlarged by omitting the radial cut, increasing the number of clusters to ~ 500 . Fig. 6.14 shows the time profile of the events and the fit according to Eq. (6.6). The last 400 μs are not included in the fit as the corresponding bins are nearly empty. The result for the capture time $\tau_C = (260 \pm 30) \mu\text{s}$ is within its large uncertainties in good agreement with the value derived for Hydrogen.

6.2.4 Neutron Rate

In order to determine the rate of neutrons produced by cosmic muons inside the IV, it is necessary to reject events inside the neutron gates that are caused by ^{14}C or by short-lived cosmogenic radionuclei. Equally important is the exact determination of the regarded detection volume. There are two possible strategies to obtain the total number of neutrons N_n in the data set of $T = 333$ days:

1. The information of the cluster position reconstruction can be used (Fig. 6.13) to limit the neutron candidates to the IV volume of 4.25 m radius. This cut is introduced to reject neutrons captured in the buffer. The number of neutrons is determined from a capture time fit to the selected clusters. In this way, 72 089 clusters are identified as neutron candidates. From the fit (not shown), the con-

stant background featuring no time correlation with the muons is determined to 1785 ± 111 . Subtracting from the total number of clusters, one obtains $N_n = 70\,304$.

2. Clusters of a visible energy between 300 and 900 hits can be selected as neutrons, based on the N_{hits}^* energy spectrum of Fig. 6.11. This cut is probably underestimating N_n , as it neglects neutrons near to the IV surface that loose part of their visible energy to the buffer, quenching the signal to the ^{14}C regime. After subtraction of the time-constant background contribution that is shown in Fig. 6.13, the resulting number of neutrons is $N_n = 66\,845$.

While the first approach in principle selects the wanted event sample, the uncertainty in position reconstruction and the IV deformation introduce systematic uncertainties that are hard to determine. Therefore, the mean value returned by the two approaches, $N_n = 68\,575 \pm 1730$, is used in the further calculation. It also is necessary to correct for inefficiencies in neutron detection: As only clusters inside the neutron gate are considered as neutrons in the analysis, the detection efficiency is reduced to $\varepsilon_g = \exp(t_g/\tau) = 0.94$ ($\tau = 258 \pm 2 \mu\text{s}$). 6% of the neutrons are captured before the start of the neutron gate $t_g = 16 \mu\text{s}$ after the muon signal⁸. As the neutron gate duration of 1.6 ms corresponds to more than 6τ , the proportion of neutrons captured after the gate end is 0.2%. Moreover, the efficiency of the neutron clustering algorithm ε_c has to be considered: In some cases, very luminous muons reduce due to the *empty boards* effect the signal height of succeeding neutrons below the clustering threshold. The value $\varepsilon_c = 0.99 \pm 0.01$ has been determined by comparison to the *Neutron* FADC system described in Sect. 3.3 [116]. Including these corrections, the IV neutron rate can be determined to

$$R_n^{\text{iv}} = \frac{N_n}{T \varepsilon_g \varepsilon_c} = 211 \pm 5 \text{ d}^{-1}. \quad (6.7)$$

It is common to quote the number of neutrons produced per path length of the parent muon to obtain a neutron rate that is more independent of a given detector. The neutrons considered for R_n^{iv} are limited to the IV. Therefore, the mean muon path length $\langle P_\mu^{\text{iv}} \rangle$ as well as the muon rate R_μ^{iv} that are used for normalization must refer to the IV. It is evident that some of the muons passing the IV generate neutrons in the buffer which are captured in the IV, while a proportion of the neutrons produced inside the IV escapes into the buffer and therefore is lost for detection. As both parent muon and neutron distribution are homogenous on the scale of the detector, the neutron leakage in both directions cancels out exactly.

To be independent of the tracking accuracy, the mean muon path $\langle P_\mu^{\text{iv}} \rangle$ can be calculated by weighting the radial-dependent path length $P_\mu(r) = 2\sqrt{r_{\text{iv}}^2 - r^2}$ with the muon flux $\phi_\mu(r) \propto r$: The flux is dependent on the radius as the area of rings of infinitesimal width around the detector center scales with r . $\langle P_\mu^{\text{iv}} \rangle$ is obtained by the integration

$$\langle P_\mu^{\text{iv}} \rangle = \frac{\int_0^{r_{\text{iv}}} \phi_\mu(r) P_\mu(r) dr}{\int_0^{r_{\text{iv}}} \phi_\mu(r) dr} = \frac{4}{3} r_{\text{iv}} = 5.67 \text{ m}. \quad (6.8)$$

⁸This inefficiency is visible in Fig. 6.8: Roughly 10 and 18 μs after the muon, but still inside the muon DAQ gate, two signals are visible on top of exponential decay of muon afterpulses. In the current configuration of *echidna*, these neutrons are not taken into account for analysis.

The muon rate in the IV, R_{μ}^{iv} , can be calculated analogously to be 38.5 % of the total rate in the ID. Combining this information with R_n^{iv} , one obtains as result for the neutron production per muon path length

$$R_{n/\mu} = \frac{R_n^{\text{iv}}}{R_{\mu}^{\text{iv}} \langle P_{\mu}^{\text{iv}} \rangle} = (2.25 \pm 0.05) \times 10^{-2} / \text{m} = (1.98 \pm 0.04) \times 10^{-4} / (\text{g}/\text{cm}^2). \quad (6.9)$$

The last expression takes the density of PC of $0.88 \text{ g}/\text{cm}^3$ into account. This result can be compared to a similar analysis performed for the LVD detector [93]. The LVD result of $(1.5 \pm 0.4) \times 10^{-4}$ neutrons/muon/ (g/cm^2) is slightly lower than the BOREXINO one. Contrariwise, Monte Carlo (MC) simulations performed in [95] predict a slightly higher rate of 2.5×10^{-4} neutrons/muon/ (g/cm^2) . The BOREXINO result is inside the range of expected values.

6.2.5 Neutron Multiplicity

From the comparison of muon rate (4307 d^{-1}) and neutron rate (211 d^{-1}) in BOREXINO, it is obvious that most of the muons produce no neutrons when passing through the detector. Moreover, most of the neutrons are not produced one at a time, but are part of whole neutron showers induced by muons. The number of neutrons that are generated simultaneously by a single parent muon is known as neutron multiplicity.

Fig. 6.15 shows the multiplicity distribution for the whole data period. Only clusters between 300 and 900 N_{hits}^* are considered. In total, 67 046 neutrons were generated by 22 161 out of the 1 412 673 muons contained in the whole data sample. The mean neutron multiplicity in this sample is $(4.7 \pm 0.2) \times 10^{-2}$. If one considers exclusively muons that produced at least one neutron, the mean value is 3.0 ± 0.2 . The maximum multiplicity reached is close to 180 neutrons produced by a single muon.

The multiplicity results of BOREXINO can be compared to neutron background measurements at the ZEPLIN II experiment [117]. Although the experiment is located in the underground laboratory at Boulby (GB), overburden and average muon energy are comparable. However, the target material is lead, influencing the neutron production rate that is increased by more than a factor 5 compared to BOREXINO. Fig. 6.16 shows the multiplicity distributions of the two experiments: While the proportion of neutron-producing muons is higher for lead than for liquid scintillator, the general shape of the distributions are in fairly good agreement.

Fig. 6.17 (*left*) shows an integral version of Fig. 6.15: The probability of a neutron to be part of a neutron event of multiplicity M or less is plotted in dependence of M . It is evident that about 40 % of all neutrons are part of neutron showers comprising at least 10 neutrons.

6.2.6 Veto of Cosmogenic ^{11}C

Aiming at a *pep/CNO- ν* analysis, it is interesting to study the implications of neutron multiplicity for the veto of cosmogenic radionuclei, especially ^{11}C (Sect. 2.3.3). The basic veto of ^{11}C will be the three-fold coincidence (TFC) technique. The TFC relies on the veto of detector-subvolumes that are determined by the intersection of vetoed cylinders around the muon track and spheres surrounding associated neutron capture vertices. The veto is applied for a time span of several ^{11}C half-lives after the μn -pair.

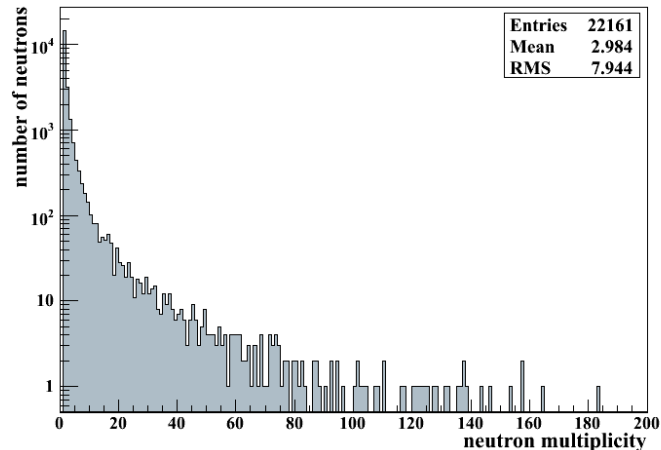


Figure 6.15: Distribution of the number of neutrons produced by a muon in the IV of the BOREXINO detector. The mean value of the neutron multiplicity of ~ 3 excludes muons without neutrons. About half of the neutrons are part of showers of more than 10 neutrons.

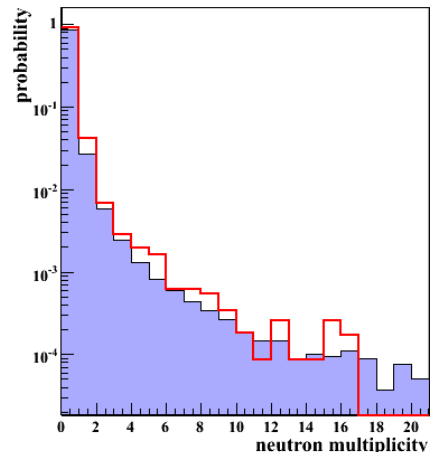


Figure 6.16: Comparison of the neutron multiplicities measured in BOREXINO (*shaded blue region*) and for ZEPLIN-II (*red line*) [117]. Although a lead target was used in case of ZEPLIN-II, the resulting distributions are similar.

Opposed to this approach, the large number of neutrons that are part of high multiplicity events (Fig. 6.15) implies that a relevant amount of neutrons is produced in secondary processes of a hadronic shower. This means that the location of ^{11}C production is not longer limited to the muon track itself, but is distributed over the volume covered by the shower particles. Effectively, the veto around the muon track loses validity, and the neutron vertices offer the only valid spacial information on ^{11}C .

However, neutrons in the wake of a high-luminosity muons occasionally feature due to their reduced number of hits only poor position reconstruction or are in the worst case entirely lost to detection (Sect. 6.2.1). In such cases, a veto of the total Fiducial Volume (FV) is necessary to sustain the efficiency of ^{11}C elimination. This section therefore investigates the achievable efficiency and dead time of a FV veto of $T=1\text{ h}$ ($\sim 3T_{1/2}$) that uses high muon luminosity or high neutron multiplicity as a veto criterion. This could be applied as an expansion of the regular TFC technique.

Neutron Multiplicity Veto

To compute the ^{11}C veto efficiency ε_n and remaining exposure L for a veto based on neutron multiplicity M , the proportion of neutrons p_n covered by the veto and the multiplicity-dependent muon rate $R_\mu(M)$ are the key ingredients. In first approximation, it can be assumed that the number of cosmogenic ^{11}C produced by a muon in the FV is proportional to M . Therefore, ε_n is proportional to the percentage of all neutrons included by the veto: $\varepsilon_n \propto p_n$.

Fig. 6.17 (*right*) depicts ε_n (*red circles*) as a function of the applied multiplicity threshold: The values for the percentage p_n are derived from the data, including the statistical uncertainties. For obtaining the efficiency ε_n , the values of p_n have to be normalized to the maximum efficiency ε_{\max} . It depends on the relative values of veto

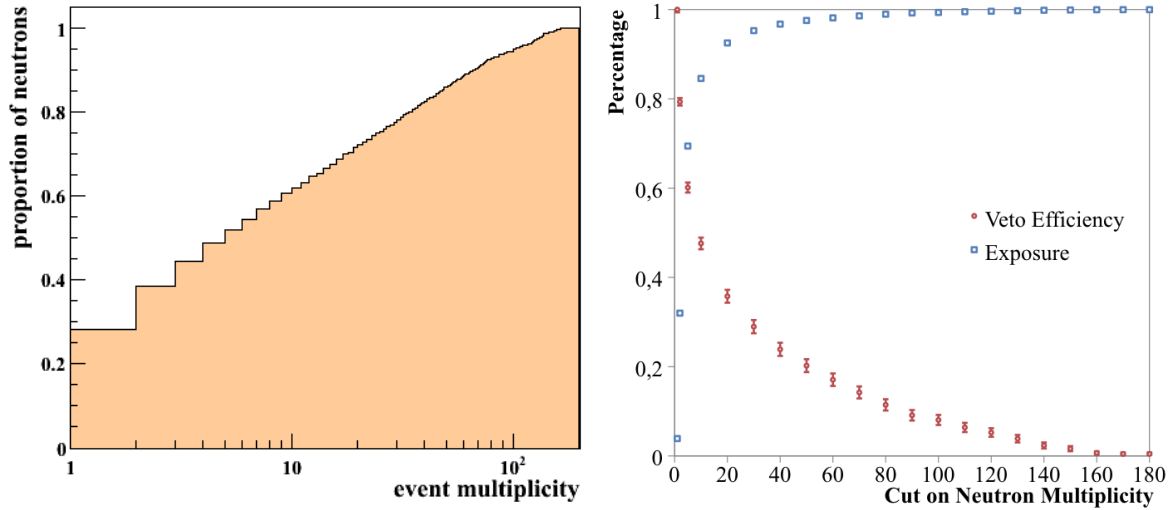


Figure 6.17: *Left:* The proportion of neutrons contained in neutron showers of maximum multiplicity M as a function of M . About 40 % of the neutrons are part of events exceeding a multiplicity of 10. *Right:* The percentage of neutrons p_n included in a veto triggered by high neutron multiplicity of threshold M . In case of a FV veto of 1 h after a trigger event, the corresponding efficiency is $0.83p_n$. The remaining live exposure is shown as well.

time span $T=1$ h and ^{11}C live time $\tau=29.4$ min:

$$\varepsilon_n = \varepsilon_{\max} p_n = (1 - e^{-T/\tau}) p_n = 0.87 p_n. \quad (6.10)$$

It can also be argued that the branching ratio of $\sim 5\%$ for neutron-less ^{11}C production should be considered to lower ε_{\max} . However, if this "invisible" ^{11}C production occurs in parallel to the neutron channel and the branching is independent of M , it will be included by a FV veto as well; the correction is then very small.

The threshold value for the veto should be chosen starting from relatively high values of M and is mainly governed by the desire to introduce a tolerable amount of dead time. In Fig. 6.17 (*right*), the remaining live exposure L (*blue squares*) is shown as a percentage of the total data sample. L is a function of veto duration T and the rate $R_v(M)$ on that the veto occurs: $L = \exp(-TR_v)$ [79]. The value of $R_v(M)$ depends on the veto threshold and the measured values of multiplicity-dependent muon-rate $R_\mu(M)$. Therefore, the live exposure L is

$$L = \exp(-R_v(M) T) = \exp\left(-T \sum_{M=M_0}^{\infty} R_\mu(M)\right). \quad (6.11)$$

A reasonable value for the multiplicity threshold could be $M_0=20$, which would result in an efficiency of $\varepsilon_n=0.36 \times 0.87=0.31$ and a remaining live exposure $L=0.93$.

Muon Luminosity Veto

A second approach is a veto triggered by muons featuring unusual large light outputs: As described in Sect. 5.2.3, regular muons passing through the center of the IV produce at most a visible energy of $N_{\text{hits}}=3 \times 10^4$, including their after pulses (*laben.n_decoded_hits*).

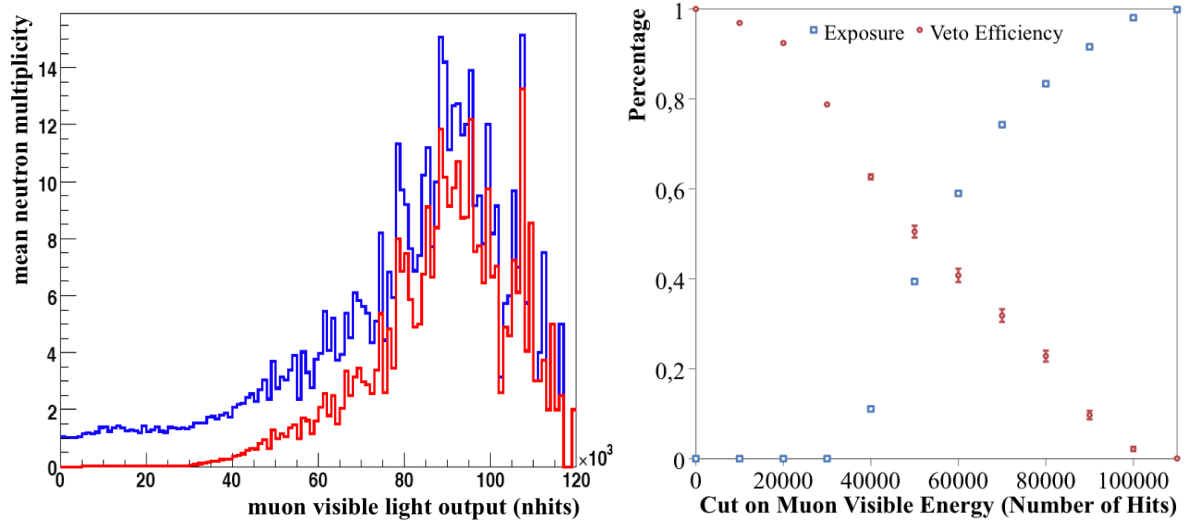


Figure 6.18: The mean neutron multiplicities induced by a muon depends on its visible energy (*laben.clusters.nhits*). The mean for all neutron-producing muons is shown in *blue*, the overall mean in *red*. Muons of more than 30 000 hits are usually followed by high-multiplicity events. The right plot shows the percentage of cosmogenic ¹¹C by vetoing the whole detector after muons above a certain visible energy threshold. The corresponding remaining live time is depicted as well.

However, the maximum light output observed in a muon event is $N_{\text{hits}}=12 \times 10^4$. The additional light cannot be created by the muon on its own but points towards the evolution of a hadronic shower in the ID. Fig. 6.18 (*left*) indicates that muon events featuring $N_{\text{hits}} > 3 \times 10^4$ have an increased probability to produce neutrons: The average neutron multiplicity $\langle M \rangle$ is shown as a function of N_{hits} . This observation is independent of the normalization to all muon events (*red curve*) or neutron-producing muons ($M > 0$) only (*blue*). It is remarkable that $\langle M \rangle$ rises steadily for $N_{\text{hits}} < 9 \times 10^4$ but decreases for higher muon luminosities; this might be an indication for a severe loss in neutron detection efficiency for the degraded neutron events following the most luminous muons.

Similar to the neutron multiplicity veto, the efficiency ε_μ can be calculated by the proportion of neutrons p_μ comprised by muons triggering a veto, $\varepsilon_\mu \propto p_\mu$. Again, the scaling factor ε_{max} is determined by the duration and detector subvolume blocked by the veto. In case of a FV veto for 1 h, the obtained efficiency $\varepsilon_\mu = 0.87 p_\mu$ corresponds to Eq. 6.10. The dependence of the live exposure L on the trigger threshold N_0 can be determined analogously to Eq. 6.11: $L = \exp(-R_\mu(N_0) T)$.

Fig. 6.18 (*right*) depicts both p_μ and the live exposure L as function of the muon luminosity threshold. Naturally, the large integral muon rate of about 4 300 cpd only allows to apply a veto following a small percentage of these muons. A reasonable threshold could be set to $N_0 > 9 \times 10^4$. In this case, the remaining exposure L would cover 92% of the data, while the efficiency would be at least $\varepsilon_n = 0.09 \varepsilon_{\text{max}} = 0.08$. Due to the inefficiencies in neutron detection for high muon luminosities, this result is a lower limit.

6.2.7 Distance to Parent Muon

The distance d of neutrons to their parent muon track is interesting for two reasons: A distance distribution generated on basis of a large neutron sample can be used to deter-

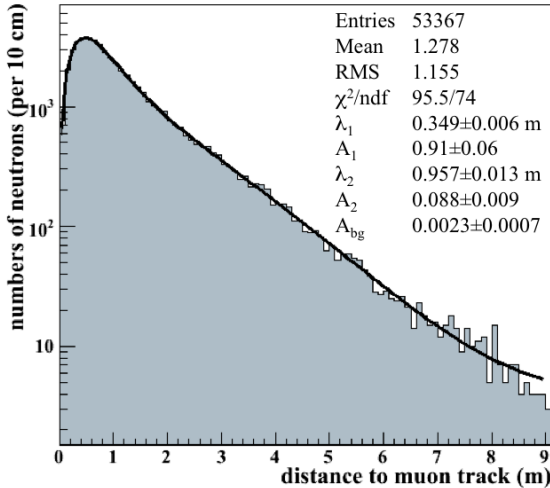


Figure 6.19: Distribution of the distance of neutrons to their parent muons as derived from the BOREXINO global tracking. A fit according to Eq. (6.12) returns information on the neutron range $\lambda_{1/2}$ as well as on the lateral resolution of the tracking σ .

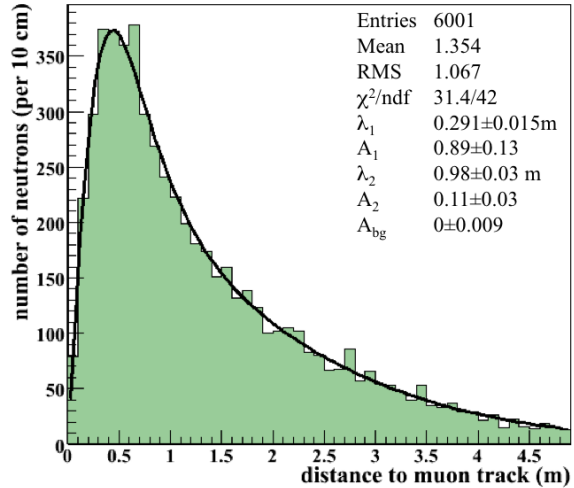


Figure 6.20: Muon-neutron distance distribution including a 2 m radial cut for neutrons around the detector center. As the distance of the neutrons to the rim of the ID increases, the result should be not affected by geometrical effects up to a distance of almost 5 m.

mine the free mean path of a cosmic neutron in the scintillator before it is thermalized and captured (mostly by Hydrogen). The same distribution provides for short distances information on the precision of track reconstruction.

In Fig. 6.19, the distance distribution derived from the global tracking is shown for a sample of more than 5×10^4 neutrons, selected for their corrected visible energy $N_{\text{hits}}^* \in [300, 900]$ as described in Sect. 6.2.2. In addition, a condition for more than 100 uncorrected hits is set to ensure the quality of the neutron spacial reconstruction. This might introduce a small bias by penalizing the contribution of high multiplicity neutron showers that more often feature low-hit neutrons (Sect. 6.2.1). The only prerequisite demanded from muons is the presence of a converged global track. The resulting distribution $F(d)$ can be parameterized by the convolution

$$F(d) = \int_0^\infty dx' x (A_1 e^{-x/\lambda_1} + A_2 e^{-x/\lambda_2} + A_{\text{bg}}) e^{-\frac{(x-x')^2}{2\sigma^2}}. \quad (6.12)$$

The amplitudes A_1 and A_2 indicate the relative weights of the two parameters describing the neutron mean free path, λ_1 and λ_2 . A Gaussian of width σ is introduced to take the spacial resolution into account. The constant term A_{bg} is added to allow for misreconstructed muon tracks that are uncorrelated to their daughter neutrons. Finally, a factor x has to be added to consider the cylindrical geometry of the problem.

Neutron Mean Free Path

The energy spectrum of cosmic muons stretches over several orders of magnitude and does not allow to describe the distance distribution by a single exponential: The range of individual neutrons is determined by their initial kinetic energy, while the shape of the total distribution is a function of the initial neutron spectrum. This deviation from a simple exponential behavior is also observable in MC simulations [95].

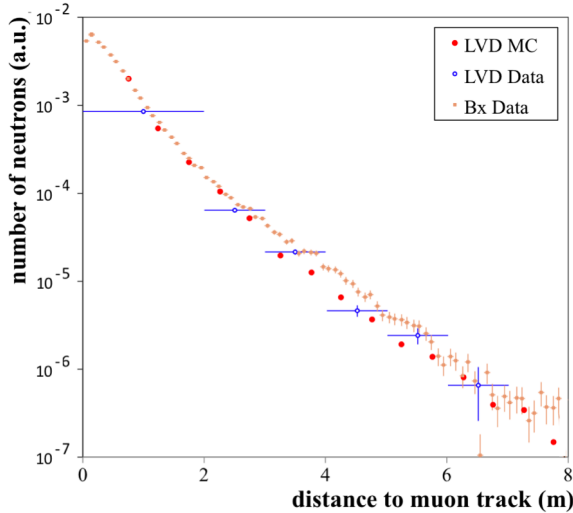


Figure 6.21: Distance of neutrons to their parent muons in liquid-scintillator derived from several sources: *Blue* data points represent measurements of LVD [93], while *red* dots represent the result of a MC simulations reproducing the LVD geometry [95]. The *orange* data points are the result of the BOREXINO global tracking.

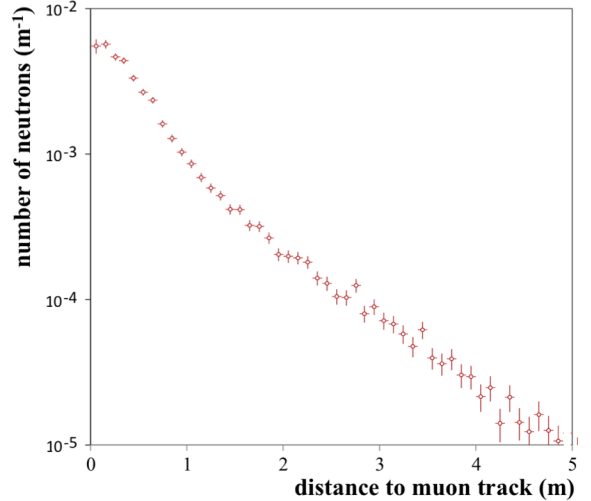


Figure 6.22: Muon-neutron distance distribution including a 2 m radial cut for neutrons around the detector center. The resulting curve for distances above 2.6 m is significantly flatter compared to Fig. 6.21 as the radial cut reduces volume effects due to the limited detector size.

An approach using two exponential decay functions of decay length $\lambda_{1,2}$ for the fit reproduces the data of the present analysis rather well. An effective neutron mean free path λ can be calculated as the weighted mean of the two exponentials: Using the *global tracking* fit values presented in Tab. 6.6, the effective value for the mean free path as shown in Fig. 6.19 is $\lambda=(40\pm 2)$ cm.

Located in Hall B of the LNGS, the LVD experiment (Large Volume Detector) is a liquid-scintillator detector dedicated to the observation of SN neutrinos [93]. The total active target mass of 1 000 t is segmented in 840 cuboidal modules of 1.5 m^3 each. The segmentation allows a quite precise reconstruction of cosmic muons, while the liquid scintillator allows for the detection of neutron captures on Hydrogen. BOREXINO and LVD data are quite comparable because of the similarities in detector materials and dimensions. Fig. 6.21 displays the neutron distance distribution⁹ measured in BOREXINO to data points of LVD [93]. As expected, the experimental distributions are in good agreement over the whole distance range within the rather large error bars of LVD data. The same is true for the Monte Carlo simulation of Kudryavtsev *et al.* [95] that reproduces the result of LVD, at least for neutrons not further than 2 m from the track.

In the distance range from 2 to 6 m, BOREXINO data is systematically shifted relative to the LVD data and MC points. While this could in principle be caused by inaccuracies in BOREXINO track reconstruction, it can also be interpreted as an effect of the detector geometry that is in both analyses neglected. In general, the limited volumes of a detector do not only determine the maximum muon-neutron distance detectable but also

⁹Different to Fig. 6.19, the data points of Fig. 6.21 are scaled with the inverse of the distance: The reason is the segmented structure of the LVD detector: Results are presented normalized to the individual detector submodules. Their number is proportional to the distance from the muon track.

Tracking Module	Resolution [cm]	λ_1 [cm]	A_1 [%]	λ_2 [cm]	A_2 [%]	A_{BG} [%]	χ^2/ndf
OD	24±2	39.5±0.4	95±7	140±9	3.1±0.3	1.2±0.2	1.19
ID	109±4	70±2	100	–	–	–	7.7
global	31±3	34.7±0.6	91±6	90±1	8.8±0.9	0.23±0.07	1.29
$R_n < 2$ m	29±7	29±1	89±13	99±3	11±3	< 1	0.75

Table 6.6: Result of fits (according to Eq.6.12) to muon-neutron distance distributions for the three BOREXINO tracking modules. The lateral resolution σ is best for the OD tracking, followed by the global tracker and the poor ID tracking. The value pairs λ_1, A_1 and λ_2, A_2 parameterize the neutron range. A_{BG} indicates the number of uncorrelated muon-neutron pairs.

diminishes the contributions at large distances. In case of BOREXINO, only neutrons inside the IV radius of 4.25 m are considered. The chance of a neutron to be detected at an arbitrary point in the IV at a distance d from the track scales with $1/d$ due to the size of the solid angle. On the other hand, the number of muon tracks at distance d from the same point scales with d (assuming a homogenous muon flux). Only if all muons at distance d from the point are detected (i.e. a circle of radius d around the point is fully contained inside the detector), solid angle and number of tracks cancel and the detected number of μn -pairs corresponds to the one in an infinitely large detector. Integrating over the whole IV, this condition is no longer met if d exceeds the difference in radius of the active neutron detection volume R_{iv} to active muon detection volume R_{id} . The contribution of muon-neutron pairs is suppressed as part of the muons at $d = R_{id} - R_{iv} = 2.6$ m are not detected. The same volume effects are present in LVD albeit in slightly modified form caused by the differences in detector geometry.

In BOREXINO, it is possible to reduce the effect by artificially choosing a smaller neutron detection volume. In this way, the maximum value of d not influenced by detector geometry increases. Fig. 6.20 shows the muon-neutron distance distribution for an active neutron volume of 2 m in radius, corresponding to $d_{max} = 4.85$ m. Upward-going or badly reconstructed muons ($\chi^2/ndf > 3$) were excluded to obtain a cleaner sample. Compared to the distributions depicted in Fig. 6.19 and 6.21, the slope at distances above 2.6 m is significantly less steep. The fit values for Eq. (6.12) parameterizing the neutron free mean path (Tab.6.6) can be combined to an effective value of $\lambda_{5m} = (37 \pm 5)$ cm. The result is afflicted with a relatively large error compared to the one of Fig. 6.19 as statistics are reduced by about a factor 10 by the volume cut. Fig. 6.22 shows the result including statistical error bars.

Muon Lateral Resolution

The second output of the fits to the muon-neutron distance d distribution is the lateral resolution of the muon tracking. The parameter σ in Eq. (6.12) represents the resolution of d , and is a combination of the two spatial uncertainties on the muon track σ_μ and the neutron vertex σ_n . They add quadratically: $\sigma = \sqrt{\sigma_\mu^2 + \sigma_n^2}$.

Several contributions enter into σ_n : The range of the 2.2 MeV γ produced by the neutron capture in liquid scintillator is 20–30 cm. The vertex is normally reconstructed in the middle of the γ track [96]. MC simulations have shown that the effective spatial

resolution for γ events is ~ 12 cm at energies above 0.5 MeV [118]. The actual resolution might be a bit worse as some of the neutrons are depleted in hits due to the effect of empty boards (Sect. 6.2.2).

The muon lateral resolution σ_μ can be derived by subtracting σ_n from the fit result: The best resolution of (21 ± 2) cm is derived for the OD tracking. The global tracking follows with an accuracy of (28.6 ± 0.6) cm. The ID tracking returns a value of (108 ± 4) cm. However, the χ^2 value of the ID fit is very large, and both quoted result and error should be handled with care. Comparing OD and global tracking, it is also important not to forget the contribution of muon tracks that are uncorrelated to their daughter neutrons and therefore included in the constant contribution A_{BG} . The value of 1.2% of all tracks in the case of the OD tracking is rather low, but 5 times larger than for the global tracking. While it is therefore not obvious if OD or global tracking return the more accurate results, it is clear that the ID tracking alone is inferior to both. However, its contribution to the global tracking is useful, as large discrepancies of OD and ID tracking are an important indicator for systematic variances in track reconstruction.

As expected, the amount of mis-reconstructed muon tracks derived from A_{BG} is in general much smaller than the values obtained in the investigation of the angular resolution (Sect. 6.1.5). This confirms again the higher tracking accuracy for muons passing the IV and the decreased relevance of angular information for the distance-determination between IV events and buffer muons.

Implications for the Threefold Coincidence (TFC) Veto

As stated in Sect. 2.3.3, the TFC technique for the veto of cosmogenic ^{11}C relies on the spacial information of muon track and neutron capture vertex to define veto volumes [100]. To minimize the loss in exposure, only the intersection of a cylinder around the muon track and a sphere around the neutron is effectively blinded out for several ^{11}C half-lives. The necessary radii $r_{\mu,n}$ of both cylinder and sphere are determined both by the accuracy of the position reconstruction and the mean free path of the neutron. Excluding for the moment more complex ^{11}C production processes in hadronic showers and convection of the scintillator, cosmogenic nuclei should be generated within a few centimeters of the muon track [99]. The percentage of ^{11}C included in the muon cylinder is therefore solely a function of the ratio of cylinder radius r_μ to lateral resolution σ_r : Taking into account the cylindrical geometry, a percentage of 99.3% of all ^{11}C events should be included by a cylinder of $r_\mu=3\sigma_r$. In case of the global tracking, this corresponds to $r_\mu\approx 1$ m.

Similarly, a multiple of the neutron vertex resolution of $\sigma_v\approx 12$ cm is the starting point for the sphere radius r_n surrounding a neutron. However, the minimum value of r_n is dominated by the natural offset between neutron and ^{11}C position which is $\lambda_{nC}=18$ cm [119]. The value is lower as for the direct neutron production by a muon determined in this chapter, as knock-out neutrons are less energetic. Considering the spherical symmetry, a veto radius of $r_n = 1.5$ m is necessary to include 99% of all ^{11}C nuclei.

Choosing the spacial vetoes according to these values, the upper limit for the efficiency of the TFC veto is in principle as large as $\varepsilon_V=0.99$. However, several other factors have to be included: The neutron detection efficiency (Sect. 6.2.4) of $\varepsilon_n=0.94$, the ratio of neutron-less ^{11}C production channels of $r_{0n}=0.05$, and the limited ^{11}C

veto time span T (Sect.6.2.6). A veto duration of $T=1.5$ h corresponds to a factor of $\varepsilon_T = 1 - \exp(-T/\tau) = 0.95$ in the total efficiency. If all ^{11}C was created along the muon track, the corresponding veto efficiency was $E = \varepsilon_V \varepsilon_n \varepsilon_T (1 - r_{0n}) = 0.84$. Applying the TFC veto in this way to the data would reduce the detector live exposure by about 30%. The combination with the neutron multiplicity and muon luminosity cuts described in Sect.6.2.6 would increase this ratio by another 10%.

Chapter 7

The LENA Project

The recent achievements of the BOREXINO and KAMLAND experiments have demonstrated the large potential of liquid-scintillator detectors (LSDs) as neutrino observatories (Chap. 2) [12, 25]. In recent years, a next-generation large-volume LSD has been proposed from various sides: The Hawaiian Antineutrino Observatory HANOHANO and the European LENA (Low Energy Neutrino Astronomy) are currently the most advanced projects [8, 13, 120, 121]. Due to its large target mass of 50 kt, LENA will greatly gain in sensitivity compared to contemporary detectors. This provides the opportunity to perform high-statistics measurements of strong astrophysical neutrino sources like our Sun or a galactic Supernova (SN) explosion, resolving substructures in the ν flux concealed to present-day detectors. At the same time, very rare event search becomes possible, as the excellent background rejection allows to identify a handful of events out of several years of data taking. Sect. 7.1 presents an overview of the various physics objectives of LENA. Sect. 7.2 gives an outline of the current detector design and of the on-going activities inside the European LAGUNA framework.

The present work studies aspects of the physics potential and of the technical feasibility of the LENA experiment: Chap. 8 describes the setup and results of a laboratory experiment determining the optic scattering length of several candidate scintillators for LENA. The optical transparency of the scintillator has substantial influence on energy and time resolution of a large-volume detector. Chap. 9 on the other hand evaluates the sensitivity of LENA to the diffuse background of Supernova neutrinos (DSNB), and the information on the SN neutrino spectrum that could be gained by spectroscopy of these neutrinos (Sect. 1.2.3). While both experimental and phenomenological studies are evaluated for the detector geometry of LENA, the results are of general interest for future LSDs.

7.1 Physics Program

The main motivation for LENA is the creation of an observatory for astrophysical neutrinos: The large volume will allow the detection of solar [122], Supernova (SN) [107] and geoneutrinos [88] at large event numbers (Sect. 1.2). Furthermore, it has been pointed out that a LSD the size of LENA will be sensitive to neutrinos produced by the annihilation of dark matter particles, provided these particles are relatively light [123]. From the point of view of particle physics, the primary goal of LENA is the search for nucleon decay [124]. Moreover, neutrino physics would profit from the detector: Reactor, at-

Channel	Source	Neutrino Rate [d ⁻¹]	
		BPS08(GS)	BPS08(AGS)
νe	pp	24.92±0.15	25.21±0.13
	pep	365±4	375±4
	hep	0.16±0.02	0.17±0.03
	⁷ Be	4984±297	4460±268
	⁸ B	82±9	65±7
	CNO	545±87	350±52
¹³ C	⁸ B	1.74±0.16	1.56±0.14

Table 7.1: Solar neutrino event rates in LENA, assuming an energy threshold of 250 keV for detection. Both νe scattering events and reactions on ¹³C are listed (Sect. 2.2). Calculations are based on the high-metallicity BPS08(GS) and low-metallicity BPS08(AGS) models. The errors indicate the model uncertainties [38].

ospheric and beam neutrinos could be utilized to determine neutrino mass differences and mixing parameters in precision oscillation experiments [125, 126].

7.1.1 Solar Neutrinos

The experience with BOREXINO has shown that it is possible to reduce the radioactive contamination of a liquid-scintillator detector (LSD) far enough to allow the measurement of the solar ν spectrum down to energies of a few hundred keV [81]. The spectroscopic performance of LENA will probably be inferior to the one of BOREXINO as the expected photoelectron yield is lower (Sect. 8.6). Nevertheless, the neutrino event rates in LENA will surpass the signal in BOREXINO by at least two orders of magnitude. In the following, a very conservative fiducial volume of merely 18 kt is chosen to provide an additional shielding layer of 3 m against external gamma-ray background. Tab. 7.1 lists the expected rates for the ν 's emitted in the *pp* chain and the *CNO* cycle, using the most recent solar model predictions (Sect. 1.2.1). The values were scaled from [122], assuming a detection threshold of 250 keV.

About 25 *pp*- ν -induced electron backscattering events per day are expected above 250 keV in LENA. It is doubtful if this rate is sufficient to be distinguished from the overwhelming ¹⁴C background. About 5 000 ⁷Be- ν events per day are expected: Presuming background levels comparable to BOREXINO, the high statistics will allow a measurement of the ⁷Be- ν flux at an accuracy unprecedented in neutrino physics. It might be particularly interesting to search for temporal variations in the detected rate: A first analysis performed in [122] indicates that one year of exposure will be sufficient to identify count rate modulations on a level of 1.5%. The result is to a large extent independent of frequency and phase. In this way, temporal variations of neutrino production rates caused by temperature and density changes in the solar core could be probed.

After two years of BOREXINO data taking it is evident that the detection of *CNO* and *pep* neutrinos delicately depends on the background level induced by cosmogenic ¹¹C β -decays (Sect. 2.3). The ¹¹C production rate is mainly a function of the rock overburden shielding the detector (Sect. 7.2.2). If LENA was operated at the intended

Channel	Rate
(1) $\bar{\nu}_e + p \rightarrow n + e^+$	7 500–13 800
(2) $\bar{\nu}_e + {}^{12}\text{C} \rightarrow {}^{12}\text{B} + e^+$	150–610
(3) $\nu_e + {}^{12}\text{C} \rightarrow {}^{12}\text{N} + e^-$	200–690
(4) $\nu_e + {}^{13}\text{C} \rightarrow {}^{13}\text{N} + e^-$	~ 10
(5) $\nu + {}^{12}\text{C} \rightarrow {}^{12}\text{C}^* + \nu$	680–2 070
(6) $\nu + e^- \rightarrow e^- + \nu$	680
(7) $\nu + p \rightarrow p + \nu$	1 500–5 700
(8) $\nu + {}^{13}\text{C} \rightarrow {}^{13}\text{C}^* + \nu$	~ 10

Table 7.2: Overview of the detection channels for SN neutrinos available in LENA. The rates are derived from [107] and vary with the assumed SN explosion model. Total event rates vary from 10 000 to 15 000 events for the standard SN scenario ($8 M_{\odot}$ progenitor in 10 kpc distance).

depth of 4 000 mwe (meters water equivalent), the ratio of $CNO/pep-\nu$ signal to ${}^{11}\text{C}$ background rate would be 1:5, a factor 5 better than in BOREXINO. A high-statistics measurement of about 500 CNO neutrinos per day will provide valuable information on solar metallicity, especially if the contributions from the individual subfluxes can be distinguished. At the same time, the measurement of the $pep \nu$ flux could be used for a precision test of the ν_e survival probability in the MSW-LMA transition region. Calculations done in [122] indicate that also the onset of the transition region could be tested utilizing low-energetic ${}^8\text{B}$ neutrinos. The charged current reaction on ${}^{13}\text{C}$ is due to a threshold of more than 2 MeV only accessible to ${}^8\text{B}-\nu$'s: About 500 counts per year are expected, offering a background-free channel due to the coincidence structure of the signal (Sect. 2.2.3).

7.1.2 Supernova Neutrinos

While the dominant ν detection channel in LSDs in case of a galactic core-collapse SN is the inverse beta decay, the target mass of LENA is large enough to exploit a variety of reaction channels accessible to all neutrino flavors. In the standard SN scenario that describes the explosion of an $8 M_{\odot}$ progenitor star at the center of the milky way, LENA will detect between 10 000 and 15 000 events [107]. The numbers vary with the assumed SN neutrino spectra and with the occurrence of matter effects in the stellar envelope (Sect. 1.2.2). An overview of the detection channels and their rates in LENA is given in Tab. 7.2.

More than half of the events are caused by the inverse beta decay (1) which allow a precision measurement of the $\bar{\nu}_e$ energy spectrum and the temporal evolution of the $\bar{\nu}_e$ flux. According to [127], the energy resolution of a large-volume LSD offers the possibility to study the imprints of matter effects in the $\bar{\nu}_e$ spectrum that are a result of the transit through the matter-potential of the progenitor star envelope or of the Earth. As the occurrence of these effects is closely linked to the size of the mixing angle θ_{13} and the neutrino mass hierarchy, SN ν detection in LENA is also sensitive to these up to now undetermined neutrino parameters.

The charged current (CC) reaction of ν_e on Carbon (3) will be mainly used to determine the ν_e flux. The event signature is very similar to the CC reaction of $\bar{\nu}_e$'s (2)

that provides a very similar signature (Sect. 2.2.3). However, statistical subtraction of the $\bar{\nu}_e$ flux which is determined very accurately by channel (1) can be used to isolate the ν_e signal at a 10 % level. The remaining uncertainty is mainly due to the uncertainties of the reaction cross sections [107].

While the channels (1-4) allow to discriminate ν_e and $\bar{\nu}_e$, channels (5-8) are accessible for all neutrinos independent of their flavors or anti-flavors. The NC reactions on Carbon (5+8) are flux measurements only and bear no spectral information. Both elastic electron scattering (6) and proton scattering (7) on the other hand provide spectral data for the combined flux of all flavors. The signal on protons is dominantly caused by ν_μ and ν_τ (and their ant flavors) as their expected mean energies are larger. Due to the strong dependence of the measured event rate on the mean neutrino energy, proton scattering is very sensitive to the temperature of the SN neutrinosphere.

LENA also is sensitive to the diffuse SN background neutrinos. The expected signal is ~ 10 $\bar{\nu}_e$ events per year [128]. An analysis of the expected event rate and spectrum inside the observation window defined by the background signals in a LSD is presented in Chap. 9. The information that can be obtained by spectroscopy of these neutrinos on the SN ν spectrum is investigated, too.

7.1.3 Geoneutrinos

Due to their low energy thresholds, LSDs are sensitive to geoneutrinos via the inverse beta decay (Sect. 1.2.4). The large target mass of LENA corresponds to roughly 1 000 events per year if the detector is located at the currently favored site adjacent to the Pyhäsalmi mine in Finland. The actual event rate is dependent on the detector location, as the U/Th content of continental crust is larger than the one of the thinner oceanic crust. A detector of the same target mass at Hawaii would therefore measure only ~ 350 events per year.

If the radiopurity levels of BOREXINO are reached in LENA, geoneutrino detection will suffer much less from internal α -induced background than the measurements done in KAMLAND (Sect. 7.2.2) [25]. In addition, the background from reactor neutrinos will be significantly lower, especially if the detector is located at Pyhäsalmi. A spectral discrimination of the $\bar{\nu}_e$ proportions originating either from the ^{238}U or from the ^{232}Th chain will be achievable (Fig. 1.9).

Albeit the high statistics, the directional information of the inverse beta decay events is most likely not significant enough to distinguish the contributions of core, mantle, and crust to the total $\bar{\nu}_e$ flux: Ten years of exposure would be necessary to positively identify a very strong geoneutrino source of the order of 20 TW located at the Earth's core [88]. A more promising approach is the combination of geoneutrino rate measurements in several LSDs at different detector sites: The data of KAMLAND, BOREXINO, SNO+, LENA, and possibly HANO HANO could be combined to disentangle the geoneutrino fluxes of crust and mantle [121].

As about half of the Earth's thermal heat flow is unaccounted for, the occurrence of natural nuclear burning of ^{235}U in the terrestrial core has been repeatedly proposed in literature [65]: The emitted ν spectrum is assumed to be similar to the one of regular nuclear reactors (Sect. 9.2.1) which constitute the main background to detection. The current best limit of 6.2 TW on the thermal power of this "georeactor" is set by the KAMLAND experiment [25]. LENA could lower this limit to 2 TW in Pyhäsalmi,

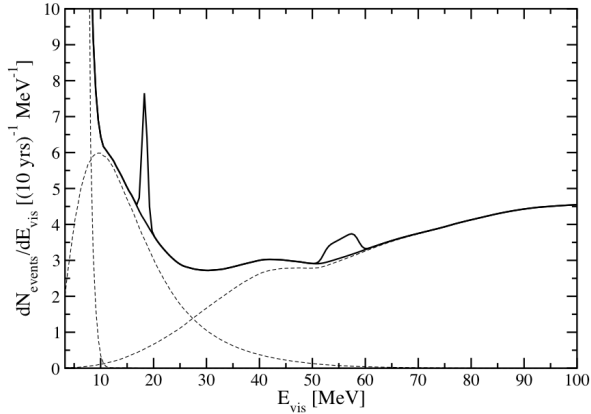


Figure 7.1: Expected dark matter signal in LENA after 10 years of data taking [123]. Two possible scenarios assuming particle masses of 20 and 60 MeV are depicted. The background sources of reactor, diffuse SN, and atmospheric neutrinos (from low to high energies) are shown as dashed lines. Superimposed as solid lines are sum spectra including the dark matter signal.

mainly because of the reduced reactor neutrino background [88].

7.1.4 Dark Matter Annihilation Neutrinos

It has been demonstrated in [123] that LENA would be very sensitive to $\bar{\nu}_e$ originating from the annihilation of light dark matter particles (Sect. 1.2.5). The observational window is very similar to the one for the observation of the DSNB: It is mainly governed by reactor, diffuse SN and atmospheric neutrinos. Fig. 7.1 shows the expected signal in LENA, assuming a typical annihilation cross section. The discovery potential will be very large as the annihilation $\bar{\nu}_e$ create a discernible line in the energy spectrum that corresponds to the mass of the dark matter particle. On the other hand, the low background level in this energy regime will also allow to put a very stringent limit on the existence of dark matter of MeV mass scale if no signal is detected.

7.1.5 Nucleon Decay

One of the most interesting questions in modern particle physics is the stability of the proton [129]. While the baryon number is conserved in the standard model, its most important extensions predict a violation of this quantity. In addition, the instability of matter and therefore the proton is strongly favored from a cosmological point of view. Grand unified theories usually prefer the proton decay into π^0 and e^+ . This is also the channel where Čerenkov detectors (WCDs) are able to put the most stringent limits on [130]. Supersymmetry on the other hand favors the decay into K^+ and $\bar{\nu}$. Here, WCDs are at a disadvantage: Both particles are invisible in the detector as the Kaon is generated at a kinetic energy below the Čerenkov threshold, greatly reducing the detection efficiency.

Regarding the later decay channel, LSDs offer a natural advantage as they are able to detect the kinetic energy deposited by the Kaon [124]. The subsequent decay into $\pi^+\pi^0$ or $\mu\nu_\mu$ provides a very fast coincidence signal ($\tau_{K^+} \simeq 12$ ns) that can be used

for background discrimination. The main background are atmospheric neutrinos in the energy regime of several 100 MeV: Pulse shape analysis can be exploited to reduce the atmospheric background to less than 1 count in 10 years, at the same time loosing about 1/3 in proton decay sensitivity. If no signal was seen in this time span, the proton lifetime limit could be increased to $\tau_p \geq 4 \times 10^{34}$ yrs (at 90 % C.L.) [124]. This surpasses the present best limit set by the SUPER-KAMIOKANDE experiment by about one order of magnitude [130].

7.1.6 Neutrino Parameters

The measurement of astrophysical neutrinos in LENA will also allow to learn about the neutrinos themselves: As stated in Sect. 1.1.2, solar neutrino detection is most sensitive to the mixing angle θ_{12} . The measurement of the ν_e survival probability in the transition region of matter to vacuum-governed oscillations provides the opportunity to test the standard MSW-LMA oscillation solution (Sect. 1.1.3). On the other hand, supernova neutrinos offer the possibility to investigate mass hierarchy and mixing angles (Sects. 1.2.2 and 7.1.2).

There are also several terrestrial sources that allow to investigate the neutrino properties: While *reactor neutrinos* usually pose a background for $\bar{\nu}_e$ detection, they can as well be exploited for a precision measurement of the solar mixing parameters. If LENA was located in Fréjus, θ_{12} could be determined at 1 % and Δm_{12}^2 at a 10 % accuracy level after 7 years of exposure [125].

Analogously to the SUPER-KAMIOKANDE measurements, *atmospheric neutrinos* can be used to further improve the knowledge of θ_{23} and Δm_{23}^2 [15]. As the length of the oscillation baseline is determined by the direction of arrival of the neutrino, the tracking capabilities of the detector are vital for analysis: While this information is not available for low neutrino energies, neutrinos in the GeV energy range induce e^\pm/μ^\pm tracks in the scintillator that are several meters in length. It has been shown that basic track reconstruction is possible under these circumstances [82]. Not least, the BOREXINO ID track reconstruction demonstrates that it is possible to determine the orientation of track-like events.

Finally, LENA could be used as the far detector of a next-generation *beta beam* experiment [131]: The underlying concept is the production of a pure ν_e or $\bar{\nu}_e$ beam by acceleration of β -unstable isotopes in a storage ring. Straight decay lines are embedded in the ring to produce the ν beam. As in the case of a conventional neutrino beam, the far detector is positioned in the first oscillation maximum, at a typical distance of several hundred kilometers: The beam energy is chosen accordingly. By combination of ν_e or $\bar{\nu}_e$ measurements, the sensitivity that could be reached on θ_{13} and the CP-violating phase δ would exceed by far the present state of knowledge (Sect. 1.1.2). The capability to discern ν_e -like and ν_μ -like events as well as the energy resolution of the detector are central for this analysis. Studies performed in [126] show that ν_μ could be identified at 90 % efficiency in LENA, accepting a ν_e contamination of this sample on a 1 % level. The discrimination capability was investigated in the energy region from 0.2 to 1.2 GeV and used both pulse shape analysis and the occurrence of muon-decay electrons as criteria.

Nevertheless, detailed simulations of the tracking capability of LENA are needed for both atmospheric and beam neutrinos. Especially the production of secondary mesons makes energy reconstruction and particle identification more difficult.

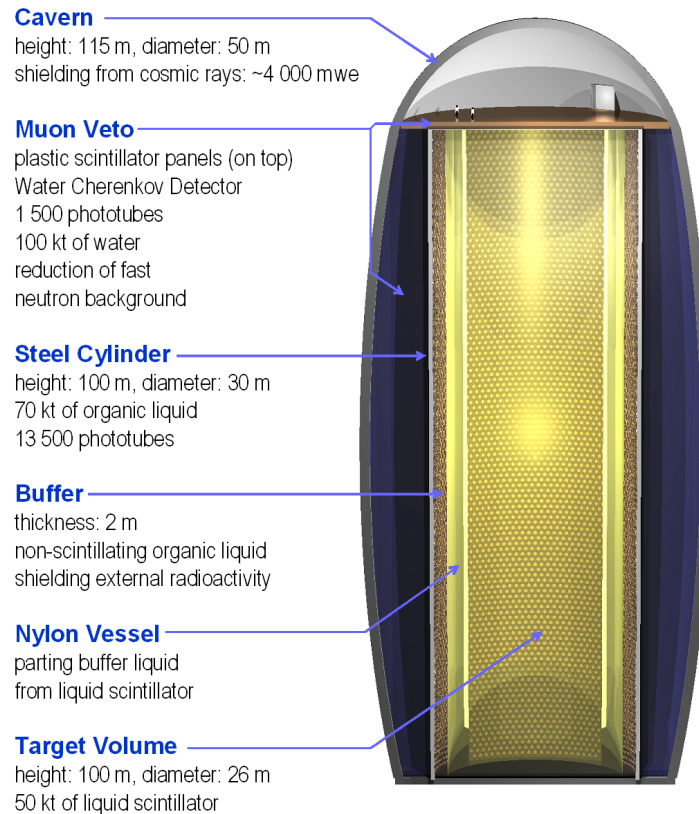


Figure 7.2: Sketch of the LENA detector layout.

7.2 Detector Design

The LENA detector foresees to house about 50 kt of liquid scintillator in a radiopure environment: The general detector layout is described in Sect. 7.2.1, while shielding and purity requirements are discussed in Sect. 7.2.2. The amount of shielding is naturally connected to the detector site: Sect. 7.2.3 presents the laboratories and mines that are considered in the LAGUNA site study [132], one of which could be the future host of the LENA detector.

7.2.1 Detector Layout

The basic design concepts of LENA are very similar to those of BOREXINO (Sect. 3.2): As depicted in Fig. 7.2, the components are arrayed in shells around a single central active volume of about $50\,000\text{ m}^3$. The central liquid-scintillator detector is enclosed by a steel tank (30 m diameter, 100 m in height) that contains the active target and is equipped with photomultipliers. It is surrounded by a water Čerenkov detector for the rejection of cosmic muons and external radioactivity. The role of BOREXINO's outer steel dome is filled by the detector cavern itself. The following paragraphs are meant to give a more detailed insight in the subsystems and addresses design aspects currently under discussion.

The central detection volume of LENA is foreseen to be a monolithic volume of *liquid scintillator*. Due to the limits set by optical transparency, the volume is cylindric instead of spheric to limit the maximum distance to the PMs: An upright cylinder of

26 m in diameter and 100 m in height corresponds to an active volume of $5.3 \times 10^4 \text{ m}^3$. As liquid scintillators feature densities of 0.85 to 0.99 t/m³, the target mass ranges from 45 to 53 kt (Sect. 8.2). Both the organic solvent and the wavelength shifters have to accommodate the fact that the scintillation light must be propagated over a distance of the order of the cylinder radius: PXE (with a possible admixture of dodecane) and pure LAB have been shown to be adequate solvents, providing attenuation lengths of more than 10 m at a wavelength of 430 nm. Sect. 8.1 discusses the macroscopic light transport in more detail. The influence of the optical scattering length of the scintillator on the performance of LENA is highlighted in Sect. 8.6.

The outer shells of the detector are meant to shield the central region from external radioactivity, allowing to use most of the active volume for neutrino detection. The scintillator is contained in a *cylindrical stainless steel tank* of the same height but a larger diameter of 30 m. Currently, two possibilities are considered: Either, the inner volume is subdivided by a cylindrical nylon vessel like the one in BOREXINO which contains the liquid scintillator. The outer shell of 2 m thickness is filled with an inactive buffer liquid. This liquid must feature a very similar density to the scintillator to avoid buoyancy forces. As can be observed in BOREXINO, such a membrane carries a certain risk of leakage between the two volumes. Alternatively, the encapsulation of each individual photomultiplier could incorporate an inactive buffer volume in front of the photocathode as well as a light concentrator. This would allow to fill the whole steel tank with scintillator, but might also give need for a high trigger threshold to limit the rate of low-light background events generated by surface radioactivity. The consequence would be a loss in sensitivity to low energy events.

The planned optical coverage of the detector walls of 30 % requires 13 500 *photomultipliers (PMs)* of the SUPER-KAMIOKANDE type, featuring a photocathode diameter of 20 inch. A design including the equipment of the PMs with reflective light-concentrators (Sect. 3.2) might be used to either reduce the number of channels or allow for smaller PMs. The influence of the light cones on the detector performance has still to be studied in MC simulations. Combinations of small and large photomultipliers might allow to widen the dynamic energy range of the detector that has to cope with sub-MeV neutrino events as well as GeV proton decay signals. Also the installation of the PMs is an important question: Similar to SUPER-KAMIOKANDE, the PMs could be mounted to a narrow scaffolding in front of the cylinder walls. In this case, the necessary cabling for high-voltage supply and signal readout runs behind the PMs inside the tank. A further option is the direct attachment of high-voltage supply, voltage divider, and signal digitizers to the PM base, superseding the high-voltage cabling and probably improving signal transmission fidelity. Corresponding studies are in preparation.

The interspace between the detector tank and the surrounding cavern walls will be filled by a *water buffer*. This has several advantages: It provides, depending on the relative size of detector and cavern, considerable shielding from external radioactivity and fast neutrons. Similar to BOREXINO, it could be fashioned as an active Čerenkov veto for cosmic muons crossing the water volume, which would imply the installation of about 1500 additional PMs on the outer tank wall. It also simplifies construction as the pressure of water on the outside of the tank walls compensates the forces generated by the liquid-scintillator on the inside.

The water veto could be extended above the steel tank to provide the necessary veto for cosmic muons entering the detector from above. Alternatively, layers of *plastic*

scintillator panels could be placed on top, covering the scintillator tank and part of the water veto. In a deep mine most of the cosmic muon flux is vertical (Sect. 2.3.2): A dense instrumentation on top of the detector would provide high detection efficiency and precise muon tracking, optimizing background rejection.

Shape and lining of the *cavern* walls as well as the cavern depth are dependent on the detector site and investigated in the European LAGUNA site study (Sect. 7.2.3). In Fig. 7.2, the cavern walls are curved, the preferred solution to resist the horizontal rock stresses in the bedrock of Pyhäsalmi. Due to the different geological circumstances, straight cavern walls covered in a relatively thick layer of concrete are the most likely solution for Fréjus. In any case, a minimum width of 2 m water buffer is set as a design benchmark to provide the necessary shielding from fast neutrons.

7.2.2 Background Levels

The default scenario for LENA assumes the replication of the radiopurity conditions achieved in the BOREXINO experiment in 2007. The energy threshold of LENA will strongly depend on the amount of radioactive impurities contaminating the scintillator and the surrounding materials. The strongest bound of about 0.5 counts per day and ton is set by the background requirements of solar neutrino detection, corresponding to a concentration of 10^{-18} g/g of natural ^{238}U and ^{232}Th in the scintillator. The search for geoneutrinos as well as reactor neutrino experiments implies a limit on the background rate of αn -reactions on ^{13}C and therewith the content of α -emitters like ^{210}Po : Scaling from KAMLAND data, a ^{210}Po α -decay rate of about 2×10^3 per day and ton (10^{-22} g/g) would be sufficient to reach a signal-to-background ratio of 1:1 for geoneutrino detection (Sect. 1.2.4) [25]. The initial background rates in BOREXINO were lower than these values.

If the radiopurity level of BOREXINO is reached in LENA, cosmogenic radionuclides and neutrons are the dominant background source for the majority of the physics objectives. The deeper the detector cavern, the lower will be the muon flux and therewith the rate of neutron production and spallation processes (Sect. 2.3). Cost and technical feasibility of the cavern construction currently seem to dictate a compromise depth of 1 400 m, corresponding to about 4 000 meters water equivalent (mwe) of shielding and a muon rate of 0.07 Hz in the detector. Long-lived cosmogenic nuclei pose the most serious background: ^{11}C β decays are the main background for solar *CNO/pep* ν detection (Sect. 2.3.3). Scaling from BOREXINO data, a signal-to-background ratio of 1:5 is expected at 4 000 mwe. Comparably important is the influence of short-lived βn -emitters on the $\bar{\nu}_e$ detection. A time veto of 2 seconds after each muon would exclude $\sim 10\%$ of the detector life-time from analysis. In this context, especially ^9Li is a background for the diffuse SN neutrino background (DSNB) detection presented in Chap. 9. The depth-dependence of the fast neutron background also plays a role for $\bar{\nu}_e$ detection; however, the increase in production rate at lower depth can be compensated by enforcing the external water shielding.

7.2.3 The LAGUNA Detector Site Study

The LAGUNA (Large Apparatus for Grand Unification and Neutrino Astrophysics) collaboration represents the European effort towards a very large-volume low-energy neu-

trino and proton decay detector. Apart from LENA, a next-generation water-Čerenkov detector of 500 kt detector mass (MEMPHYS) and a liquid Argon time projection chamber (TPC) of 100 kt (GLACIER) are discussed inside this framework [132]. While the detection techniques differ, the physics objectives are closely related, as well as many of the problems in the construction and operation of a large-volume detector. LAGUNA encompasses about a hundred scientists and engineers from more than twenty different scientific institutes, underground and tank construction companies. The head offices are distributed on eleven European countries, including the LENA group at the TU München. Currently, the main item of the collaborative activities is the identification of an optimal site for an underground laboratory able to host one of the large-volume detectors. This study has been funded by the European Union and proceeds until 2010.

The detector locations discussed in this framework encompass six already existing sites: the Canfranc laboratory in Spain, the Slanic mine in Rumania, and the Boulby mine in Great Britain are presently not deep enough to house the LENA detector¹. The remaining three sites are presented below. A final decision on the site is not foreseen before the end of 2010.

- **CUPP:** The Center for Underground Physics in Pyhäsalmi (Finland) is connected to the local copper and nickel mine. Mining shafts stretch as deep as 1 400 m (4 000 mwe). The termination of mining activities is not expected before 2017. The excavation of a large underground laboratory attached to the deepest level could be started while the mine is still operative. Rock conditions are favorable even though the large stresses in the rock dictate an egg-shaped and also horizontally oval cavern. The large distance to central European nuclear power plants (NPPs) favours the detection of geoneutrinos and the DSNB.
- **LSM:** The Laboratoire Souterraine de Modane (France) is located in the French-Italian Alps. The present laboratory is connected to a highway tunnel passing through the Fréjus mountain. The effective shielding corresponds to about 4 000 mwe. The rock quality is worse than in Finland and demands a considerable amount of concrete lining. On the other hand, the lower rock stresses allow a strictly cylindrical cavern shape. The reactor neutrino background is large, as several French NPPs are located at a distance of merely 100 km.
- **Sunlab:** The Sieroszowice Underground Laboratory in the vicinity of Wrocław (Poland), around 100 km from the Polish-German border. While the original idea was to integrate an underground laboratory in the inactive shafts of a salt mine in 950 m depth, more recently an investigation of a deeper laboratory in the hard anhydrite rock below the salt body has begun. A location at a depth corresponding to 3 600 mwe has been identified. However, the thickness of the rock layer allows only for a horizontal version of LENA. Also shafts accessing this depth would have to be built before start of the cavern excavation.

¹There are efforts on-going at Boulby mine to evaluate the possibility for a detector cavern in more than 1 300 m depth.

Chapter 8

Scattering Length Experiment

The optical transparency of the scintillator solvent to the scintillation light is one of the key parameters of a large-volume detector. Absorption processes will attenuate the light signal as not all photons generated by an event in the bulk of the detector will reach the photomultipliers. Light scattering will redirect the propagation direction of photons and effectively lengthen their trajectory, thereby smearing both arrival time and hit pattern at the phototubes. The less photons undergo these processes, the better in the end energy, time, and spacial resolution of a detector will be. For LENA, being roughly fifty times the size of the largest running liquid-scintillator detector KamLAND [133], large-scale transparency therefore gains a vital importance.

While some of the optical properties of a given solvent can in principle be calculated, precise knowledge can only be obtained by laboratory experiments. Sect. 8.1 describes attenuation and scattering lengths as the central values quantifying light propagation in a scintillator and establishes the connection to the underlying microscopic processes. While the attenuation length of different scintillator samples has been measured to quite high accuracy in the past [133, 134, 80], for many of the common solvents the scattering length is unknown. Therefore, a laboratory-scale experiment was designed in course of this thesis to allow the characterization of the scintillator candidates for LENA. Scattering processes were investigated as a function of the wavelength of the incident light, of the scattering angle and of the polarization of the scattered light. The investigated organic solvents are presented in Sect. 8.2. In the following, Sect. 8.3 to 8.5 describe the setup of the experiment, the performed analysis, and uncertainties introduced by background and used materials. Sect. 8.6 evaluates the resulting scattering lengths of the measured samples, and discusses the obtained values in the more general context of other scintillation parameters and the impact on the LENA detector.

8.1 Light Propagation in a Medium

On macroscopic scales, both the impact of light absorption and of light scattering can be quantified by the absorption length ℓ_A and the scattering length ℓ_S of a medium. Both lengths are defined assuming a parallel light beam of N_0 photons that has travelled a certain distance x from its origin. On any infinitesimally short piece of its way dx , a constant fraction γ of the number of photons $N(x)$ at this point is either absorbed or

scattered. This leads to a differential equation for the loss in intensity:

$$dN = -\gamma N(x) dx. \tag{8.1}$$

The equation is solved by an exponential decay function for $N(x)$,

$$N(x) = N_0 e^{-\gamma x} = N_0 e^{-x/\ell}. \tag{8.2}$$

The optical length ℓ is therefore the distance light of the initial photon number N_0 has to travel before its intensity drops to $1/e$.

Light propagating through a medium, in this case the liquid scintillator, is attenuated by several effects, which will be described later in this section. In the simplifying approximation of a one-dimensional system, all these effects can be combined to a common attenuation length L . Assuming γ to be the sum of several γ_i all representing a percentage of light loss due to a certain process, Eq. (8.2) can be extended to:

$$N(x) = N_0 e^{-\sum_i \gamma_i x} = N_0 e^{-\sum_i (x/\ell_i)} = N_0 e^{-x/L}. \tag{8.3}$$

The inverse of L can be obtained by summing the inverse values of the individual optical lengths ℓ_i ,

$$\frac{1}{L} = \sum_i \frac{1}{\ell_i}. \tag{8.4}$$

The connection of ℓ to microscopic processes can be made by assuming dN to be due to interaction of light with the molecules in the medium, $dN = -n\sigma N(x) dx$, where n is the number density of interaction centers and σ the interaction cross section. From Eq. (8.2) follows

$$\ell = \frac{1}{n\sigma} = \frac{\mathcal{M}}{N_A \rho \sigma}, \tag{8.5}$$

where \mathcal{M} is the molecular weight, N_A the Avogadro constant, and ρ the specific gravity.

In a three-dimensional scintillator detector, several processes affect the transparency of the liquid. Only absorption processes lead to an instant loss of light intensity. If the photons are reemitted, or merely scattered off the solvent molecules or suspended particles, the trajectory changes, but the light may still reach the phototubes. In the following, a short overview of the possible photon interactions is given. They can be classified according to the resulting angular dependence of the scattered light intensity: The isotropic absorption-reemission processes contribute to ℓ_{is} , while the anisotropic Rayleigh scattering adds to ℓ_{an} . Mie scattering can be assumed to contribute to both lengths. The nomenclature of all the optical lengths used in this chapter is shown in Tab. 8.1.

8.1.1 Absorption/Re-Emission

In all the investigated samples, light absorption by the solvent molecules themselves plays a negligible role: The dissolved fluor (Sect. 8.2) shifts the scintillation light to longer wavelength, far above the molecular absorption bands. However, due to the

Abbr.	Optical Length
L	Attenuation Length
ℓ_A	Absorption Length
ℓ_S	Scattering Length
ℓ_{are}	Absorption/Re-Emission Length
ℓ_{ray}	Rayleigh Scattering Length
ℓ_{mie}	Mie Scattering Length
ℓ_{an}	Anisotropic Scattering Length
ℓ_{is}	Isotropic Scattering Length

Table 8.1: Abbreviations used for the optical lengths.

chemical manufacturing process no solvent is completely pure; small contaminations with other organic molecules are unavoidable. The foreign molecules possibly feature absorption bands at the wavelength of the shifted scintillation light. The actual impact on light propagation depends on the molecular concentration and cross section. Alternatively, also fluors and suspended particles might feature absorption at the considered wavelength and add to the effect.

The absorption of light by a molecule leads to an excitation of its electronic shell. From the point of view of a scintillation detector, the deexcitation has two possible outcomes: either the light is re-emitted at a wavelength where the phototubes are still sensitive; or the energy is converted into a non-detectable form (internal heat, infrared light etc.). In the first case, the propagation direction of the light changes randomly, as the re-emission is both isotropic and unpolarized. Reemission processes can therefore be interpreted as isotropic scattering; ℓ_{are} contributes to ℓ_{is} .

8.1.2 Rayleigh Scattering

The scattering of light on bound electrons is named after Lord Rayleigh III [135, 136]. In a classic approach, the bound electron is treated as an oscillator which is excited by the incident electromagnetic wave. The total Rayleigh cross section σ_{ray} can be written as:

$$\sigma_{\text{ray}}(\lambda, \lambda_0) = \frac{8\pi}{3} \sigma_{\text{tho}} \left(\frac{\lambda_0}{\lambda} \right)^4 = \frac{8\pi}{3} r_e^2 \left(\frac{\lambda_0}{\lambda} \right)^4, \quad (8.6)$$

where $r_e = e^2/4\pi\epsilon_0 m_e c^2 = 2.9 \text{ fm}$ is the classic electron radius [136]. Different to the Thompson cross section σ_{tho} that describes the scattering of light on free electrons [136], σ_{ray} depends on two wavelengths: the one of the incident light λ , and the one corresponding to the resonance wavelength of the molecular oscillator λ_0 . The normalisation factor $8\pi/3$ is due to the angular dependence of the scattered light.

If the incident light is polarized linearly, the bound electrons are forced to oscillate in a direction parallel to the electric field vector and to each other. The scattered light will therefore feature characteristics of dipole radiation: perpendicular to the oscillation direction, the intensity is at a maximum, while it will be fully suppressed along the dipole axis. In the case of unpolarized light, the electrons oscillate no longer all in the same direction. Corresponding to the electric field vector of the light, the dipole axes are still

aligned to a plane perpendicular to the direction of light propagation. Consequently, on average only half of the dipoles add to the scattered intensity under a scattering angle of $\theta = 90^\circ$ perpendicular to the incident light, while all of them evenly contribute in direction to the beam at $\theta = 0^\circ, 180^\circ$. The resulting differential cross section is

$$\left(\frac{d\sigma}{d\Omega}\right)_{\text{ray}} = r_e^2 \left(\frac{\lambda_0}{\lambda}\right)^4 f(\theta) = r_e^2 \left(\frac{\lambda_0}{\lambda}\right)^4 \left(\frac{1 + \cos^2 \theta}{2}\right), \quad (8.7)$$

where $f(\theta) = \frac{1}{2}(1 + \cos^2 \theta)$ describes the angular dependence [136]. Rayleigh scattering is therefore anisotropic. Despite being derived from a classic picture, Eq. (8.7) is still valid in a correct quantum mechanical treatment of the problem [136].

Rayleigh scattering is an intrinsic property of the solvent molecules of a scintillator and represents even in an ideally pure liquid a natural limit to light propagation. As will be shown in Sect. 8.2, Eq. (8.6) can be used to predict the Rayleigh scattering lengths ℓ_{ray} of the investigated solvents.

8.1.3 Mie Scattering

The Mie theory describes the scattering of light on microscopic but spatially extended particles in dependence on both the wavelength λ and the diameter of the scattering center d [137, 138]. Both amplitude and differential cross-section strongly depend on the ratio of these two values. In the case of a solvent, Mie scattering describes the effect of microscopic foreign particles suspended in the liquid.

The Henyey-Greenstein phase function P_{HG} is often used as an approximation to the Mie differential cross section [139]. P_{HG} can be written as

$$P_{\text{HG}}(\theta) = \frac{1 - g^2}{(1 + g^2 - 2g \cos \theta)^{3/2}}. \quad (8.8)$$

The function describes the deviation from the Rayleigh differential cross section as denoted in Eq. (8.7). θ is the scattering angle. The asymmetry parameter $g(\lambda/d)$ describes the degree of this deformation: While $g = 0$ states no deviation, $g = +1$ corresponds to maximum forward scattering. This approximation holds in the case of dielectric particles, where Mie scattering shows the same polarization as Rayleigh scattering and adds therefore the anisotropic scattering length ℓ_{an} . For metal particles, however, the polarization is less prominent [137].

For the concerns of the laboratory experiment, it is instructive to distinguish three regimes of λ/d (wavelength over particle diameter):

- $d \ll \lambda$: In this case, the deviation from Rayleigh scattering is small, and it is impossible to distinguish Mie from actual Rayleigh scattering. However, no severe error is done by including the Mie contribution in the anisotropic scattering length ℓ_{an} . Moreover, a comparison to the Rayleigh scattering length ℓ_{ray} calculated by Eq. (8.6) can be used to estimate the Mie contribution.
- $d \approx \lambda$: The closer d is to λ , the more prominent becomes the excess of forward over backward scattering amplitude. As the experiment measures the scattered intensity at angles both larger and smaller 90° , it is in principle possible to discover such contributions if their amplitudes are large enough. However, without further

information on the size of the particles it is impossible to correct the scattering length for the asymmetric effects.

- $d \gg \lambda$: For large particles, the enhanced forward-scattering cross section becomes very prominent. While it is not possible to determine such a contribution in the experiment, the relevance for the scattering length will be small, as the relatively large particles of the order of micrometers can be filtered from the liquid scintillator in the final experiment. Moreover, the forward focussing of the scattered intensity increases with the size of the scatter centers, smearing out the difference between Mie scattering and linear light propagation.

The sensitivity of the experiment on Mie scattering is limited. However, only particles the size of the wavelength would cause a severe problem in the determination of an effective scattering length including Mie scattering partly in ℓ_{is} and partly in ℓ_{an} . The presence of such particles is in principle noticeable due to an increase of the forward scattering amplitude.

8.2 Investigated Scintillators

The solvents considered for use in the LENA detector have to fulfill a number of requirements concerning transparency, light yield, radiopurity and handling safety. At the moment, there are three scintillator solvents under consideration: phenyl-*o*-xylylene (PXE), linear alkylbenzene (LAB), and a 1:4 mixture of PXE and dodecane (C12). For the wavelength shifter, the solute, either a combination of PPO and bisMSB or the use of PMP is being discussed. The following section will describe both the solvents and solutes, summarizing their already known parameters.

In addition, three further samples have been investigated that will be described in this section. Deionized water (H_2O) is used as a background standard for the whole experiment. Cyclohexane (CH) is a solvent often used in spectroscopy and therefore well described in the literature [140, 141, 142]. As it is available at high purity and therefore high transparency, it is well fit to serve as a standard for optical measurements. Pseudocumene (PC) is well known as scintillator solvent as it used in the BOREXINO detector [134]. These samples were tested along with the solvent candidates in the setup described in Sect. 8.3. The results have been used to cross-check with the corresponding literature values and guarantee the validity of the experimental method.

8.2.1 Solvents

The parameters relevant for the solvents are presented in Tab. 8.2, the molecular structure is shown in Fig. 8.1. Manufacturers, product names and Chemical Abstracts Service Numbers (CAS#) are cited in Tab. 8.3. The following section discusses the most prominent features of each solvent to give an impression of its advantages and drawbacks.

- **PXE** has been first used as scintillator solvent in the CTF-II phase of the BOREXINO R&D [80]. The relatively high density maximizes both target material and self-shielding of the liquid for a fixed volume. Moreover, it allows to use water as a buffer liquid, as buoyancy forces are minimized. The first fluorescence decay component is very fast [126]. On the other hand, its initial optical transparency is

Solvent	PXE	LAB	C12	PC	CH	H ₂ O
<i>Physical and Chemical Data</i> [143, 144, 145, 146, 147]						
Chemical Formula	C ₁₆ H ₁₈	C ₁₈ H ₃₀	C ₁₂ H ₂₆	C ₉ H ₁₂	C ₆ H ₁₂	H ₂ O
Molecular Weight \mathcal{M} [g/mol]	210	241	170	120	84	18
Specific Gravity ρ [g/cm ³]	0.99	0.86	0.75	0.88	0.78	1.00
Viscosity [cps]		4.2	1.3		1.0	1.0
Flash Point [°C]	167	140	83	48	-18	
molecular density n [10 ²⁷ /m ³]	2.8	2.2	2.7	4.4	5.5	33.5
free protons [10 ²⁸ /m ³]	4.7	6.6	7.0	5.3	6.6	6.7
Carbon nuclei [10 ²⁸ /m ³]	4.2	4.0	3.2	4.0	3.3	
total p/e ⁻ [10 ²⁹ /m ³]	3.2	3.0	2.6	2.9	2.6	3.4
<i>Hazardous Materials Identification System (HMIS) Rating</i> [143, 144, 145, 146, 147]						
Health	1	1	1	2	1	0
Flammability	1	1	0	2	3	0
Reactivity	0	0	0	1	0	0
<i>Optical Properties (n, L, ℓ_{ray} at 430 nm)</i> [80, 140, 141, 142, 148, 107, 126, 149, 150]						
Refractive Index n	1.57	1.49	1.42	1.50	1.43	1.33
Relative Light Yield y	1.	1.	<0.4	$\leq 1.$		
Fast Decay Constant τ_1 [ns]	2.63	5.21		3.57		
Absorption Maximum [nm]	270	260		265	<120	
Emission Maximum [nm]	290	283		290		
Attenuation Length L [m]	12	~ 20	>12	8	44	90
Rayleigh Scat. Length ℓ_{ray} [m]	32	45	(37)	21	44	90

Table 8.2: Overview of the solvent parameters of PXE, LAB, dodecane (C12), PC, cyclohexane (CH) and water (H₂O). The information on physical parameters, HMIS rating, and refractive index are cited from material safety and product specification sheets of the producers [143, 144, 145, 146, 147]. The HMIS rating quantifies the danger in handling the liquid (from 0 - safe to 4 - dangerous). The molecular, proton and Carbon densities were computed using this information. The relative light yield is taken from [148, 107], the fast decay constant from [126, 134]. In both cases, an admixture of 2 g/l PPO is assumed. The absorption and emission maxima of PXE and LAB are also from [126], the ones of PC from [151]. The cited L were gathered from various sources: PXE [80], LAB [149], C12 [148], PC [134], and water [150], always assuming the value at 430 nm. ℓ_{ray} is computed using Eq. (8.5) and the absorption maxima for PXE, LAB and PC, again at 430 nm. For C12 and CH, the length is derived from measurements at longer wavelength [140, 141, 142]. $L = \ell_{\text{ray}}$ is assumed for CH.

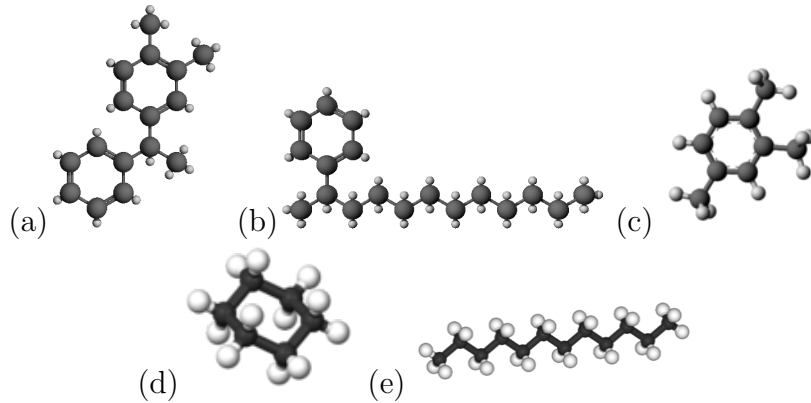


Figure 8.1: Molecular structure of the solvents: (a) PXE, (b) LAB, (c) PC, (d) CH, and (e) C12. Dark spheres symbolize Carbon, light ones Hydrogen atoms.

relatively poor. Al_2O_3 column chromatography is needed to reach an attenuation length of 10 to 12 m [80]. The PXE used in the experiment is of relatively low purity [143]. It has been provided by Dixie¹.

- **LAB** is a basic ingredient of many detergents. Its qualities as a solvent for large-scale liquid-scintillator detectors was discovered during the R&D phase of the SNO+ experiment [149]. It features a high light yield comparable to the one of PXE [107], and it is in addition intrinsically very transparent. On the other hand, the signal decay is quite slow, which will possibly reduce time and spacial resolution of the final detector. It is very favorable from an economic point of view, as its price is $\sim 1 \text{ €/l}$. Three different brands of LAB produced by Petresa² are tested in the experiment: While the products PETRALAB P500 and P550 originate from a Spanish distillation plant, the sample 550Q was produced in Quebec. The numbers indicate small differences in the mean molecular weight that depends on the length of the Carbon chain.
- **C12** and other n-decanes can be used to dilute organic solvents down in liquid-scintillator experiments. As these molecules feature no benzene rings, they feature no absorption bands in the near UV. Some residual scintillation has been observed in experiments that is attributed to ionization processes. The most prominent example is the KAMLAND experiment where the scintillator consists of 20 % PC and 80 % n-decanes. Addition of C12 increases both the transparency and number of free protons per unit volume of the solvent. The C12 used for the investigation is provided by two companies: Fluka³ and Alway Chem⁴. The quoted Rayleigh scattering length can be estimated from measurements of C10 and C15 [142].
- **PC** is the scintillator solvent presently in use in the BOREXINO detector, with 1.5 g/l PPO as wavelength shifter. The light yield is comparatively high, while the optical transparency is relatively poor. Especially the Rayleigh scattering length ℓ_{ray} is rather low. Also the handling of the liquid is not easy, as HMIS

¹Dixie Chemical Co., Houston TX (US).

²Petresa Canada, part of the CEPSA Group, Becancour QC (CDN).

³Fluka Chemical Corp, Milwaukee WI (US), part of Sigma-Aldrich

⁴Alway Chem International Co., Qingdao (CI)

Abbr.	CAS#	Purity	Product	Manufacturer
PXE	6196-95-8	>0.97	POXE	Dixie
LAB P500 LAB P550 LAB 550Q	67774-74-7	0.992	Petrelab 500 Petrelab 550 Petrelab 550 Q	Petresa Cnd
C12 SA C12 AC	112-40-3	≥ 0.98	44020	Fluka Alway Chem
PC	95-63-6	>0.98	814505	Merck
CH	110-82-7	0.9999	102822	Merck Uvasol
PPO	92-71-7	0.99	D210404	Sigma-Aldrich
Bis-MSB	13280-61-0	0.99	222445	Sigma-Aldrich
PMP	60078-97-9	-	-	Merck

Table 8.3: Overview of the CAS numbers, molecular purities, product names and manufacturers of the used solvents and solutes.

Solute	PPO	bisMSB	PMP
Chemical Formula	$C_{15}H_{11}NO$	$C_{24}H_{22}$	$C_{18}H_{20}N_2$
Absorption Maximum [nm]	303	345	294
Emission Maximum [nm]	365	420	415

Table 8.4: Overview of the solute parameters of the fluors PPO, bisMSB, and PMP. Chemical formulae are taken from specification sheets [153, 154] and [155]. Mean values of light absorption and emission bands have been retrieved from [126].

ratings and flammability are high. PC has been used as a known standard in the measurements described below [134]. The manufacturer is Merck⁵.

- **CH** is a primary solvent for UV-VIS spectroscopy. Its optical parameters are well-known at long wavelengths and can be extrapolated to 430 nm [140, 141, 142]. The relatively high toxicity and flammability makes careful handling necessary. The sample from Sigma-Aldrich⁶ is of high purity (99.99%), so only Rayleigh scattering off the molecules contributes to the scattering length L . Similar to PC, it is used to calibrate the measurements.
- **H₂O** is used for background measurements in the experiment (Sect. 8.5). For this end, deionized water has been retrieved from [152]. The optical properties of water have been investigated in large Cherenkov detectors as the Super-Kamiokande experiment [150].

8.2.2 Wavelength Shifters

Three wavelength shifters (fluors) are currently discussed for a usage in LENA: 2,5-diphenyl-oxazole (PPO) as well as 1-phenyl-3-mesityl-2-pyrazoline (PMP) match due

⁵Merck KGaA, Darmstadt (D)

⁶Sigma-Aldrich Chemie GmbH, Munich (D)

to their absorption wavelength of ~ 300 nm the emission bands of PXE, LAB, and PC. However, as the scintillation light must be shifted to ~ 430 nm, PPO has to be combined with a secondary wavelength shifter, 1,4-bis-(*o*-methylstyryl)-benzene (bisMSB) to achieve the necessary gap between the emission band of the solute and the absorption band of the solvent. The exact wavelengths characterizing the fluors are reported in Tab. 8.4, product names, providers and purity are listed in the lower half of Tab. 8.3.

- **PPO and bisMSB:** PPO has been used as a fluor both in the CHOOZ [28] and, more recently, the BOREXINO [134, 12] experiment. It is comparatively easy to handle as its solubility is quite high, allowing concentrations of ≥ 100 g/ ℓ . Solutes have proven to carry a relatively high amount of radioimpurities; giving special attention to the purging of such a “master solution” offers an efficient way of purification. BisMSB has to be added in small quantities to retrieve a sufficient Stoke’s shift. However, there is a certain amount of re-absorption of the long-wave photons as there is an overlap of its emission and absorption bands.
- **PMP** was the wavelength-shifter added to the scintillator of the KARMEN experiment [156]. Its most prominent feature is the large Stoke’s shift, that allows a transfer of the scintillation light to the blue part of the spectrum in a single step. However, there is currently no company producing PMP. The samples that were tested recently for their fluorescence decay times and emission spectra [126] come from the stock of the KARMEN experiment.

8.3 Experimental Setup

The aim of the laboratory experiment is two-fold: On one hand, it is designed to provide reliable values for the scattering length of the above described scintillators. These values will enter into the Monte Carlo simulations which aim at the determination of the detector performance of LENA. More importantly, they will be a selection criterium for the finally used scintillator. On the other hand, the experiment is meant to disentangle the various contributions to scattering in the scintillator sample: the experiment is sensitive to the angular dependence and polarization of the scattered photons as a function of the incident wavelength.

8.3.1 General Layout

The basic concept of the experiment is to send a collimated light beam of a well-defined wavelength through a sample of liquid scintillator, contained in a glass vessel. The number of photons in the beam η_B is monitored by a photomultiplier P_B . A second multiplier P_S can be set off-beam at a number of different scattering angles θ and registers the photon number η_S scattered by the scintillator. A set of collimators in front of P_S allows to calculate the solid angle the PM is sensitive to. An additional polarization filter allows to determine to which extent the scattered light is polarized, selecting the linear polarization component p . The result of each measurement is the quotient $q = \eta_S/\eta_B$ of the measured photon numbers. Fig. 8.2 shows on the left the incident light beam, the sample, and the off-beam phototube P_S collecting the scattered light. On the right hand side, a top view of the sample and the rotatable platform is depicted.

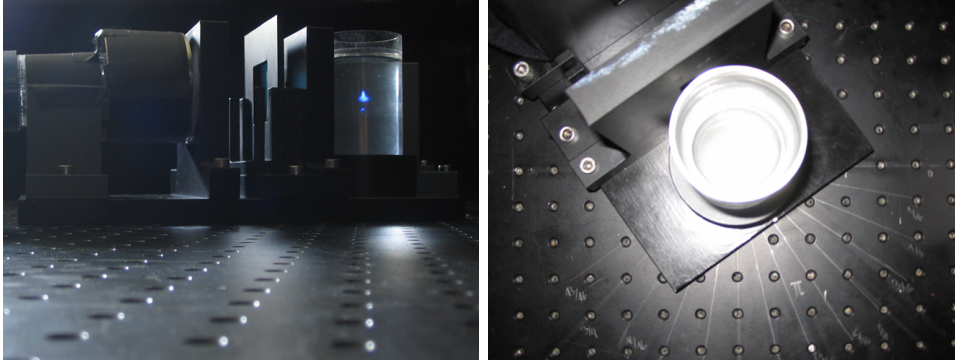


Figure 8.2: Photographs of the experimental setup for the scattering length measurements.

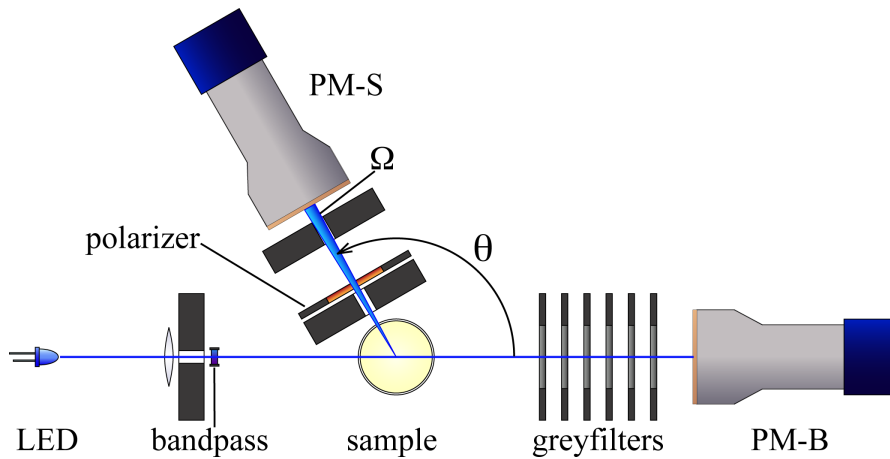


Figure 8.3: Sketch of the experimental setup for the scattering length measurements.

8.3.2 Optical Components

Fig. 8.3 shows the experimental setup in more detail. It is mounted on an optical bench (100×20 cm) of blackened PVC, with threaded holes along the longer sides that allow to mount the optical modules. The setup rests on a metal laboratory bench that is in turn fully contained in a light-tight box. The inside walls are covered with black felt in order to protect the phototubes from external light.

As beam source, the light of an LED emitting a relatively broad wavelength spectrum centered around 430 nm⁷ (Fig. 8.6) is collimated by a collective lens of 20 cm focal length, followed by a circular aperture of ~5 mm diameter. The focussing is good enough to inhibit a significant widening of the beam over the whole distance of 70 cm to the photomultiplier P_B⁸ that is monitoring the beam intensity.

Several objects are positioned along the beam. The first one is a narrow-bandpass filter⁹ limiting the beam spectrum to ~10 nm around the central wavelength of the filter. Three filters at 415, 430, and 442 nm wavelength are used, covering the main emission region of the wavelength shifters described in Sect. 8.2. A spectroscopic measurement of the emission spectrum of the LED and the wavelength bands selected by the filters

⁷LED430-06U, Roithner Lasertechnik, Vienna (A)

⁸Model 9305KB, Electron Tubes Ltd., Rockaway (NJ), USA

⁹Narrow-bandpass interference filter, Edmund Optics Germany, Karlsruhe

is depicted in Fig. 8.6.

The second is the scintillator sample, contained in a cylindrical beaker glass. The beam is entering and leaving the vessel perpendicularly to the surface. Following a series of trials with custom-made quartz glasses, an everyday juice glass proves to be the best choice in terms of optical transparency and surface evenness. The set of measurements reported here have been acquired using two glasses of 6 cm diameter, and ~ 15 cm in height; the repeated cleaning of the surfaces wetted by organic liquids using water, isopropanol, and acetone, visibly degrades the optical qualities of the glass and made a replacement necessary. The beaker is covered by a glass cap in order to minimize the contact and dissolution of aerial oxygen into the sample and to impede dust from falling into the sample.

In front of the beam-monitoring phototube P_B , an array of six optical greyfilters¹⁰ reduces the light intensity to a level compatible to the high sensitivity of the light detector. The nominal total transmission of the used filters is supposed to be $T_{\text{nom}} = 0.5^2 \times 0.25 \times 0.1^3 = 1.25 \cdot 10^{-4}$. The actual value is however considerably lower in the investigated wavelength region, and decreasing to smaller wavelengths. It had to be measured separately for each filter. Details are discussed in Sect. 8.5.

The effective aperture of filters and P_B is quite large: the diameter of the photocathode is 3 inch. The filters are mounted on black plastic frames with an quadratic opening of about 5 cm edge length. In this way, the intensity measurement is not affected by small changes in the geometry that might lead to a deflection of the beam from its ideal line. Attached to the mounting of the last filter, a piece of black felt is covering P_B in order to minimize the effects of stray light. A cylinder of diamagnetic μ -metal foil is covering the distance of acceleration between the photocathode and the first dynode, minimizing the effects of external magnetic fields on the gain of the PM.

The scintillator sample as well as the second photomultiplier P_S are mounted on a rotatable platform. The rotation axis is along the axis of the beaker glass and crosses the light beam. Five scattering angles are accessible: 60° , 75° , 90° , 105° , and 120° ; the angle can be fixated by a screw passing through threaded holes in the optical bench and the rotatable platform.

P_S is identical in construction to P_B . Its field of vision is narrowed and thereby well defined by a pair of rectangular apertures, the front one of 2 cm in height and 1 cm in width, the second of the same width and 6 cm height. The maximum acceptance angles in the plane of the beam and perpendicular to it, $\theta_{\text{max}} \approx 4^\circ$ and $\varphi_{\text{max}} \approx 10^\circ$ are chosen in order to reach a large sensitivity on the θ -dependence of the scattered intensity while maximizing the amount of registered light by allowing a large span of the intensity-uncorrelated angle φ (Fig. 8.7). Moreover, the forward aperture is shielding the phototube from the diffuse scattering of light that occurs at the entry and exit points of the beam in the beaker glass. Similar to P_B , P_S is covered by black felt and a μ -metal shielding.

To be able to determine the polarization of the scattered light, a linear polarizer is mounted between the two apertures in front of P_S . The selected polarization direction p is either parallel to the bench surface (horizontal, $p = h$) or perpendicular to it (vertical, $p = v$); in this way, the intensity for Rayleigh scattering under all angles is at maximum for one polarizer setting and at minimum for the other one.

¹⁰TechSpec Absorptive Neutral Density Filters, Edmund Optics Germany, Karlsruhe

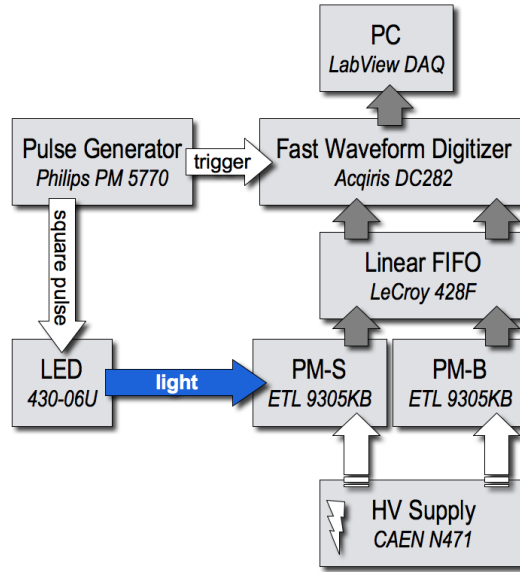


Figure 8.4: Block diagram of the electronics and DAQ chains.

8.3.3 Electronics and DAQ Components

The layout of the electronics and DAQ chains is shown as a block diagram in Fig. 8.4: A pulse generator¹¹ is used both to supply short voltage pulses to the LED and a NIM trigger signal to the DAQ system described below. The LED is operated with square pulses $\sim 25 \mu\text{s}$ in length and $\sim 2\text{V}$ in amplitude.

Both photomultipliers are operated in single-photon mode at a voltage of 1.4 kV , using a high voltage module¹². A voltage divider is directly mounted to the base of the photomultipliers. Both high voltage and signal cables are fed through a light-tight port at the base of the surrounding black box. The signals are passed through a linear FIFO¹³ unit in order to protect the DAQ system from voltage peaks. The DAQ system itself is a combined unit of ADCs and a PC for controlling the DAQ¹⁴; It provides four input channels that are run at a time resolution of 500 ns (so 2 GS/s). The voltage range can be chosen freely from 50 mV to 10 V , the resolution is 10 bit. The reference signal from the pulse generator is connected to a fifth input channel foreseen for external triggering. The time gate of the acquisition is $25\text{ }\mu\text{s}$ wide, with a slight offset of a few tenth of μs relative to the beginning of the LED light pulse to allow a undisturbed sampling of the baseline. The voltage of the LED is chosen in a way that – after passing the filters – between 0.1 and 20 photons per gate are registered by the phototubes. This allows an analysis based on the counting of single photon pulses statistically distributed over a large time span. The number of dark counts of the PMs in the same time is typically 3×10^{-3} and can therefore be neglected in most measurements (Sect. 8.5). The PM pulses feature negative amplitudes and are forwarded to the DAQ system without further amplification. As the exact value of the amplitude itself is not used in the analysis, the input range for the voltage has been chosen to cover $+5\text{ mV}$ to -45 mV ,

¹¹Philips PM 5770, Hamburg (D)

¹²NIM, 2-fold HV power supply, CAEN N471, Viareggio (I)

¹³NIM, Linear Fan-In/Fan-Out, LeCroy 428F, Heidelberg (D)

¹⁴Acqiris DC282 Fast Waveform Digitizer, Agilent Technologies, Santa Clara (US)

which means that many of the PM pulses are in saturation. The positive tolerance is large enough to compensate for fluctuations in the baseline.

The DAQ software is based on LabView¹⁵. It has been customized for simultaneous readout of the two input channels that are used for the acquisition of the PM signals. Most of the basic analysis is performed online: For both channels, the acquired waveforms are scanned for the (negative) single photon pulses distributed over the time gate by searching for the voltage minimum. Every peak identified in this way is counted as one photon. After that, a time gate of 100 ns is blocked around the position of the peak. This avoids recounting of the same photon in the further search. The stop condition for the search loop is reached as soon as the largest deviation from baseline found is lower than a threshold value of 3 mV.

There is a small probability that two photons close enough in time are counted only as one photon due to the recounting veto. To compensate this effect, a correction term has to be introduced: The LEDs were operated with square pulses slightly longer than the gate length to produce an equal distribution of photons over the whole time gate T (with the exception to a few 100 samples in the beginning of the gate to allow for the determination of the baseline offset). Therefore, the chance of two photons being registered in an individual time gate τ is $p = \tau/T \times N(N - 1)$. The correction is rather small, as $\tau/T = 100 \text{ ns} / 25 \text{ } \mu\text{s} = 4 \times 10^{-3}$, but can reach percent level if the number of photons N is of the order of 10.

For each measurement, 50 000 waveforms are acquired for both channels. The resulting measurement duration of 30 min is governed by the maximum trigger rate of the system. For each waveform, the number of registered photons is written to one of the two online histograms that save the photon distributions for both channels. When the acquisition is stopped, the code calculates the mean values and standard deviations of the histograms. The quotient q of the obtained mean photon numbers serves as input parameter for the further analysis.

8.4 Data Analysis

As the determination of the scattering length requires a sequence of steps and the combination of several measurements, a software routine based on C++ and ROOT [110] has been developed, dedicated to this task. The sequence of the individual tasks is shortly outlined in the following; measurement values directly retrieved from experiment will be indicated by small letters, while the "real" values considering all correction terms are written as capital letters.

1. The program screens a master document containing all measured quotients q . $q(\theta, p) = \eta_S/\eta_B$ is the ratio of photon numbers registered by the phototubes P_S and P_B for the scattering angle θ and the polarizer orientation p ¹⁶. All measurements for a certain sample and wavelength are selected. If there is more than one result for a individual combination of θ and p , the values are combined. The systematic uncertainties applying to each individual measurement point are added (Sect. 8.5).

¹⁵National Instruments Germany GmbH, München

¹⁶The orientation of the polarizer is defined relative to the bench surface: for the vertical case $p = v$, and $p = h$ for the horizontal case (Sect. 8.3).

2. The result of a background measurement with water, $q_{\text{bg}}(\theta, p)$, is subtracted from each data point. For this, q_{bg} has to be corrected by a small value q_{w} which is corresponding to the amount of light scattered by the water inside the beaker glass (Sect.8.5). The remaining intensity ratio $q_{\text{rm}}(\theta, p)$ for the sample is

$$q_{\text{rm}} = q - q_{\text{bg}}^* = q - (q_{\text{bg}} - q_{\text{w}}). \quad (8.9)$$

3. Several corrections have to be applied to q_{rm} to obtain a value $Q = N_{\text{S}}/N_0$ which describes the total scattered intensity divided by the initial intensity entering the sample:

- The phototubes P_{B} and P_{S} are not identical in photoefficiency. Therefore, q has to be multiplied with the relative efficiency $\varepsilon = \varepsilon_{\text{B}}/\varepsilon_{\text{S}}$ to correct for this effect.
- The amount of light registered by P_{B} has to be corrected by the transmission coefficients of the six greyfilters, $t_{\text{gf}}(i)$. The actual intensity leaving the sample, N_{B} , has therefore to be divided by the product of all transmission coefficients: $N_{\text{B}} = \eta_{\text{B}}/\prod_i t_{\text{gf}}(i)$.
- To retrieve the incident photon number N_0 , N_{B} has to be corrected for the reflections on the boundary layers air-glass and glass-air[136]:

$$N_0 = N_{\text{B}} \left(1 - \left(\frac{n_1 - n_2}{n_1 + n_2} \right)^2 \right)^{-2} = 1.09 N_{\text{B}} = N_0/\varrho, \quad (8.10)$$

assuming the refractive indices $n_1 = 1$ for air and $n_2 = 1.52$ for glass, respectively. In principle, one should also correct for the boundary layers glass-sample and sample-glass and for the absorption of light in the sample. All these effects are however of the order of 10^{-3} and can be neglected in good approximation (Sect. 8.5).

- The photon number N_{S} (of a given polarization) scattered into the solid angle of P_{S} is attenuated by the polarization-independent residual absorbance of the polarizer t_{pol} . Similar to N_{B} , the intensity $N_{\text{S}} = \eta_{\text{S}}/t_{\text{pol}}$.

Applying all corrections, one obtains

$$q_{\text{cor}} = \underbrace{\frac{\prod_i t_{\text{gf}}(i)}{t_{\text{pol}}}}_T \underbrace{\frac{\varepsilon_{\text{B}}}{\varepsilon_{\text{S}}}}_{\varepsilon} \underbrace{\left(1 - \left(\frac{n_1 - n_2}{n_1 + n_2} \right)^2 \right)^2}_{\varrho} q_{\text{rm}} = T \varepsilon \varrho q_{\text{rm}} \quad (8.11)$$

4. In the quotient q_{cor} , N_{S} is limited to the solid angle left open by the apertures in front of P_{S} . The most feasible way of correlating q_{cor} to a scattering length ℓ is to compare the obtained values to a Monte Carlo simulation of the experiment. GEANT4 [157] has been used to retrieve effective values $\Omega_{\text{is}}(\theta)$ that reflect the amount of light arriving at the photocathode of P_{S} assuming the scattering length ℓ_{MC} to be 1 m (Sect. 8.5). Only isotropic scattering is considered; the angular dependence of anisotropic scattering will be introduced later. The dependence of

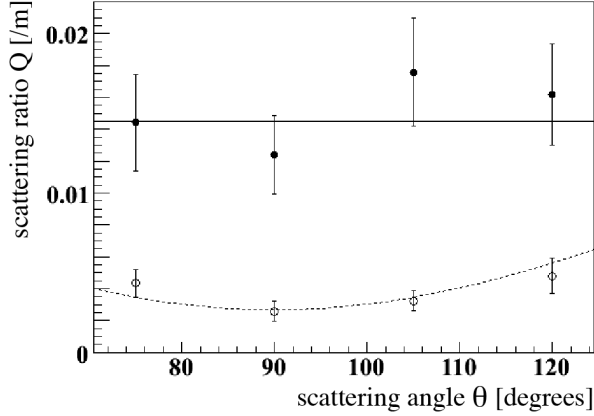


Figure 8.5: Corrected ratio Q in dependence of the scattering angle θ . Filled circles represent vertical, empty horizontal polarization. The two lines correspond to fits to the data points, parameterized according to Eqs. (8.12). The result of the fits is used to compute the scattering lengths (Sec. 8.4).

Ω_{is} on the scattering angle θ is therefore only reflecting the change in the size of the solid angle. By dividing the two values, one obtains the value $Q = q_{\text{cor}}/\Omega_{\text{is}}$ that is independent of the solid angle. Q has already the dimension of an inverse scattering length.

5. In total, eight values are retrieved for $Q(\theta, p)$ due to the four angles used in analysis ($\theta = 75^\circ, 90^\circ, 105^\circ$, and 120°) and the two polarization states p . The values at $\theta = 60^\circ$ are not used as evidence of a geometrical light reflex overlaying the signal was found (Sect. 8.5). As stated in Sect. 8.1, the scattering in the sample can be approximated by two processes: a polarized anisotropic contribution $\mathcal{A}_p(\theta)$ with an intensity distribution following $f_{\text{an}}(\theta) = \frac{1}{2}(1 + \cos^2 \theta)$ (Eq. (8.7)); and an unpolarized and isotropic component $\mathcal{I}_p(\theta)$ that represents mainly absorption-reemission processes with $f_{\text{is}}(\theta) = 1$. Contributions from Mie-scattering following a different angular distribution are for the moment neglected. Due to the different dependence on θ and p , the contributions of the two processes in the sample can be determined by fitting the sum $\mathcal{F}_p(\theta) = \mathcal{A}_p(\theta) + \mathcal{I}_p(\theta)$ to the measured values $Q(\theta, p)$:

$$\begin{aligned}\mathcal{F}_v(\theta) &= \mathcal{A}_v(\theta) + \mathcal{I}_v(\theta) = \frac{1}{2}Q_{\text{an}} + \frac{1}{2}Q_{\text{is}} \\ \mathcal{F}_h(\theta) &= \mathcal{A}_h(\theta) + \mathcal{I}_h(\theta) = \frac{\cos^2 \theta}{2}Q_{\text{an}} + \frac{1}{2}Q_{\text{is}}\end{aligned}\quad (8.12)$$

Q_{an} and Q_{is} are fit parameters and represent the contributions of anisotropic and isotropic scattering summed for both polarization states p .

Fig. 8.5 shows the corrected data points $Q(\theta, p)$ and the fitted curves for the case of C12 (dodecane) and a wavelength of 415 nm. Filled circles correspond to $p = v$, empty ones to $p = h$.

6. The isotropic scattering length ℓ_{is} is the inverse of Q_{is} (Tab. 8.1). As stated in Step 4, Ω and therefore Q is calculated assuming isotropic scattering. The anisotropic

scattering length ℓ_{an} has to be corrected by an additional factor to reflect the difference in the total solid angle due to the θ -dependence $f_{\text{an}}(\theta)$. Therefore,

$$\ell_{\text{is}} = \frac{1}{Q_{\text{is}}}, \quad \ell_{\text{an}} = \frac{4/3}{Q_{\text{an}}}, \quad \frac{1}{\ell_{\text{S}}} = \frac{1}{\ell_{\text{is}}} + \frac{1}{\ell_{\text{an}}}. \quad (8.13)$$

While possible in most cases, for some samples the scattering of the data points is too large to retrieve a fit with a reasonable χ^2 -value. Under these circumstances, Step 5 in the routine is replaced by an alternative analysis using mean values: The difference in the mean vertical ratio $\langle Q_v \rangle$ and the mean horizontal ratio $\langle Q_h \rangle$ is due to anisotropic scattering only. Averaging over the θ -dependence of the polarization components, the ratios of isotropic and anisotropic scattering can be written as:

$$Q_{\text{an}} = \frac{2\langle Q_v \rangle - 2\langle Q_h \rangle}{1 - \langle \cos^2 \theta \rangle}; \quad Q_{\text{is}} = \frac{2\langle Q_h \rangle - 2\langle Q_v \rangle \langle \cos^2 \theta \rangle}{1 - \langle \cos^2 \theta \rangle}$$

The uncertainties of the results obtained in this way are usually larger. The values for the scattering lengths obtained in this way are in good agreement with the results of the fit to the data points, especially if the χ^2 -value of the fit is low. The results are shown in Sect. 8.6.

8.5 Systematic Uncertainties

In the following, the determination of the parameters contributing to the analysis and the corresponding uncertainties is presented. According to their contribution to the final result, they can be divided into two subgroups:

- Uncorrelated uncertainties apply to each single measurement, defined by a sample, an incident wavelength λ , a scattering angle θ , and a chosen polarizer orientation p . In the analysis described in Sect. 8.4, these uncertainties are treated according to the Gaussian error propagation. Their impact is largely reduced by the fit that is performed to combine the results of different angles for one sample.
- Correlated uncertainties affect all values measured for a given sample in the same manner. They are mostly governed by the extent of knowledge to which parameters and performance of the optical components and the photomultipliers are known. In order to consider their contributions correctly, they are reported as a separate value and not included in the fit described in Sect. 8.4.

The items are listed in the following sections in the order of appearance in the analysis, pointing out the kind of their contribution to the final uncertainty. The resulting uncertainties for the scattering length of each sample will be reported in Sect. 8.6 along with the computed scattering lengths.

8.5.1 Measured Intensity Ratio

The measurement of the samples and the background uses the quotient q of the photon number η_{S} scattered into the solid angle of the phototube P_{S} and the photons η_{B} registered by the beam phototube P_{B} . Therefore, q is the result of a relative measurement, and independent of intensity fluctuations of the LED.

It can however be influenced by the absorption of light due to impurities on the beaker glass surface. For all samples, the glass vessel has been carefully prepared by washing and wiping it in several steps using water, isopropanol, and acetone. About 200 ml of each sample are used so that the beaker is filled high enough above the beam to avoid total reflection on the surface of the liquid. However, measurement series in which the glass was rotated around its axis, leaving all other parameters the same, show that the variation in q is larger than the statistical error would suggest. The evaluation of the fluctuations leads to a relative uncertainty $\delta q = 4\%$ (1σ) that has to be applied to each measurement. It adds to the uncorrelated uncertainties.

8.5.2 Background Correction

Several measurements have been performed in order to determine the background ratios q_{bg} : A measurement without the beaker glass in the setup reveals that there is no light scattered or reflected from the surfaces of the optical bench and modules. However, adding the empty glass shows a large increase in counting rate in P_S ; actually, the values are larger than the ones obtained by measuring optically clear liquids as water or cyclohexane. This is not surprising, as due to the additional boundary layer glass-air on the inside of the beaker mantle, the light can be trapped inside the glass by total reflection, leading to an increase in stray light.

To avoid this additional effect, the refractive index of the medium inside the beaker has to be matched to the one of glass, $n_g \simeq 1.52$. At the same time, the scattering length of this medium must be substantially larger than the ones expected for the samples so that the scattering light caused by the glass is not superposed by the one of the medium. Even better, a medium of known scattering length should be used, further reducing the introduced uncertainty.

For the present laboratory experiment, deionized water ($n = 1.33$) is used as background standard. Measurements done in the target of the Super-Kamiokande experiment suggest that the scattering length is $\ell_{w,0} = 88 \pm 12$ m at a light wavelength of $\lambda_0 = 430$ nm [150]. Moreover, Rayleigh scattering is clearly dominant, so the measured scattering ratios q_{bg} are corrected for the ratio

$$q_w(p) = \frac{\Omega_w}{\ell_{w,0}(T\varepsilon\rho)} \left(\frac{\lambda_0}{\lambda}\right)^4 \times \begin{cases} \frac{1}{2} & \text{if } p = v \\ \frac{\cos^2\theta}{2} & \text{if } p = h \end{cases} \quad (8.14)$$

where T , ε , and ρ are the corrections for filter transmission, PM efficiency and surface reflections introduced above. The last two factors represent the wavelength and angular dependence of Rayleigh scattering. For 90° , the correction term $q_w(v)$ is about 1/3 of the measured vertical component of the background $q_{\text{bg}}(v)$.

The use of water as background standard was in the beginning not without concerns: The refractive index of water is not optimally adjusted to the one of the beaker glass, even though near enough to make reflection on the boundary layers a minor issue. Moreover, the Super-Kamiokande value for the scattering length might be misleading, as the deionized water in the laboratory and the large-scale experiment is probably not of the same purity. However, the background values determined in this way can be cross-checked by the measurement results of cyclohexane and PC, which reproduce the expected values rather well (Sect. 8.6). Therefore, only the uncertainty in the back-

ground measurement $\delta q_{\text{bg}} = \delta q$ and the correlated uncertainty given by the scattering length of water ℓ_w are applied.

8.5.3 Photomultiplier-Induced Uncertainties

The relative photo-efficiency of P_B and P_S is necessary to do a correct normalization of the scattered on the transmitted light. This can be achieved by replacing the position of one photomultiplier with the other; in this case, P_B has been replaced with P_S as – due to the larger mean number of photons per waveform – the measurement is less sensitive to dark noise. The ratio of the efficiencies, $\varepsilon = \varepsilon_B/\varepsilon_S$, has been determined to $\varepsilon = 0.69 \pm 0.05$.

The quoted uncertainty is obviously affecting all measured values in correlation. It is caused by the dependence of the PM efficiency on the location and orientation of a photomultiplier. Small variations in gain are due to different external magnetic fields and their influence on the photoelectron gain. A measurement series has been performed in which the whole setup has been rotated around the beaker glass axis in steps of 15° . A correlation with the direction of the Earth magnetic field could have been used to correlate the efficiency with the scattering angle θ . As no functionality can be found, local magnetic fields are dominating. The standard deviation of the measured efficiencies $\delta\varepsilon = 7\%$ adds to the uncorrelated uncertainties.

As both phototubes are of the same type series and operate at comparable voltage, the probability for the occurrence of pre- and afterpulses can be assumed to be roughly the same in both cases. Even in the case of a deviation, these effects would add to the effective photo efficiency and be included in $\delta\varepsilon$.

The dark noise of both phototubes has been monitored from time to time by deactivating the LED and measuring the remaining signal rate in the phototubes over the regular number of 50 000 samples. The result is comparatively low, the average rate is 3×10^{-3} per waveform, corresponding to 120 Hz. For most measurements, this value is negligibly small. However, there is evidence of an increase in rate after periods in which the black box has been opened. The exposure of the switched-off phototubes to direct light is able to temporarily increase the dark rate by a factor 4-5. While not as likely to happen during normal data taking where both phototubes are covered by felt, this effect has been clearly visible during the measurements of filter transmission described below.

8.5.4 Reflective Correction

For the calculation of the reflective correction term ρ , the Fresnel formula for a vertically incident light beam is used:

$$r = \left(\frac{n_1 - n_2}{n_1 + n_2} \right)^2, \quad (8.15)$$

where r is the backscattered intensity and $n_{1,2}$ are the refractive indices of the materials on both sides of the boundary layer [136]. Three effects are conceivable to cause deviations from the value obtained by Eq. (8.15):

- The boundary layer glass-sample is neglected in the calculation of ρ . As r increases with the difference between the refractive indices n_g and n_s , the transition of glass

to water would cause the maximum effect, $r_{\text{gs}} < 5 \times 10^{-3}$. As this value is one order of magnitude smaller than r_{ag} (see below), it can be neglected.

- The exact refraction index of the used beaker glass is unknown. However, a typical value for crown glass in the blue-violet regime is $n_{\text{g}} = 1.52 \pm 0.01$ [158]. The resulting ratio of reflected light for the boundary air-glass is $r_{\text{ag}} = (4.25 \pm 0.13) \%$. However, the effect on the correction term $\rho = (1 - r)^2$ is small, corresponding to a relative uncertainty of $\delta\rho = 0.3 \%$.
- Eq. (8.15) holds only if the incident beam is perpendicular to the surface. However, for deflections of a few degree the difference in result is very small, as the angular dependence of r is governed by the sine of the incident angle ([136] for more details).

As the correction terms for ρ are all on a sub-percent level, they are neglected in the further analysis. Only r_{ag} is considered.

8.5.5 Transmission of Greyfilters and Polarizer

An important issue is the wavelength-dependent transmission T of both the greyfilters and the polarizer. Several measurement series have been performed, using both the setup itself and a spectrometer for determination of these values.

Using the setup, the sample is removed from its position in the light beam. As a reference value, the number of photons registered by P_{B} is measured when all greyfilters are attenuating the beam. Removing the individual greyfilters one after each other and comparing the resulting photon number in this configuration with the reference intensity, the transmission factor of each filter $t_{\text{gf}}(i)$ can be determined. In the same way, the transmission factor of the polarizer t_{pol} can be measured by replacing one of the greyfilters. One must be careful to multiply the measured value t_{pol} by 2, as the incident light is unpolarized and therefore one half of the intensity is fully absorbed. Thus, the double of the measured value corresponds to the transmission factor of the selected polarization. The results for the individual filters as well as the combined value $T = \prod_i t_{\text{gf}}(i)/t_{\text{pol}}$ in Tab. 8.5.

In the course of these measurements, it proves to be extremely important to monitor the dark noise. As the greyfilter directly in front of P_{B} shields it from stray light whenever the black box is opened, the dark noise increases if this filter has to be changed for measuring its transmission. It is therefore necessary to monitor the acquired dark rate in between measurements when the LED can be disabled. Moreover, as only one photomultiplier is used, the measurements will be falsified if a drift in the LED intensity is not noticed. For this means, every odd measurement the reference intensity has to be checked to identify and reject values obtained in periods of evident drifting. Only taking this precautions allows to obtain reproducible absolute values for the filter transmission.

In an alternative approach, the transmission coefficient of the filters was measured using a portable UV-VIS spectrometer¹⁷. For this purpose, the phototube P_{B} is dismantled from the setup to make room for the optical quartz fiber that is used to feed the signal into the spectrometer. A collection lens of 5 mm diameter attached to the fiber head increases the light-sensitive area, suppressing uncertainties introduced by

¹⁷Maya 2000, Ornet, Seri Kembangan, Malaysia

slight variations in beam collimation induced by the filters. The remaining setup is left unchanged.

The spectrometer is based on an optical grating. Combined with the number of pixels on the CCD chip registering the light, an optical resolution of 0.53 nm (FWHM) is reached. The sensitive region ranges from 200 to 1100 nm, well including the LED spectrum. As in the case of the PM measurements, a reference and an attenuated recording are necessary for each filter. The acquired spectra are corrected for background caused by stray light. The intensity is determined by an integration in the relevant wavelength region. Tab. 8.5 quotes the results of the measurements for the greyfilters. The polarizers were not investigated in this way as the spectrometer grating is sensitive to the polarization of the incident light.

When comparing the results to the PM measurements, a systematic shift of about 2% to higher transmission intensities can be observed. This effect can be attributed to a small non-linearity of the intensity measurement for each wavelength. The manufacturer quotes this non-linearity to be $\sim 4\%$. Therefore, the transmission factors measured by the spectrometer have been scaled to 98% of their original value before combining them with the PM measurements. In addition, a 2% uncertainty is added to the small statistical error inherent to the spectral integration. The result for the combined values are listed in Tab. 8.5.

8.5.6 LED emission waveband

Using the spectrometer described in Sect. 8.5.5, the bandwidth of the incident light beam has been determined. The nominal bandwidth of the narrow bandpasses in use is 10 nm. In Tab. 8.6 the measured mean values are reported together with the asymmetric 1σ deviation. The values are smaller than the expected ± 5 nm specified by the manufacturer and represent the uncertainty of the wavelength in the final result. Fig. 8.6 shows the emission spectrum of the LED and the wavebands allowed to pass by the narrow bandpass filters.

8.5.7 Solid Angle Ω

The solid angle covered by the field of vision of the off-beam photomultiplier P_S is determined by the apertures placed in front of it, and the refraction on the surface of the sample. The latter effect differs from sample to sample as the refraction indices n are slightly different. It is possible to do a rough analytical estimate. However, a Monte Carlo (MC) simulation of the scattering process is used for the evaluation of the experiment.

In an analytical approximation, the influence of the beaker glass on the refraction can be neglected as the mantle thickness is ~ 1 mm and the refraction index of glass, $n_{\text{glass}} \simeq 1.52$, is very similar to the one of the samples. Therefore, considering only the transition from sample ($n_{\text{sample}} \simeq 1.5$) to air ($n_{\text{air}} \simeq 1$) and the width (1 cm) and height (6 cm) of the second aperture for light beams emitted by the center of the sample vessel, the angular span of the field of vision are $\Delta\varphi = \pm 10^\circ$ and $\Delta\theta = \pm 4^\circ$ (Fig. 8.7). Comparing this solidangle to the full 4π and assuming isotropic scattering, the fraction of light scattered and actually reaching P_S is 4×10^{-3} .

Filter	Wavelength [nm]	Transmission t [%]		
		Setup	Spectrometer	Combined
2x1	415	44.4±0.9	44.4±0.9	44.4±0.6
	430	46.6±0.8	46.5±1.0	46.5±0.6
	442	45.3±0.6	46.2±1.0	45.5±0.5
2x2	415	44.9±1.0	44.9±1.0	44.9±0.7
	430	47.8±0.7	47.1±1.0	47.5±0.6
	442	47.5±0.9	46.6±1.0	47.1±0.7
4x1	415	18.9±0.7	18.9±0.4	18.9±0.3
	430	20.7±0.2	20.8±0.4	20.7±0.2
	442	20.9±0.4	20.8±0.4	20.8±0.3
10x1	415	6.22±0.08	6.44±0.13	6.28±0.07
	430	7.50±0.11	7.50±0.15	7.50±0.09
	442	7.27±0.09	7.61±0.16	7.36±0.08
10x2	415	6.16±0.11	6.42±0.13	6.27±0.08
	430	7.43±0.07	7.42±0.15	7.42±0.07
	442	7.43±0.11	7.57±0.15	7.48±0.09
10x3	415	6.30±0.15	6.38±0.13	6.34±0.10
	430	7.34±0.13	7.45±0.15	7.39±0.10
	442	7.22±0.10	7.56±0.15	7.32±0.08
pol	415	17.22±0.34	–	17.22±0.34
	430	24.28±0.42	–	24.28±0.42
	442	27.02±0.90	–	27.02±0.90
T [10^{-3}]	415	5.26±0.38	–	5.47±0.22
	430	7.74±0.38	–	7.75±0.26
	442	6.47±0.50	–	6.65±0.30

Table 8.5: Transmission (and statistical uncertainties) of the greyfilters $t_{\text{gf}}(i)$ and of the linear polarizer t_{pol} as a function of the wavelength. Values have been determined using the experimental setup and a portable spectrometer (Sect. 8.5.5). The combined value has been obtained by error-weighted addition. $T = \prod_i t_{\text{gf}}(i)/t_{\text{pol}}$ is the transmission correction entering in Eq. (8.11). See text for further details (Sect. 8.5.5).

Nominal Value	Spectrometer Result
(415 ± 5) nm	(415.0 ^{+3.4} _{-3.7}) nm
(430 ± 5) nm	(430.3 ^{+4.5} _{-4.2}) nm
(442 ± 5) nm	(441.5 ^{+4.8} _{-3.6}) nm

Table 8.6: Spectral bandwidth of the narrow bandpass filters used. The left column reports the specifications given by the manufacturer, right column the central values together with the asymmetric 1σ deviations.

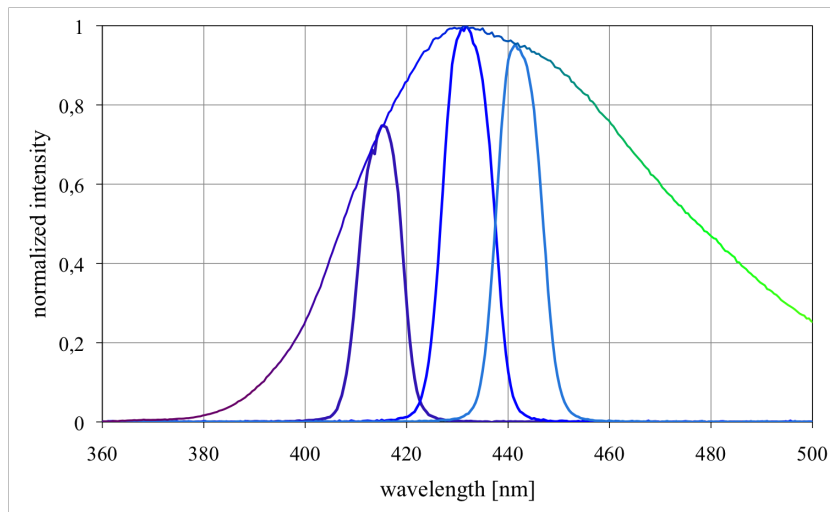


Figure 8.6: Emission spectrum of the LED430-06U (broad curve) and the wavelength bands selected by the narrow-bandpass filters (at 415, 430, and 442 nm). Intensities are normalized. The measurements are done using a spectrometer of type Maya 2000 Pro that is described in Sect. 8.5.

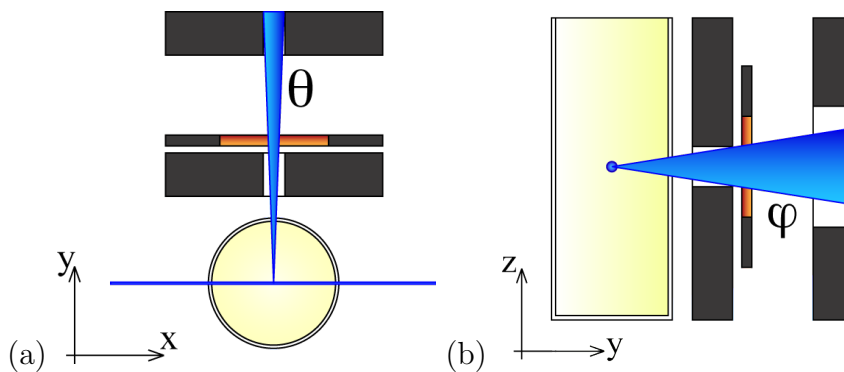


Figure 8.7: Schematic of the solid angle defined by the apertures in front of P_S . (a) shows the angular span covered for the scattering angle θ , (b) depicts the relatively large allowed region for φ . The effect of refraction on the boundary layer glass-air is small and not reproduced in the figures.

However, not only the center of the beaker glass will contribute, but (for a scattering angle of 90°) at least the part of the beam directly in front of the first aperture. If the sample had a scattering length of $\ell = 1$ m, over the distance of $w = 1$ cm (the width of the aperture), the loss in photon number is $dN = N_0(1 - e^{-w/\ell}) = 0.01 N_0$. The percentage of light scattered into P_S is therefore $\Omega_{\text{est}} = 4 \times 10^{-5}$ of the incident intensity.

The MC simulations used in the analysis are based on the GEANT4 toolkit [157]. The simulated geometry comprises the beaker glass, the contained sample and the two apertures. A photon generator is positioned at different angles to this array, and the photons passing the second aperture are counted as registered by P_S . A scattering length $\ell_{\text{MC}} = 1$ m is assumed, only Rayleigh scattering is simulated. Therefore, the simulations for different samples vary only in the input of the sample refractive index n (Sect. 8.2).

It is necessary for the analysis to disentangle the geometrical effects from the angular dependence of the scattering mechanisms. A relation between the solid angles of anisotropic Rayleigh $\Omega_{\text{ray}}(\theta) = \Omega_{\text{an}}(\theta)$ and of isotropic scattering $\Omega_{\text{is}}(\theta)$ can be derived by integration of the differential scattering cross sections:

$$\begin{aligned}\sigma_{\text{an,tot}} &= \int d\Omega \omega_{\text{an}} f_{\text{an}}(\theta) = \int d\theta \int d(\cos \varphi) \omega_{\text{an}} \frac{1 + \cos^2 \theta}{2} = 3\pi \omega_{\text{an}} \\ \sigma_{\text{is,tot}} &= \int d\Omega \omega_{\text{is}} f_{\text{is}}(\theta) = \int d\theta \int d(\cos \varphi) \omega_{\text{is}} = 4\pi \omega_{\text{is}}\end{aligned}\quad (8.16)$$

where ω_{an} and ω_{is} are constant factors. Using Eq. (8.5), two scatterers of the same ℓ must necessarily feature the same total cross sections (if the particle density is the same). Equating the two equations (8.16), the resulting relation is $\omega_{\text{is}} = 3/4 \omega_{\text{an}}$. As the solid angles Ω_i are proportional to σ_i , it follows that

$$\Omega_{\text{is}}(\theta) = \frac{3}{4} \frac{f_{\text{is}}(\theta)}{f_{\text{an}}(\theta)} \Omega_{\text{an}}(\theta) = \frac{3}{4} \left(\frac{2}{1 + \cos^2 \theta} \right) \Omega_{\text{an}}(\theta). \quad (8.17)$$

The result of these considerations is crucial for the analysis in Sec. 8.4: In the 4th step, $\Omega_{\text{is}}(\theta)$ is used to normalize the individual $q(\theta)$ to their geometrical solid angle. As a consequence, a factor $4/3$ has to enter when calculating the scattering length ℓ_{an} from the fit to the corrected values Q to compensate for the difference in the differential cross sections.

Fig. 8.8 shows the solid angles $\Omega_{\text{an}}(\theta)$ and the resulting $\Omega_{\text{is}}(\theta)$ for the investigated samples. For $\theta = 90^\circ$, the MC finds a solid angle of $\sim 2 \times 10^{-5}$, which is within a factor 2 of the analytical estimate. As expected, materials of larger refractive index n effectively feature smaller solid angles: As the refraction angles at the surface sample-(glass)-air increase, more light is refracted away from the apertures. The simulated Rayleigh solid angle is clearly dominated by the angular dependence of the process illustrated by Eq. (8.7). The isotropic solid angle is relatively flat. This is a bit surprising, as geometrical considerations would imply it to rise considerably for angles different from $\theta = 90^\circ$: The proportion of beam length L visible to P_S through the apertures is described by $L(\theta) = L(90^\circ)/\sin(\theta)$. While a rise in $\Omega_{\text{is}}(\theta)$ can be observed near to $\theta = 90^\circ$, it may be suppressed for more remote angles by reflections on the sample-air surface.

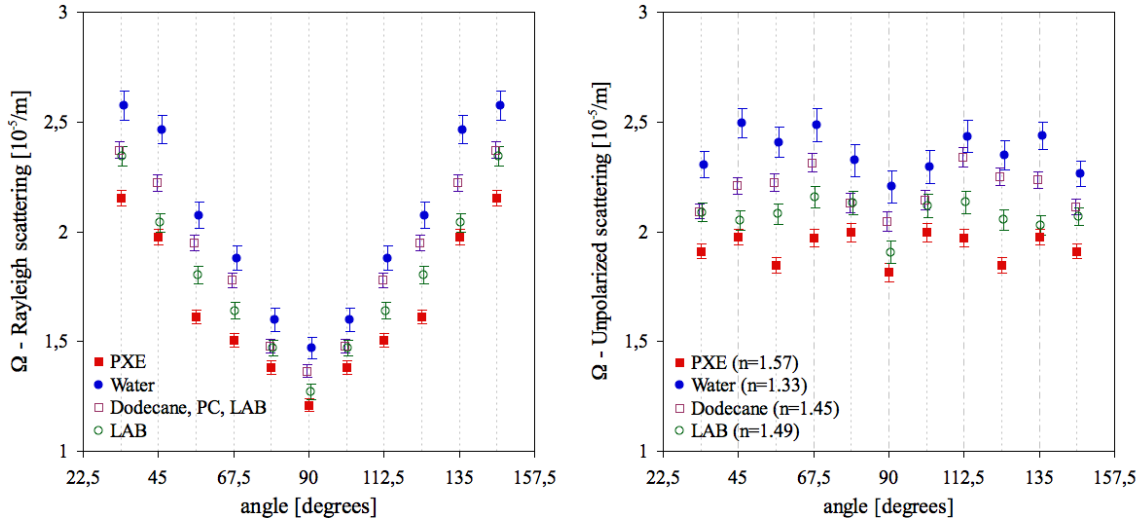


Figure 8.8: Solid angles for the experimental setup, depending on the scattering angle θ . The anisotropic Rayleigh solid angle (left) has been obtained by MC simulations. The quoted error bars reflect the statistical uncertainty. The isotropic (unpolarized) solid angle (right) has been derived via Eq. (8.17).

8.6 Results

The results reported here are from two measurement series: The first one covers a large variety of solvent samples, while the incident light wavelength is fixed at 430 nm. The second series investigated the wavelength dependence of a subgroup of solvents by taking measurements at three different wavelengths.

8.6.1 First series: Screening Materials

The measurements have been performed at the typical wavelength of 430 nm at which scintillation light is effectively transmitted in a scintillator. A broad selection of materials has been screened, including PXE, PC, Dodecane 'C12' by two different manufacturers ('SA' for Sigma Aldrich, 'AC' for Alway Chem), and three brands of LAB produced by Petresa ('P500', 'P550', and '550Q'). In addition, the solvent Cyclohexane 'CH' has been tested; it is a standard for spectroscopic measurements. An overview of the used materials is given in Sect. 8.2.

Tab. 8.7 summarizes the results of the analysis according to Sect. 8.4. Both the anisotropic scattering length ℓ_{an} and the isotropic ℓ_{is} are shown. From them, the total scattering length ℓ_{S} can be derived via $\ell_{\text{S}}^{-1} = \ell_{\text{an}}^{-1} + \ell_{\text{is}}^{-1}$ (Eq. (8.4)). The origin of the reported uncertainties has been discussed in Sect. 8.5. For ℓ_{an} and ℓ_{is} the uncorrelated uncertainties are shown, while the second uncertainty given for ℓ_{S} reflects the correlated effects. These mainly arise from the transmission factors of the greyfilters and polarizer, and from the relative photoefficiency of the phototubes. The last column shows the reduced χ^2 -values from the fit to the scattering ratios $Q(\theta)$. As all of the values are not too far from 1, the actual fit parameters are used.

- **PXE:** In this series, the sample was not purified before the measurement. $\ell_{\text{an}} = 34 \pm 4$ m is in good agreement with the expected value for $\ell_{\text{ray}} = 32$ m calculated

in Sec. 8.2. $\ell_{\text{is}} = 23 \pm 1$ m is the shortest of the measured samples. As the anisotropic scattering shows no sign of Mie contributions, it will be mainly due to absorption-reemission processes, $\ell_{\text{is}} \approx \ell_{\text{are}}$. This is consistent with the relatively low purity of 97% reported in the product specification sheet [143]. The main organic impurities are molecules closely related to regular PXE: PPXE and PMXE feature benzene rings and probably absorption bands at longer wavelengths. The resulting $\ell_{\text{S}} = 13.6 \pm 1.2$ m is therefore relatively short. PXE is here only evaluated in its unpurified form. The second measurement series suggests that purification increases ℓ_{S} by about 50%.

- **LAB:** $\ell_{\text{an}} \approx 40 \pm 5$ m is similar for all samples and a bit lower than the value derived from the absorption band maximum $\ell_{\text{ray}} = 45$ m. $\ell_{\text{is}} \approx 67 \pm 6$ m is quite long; this corresponds to the relatively low contamination with organic impurities. These are in fact mostly n-decanes which are not supposed to lower the transparency (see C12). Concerning $\ell_{\text{S}} \approx 25 \pm 2$ m, no significant difference can be found between the three different brands.
- **C12** is as expected the most transparent of the three liquids intended for use in LENA. Both the samples from Sigma Aldrich and Alway Chem show only small isotropic contributions, $\ell_{\text{is}} \approx 150$ m. The comparison of $\ell_{\text{an}} \approx 45 \pm 5$ m is a bit larger than the estimated value $\ell_{\text{ray}} \approx 37$ m. No large difference between the products of Sigma Aldrich and Alway Chem can be found. The total scattering length adds up to $\ell_{\text{S}} \approx 35 \pm 4$ m, the longest of the three solvents, reflecting the high transparency of C12.
- **CH** finally can be used to cross-check the validity of the measurement results. As pointed out in Sec. 8.2, CH shows no significant absorption for $\lambda > 150$ nm. This is well reproduced in the measurements of the very pure sample: The inverse of ℓ_{is} , $Q_{\text{is}} = (8 \pm 64) \times 10^{-5} \text{ m}^{-1}$, is compatible with 0. The measured anisotropic scattering length $\ell_{\text{an}} = \ell_{\text{S}} = 45 \pm 5$ m is in excellent agreement with the predictions for $\lambda_{\text{ray}} = 44$ m [140, 141, 142]. CH can therefore be seen as a benchmark for the reliability of the other measurements; ℓ_{an} is very sensitive to the correct treatment of the background measurement, especially the used Rayleigh scattering length of water (Sect. 8.5).

In general, $\ell_{\text{ray}} \approx \ell_{\text{an}}$ seems to hold rather well for all samples. There are no hints for a substantial contribution of Mie scattering. Therefore, ℓ_{is} can be directly associated with absorption-reemission scattering length.

8.6.2 Second Series: Testing Wavelength Dependence

In the second series, C12, PXE (both original 'U' and purified 'P'), and PC (the solvent currently used in the BOREXINO experiment) were tested along with CH. The latter two were added to provide a standard for comparison with former measurements.

To monitor the wavelength-dependence of the individual scattering components, the narrow bandpass in front of the sample was exchanged by substitutes, as well as the LED. Measurements at 415, 430, and 441 nm were performed (Tab. 8.5 for exact values). The resulting scattering lengths are shown in Tab. 8.8. The results for the scattering lengths of PC and CH are in good agreement with former measurements [134, 140, 141, 142].

Sample	ℓ_{is} [m]	ℓ_{an} [m]	ℓ_{S} [m]	χ^2/ndf	ℓ_{ray}
PXE U	22.8±1.0	33.6±4.0	13.6±0.7±1.0	1.39	32
C12 SA	258±54	40.9±3.9	35.3±3.0±2.2	0.92	37
C12 AC	132±16	48.5±5.6	35.4±3.1±2.3	0.77	37
LAB P500	75.3±5.3	40.2±4.4	26.2±1.9±1.6	1.23	45
LAB P550	60.5±3.7	40.5±5.2	24.3±1.9±1.5	1.29	45
LAB 550Q	66.3±5.7	40.0±4.6	25.0±1.9±1.6	0.80	45
CH	n.a	45.0±4.5	44.9±4.5±2.9	0.74	44

Table 8.7: Results from the first measurement series performed at 430 nm. Isotropic ℓ_{is} , anisotropic ℓ_{an} resulting total scattering length ℓ_{S} are reported for a variety of samples (Sect. 8.2). For ℓ_{is} and ℓ_{an} , only the uncorrelated uncertainties are quoted, for ℓ_{S} also the correlated uncertainties (Sec. 8.5). The last column shows the reduced χ^2 -value of the analysis fit.

The expected decrease in scattering length with the investigated wavelength is observed for all samples. Fig. 8.9 shows the measured anisotropic scattering lengths ℓ_{an} of PXE U, PC, C12, and CH for the three wavelength. For comparison, the predicted $\ell_{\text{ray}}(\lambda) \propto (\lambda - \lambda_0)^4$ dependence for Rayleigh scattering in these materials is indicated by solid lines. The values quoted in Tab. 8.2 for $\ell_{\text{ray}}(430 \text{ nm})$ and the peak of the absorption band λ_0 are used. In case of PXE, PC, and CH, the data points are in reasonable agreement with both the shape and the absolute normalization of the curves. However, the data points at 415 nm of all samples seem to be slightly shifted to larger scattering lengths. This probably indicates a systematic uncertainty arising from the filter transmission measurements. For C12, a reasonable agreement can for instance be found for a relatively large value of $\ell_{\text{ray}}(430 \text{ nm}) = 52 \text{ m}$ and $\lambda_0 = 250 \text{ nm}$.

In general, the quality of the second measurement series is lower than in the first one. This is correlated to the degrading of the beaker glass and probably also the frequent changes in bandpasses and LED light intensity that decrease the stability of the LED emission. Nevertheless, reasonable values can be obtained by use of the mean values of vertical and horizontal measurement points as described in Sect. 8.4. These results are quoted in Tab. 8.8 along with the reduced χ^2 values to give an indication of the general quality of the data point. Nevertheless, the results for 430 nm featuring the worst χ^2 values are in good agreement with the measurements of the same samples in the first series.

Unfortunately, the purified sample of PXE P is affected the most by the measurement uncertainties. While the data point at 415 nm is rather reliable, the one at 430 nm should be used with care, and the data of the 442 nm measurement is not usable and therefore omitted from Tab. 8.8.

8.6.3 Implications for LENA

The scattering length ℓ_{S} is one of several parameters governing the light propagation in a large-volume LSD. The impact of ℓ_{S} on the overall detector performance arises can only be determined by an analysis including all the features of a given scintillator solvent (and solute) and the detector geometry. In the following, the results of a Monte Carlo (MC) simulation of LENA investigating energy and time resolution in dependence

PXE U	ℓ_{is} [m]	ℓ_{an} [m]	ℓ_{S} [m]	χ^2/ndf
415 nm	14.0 ± 0.8	27.8 ± 5.2	$9.3 \pm 0.6 \pm 0.7$	0.52
430 nm	18.6 ± 1.4	32.1 ± 7.1	$11.8 \pm 1.0 \pm 0.9$	1.86
441 nm	21.1 ± 0.4	41.7 ± 9.5	$14.0 \pm 1.2 \pm 1.1$	0.92
PXE P	ℓ_{is} [m]	ℓ_{an} [m]	ℓ_{S} [m]	χ^2/ndf
415 nm	37.5 ± 2.9	65 ± 17	$23.8 \pm 2.5 \pm 1.8$	0.72
430 nm	40.0 ± 3.9	51 ± 13	$22.3 \pm 2.7 \pm 1.6$	3.71
C12 SA	ℓ_{is} [m]	ℓ_{an} [m]	ℓ_{S} [m]	χ^2/ndf
415 nm	158 ± 32	36.9 ± 4.9	$29.9 \pm 3.4 \pm 2.3$	0.60
430 nm	133 ± 29	49 ± 10	$36.0 \pm 5.6 \pm 2.6$	2.62
441 nm	381 ± 149	76 ± 18	$63 \pm 13 \pm 5$	0.82
PC	ℓ_{is} [m]	ℓ_{an} [m]	ℓ_{S} [m]	χ^2/ndf
415 nm	11.4 ± 0.7	19.6 ± 3.2	$7.2 \pm 0.5 \pm 0.6$	0.51
430 nm	13.0 ± 0.9	19.3 ± 3.3	$7.8 \pm 0.6 \pm 0.6$	1.52
441 nm	17.0 ± 1.1	33.8 ± 7.2	$11.3 \pm 0.9 \pm 0.9$	0.37
CH	ℓ_{is} [m]	ℓ_{an} [m]	ℓ_{S} [m]	χ^2/ndf
415 nm	n.a.	41.1 ± 5.4	$44.2 \pm 6.4 \pm 3.4$	0.33
430 nm	n.a.	40.8 ± 6.0	$45.1 \pm 7.9 \pm 3.3$	2.48
441 nm	512 ± 389	53.0 ± 9.8	$48.0 \pm 8.5 \pm 3.8$	1.16

Table 8.8: Results from the second measurement series performed at the four wavelengths denoted in the first column. Rayleigh ℓ_{R} , unpolarized ℓ_{U} and the resulting total scattering length ℓ_{S} are reported for original and purified PXE, dodecane, pseudocumene, and cyclohexane. The last column shows the reduced χ^2 -value of the analysis fit.

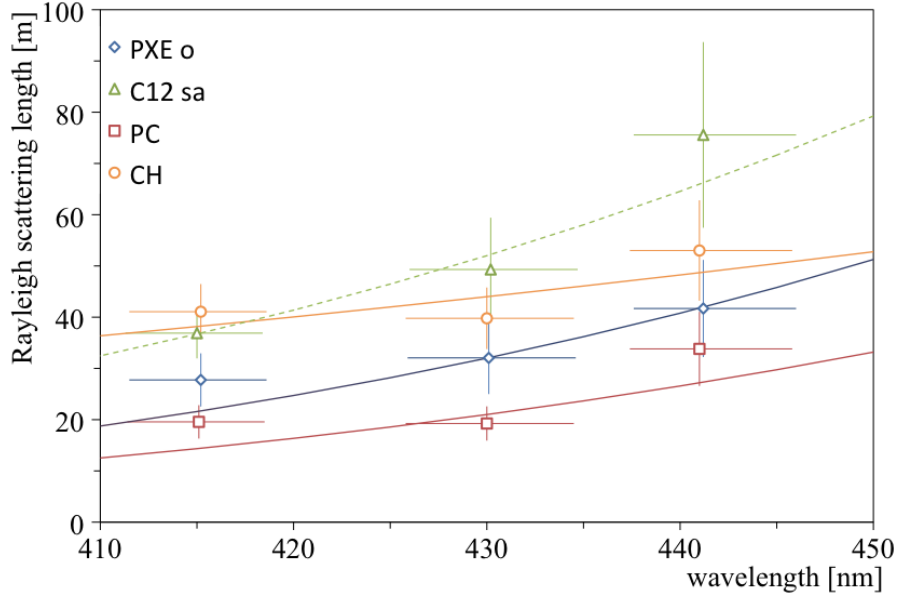


Figure 8.9: Results for the anisotropic scattering length ℓ_{an} for PXE, C12, PC, and cyclohexane (CH) at three different wavelength. For comparison, the predicted Rayleigh scattering length ℓ_{ray} is shown as solid curves of the same color. The necessary input values ℓ_{ray} at 430 nm and the wavelengths of the absorption bands λ_0 in the UV are taken from Tab. 8.2. For PXE, PC, and CH, the data points are in good agreement. Also for C12 a curve reproducing the data can be found using a reasonable value for λ_0 .

of the solvent are presented. The candidate solvents are PXE, LAB, and a mixture of PXE and C12 in a volume ratio of 1:4.

LENA Simulation

The MC simulation of LENA used for the present analysis is based on a C++/ROOT macro [110] that has been written as part of this thesis. Photons are created in the very center of a cylindrical detector and tracked to a photoactive cylindrical surface at a radius of 14.5 m (corresponding to the PM photocathodes). During the propagation, four parameters of the optical medium are taken into account: The scintillation light is generated according to the fast fluorescence decay time τ_f that describes the main component of the scintillators light output. The light is emitted isotropically. The propagation speed is determined by the refractive index n . The photons are propagated over a distance that is statistically correlated to the attenuation length L . If the photon crosses either the mantle or the end caps of the cylinder (at 50 m distance), it is counted as detected. Else, the photon is either eliminated (if it is absorbed), or propagated again in a random direction (corresponding to isotropic scattering), until it is either absorbed or detected. The values for the combined scattering length ℓ_s is used to describe the scattering probability. The negligence of separate anisotropic scattering processes causes a tolerably small error in the results.

Energy Resolution

In a LSD, the energy resolution is described by the photoelectron (pe) yield Y_{pe} : It quotes the number of photons (or photoelectrons) N_{pe} registered by the PMs for a typical event energy of 1 MeV (Chap. 2). The actual resolution is governed by the square root of this number,

$$\frac{\Delta E}{E} = \frac{\sqrt{N_{\text{pe}}}}{N_{\text{pe}}} = \frac{1}{\sqrt{N_{\text{pe}}}} = \frac{1}{\sqrt{Y_{\text{pe}}E}} = \frac{r}{\sqrt{E}}. \quad (8.18)$$

If E is in units of MeV the last term, $r = (N_{\text{pe}})^{-1/2}$ represents the relative energy resolution at $E = 1$ MeV. The typical light output of a liquid scintillator is about 10^4 photons per MeV of deposited energy. Neglecting effects of light propagation, the maximum value for Y_{pe} , Y_{max} , can be found by including the limited photoactive coverage of the detector walls, $c = 0.3$, and the typical photoefficiency of the PMs, $\varepsilon = 0.2$ ⁽¹⁸⁾. Assuming a light yield of 10^4 photons per MeV, the corresponding value of Y_{max} is 600 pe/MeV.

Both L and ℓ_S influence the light propagation and thereby the chance of a photon to be absorbed in the medium before reaching the PMs. The relation between attenuation (L), absorption (ℓ_A) and scattering length ℓ_S is described by $L^{-1} = \ell_A^{-1} + \ell_S^{-1}$ (Sect. 8.1). For each individual sample, about 10^6 photons are generated and propagated according to the special set of L and ℓ_S . The proportion of detected photons is multiplied with Y_{max} to obtain Y_{pe} . Fig. 8.10 shows the light yield Y_{pe} as a function of the scattering length ℓ_S . The black curves illustrate Y_{pe} for fixed values of L : As expected, a larger value of L in general increases Y_{pe} as the probability for a photon to be absorbed decreases. Along the curves, large value of ℓ_S means a shorter absorption length ℓ_A . Therefore, Y_{pe} decreases with ℓ_S . For $L \approx \ell_S$, Y_{max} is reached as $\ell_A \rightarrow \infty$.

In addition, Fig. 8.10 indicates regions which correspond to the allowed regions of L and ℓ_S for the three solvent candidates. While the results of the present work have been used for ℓ_S , the values for L have been taken from several sources [148, 149, 159]. Input parameters and results are quoted in Tab. 8.9. In the case of PXE, Y_{pe} can be determined to ~ 200 pe/MeV featuring a 50 % uncertainty. The span for LAB is much larger due to the variability assumed for L : While measurements performed at the MPI-K in Heidelberg indicate $L > 10$ m [159], a value of 20 m is cited in connection with the R&D activities for the SNO+ experiment [149]. If the later value was correct, a result of $Y_{\text{pe}} \approx 480$ pe/MeV could be expected. In the case of the PXE/C12 (1:4) based solvent, L and ℓ_S correspond to the weighted mean of the values for the individual liquids. The light yield is diminished to ~ 83 % of PXE as C12 misses the benzene rings necessary for effective scintillation. Using $L = 12$ m for the C12 component according to [148], the small increase in transparency does not compensate for the original loss in photons. However, the input for L might be underestimated: Measurements at the MPI-K hint that higher transparency can be reached by purification.

Presently, the uncertainty of ℓ_S account for an uncertainty contribution of ~ 25 % of the result. In the future, measurements featuring better accuracy for LAB and C12 attenuation length L could be used for more precise estimates of Y_{pe} . Until then, LAB can be regarded as the best solvent candidate in terms of light yield.

¹⁸This value is conservatively low, as more recent developments of high-efficiency photocathodes allow PMs to reach $\varepsilon = 0.3 - 0.4$.

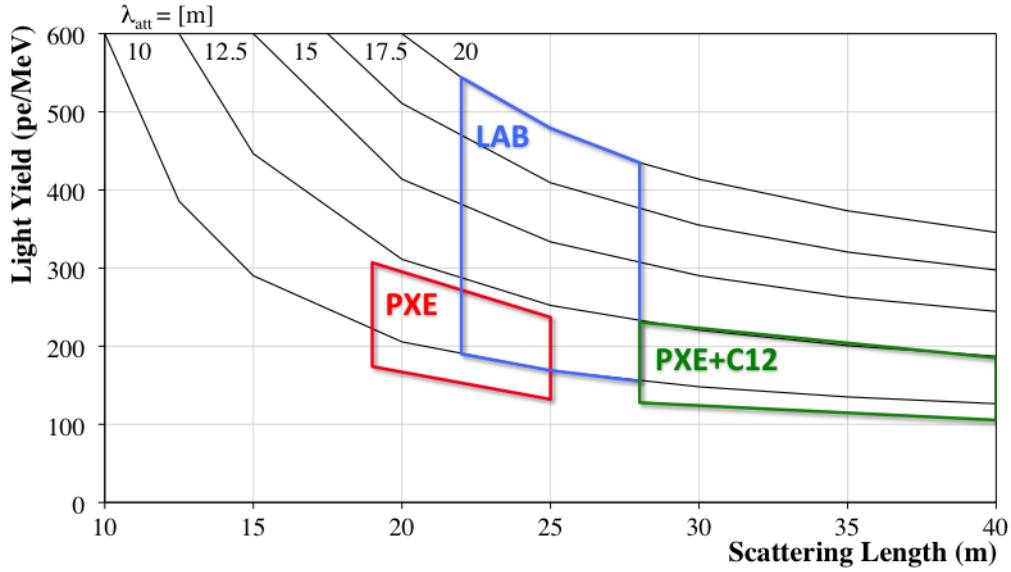


Figure 8.10: Photoelectron yield Y_{pe} as a function of the attenuation length L and the scattering length ℓ_S . The black lines indicate Y_{pe} for fixed values of L , varying ℓ_S . The colored boxes indicate the possible Y_{pe} results if L and ℓ_S correspond to the parameter spans indicated in Tab. 8.9.

Solvent Parameters					Energy Resolution		Time Res.	
Sample	L [m]	ℓ_S [m]	τ_f [ns]	n	Y_{pe} [/MeV]	r [%]	t_s [ns]	τ_s [ns]
PXE	10.5 ± 1.5	22 ± 3	2.63(3)	1.57	207^{+100}_{-75}	$7.0^{+1.7}_{-1.3}$	4.7 ± 0.4	27 ± 2
&C12	12 ± 2	34 ± 6	—	—	159^{+72}_{-54}	$7.9^{+1.8}_{-1.3}$	—	—
LAB	15 ± 5	25 ± 3	5.21(6)	1.49	334^{+207}_{-179}	$4.5^{+2.5}_{-1.1}$	6.9 ± 0.5	30 ± 5

Table 8.9: Properties of the three LENA candidate solvents PXE, LAB, and PXE/C12 (1:4). Attenuation length L , scattering length ℓ_S , fast decay constant τ_f and refractive index n are governing both the energy and time resolution of the final detector: The photoelectron yield Y_{pe} determines the energy resolution r at 1 MeV and is closely related to L and ℓ_S . The fluorescence time τ_f has the main impact on signal rise time t_s and decay time τ_s .

Time Resolution

The light emission of liquid scintillators is on a time scale of nanoseconds. In a large-volume detector, this initially sharp information is smeared out by the differences in light propagation times to the individual PMs. The minimum time difference needed for distinguishing two nearly coincidental events in the detector is therefore given by this effective signal shape. In first approximation, it can be parameterized by the rise time t_s and the effective decay constant τ_s of the combined signal of all PMs. While these values are mainly governed by the detector geometry and the emission time scale of the scintillation light (τ_f), also the contribution of the other optical parameters must be included in the analysis.

As not only the solvent but also the wavelength shifter type and concentration influence τ_f , the values for PPO at a concentration of $2 \text{ g}/\ell$ are chosen for both PXE and LAB to obtain comparable results. The values are adopted from [160]. PXE/C12 is not investigated here as no data on τ_f is available. In the case of PXE and LAB, the addition of bisMSB increases τ_f [160]. A measured value for LAB is not available but a similar extension of the emission time is expected [161].

In the MC simulation, the time constants are determined using a histogram of the photon arrival times at the PMs, obtaining a probability density function for the ideal pulse shape. To include the influence of the PMs, the arrival time was smeared by a time jitter of 1 ns which corresponds to the performance of the PMs used in BOREXINO [12]. The parameter t_s is determined by the time span passing in the leading edge of the signal while rising from 10 % to 90 % of the maximum pulse height. The decay time τ_s is obtained by an exponential fit to the trailing edge of the pulse. The resulting values for PXE and LAB are included in Tab. 8.9. While the difference in t_s is significant for the two solvents, τ_s is mainly governed by the detector geometry. The analysis performed for the time resolution in proton decay events in [160] indicates that t_s has a larger meaning for the time resolution. Concerning this aspect, PXE would be preferable to LAB.

Several further tests have been performed to understand the impact of the input solvent parameters on the effective rise time t_s . For this, the natural parameters of PXE (as quoted in Tab. 8.9) are varied by significant amounts within the parameter regions conceivable for liquid scintillators. Comparing to the initial value of $t_s = 4.4 \text{ ns}$, the following tendencies can be found:

- *Fast Decay Constant:* An increase of τ_f to 7 ns has the most significant impact on the signal shape: t_s is elongated to 7.8 ns.
- *Refractive Index:* Decreasing n from 1.57 to 1.49 (corresponding to the index of LAB) has no visible influence on $t_s = 4.4 \text{ ns}$.
- *Scattering Length:* Doubling ℓ_S but leaving L unchanged reduces the proportion of scattered photons. The result is a sharper signal rise $t_s = 3.7 \text{ ns}$.
- *Attenuation Length:* Doubling L but leaving ℓ_S unchanged increases the relative amount of scattered photons. Consequently, the signal is slightly smeared out, $t_s = 4.7 \text{ ns}$.

- *Optical Transparency*: Doubling both L and ℓ_S leaves the ratio of scattered to absorbed light constant but allows more light to reach the PMs on a direct trajectory. The result is $t_s = 3.9$ ns.

The fluorescence time τ_f of the initial scintillation light propagation has clearly the largest impact on the time resolution. Light propagation has a small influence by photon scattering, while n can be neglected. From the time resolution point of view, PXE is therefore intrinsically preferable to LAB as τ_f is in general shorter: The excitation transport by the solvent molecules is more efficient [126]. However, more detailed simulations might be needed to investigate the influence of the light yield on the time resolution. There is an indication that t_s might be even shorter for PXE/C12 than for pure PXE as ℓ_S is substantially larger. On the other hand, measurements performed in [148] indicate that the admixture of C12 to PXE increases the signal duration by a few percent.

Chapter 9

Detection of the DSNB in LENA

All Supernovae (SNe) explosions in the universe contribute to an on cosmic scales constant and isotropic flux of neutrinos, the Diffuse Supernova Neutrino Background (DSNB). The expected flux can be computed combining measurements of the redshift-dependent Supernova Rate R_{SN} and the energy spectra of SN neutrinos that are derived from MC simulations (Sect. 1.2.3). The predicted flux is with $\sim 10^2$ neutrinos per cm^2s about eight orders of magnitude smaller than the terrestrial flux of solar neutrinos.

In a SN explosion, neutrinos of all flavors and antineutrinos are generated (Sect. 1.2.2). The most accessible for detection are $\bar{\nu}_e$, as the inverse beta decay reaction features the largest cross section at low energies (Sect. 2.2.2). According to contemporary models, about 4 events per year are expected for SUPER-KAMIOKANDE [162]. Unfortunately, the 2.2 MeV γ quantum emitted by the capture of the final state neutron on Hydrogen is below the instrumental detection threshold of a water Čerenkov detector (WCD): As a consequence, $\bar{\nu}_e$ events are covered by various backgrounds¹. In a liquid-scintillator detector (LSD), the neutron capture γ is well visible and offers a very distinctive signature in the detector that allows to reduce the background considerably. However, present day LSDs lack the target mass necessary to detect the very rare DSNB ν 's in relevant numbers. The proposed LENA detector featuring a target volume about twice the size of SUPER-KAMIOKANDE might be the first detector capable of detecting these relic SN neutrinos.

A general description of the SN and DSNB neutrinos can be found in the corresponding sections of Chap. 1: They reflect mainly the approach followed in [49] for an estimate of the DSNB flux that is adopted for the present analysis: This chapter comprises calculations of the expected DSNB rate and spectrum in LENA (Sect. 9.1) as well as an investigation of the relevant background sources in a LSD: Both rates and spectra of $\bar{\nu}_e$'s originating from nuclear reactors and atmospheric cosmic ray production are determined (Sect. 9.2). Moreover, the background arising from cosmogenic ${}^9\text{Li}$ and fast neutrons that mimic the $\bar{\nu}_e$ coincidence signal is derived from Monte Carlo (MC) simulations (Sect. 9.3). The resulting observation window and DSNB event rate is presented in dependence of the LENA detector site. Exceeding mere detection, it might be possible that the measurement statistics allow to derive information on the SN ν spectrum by spectroscopy of the detected $\bar{\nu}_e$ events (Sect. 9.4).

¹Recent R&D activities aim towards the detection of the neutron by adding Gd to the water [85, 86, 162].

9.1 $\bar{\nu}_e$ Signal

The expected DSNB event rate R in LENA can be obtained by the integral over the product of the DSNB spectrum dF_ν/dE_ν , of the cross-section of the inverse beta decay $\sigma_{\bar{\nu}_e p}$, and of the number of free protons in the target N_p :

$$R = \int_0^\infty \frac{dF_\nu}{dE_\nu} \sigma_{\bar{\nu}_e p}(E_\nu) N_p dE_\nu. \quad (9.1)$$

In the following, the necessary input values and their sources are presented along with the corresponding DSNB event rates in LENA (s. Sects. 1.2.2 and 1.2.3 for more information).

DSNB Flux

In the present analysis, the input DSNB fluxes and spectra were chosen according to the work by S. Ando in [49]. The spectrum can be obtained by the following integration:

$$\frac{dF_\nu}{dE_\nu} = \frac{c}{H_0} \int_0^{z_{\max}} R_{\text{SN}}(z) \frac{dN_\nu(E'_\nu)}{dE'_\nu} \frac{dz}{\sqrt{\Omega_m(1+z)^3 + \Omega_\Lambda}}, \quad (9.2)$$

The Hubble constant H_0 and the cosmological parameters for matter density Ω_m and the cosmic constant Ω_Λ enter this equation to account for the cosmic expansion. Two basic input quantities are needed: The neutrino spectrum emitted by a core-collapse SN,

$$\frac{dN_\nu}{dE_\nu} = \frac{(1 + \beta_\nu)^{1+\beta_\nu} L_\nu}{\Gamma(1 + \beta_\nu) \langle E_\nu \rangle^2} \left(\frac{E_\nu}{\langle E_\nu \rangle} \right)^{\beta_\nu} e^{-(1+\beta_\nu)E_\nu/\langle E_\nu \rangle}, \quad (9.3)$$

that is represented by a slightly modified Fermi distribution: The distortion of the distribution that is induced by the spatial extension of the SN neutrino spheres is parameterized by the pinching parameter β_ν (Sect. 1.2.2). The integral flux depends on the neutrino luminosity L_ν . $E'_\nu = (1+z)E_\nu$ in Eq. (9.2) takes the redshift of the initial SN ν spectrum into account.

To cover the possible parameter space allowed in Eq. (9.3), four SN explosion scenarios were investigated: They are based on the Monte Carlo (MC) simulations of SN core-collapse explosions by the Lawrence-Livermore group (LL) [46], by Thompson, Burrows, and Pinto (TBP) [47], and by Keil, Raffelt, and Janka (KRJ) [48]. The mean energies \bar{E}_{ν_i} of the individual ν flavors are shown in Tab. 1.4. As $\bar{E}_{\bar{\nu}_e}$ and $\bar{E}_{\bar{\nu}_x}$ ($x=\mu, \tau$) are substantially different in the case of the LL explosion, it makes sense to distinguish a case featuring a resonant flavor conversion in the $\bar{\nu}$ sector (LL*res*) from the regular non-resonant scenario LL (Sect. 1.2.3). For both KRJ and TBP, mean energies of $\bar{\nu}_e$ and $\bar{\nu}_x$ are very close so that the effect is less prominent.

Also the redshift-dependent Supernova rate enters into the DSNB spectrum:

$$R_{\text{SN}}(z) = 3.9 \times 10^{-4} f_{\text{SN}} h_{70} \frac{e^{3.4z}}{e^{3.8z} + 45} \frac{\sqrt{\Omega_m(1+z)^3 + \Omega_\Lambda}}{(1+z)^{3/2}} \text{yr}^{-1} \text{Mpc}^{-3}. \quad (9.4)$$

The factor f_{SN} describes the overall normalization of R_{SN} , while the fraction featuring exponential terms of z parameterizes the red-shift dependence (Fig. 1.7). The parameter

h_{70} is 1 for a value of $H_0 = 70 \frac{\text{km}}{\text{s Mpc}}$. As a matter of fact, the cosmological parameters describing the development of the volume terms in both $R_{\text{SN}}(z)$ and the DSNB spectrum cancel themselves out. The upper integration limit assumed in Eq. (9.4) is $z_{\text{max}} = 5$. It is defined by the cosmic age at which star formation and therewith gravitational collapses began [49]. Both parameterizations have been already presented in Chap. 1.

$R_{\text{SN}}(z)$ is used instead of the star formation rate $R_*(z)$: There is an uncertainty in the conversion of the two rates due to the mass distribution of forming stars (Sect. 1.2.3). However, the parameter limits $0.7 \leq f_{\text{SN}} \leq 4.2$ correspond to the range for the normalization factor f_* used for the R_* in [49]. The value presently favored by the concordance model for R_* is $f_* = f_{\text{SN}} = 2.5$ [64].

Inverse Beta Decay Cross Section

In both WCDs and LSDs, DSNB $\bar{\nu}_e$ are primarily detected via the inverse beta decay (Sect. 2.2.2). The reaction provides due to the coincidence signal of positron and subsequent neutron capture a clear event signature in a LSD. Moreover, it offers by far the highest cross section for ν detection in the relevant energy regime. At energies of several MeV, the formula

$$\sigma(\bar{\nu}_e p) = 9.45 p_e E_e \times 10^{-44} \text{ cm}^2 = 9.45 (E_\nu - 1.8)^2 \times 10^{-44} \text{ cm}^2 \quad (9.5)$$

approximates the total cross section rather well [163]. $\sigma(\bar{\nu}_e p)$ can be written either as function of positron momentum p_e and energy E_e or of the neutrino energy E_ν . However, at energies of tens of MeV, Eq. (9.5) overestimates the real value of the cross section; at $E_\nu = 30 \text{ MeV}$, the effect is already 25 % [163]. Over the whole range of energy relevant for this analysis, $\sigma(\bar{\nu}_e p)$ is therefore approximated by the parameterization

$$\sigma(\bar{\nu}_e p) = p_e E_e E_\nu^{-0.07056+0.02018 \ln E_\nu - 0.001953 \ln^3 E_\nu} \times 10^{-43} \text{ cm}^2. \quad (9.6)$$

The function agrees with detailed calculations of the cross section performed in [163] on a sub-percent level. Both parameterizations of $\sigma(\bar{\nu}_e p)$ are plotted in Fig. 9.1. For comparison, the far lower cross section of the charged current reaction of $\bar{\nu}_e$ on ^{12}C is shown [164].

Target Mass

The overall active volume of LENA is planned to comprise about $5 \times 10^4 \text{ m}^3$ in a cylindrical volume of 100 m height and 13 m radius (Sect. 7.2.1). Depending on the background conditions (especially fast neutrons, Sect. 9.3.2), it is conceivable that the total volume could be used for DSNB detection. A fiducial volume (FV) of radius 12 m is introduced for the present analysis to be conservative. The corresponding number of free protons (H) in the scintillator that are available as target for the inverse beta decay is calculated considering the density and molecular structure of the solvent (Sect. 8.2): For LAB, the FV of $4.4 \times 10^4 \text{ m}^3$ corresponds to $N_p = 2.9 \times 10^{33}$. In the case of PXE, this number would be slightly reduced but could be brought to the same level by the admixture of C12 (dodecane).

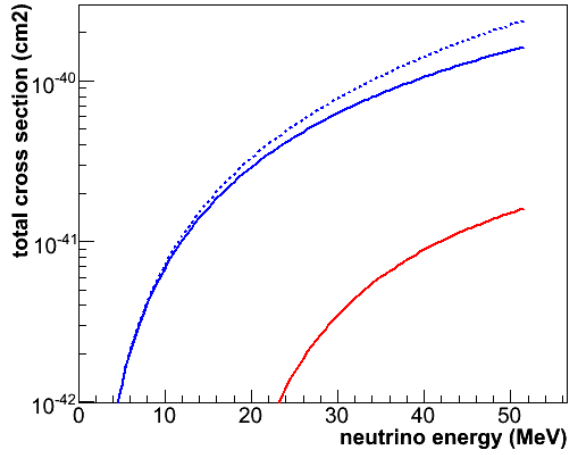


Figure 9.1: Cross section of the inverse beta decay according to the parameterizations of Eqs. (9.5) (*blue dotted line*) and (9.6) (*blue solid*). The more correct Eq. (9.6) is used in the present work [163]. The cross section of the reaction $^{12}\text{C}(\bar{\nu}_e, e^+)^{12}\text{B}$ is shown for comparison (*red*) [164].

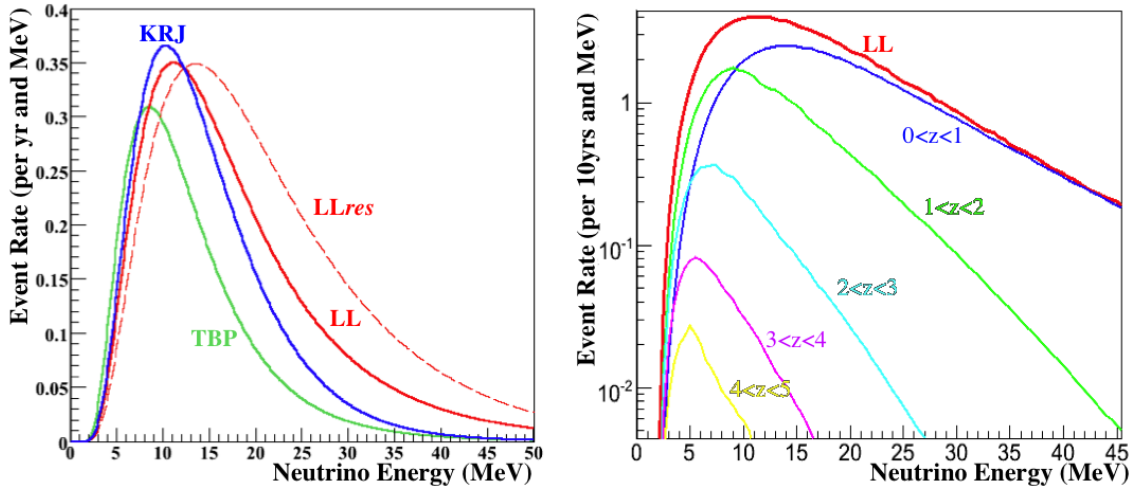


Figure 9.2: *Left*: The DSNB event energy spectra as calculated by Eqs. (9.1) to (9.4). The curves correspond to the spectra observed in case of different DSNB models [49]. *Right*: DSNB event energy spectrum according to the LL model broken down to neutrino fluxes originating from different redshift regions.

Expected Rates

Using these inputs, the rate of DSNB events in LENA can be calculated as a function of the scale factor f_{SN} and the underlying SN model: The largest event number found in the *no resonance* case is provided by the LL model which results in a rate of $\sim 6.8 f_{\text{SN}} \bar{\nu}_e$ counts per year (cpa), followed by the KRJ ($\sim 6.1 f_{\text{SN}}$ cpa) and TBP ($\sim 4.7 f_{\text{SN}}$ cpa) models. The variation of rates is caused by the differences in the spectral mean energies: As the cross-section increases with E_ν , the LL model which predicts the largest flux above 10 MeV also provides the largest event rate. Consequently, the event rate predicted for the LL *resonance* scenario is with $\sim 7.7 f_{\text{SN}}$ cpa even larger.

Fig. 9.2 (*left*) shows the event rate in LENA dependent on E_ν for the four DSNB models and $f_{\text{SN}} = 1$. Independent of the model, the bulk of the events is located in the energy regime from 2 to 50 MeV. The maxima of the *no resonance* models are located in the region around 10 MeV, while the LL*res* maximum lies at 15 MeV. A low detection threshold is therefore the prime requisite to preserve statistics. Fig. 9.2 (*right*) breaks the overall LL detection spectrum down into different red-shift regions: Due to the energy-dependence of σ , most of the detected $\bar{\nu}_e$ originate from red-shifts $z < 1$, while $\bar{\nu}_e$ from the region $z > 1$ dominate the rate below 10 MeV.

9.2 Antineutrino Backgrounds

Due to the clear coincidence signal of positron and neutron capture inherent to the inverse beta decay, the detection of DSNB $\bar{\nu}_e$'s is virtually independent of the internal radiopurity level in LENA (Sect. 2.2.2). The limiting backgrounds are primarily $\bar{\nu}_e$ from other neutrino sources that are intrinsically indistinguishable from the DSNB signal: In the energy regime of the DSNB below 50 MeV, background $\bar{\nu}_e$ fluxes are generated by air showers and nuclear power plants (NPPs)². This limits the observation window for the DSNB $\bar{\nu}_e$ to the energy region from about 10 to 30 MeV (Fig. 9.7).

9.2.1 Reactor Antineutrinos

In the energy regime below 10 MeV, the anthropogenic background of nuclear reactor $\bar{\nu}_e$ clearly dominates the DSNB flux. The lower E_ν threshold for DSNB detection is therefore determined by the high-energetic tail of the reactor spectrum. The magnitude of this background is strongly dependent on the chosen detector site, as the flux produced by a given reactor declines with the square of the distance: To get an estimate of the background flux, it is usually sufficient to consider the nuclear power plants closest to the site.

Reactor Antineutrino Spectrum

Reactor antineutrinos are created in the fission processes powering a nuclear reactor. In conventional NPPs, energy is generated by the fission of the isotopes ^{235}U , ^{238}U , ^{239}Pu , and ^{241}Pu . The resulting neutrino spectrum is best known in the region from 1.8 MeV

²It can also be argued that solar neutrinos undergoing non-standard $\nu_e \rightarrow \bar{\nu}_e$ conversions might constitute a background [165].

Isotope	Contribution to total fission rate	^{94}Br fission yield
^{235}U	0.59	1.66×10^{-6}
^{238}U	0.04	7.90×10^{-5}
^{239}Pu	0.29	2.71×10^{-5}
^{241}Pu	0.08	1.05×10^{-6}

Table 9.1: Contributions of the fission products of Uranium and Plutonium to the fission processes and therefore to the $\bar{\nu}_e$ flux emitted by a reactor (averaged over time) [36]. The last column shows the fission yields of the high-endpoint β -emitter ^{94}Br [90].

(³) to about 8 MeV in which spectral shapes can be directly derived from neutrino experiments. Alternatively, the spectrum can be calculated by measuring the β^- spectra and decay schemes of the individual fission products. The $\bar{\nu}_e$ spectrum of the given isotope is then obtained by spectral inversion. This information has to be combined with the fission production yield⁴ of the β -unstable isotopes to calculate the complete $\bar{\nu}_e$ spectrum by superposition of the individual contributions.

Although the overall reactor $\bar{\nu}_e$ spectrum decreases exponentially with energy, its high-energetic tail above 8 MeV is nevertheless interesting: The total DSNB flux is several orders of magnitude smaller than the terrestrial reactor background signal. Especially for a detector site close to several NPPs, $\bar{\nu}_e$'s from this tail determine the lower threshold for DSNB detection. Up to now, the upper end of the spectrum is only determined by indirect calculations⁵: This approach was followed by Tengblad *et al.* who have measured the β decay of the relevant fission products of ^{235}U , ^{238}U , and ^{239}Pu up to an energy of 12 MeV [167]. For ^{241}Pu , merely the results of MC simulations are available [87]. However, the error introduced by neglecting the ^{241}Pu contribution in the energy region above 8 MeV is relatively small: Tab. 9.1 lists the contributions of the U/Pu isotopes to the total fission rate, averaged over a nuclear burning cycle. ^{241}Pu contributes merely $\sim 8\%$ of the fission processes and consequently of the reactor $\bar{\nu}_e$ flux [36]. Moreover, different to ^{238}U , ^{241}Pu causes only a relatively small proportion of the fission products featuring high β endpoints [87]. In the following, the normalized reactor $\bar{\nu}_e$ spectrum is therefore approximated as a superposition of the ^{235}U , ^{238}U , and ^{239}Pu $\bar{\nu}_e$ spectra according to [167], using the relative ratios of Tab. 9.1.

The main experimental challenge of β^- -decay measurements in the high-endpoint region around 12 MeV is set by extremely neutron-rich fission products featuring half-lives in the range of 100 ms and fission yields of the order of 10^{-5} . For this reason, the analysis performed in [167] was limited to isotopes with endpoints below 12 MeV. More recent measurements have been performed by A. Letourneau *et al.* at the ILL research reactor in Grenoble. As a result, the β -unstable isotope ^{94}Br has been identified as a fission product featuring a Q-value of 13.3 MeV [168]. The ^{94}Br fission yields are listed in Tab. 9.1, the half-life is 70 ms. The branching ratios for the decay to different excited states of ^{94}Kr are unknown: merely the probability to decay directly to ^{93}Kr under the emission of an additional neutron has been determined to 30% [168]. Naturally, it is

³This energy corresponds to the threshold of the inverse beta decay

⁴The fission yield means the probability of an isotope to be produced in a single fission process.

⁵The up-coming DOUBLECHOOZ and DAYA BAY experiments might soon provide such a measurement in their near detectors [87, 166].

interesting in terms of the DSNB detection to include the ^{94}Br spectral contribution in the background estimate: Based on the available data, it is only possible to give an conservative upper limit of its spectral contribution (Fig. 9.4).

Site-Dependent Flux

The starting point for the calculation of the integral reactor $\bar{\nu}_e$ flux for a given site is the calculation of the neutrino rate $R_{\bar{\nu}_e}$ emitted by an individual NPP: The number of fission reactions per second can be determined dividing the thermal reactor power P_{th} by the average binding energy released per fission process, $E_{\text{fiss}} = 205.3 \pm 0.6 \text{ MeV}$ [169]. Averaging over the fission rates of the individual U/Pu isotopes and the resulting pairs of neutron-rich isotopes, the number of $\bar{\nu}_e$ released per fission process is $N_{\nu/\text{fiss}} \approx 6$ [20]. Finally, the actual run-time of the NPPs has to be considered: Maintenance and refueling periods in which the reactor is not operated reduce the overall $\bar{\nu}_e$ output. The energy availability factor $e = 0.75 \pm 0.06$ describes the average fraction of time a reactor is running. It can be derived from the International Atomic Energy Agency (IAEA) [170]. The online database also provides the electric power P_e of all international reactors. It corresponds to about 35 % of P_{th} [87]. The $\bar{\nu}_e$ production rate of a single reactor can therefore be written to:

$$R_{\bar{\nu}_e} = N_{\nu/\text{fiss}} \frac{P_{\text{th}}}{E_{\text{fiss}}} e = (1.38 \pm 0.14) \times 10^{20} P_{\text{th}[\text{GW}]} \text{ s}^{-1} \quad (9.7)$$

The flux Φ_0 induced by an individual reactor at the detector site in a distance d can be calculated by dividing $R_{\bar{\nu}_e}$ by the geometric sphere surface $4\pi d^2$. However, a realistic flux estimate has to take neutrino oscillations into account. This demands especially for reactors nearby the site an energy-resolved treatment of the flux as the survival probability $P_{ee}(E)$ of $\bar{\nu}_e$'s is energy-dependent:

$$\frac{d\Phi_{\text{R}}}{dE} = \Phi_0 \frac{dF_{\text{R}}}{dE} P_{ee}(E) = \frac{R_{\bar{\nu}_e}}{4\pi d^2} \frac{dF_{\text{R}}}{dE} (1 - \sin^2(2\theta_{12}) \sin^2(\pi d/\ell(E))), \quad (9.8)$$

where dF_{R}/dE corresponds to the normalized spectrum, $\ell(E) = \Delta m_{12}^2/4E$ is the oscillation length, and θ_{12} is the solar mixing angle (Sect. 1.1.2). The oscillations due to θ_{13} can be neglected in good approximation as the oscillation probability is small compared to the solar mixing. The total flux at a given detector site can be obtained by the superposition of the individual contributions of all relevant reactors. The necessary geographic coordinates of the nuclear reactors are derived from the online database of the International Nuclear Safety Center (INSC) that comprises all major NPPs operated worldwide⁶ [171].

The investigated detector sites reflect the conceivable locations of a large-volume LSD in the Northern hemisphere: Pyhäsalmi and Fréjus are the two most likely candidates for an underground laboratory in Europe that is deep enough to provide the necessary shielding against cosmic rays. The two sites are also part of the LAGUNA design study (Sect. 7.2.3). In addition, the site of the NESTOR experiment at Pylos is investigated [172]: A deep-sea plateau at 4000 meters depth provides the possibility to operate a

⁶The analysis was performed in 2005. No major changes in number and location of operated NPPs have happened in the last few years.

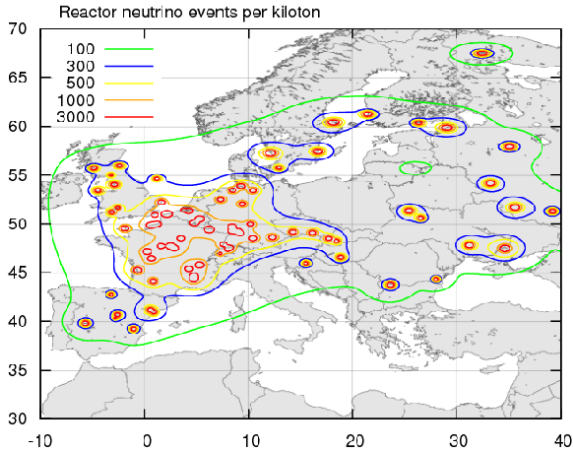


Figure 9.3: Graphical map of the European reactor $\bar{\nu}_e$ flux. The $\bar{\nu}_e$ background in a liquid-scintillator detector is presented as rate per 1 kt of target mass [174].

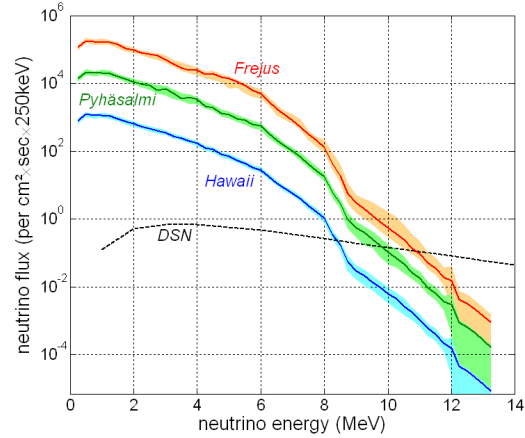


Figure 9.4: Spectra of reactor $\bar{\nu}_e$ at Frejus, Pyhäsalmi and Hawaii. Shaded regions correspond to experimental and model uncertainties. Above 12 MeV, an upper limit for the spectral contribution of ^{94}Br is added. For comparison, the DSNB flux for the KRJ model [48] and $f_{\text{SN}} = 1$ is shown.

large LSD under water, as it is foreseen for the HANO HANO detector [173]. In North America, two of the candidate sites for the Deep Underground Science and Engineering Laboratory (DUSEL) – Kimballton and Henderson mine – and the Homestake mine that was chosen as the actual location of DUSEL are evaluated. Also the Kamioka mine is included to allow a cross-check with the $\bar{\nu}_e$ flux measured in the KAMLAND experiment. Measured and calculated fluxes are in good agreement [18]. Finally, Hawaii near the equator and Wellington on the Southern hemisphere are chosen to investigate sites featuring near-to-optimum background conditions: Both places are very remote from the major concentrations of NPPs in central Europe, North America, and Japan.

The results on the reactor background fluxes and rates at the various locations are

Detector Location	reactor $\bar{\nu}_e$ flux [$\text{cm}^{-2}\text{s}^{-1}$]	reactor $\bar{\nu}_e$ events [0.5 Mt yrs]
Kamioka (J)	2.1×10^6	2.5×10^5
Frejus (F)	1.6×10^6	2.0×10^5
Kimballton (US)	6.4×10^5	7.3×10^4
Pyhäsalmi (FIN)	1.9×10^5	2.1×10^4
Pylos (GR)	9.2×10^4	11.5×10^4
Homestake (US)	7.5×10^4	8.6×10^3
Henderson (US)	7.4×10^4	8.4×10^3
Hawaii (US)	10.9×10^3	12.4×10^2
Wellington (NZ)	5.4×10^3	6.2×10^2

Table 9.2: Reactor $\bar{\nu}_e$ fluxes and event rates for LENA at various detector locations. Uncertainties of both fluxes and event rates are $\sim 14\%$.

Site	latitude (N)	s_{atm}
Hawaii	1.5°	0.8
Kamioka, Pylos, Kimballton	36.5°, 36.6°, 37.4°	1
Henderson, Wellington	39.8°, -41.5°	1.25
Fréjus, Homestake	45.1°, 44.3°	1.5
Pyhäsalmi	63.7°	2.0

Table 9.3: Dependence of the total atmospheric neutrino flux below 60 MeV on the detector location. The scaling factor s_{atm} compares this flux to the one at the Kamioka site.

presented in Tab. 9.2. For comparison, a map of the European reactor background flux fabricated by K. Loo is shown in Fig. 9.3. It depicts the reactor $\bar{\nu}_e$ rate that can be expected per kiloton of liquid-scintillator as a function of the detector site [174]. The values presented in Tab. 9.2 are in good agreement. In order to illustrate the influence of the chosen detector site on the DSNB detection threshold, Fig. 9.4 shows the expected DSNB signal in comparison to the reactor $\bar{\nu}_e$ spectra at Fréjus, Pyhäsalmi and Hawaii. The corresponding thresholds for DSNB detection range from 8.5 to 11 MeV.

The uncertainties on energy spectrum and flux of the reactor $\bar{\nu}_e$ originate on the one hand from the reactors themselves: The most relevant sources are deviations from the average annual run time that is reflected by e (8%), and the temporal variation of the contribution of U/Pu fission during the nuclear burning cycle. The later can be estimated to $\sim 5\%$ [36]. Regarding neutrino physics, the accuracy at which the solar mixing parameters are known plays an important role. The values used in the analysis correspond to the global fit of neutrino data available in 2005, $\Delta m_{12}^2 = 8.2_{-0.5}^{+0.6} \times 10^{-5} \text{ eV}^2$ and $\tan^2 \theta_{12} = 0.40_{-0.07}^{+0.10}$ [175]. In Fig. 9.4, these uncertainties are represented by shaded regions underlying the site-specific graphs.

9.2.2 Atmospheric Antineutrinos

In the energy region below 50 MeV that is of interest for the DSNB detection, the atmospheric $\bar{\nu}_e$ flux is low compared to its maximum at 500 MeV. For energies below 100 MeV, no experimental data is present. For the same reason, MC calculations for these low energies are sparse. An estimate of the atmospheric $\bar{\nu}_e$ background to DSNB detection therefore has to rely on the extrapolation of the existing spectra to lower energies. The approach followed in the publications by Ando and Sato [49] is based on model calculations by T. Gaisser, G. Barr *et al.* [176, 177] which reach down to 60 MeV. In this way, the $\bar{\nu}_e$ background spectrum at Kamioka was retrieved: The atmospheric flux starts to surpass the DSNB signal at energies around 30 MeV. As the intensity of cosmic radiation is due to the Earth magnetic field a function of the geographic latitude, the rate of atmospheric $\bar{\nu}_e$ depends on the detector site [178]. For the present analysis, the spectral shape is considered to be identical for all investigated sites which is a tolerable simplification. The dependence of the overall flux normalization on the geographic latitude is derived from the 3D simulations by Liu *et al.* [178]: The scaling factor s_{atm} is given relative to the flux at Kamioka and reaches at maximum a value of 2 for the most Northern site Pyhäsalmi. Latitude and s_{atm} of the investigated sites are presented in Tab. 9.3.

9.3 Cosmogenic Background

There are two cosmogenic background sources that are relevant for the $\bar{\nu}_e$ search in LENA: Generated inside the detector, βn -emitting radioisotopes from muon spallation can mimic $\bar{\nu}_e$ events. In the outside rock, muons produce fast neutrons that feature a small probability to enter the detector unnoticed (Sect. 2.3). For DSNB analysis, it is only necessary to consider background that falls into the observation window from about 10 to 30 MeV defined by the $\bar{\nu}_e$ background fluxes. In this energy range, only the decay of ${}^9\text{Li}$ features a large enough Q-value to remain a background candidate. Also a substantial fraction of high-energetic neutrons can be excluded as a background by their visible energy. In the following analysis, a muon flux of $\Phi_\mu^L = (1.1 \pm 0.1) \times 10^{-4} \text{ m}^{-2} \text{ s}^{-1}$ corresponding to 4000 mwe of shielding and a flat surface topology is assumed, which is comparable to the Pyhäsalmi site [92]. The corresponding muon mean energy is $\langle E_\mu^L \rangle = 300 \text{ GeV}$ [95]. Where it has influence on the analysis, the LENA detector geometry is assumed according to the vertical design presented in Sect. 7.2.1.

9.3.1 ${}^9\text{Li}$ In-Situ Production

The β^- endpoint of ${}^9\text{Li}$ is with 13.6 MeV towards the lower end of the energy regime relevant for DSNB detection. The maximum energy is further decreased to 11.2 MeV as only the decay branch featuring an electron and a neutron in the final state poses a background to $\bar{\nu}_e$ search (Tab. 2.3). Nevertheless, ${}^9\text{Li}$ contributes in the spectral region of the DSNB maximum flux which makes a simple shift of the threshold seem unfavorable.

The best estimate of the ${}^9\text{Li}$ production rate presently available is the KAMLAND analysis of $\bar{\nu}_e$ -like events in the energy region above 8.3 MeV. The observed rate is 0.6 ± 0.2 events for an exposure of $X^K = 0.28 \text{ kt yrs}^{(7)}$ [179]. To adopt this result to the target mass and rock shielding of LENA, the reduction of the cosmic muon flux Φ_μ and the influence of $\langle E_\mu \rangle$ on the production rate have to be taken into account [99]:

$$R_{9\text{Li}}^L = \left(\frac{\Phi_\mu^L}{\Phi_\mu^K} \right) \left(\frac{\langle E_\mu^L \rangle}{\langle E_\mu^K \rangle} \right)^{0.75} \left(\frac{X^L}{X^K} \right) R_{9\text{Li}}^K = (13 \pm 4) \text{ y}^{-1}. \quad (9.9)$$

For KAMLAND, a muon mean energy of $\langle E_\mu^K \rangle = (268 \pm 2) \text{ GeV}$ and a muon flux of $\Phi_\mu^K = (1.70 \pm 0.05) \times 10^{-3} \text{ m}^{-2} \text{ s}^{-1}$ are adopted from [180]. The exponent for the $\langle E_\mu \rangle$ -dependence is taken from [99] (Sect. 2.3). The resulting ${}^9\text{Li}$ rate corresponds to an exposure of $X^K = 50 \text{ kt yrs}$ in LENA. The rate is a multiple of the expected DSNB signal in this energy range and would effectively impede DSNB detection below $\sim 11 \text{ MeV}$. Fortunately, the production of ${}^9\text{Li}$ is always preceded by a cosmic muon crossing the scintillator. As the ${}^9\text{Li}$ half-life of $T_{1/2} = 0.18 \text{ s}$ is relatively short, the time correlation of muon and radionuclide can be used to veto the decays without introducing too much dead-time. Muons cross the active volume at a rate of 210 h^{-1} . Vetoing the whole detector for a time span of 1 s after each muon will reduce the residual ${}^9\text{Li}$ rate to about 2 %, while the introduced dead time corresponds to only $\sim 6 \%$ of the total measurement time. The loss in exposure can be further reduced by limiting the blinded-out volume to a cylinder surrounding the muon track. As ${}^9\text{Li}$ is usually produced very close to the

⁷The BOREXINO collaboration will probably present a similar analysis along with a study of geoneutrinos in the near to medium future.

track, a rather generous radial cut of 2 m would capture most of the background and at the same time reduce the dead exposure to the level of 0.1 %.

9.3.2 Fast Neutrons

Muons passing nearby the detector produce neutrons by spallation of atomic nuclei in the rock material. These neutrons feature a broad kinetic energy spectrum, and a small fraction is high enough in energy to reach the scintillator volume before they are moderated and absorbed. As described in Sect. 2.3.4, it is possible that these neutrons are not noticed when they cross the muon veto and the buffer region. In this case, the release of their kinetic energy by elastic scattering on protons and subsequent capture on Hydrogen possibly mimics an inverse beta decay event. An analytic estimate of the induced background rate is hard to obtain because it is strongly dependent on the detector geometry and the used materials.

Therefore, a Monte Carlo (MC) study based on the GEANT4 toolkit [157] has been conducted to determine the rate of neutrons entering the fiducial volume (FV): The used detector geometry corresponds to the current LENA design described in Chap. 7: A cylindrical nylon vessel containing the scintillator with a radius $r=13$ m, surrounded by a steel tank of $r=15$ m. Inside the vessel, the FV is defined for $r<12$ m. The outer water tank is assumed to be cylindrical with a radius $r=17$ m. In the LENA design for Pyhäsalmi, the thickness of this water shielding would be substantially larger as the cavern walls are curved (Fig. 7.2). PXE is used as scintillator, which is the most favorable solvent in terms of self-shielding due to its high density of $\rho=985$ g/ ℓ .

The neutron production rate as well as the production energy spectrum are taken from [95] (Fig. 2.6). The rock volume that is considered for external neutron production is a cylinder mantle of 2 m thickness surrounding the water tank. As 1 m of rock suppresses the neutron flux by more than 1 order of magnitude, the contribution of muons at larger radii can be safely neglected. Assuming all muon tracks to be perfectly vertical, the initial neutron production rate in the cylinder mantle can be determined to

$$R_n = R_\mu R_{n/\mu} = 4.3 \text{ s}^{-1} = 1.4 \times 10^8 \text{ y}^{-1}, \quad (9.10)$$

where $R_\mu=2.5 \times 10^{-2} \text{ s}^{-1}$ corresponds to the number of muons passing an area of 226 m^2 at 4000 mwe. The neutron rate caused by each individual muon, $R_{n/\mu}$, is the product of muon path length along the detector of 100 m, the mean rock density of 2.5 g cm^{-3} , and the number of neutrons produced per unit length of the track, $2.93 \times 10^{-4} \text{ g}^{-1} \text{ cm}^2$ at $\langle E_\mu^L \rangle \approx 300 \text{ GeV}$ [95].

Half of the neutrons miss the detector as their initial velocity vector points outwards. The chance of such a neutron to reverse its trajectory by scattering and to subsequently enter the water tank is about 2 %. Also the chance of the remaining neutrons to pass through the combined shielding of 2 m water and 3 m scintillator (PXE) has been investigated. Neutrons below an initial energy of 40 MeV have a negligible probability to cross this barrier. By limiting the simulation of neutrons to energies above 40 MeV and by demanding their initial velocity vectors to point inwards, 4×10^4 neutrons correspond to the neutron production for 1 year at 4000 mwe.

Tab. 9.4 shows the result of a simulation of 4×10^6 neutrons or 100 years of data taking. The table lists the number of neutrons remaining at a given radius from the detector axis. Similarly, Fig. 9.5 shows the stopping radii of the simulated neutron

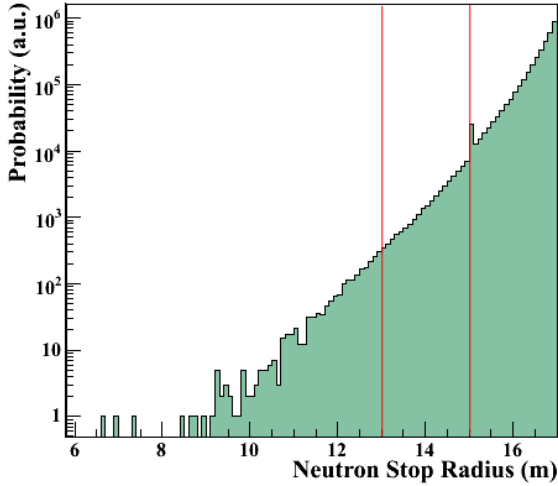


Figure 9.5: Range of external fast neutrons in LENA derived from MC simulations: The stopping point is shown as a function of the radius from the detector axis. Statistics correspond to 100 yrs at a depth of 4000 mwe. A non-negligible number of neutrons reaches the steel tank and the scintillator volume (indicated by red lines).

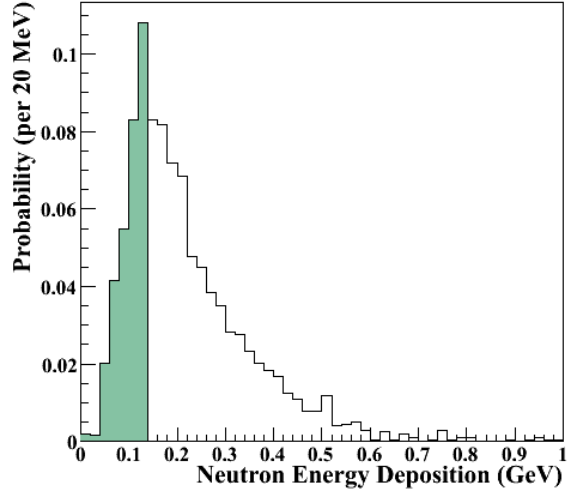


Figure 9.6: Kinetic energy deposited by neutrons entering the scintillator volume of LENA ($r < 13$ m in Fig. 9.5). The visible energy due to proton elastic scattering is quenched by a factor ~ 4 . The proportion of the spectrum relevant as a background for DSNB detection in the 10-30 MeV window is marked by the shaded region.

sample. The two red lines indicate the positions of the nylon vessel and the steel tank and correspond to the horizontal lines in Tab. 9.4. About 450 neutrons per year enter the steel tank, 21 reach the scintillator volume. Less than 5 neutrons per year would reach the surface of the fiducial volume at $r = 12$ m. Without further cuts, this would correspond to a signal-to-background (S/B) ratio of about 2:1.

Several discrimination methods are conceivable to reduce this background rate. First of all, the DSNB observational window stretches from about 10 to 30 MeV. As the neutron visible signal caused by elastic scattering on protons is quenched by about a factor 4 [107], only neutrons of a kinetic energy from 40 to 120 MeV will contribute to the signal. Fig. 9.6 shows the MC energy spectrum of neutrons entering the nylon vessel. Conservatively selecting all neutrons of a kinetic energy below 140 MeV as background candidates, their number is reduced by about a factor 3. The rejection efficiency is even larger for smaller radii as the neutrons intruding further in the detector bulk are in general more energetic. The resulting rate in the FV is 1 neutron per year, which would already mean a comfortable S/B ratio of about 10:1 for DSNB detection.

Further reduction steps are possible: High-energetic neutrons are normally part of hadronic showers that extend to a certain radius lateral distance from the muon track and have therefore an increased chance to be detected by the outer veto. A neutron entering the FV unnoticed does in addition not only scatter on free protons but also on Carbon nuclei producing knock-off neutrons. In this case, the capture of the secondary neutron(s) can be used as discrimination criterium. From a constructional point of view, an increase of the active water volume around the detector would provide additional shielding. Also the bellied cylinder of the Pyhäsalmi water tank would largely increase the shielding. As a rule of thumb, one additional meter of water reduces the

Stop Radius [m]	Shielding Layer [m]	Fiducial Mass [10^3m^3]	Number of Neutrons [/y]		Relative DSNB Rate
			Total Rate	Cut on E_{vis}	
17	0	—	34 739	—	—
16	1	—	3 497.2	—	—
15	2	—	456.70	6.30	—
14	3	—	92.94	6.30	—
13	4	51.0	21.02	6.28	1.20
12	5	42.5	4.52	0.99	1.00
11	6	35.0	1.09	0.19	0.82
10	7	28.3	0.29	0.03	0.66
9	8	22.4	0.07	0.01	0.53

Table 9.4: Neutron background rates in LENA as a function of the radius: The overall rate as well as the remaining rate after a cut on the visible energy of the neutrons is shown. For comparison, the fiducial volume (FV) that would remain for a limitation of the $\bar{\nu}_e$ analysis to smaller radii and the DSNB rate relative to the standard FV ending at 12 m radius are shown.

rate by about one order of magnitude. From Tab. 9.4, one can deduce that the minimum thickness for the active neutron shield is 5 m: In this case, the use of neutron discrimination criteria allows to minimize the influence on DSNB analysis. Already a thickness of 7 m suppresses the neutron background without further cuts to a negligible level.

For these considerations, it is also important to keep in mind that other scintillator solvents feature reduced density and decrease the self-shielding of the liquid. In a nutshell, fast neutrons have to be taken seriously in the dimensioning of the detector shielding but pose no irreducible background to DSNB detection. They are therefore not explicitly included in the further analysis.

9.4 Detection Potential

Reactor and atmospheric $\bar{\nu}_e$ limit the detection window for the DSNB in LENA to an energy regime reaching from roughly 10 to 30 MeV. The exact limits are dependent on the detector site (Sect. 9.4.1), as well as the signal-to-background ratio inside the observational window (Sect. 9.4.2). Exceeding mere detection, it may be possible to gain information from the spectroscopy of the $\bar{\nu}_e$ events – depending on the event numbers: Assuming previous knowledge on $R_{\text{SN}}(z)$ by optical measurements, at least the parameter space for the SN ν spectrum could be narrowed down (Sect. 9.4.3).

9.4.1 Energy Window

Using the information on spectral shape and rate of the two $\bar{\nu}_e$ background sources (Sect. 9.2), an optimal DSNB observation window can be defined for each of the proposed detector sites. From the point of view of spectroscopy, it is favorable to include as much of the signal as possible without increasing the background too far. The energy at which reactor $\bar{\nu}_e$ cease to surpass the DSNB flux is chosen for every site as a lower limit; the upper limit is set at the corresponding point for the atmospheric $\bar{\nu}_e$ flux. Also the resolution of the detector for the neutrino energy E_ν has to be considered as it might smear out the transition regions: Relative to the $\bar{\nu}_e$, the positron signal is shifted

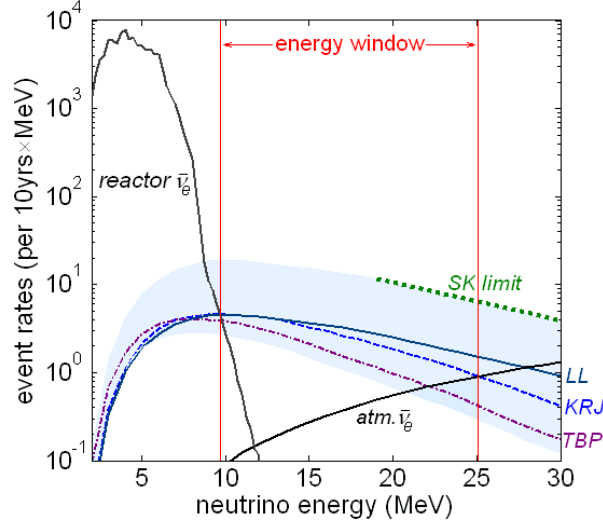


Figure 9.7: Event rates of reactor, atmospheric and DSNB $\bar{\nu}_e$ (LL, KRJ, TBP) as expected for LENA in Pyhäsalmi after ten years of measurement and $f_{\text{SN}} = 1$. The shaded region represents the possible range of the DSNB rates due to f_{SN} . The energy window is chosen such that the flux of the KRJ model exceeds the background flux. The SUPER-KAMIOKANDE limit is also indicated.

slightly in visible energy $E_{\text{vis}} \approx E_\nu - 0.8 \text{ MeV}$. The offset corresponds to the Q -value of 1.8 MeV of the inverse beta decay, reduced by the annihilation energy of the e^+e^- pair of 1.022 MeV⁽⁸⁾. For a light yield of 200 photoelectrons per MeV, the energy resolution is $\sim 2\%$ at 10 MeV and $\sim 1.3\%$ at 30 MeV, respectively. The influence on the observation window is therefore rather small.

As the KRJ model corresponds roughly to the average of the DSNB models in terms of rate and spectral mean energy, it is used as standard for the determination of the observation window. For this purpose, the R_{SN} normalization is set to $f_{\text{SN}} = 1$. Tab. 9.7 lists the resulting windows for the investigated sites. Optimal conditions would be achieved at Hawaii, where the detection region stretches from 8.4 to 29.0 MeV. For Pyhäsalmi, the limits are 9.7 and 25.1 MeV. At this site, the low reactor background allows a lower threshold slightly below 10 MeV⁽⁹⁾, while the low upper bound is induced by the high cosmic ray flux. Fig. 9.7 shows the event spectrum of the DSNB and the $\bar{\nu}_e$ backgrounds as they would be observed in Pyhäsalmi.

In general, the lower detection threshold influences the detected rate of DSNB events originating from red-shift regions $z > 1$ decisively. For Pyhäsalmi, the corresponding $\bar{\nu}_e$ contribute about 25% to the signal (dependent on the used SN model). This proportion and therewith the possibility to investigate R_{SN} at high red-shifts would be diminished significantly if the detector was located for instance in Fréjus.

⁸The offset might actually be a bit larger than the quoted value, as the two annihilation γ 's are quenched in visible energy.

⁹This threshold might actually change slightly to the worse in the coming years: The new TVO3 NPP will increase the reactor $\bar{\nu}_e$ flux by about 10%. Still in planning stage, a new Finnish reactor at 100 km distance from Pyhäsalmi would enhance the flux even on a 50% level.

Detector Location	Energy Window [MeV]	Event Rate [44 kt yrs]	
		DSNB	Background
Kamioka (J)	11.1 - 28.1	2.1-4.2	0.6
Fréjus (F)	10.8 - 26.4	2.2-4.1	0.7
Kimballton (US)	10.6 - 28.1	2.3-4.4	0.6
Pyhäsalmi (FIN)	9.7 - 25.1	2.4-4.5	0.8
Pylos (GR)	9.4 - 28.1	2.7-4.9	0.7
Homestake (US)	9.0 - 26.4	2.8-4.9	0.8
Henderson (US)	8.9 - 27.2	2.8-5.0	0.8
Hawaii (US)	8.4 - 29.0	3.1-5.4	0.7
Wellington (NZ)	8.2 - 27.2	3.1-5.3	0.7

Table 9.5: Lower and upper energy thresholds for DSNB observation and predicted signal and background events inside the energy window for LENA at different locations after 10 years of measuring time and $f_{\text{SN}} = 1$. The range in the signal rates is determined by the LL and TBP model predictions for the *no resonance* case (Sect. 9.1). The background includes atmospheric and reactor $\bar{\nu}_e$ events.

9.4.2 Event Rates

Given the detection windows, the expected DSNB rates in LENA can be calculated for the individual sites. Assuming a *no resonance* scenario in the $\bar{\nu}_e$ sector (Sect. 9.1), the variation span of the rate is limited at the lower end by the TBP and for large values by the LL model. Tab. 9.7 reports the corresponding rates for the individual sites for $f_{\text{SN}}=1$. The expected rates are larger by the cosmologically favored factor $f_{\text{SN}}=2.5$ [64]. The $\bar{\nu}_e$ background rates are presented for comparison: They correspond to the tails of reactor and atmospheric $\bar{\nu}_e$ spectra reaching into the observation window (Sect. 9.2). The background induced by fast neutrons is not included as it depends on the amount of shielding and the definition of the fiducial volume.

The resulting rate for Pyhäsalmi ranges between $2.4f_{\text{SN}}$ cpa (TBP) and $4.5f_{\text{SN}}$ cpa (LL). The occurrence of a matter resonance in the $\bar{\nu}$ sector would further increase the signal rate to $5.3f_{\text{SN}}$ cpa (LL*res*). Overall, roughly 10 cpa are expected for $f_{\text{SN}}=2.5$. At the same time, the $\bar{\nu}_e$ background rate is ~ 0.8 cpa. Within the varying flux predictions of the underlying SN models and the possible range of $f_{\text{SN}} \in [0.7, 4]$, the actual event rate might lie between 1.7 and 21 cpa. This span is depicted as shaded region around the DSNB event spectra in Fig. 9.7. Also the presently best upper limit on the DSNB flux hold by the SUPER-KAMIOKANDE experiments for $E_\nu \geq 19.3$ MeV is depicted [54]: In LENA, it would correspond to 18.5 cpa in the observational window.

Limits to the DSNB Flux

Although it is not very likely, there is the possibility that the combination of current SN model spectra and the astronomically observed value for $R_{\text{SN}}(z)$ lead to an overestimated prediction of the DSNB flux. In this case, LENA can be used to provide an upper limit on the flux: In the energy regime above 19.3 MeV, a significant improvement of the current SUPER-KAMIOKANDE limit is possible due to the superior background rejection of a LSD. However, the maximum sensitivity to the DSNB is reached below 19.3 MeV because the S/B ratio is lower in this regime (Fig. 9.7): A second analysis was therefore

Energy Range	[MeV]	10.5-19.3	19.3-25
Atmospheric $\bar{\nu}_e$ events		2.2	3.6
Reactor $\bar{\nu}_e$ events	[in 10 yrs]	0.2	0
Total background events	[in 10 yrs]	2.4	3.6
Rate limit (90 % C.L.)	[in 10 yrs]	2.5	3.1
Flux limit (90 % C.L.)		0.24	0.10
Lowest model prediction	[$\text{cm}^{-2}\text{s}^{-1}$]	1.4	0.16
Super-Kamiokande limit			1.2

Table 9.6: Using the calculated background levels in two energy bins, an upper limit on the DSN flux can be achieved. Values are given for 10 years of measuring and 100% detection efficiency both for signal and background. For comparison, the lowest model predictions for $f_{\text{SN}} = 0.7$ and the current SUPER-KAMIOKANDE limit are given.

performed for energies between 10.5 and 19.3 MeV, assuming the background conditions of Pyhäsalmi. Tab. 9.6 presents the limits that can be obtained under the assumptions that the $\bar{\nu}_e$ detection efficiency is 100 %, no DSNB events are detected and the cosmogenic background can be neglected. For 10 years of exposure, the remaining number of background events N_{bg} can be determined to 2.4 events for the 10.5-19.3 MeV energy region and 3.6 events for the 19.3-25 MeV regime, respectively. The corresponding 90 % C.L. limits on the DSNB event rate correspond to $1.64\sigma = 1.64\sqrt{N_{\text{bg}}}$.

Next, the information on the event rate can be linked to a $\bar{\nu}_e$ flux by assuming a defined shape for the DSNB spectrum. Tab. 9.6 shows the limits that are obtained using the KRJ model. For comparison, the predicted flux for KRJ and the lowest allowed value for the R_{SN} scaling factor $f_{\text{SN}} = 0.7$ are presented: The limit of $0.24 \text{ cm}^{-2}\text{s}^{-1}$ for 10 to 19.3 MeV corresponds to 17 % of the lowest flux prediction. Though the flux limit of $0.10 \text{ cm}^{-2}\text{s}^{-1}$ in the region above 19.3 MeV is lower in numbers, it is only 60 % of the lowest prediction as the DSNB spectrum decreases with energy. Nevertheless, the limit is an order of magnitude more stringent than the present $1.2 \text{ cm}^{-2}\text{s}^{-1}$ obtained by SUPER-KAMIOKANDE [54].

9.4.3 Spectral Analysis

Depending on the actual DSNB flux, about 100 events will have been registered in LENA after 10 years of measurement. As the energy resolution is on a percent level and the influence of the reaction kinematics is small, it will be possible to reconstruct the incident DSNB $\bar{\nu}_e$ spectrum with an accuracy of better than 1 MeV. This will allow to reproduce the region around the maximum and the falling slope of the DSNB spectrum within the observation window (Fig. 9.7). A spectral analysis should therefore provide information on the mean SN $\bar{\nu}_e$ spectrum and on the SN rate $R_{\text{SN}}(z)$.

However, a MC analysis performed in [181] shows clearly that it is almost impossible to make definite statements on individual variables in Eqs. (9.3) and (9.4) if at the same time all other parameters are left free: The measured DSNB spectrum can be reproduced by a multitude of different parameter combinations.

In the following, the possibility to obtain information on the SN $\bar{\nu}_e$ spectrum is investigated under the premise that $R_{\text{SN}}(z)$ is known at rather high accuracy. Even today, the star formation rate in the redshift-region $z < 1$ is known at $\sim 25\%$ accuracy

from optical measurements [162]. It can be expected that the progress made in the next 20 to 30 years in these field will be substantial. The same is true for the observation of the cosmic SN rate that is propagated for cosmological reasons. Therefore, the assumption that $R_{\text{SN}}(z)$ will be known at a sufficient accuracy during the detector live time of LENA is certainly optimistic but not far-fetched.

MC method

Assuming that both the absolute normalization f_{SN} and the z -dependence of the SN rate entering into Eq. (9.4) are known, the parameters in the DSNB spectrum that remain free are describing the SN ν spectrum of Eq. (9.3): The spectral mean energy \bar{E}_ν , the pinching factor β_ν and the overall neutrino luminosity L_ν . Actually, the spectrum is a superposition of the two initial spectra of $\bar{\nu}_e$ and $\bar{\nu}_x$ that are partially converted into each other when crossing the SN envelope. As it is certainly not feasible to discriminate these contributions based on the relatively small number of detected DSNB events, the present analysis assumes effective values for the mixed spectrum.

Similar to the study performed in [181], the potential of LENA is investigated by generating a large number of MC simulated measurement spectra based on a fixed initial set of the SN parameters \bar{E}_ν , β_ν , and L_ν of Eq. (9.3): The individual MC spectra differ among each other only by statistic fluctuations. Each of these spectra is in turn fitted by the DSNB spectrum of Eq. (9.2), leaving only \bar{E}_ν , β_ν , and L_ν as free parameters. In this way, best fit values for the SN parameters are obtained which are due to the statistical fluctuations not necessarily the same as the initial set. The distributions of the best fit values correspond to the level of accuracy at which individual parameters could be determined by an actual DSNB measurement.

Free analysis

In a first approach, no further assumptions on the SN parameters are made. For each individual MC measurement spectrum, a number of neutrino events is randomly generated according to the true SN parameters. The total number is mainly governed by the value of $L_\nu=5\times 10^{52}$ erg, by the measurement duration or exposure $X=50$ kt yrs and the normalization of the SN rate $f_{\text{SN}}=2.5$. The event energies follow a spectral distribution determined by $\bar{E}_\nu=15$ MeV and $\beta_\nu=3$. The input values correspond roughly the predictions of the KRJ model (Tab. 1.4). The resulting event spectrum is filled into a histogram featuring eight energy bins of equal width covering the observation window. Pyhäsalmi is chosen as detector site, corresponding to a window stretching from 9.7 to 25 MeV and an expected event rate of $3.5f_{\text{SN}}$ per year.

As the analytic solution of the integral in Eq. 9.2 is not suitable for a fit to the MC data spectra, the best fit values are determined by a χ^2 test based on a set of comparative spectra covering a large parameter space. They have been prepared beforehand and are binned analogously to the MC measurement data. Actually, only a set of spectra freely varying \bar{E}_ν and β_ν must be provided as the luminosity L_ν enters as a linear scaling factor.

Almost independently of the simulated event number, the resulting distributions of \bar{E}_ν , β_ν , and L_ν do not converge towards the initial parameter values. This can be understood in terms of the results of a similar χ^2 analysis depicted in Fig. 9.8: Assuming

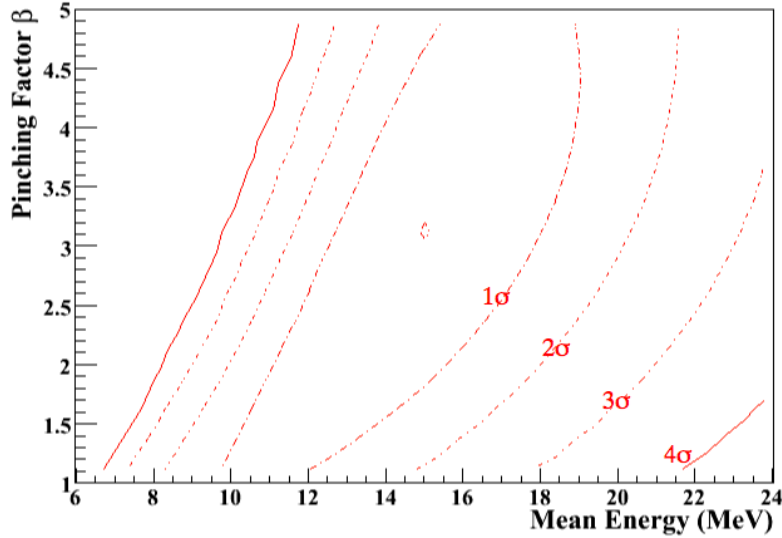


Figure 9.8: Sample exclusion plot for the neutrino mean energy \bar{E}_ν and pinching factor β_ν that describe the SN spectrum. Under the assumption that an ideal DSNB spectrum for $\bar{E}_\nu=15$ MeV and $\beta_\nu=3$ was detected in LENA, the outer parameter regions could be excluded at the indicated significance levels. Nevertheless, a curved band of allowed parameter combinations remains that do not allow to constrain one value at a time.

that a spectrum featuring no fluctuations due to limited event statistics and therefore corresponding exactly to the initial SN parameters was measured, the plot shows the level at which wrong solutions pairs of $\bar{E}_\nu:\beta_\nu$ could be excluded. While here the χ^2 result is still lowest for the true combination of parameters, the 1σ -allowed region has a longish, slightly curved shape corresponding to a large number of practically indistinguishable $\bar{E}_\nu:\beta_\nu$ solutions. By including the statistical fluctuations in the actual MC analysis, this effect is even further enhanced.

The degeneracy of possible $\bar{E}_\nu:\beta_\nu$ pairs has its origin in the free normalization of the DSNB spectrum governed by L_ν : One specific spectral shape that is detected within the observational window can be reproduced by a large set of $\bar{E}_\nu:\beta_\nu$ combinations, although the event rate would change significantly due to the energy-dependence of the detection cross-section. This can be compensated by adjusting the luminosity L_ν in the opposite direction.

Although this analysis is not able to constrain one individual parameter, it puts constraints on the combinations of parameters that describe the measured spectra correctly. Fig. 9.9 shows the best fit values to 10^4 MC spectra in the $\bar{E}_\nu:L_\nu$ -plane if $\beta_\nu = 3$ is set as a prerequisite. The results are confined to a narrow curved region centered around the initial parameters ($\bar{E}_\nu=15$ MeV, $L_\nu=5\times 10^{52}$ erg). The information contained in the DSNB spectrum would therefore allow to relate the initially independent values of the SN ν spectrum.

Introducing Pull Terms

Up to now, no previous knowledge of the parameters entering the SN ν spectrum has been assumed. However, even today some information is available, mainly due to the observation of neutrinos emitted by the SN1987A in the KAMIOKANDE-II and IMB

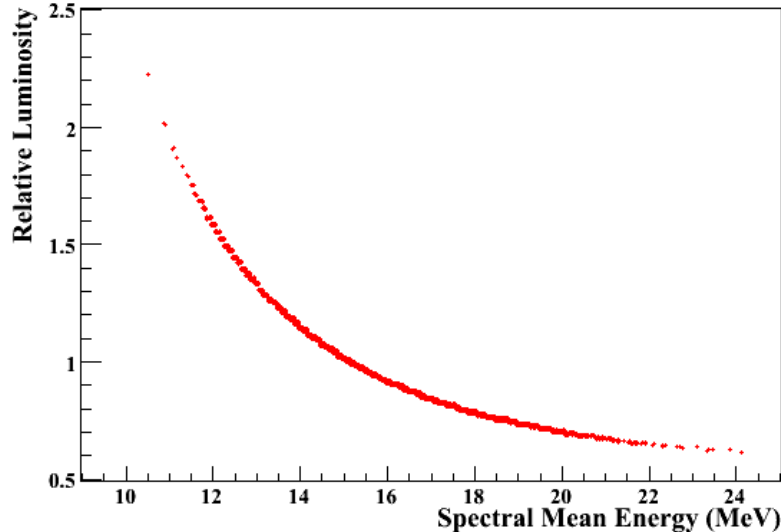


Figure 9.9: Results from a fit to 10^4 MC data spectra assuming $\bar{E}_\nu=15$ MeV, $L_\nu=5\times 10^{52}$ erg, $f_{\text{SN}}=2.5$ and a measurement duration of 10 yrs in LENA; β_ν is set as a prerequisite. While the fit value for \bar{E}_ν is not constrained, it is closely related to the relative luminosity of entering the MC data spectra and the fits. A measurement of the DSNB in LENA could therefore be used to limit the allowed parameter space of SN ν models.

detectors [51, 50]. A combined analysis of the partially contradictory measurements in the two detectors was performed in [55]: While the information on the spectral mean energy \bar{E}_ν is inconclusive, the best combined result on neutrino luminosity is with 4.4×10^{52} erg for the individual flavors very close to the commonly assumed value of $L_\nu=5\times 10^{52}$ erg.

In the following, additional pull terms are introduced in the χ^2 analysis of the MC spectra: Such a term is added as a further quadratic summand to the usual weighted sum over the spectral bins that is used in a χ^2 test; in this case, the first pull term compares the value L_ν obtained by the fit to the initial luminosity of 5×10^{52} erg that has been used for the production of the MC data. The uncertainty weighting this difference is chosen to be 50 % of the MC value of L_ν ⁽¹⁰⁾. In addition, a pull term for the value of the pinching parameter β_ν is introduced, preferring a value of $\beta_\nu=3\pm 2$. The comparison of this input to the values of β_ν in Tab. 1.4 shows that this condition encompasses all SN model values for β_ν in its 1σ -allowed region.

Tab. 9.7 shows the information that can be derived on \bar{E}_ν in this way. The uncertainty limits are reported for different levels on significance as a function of the total exposure X and the SN rate normalization f_{SN} : A measurement time of 10 yrs in a 50 kt detector and for the preferred value $f_{\text{SN}}=2.5$ corresponds therefore to $(X f_{\text{SN}})=125$ kt yrs. For this exposure, 85 DSNB events are expected for the MC spectra. In this scenario, the 1σ uncertainty that could be obtained on \bar{E}_ν is on the level of 10 %, while the 3σ limit still covers most of the parameter space defined by SN simulations (Tab. 1.4). It is remarkable that the precision of the result does not substantially increase for larger values of $(X f_{\text{SN}})$: The limits chosen on L_ν and β_ν are not stringent enough to allow a further constraint of \bar{E}_ν .

¹⁰This allows at the same time some uncertainty in the knowledge on the overall normalization of the SN rate f_{SN} .

$X f_{\text{SN}}$ [kt yrs]	Event Number	Mean Energy Limits [MeV]					
		-3σ	-2σ	-1σ	$+1\sigma$	$+2\sigma$	$+3\sigma$
50	35	12.7	13.2	14.2	18.3	22.2	25.0
125	85	13.0	13.3	14.1	17.0	21.0	22.2
250	175	12.4	13.2	14.0	16.4	17.8	19.3
375	265	11.7	12.8	13.9	16.2	17.5	18.6
500	350	11.3	12.4	13.7	16.1	17.1	18.2

Table 9.7: Constraints on the spectral mean energy $\bar{\nu}_e$ that can be derived from the spectroscopy of the DSNB by the introduction of pull terms for luminosity L_ν and spectral pinching factor $\beta\nu$. The results are presented as a function of the product of exposure X and SN rate normalization f_{SN} . The relatively weak constraints on the order of 50% of the true values are sufficient to reach a 1σ uncertainty of $\sim 10\%$ after 10 years of measurement in LENA ($X f_{\text{SN}} = 125$). The 3σ region still covers the span of output values from SN explosion simulations (Tab. 1.4).

From the analysis described in this last section, it seems not very likely that a measurement of the DSNB in LENA will on its own allow to give strong constraints on any of the individual parameters entering $R_{\text{SN}}(z)$ or the SN ν spectrum. The situation improves if either SN rate or ν spectrum are measured independently by optical observation or the detection of the ν burst of a galactic SN, respectively. Nevertheless, a measurement of ~ 100 DSNB events can in any case be expected to limit the multidimensional parameter space underlying the DSNB models and give in this way constraints for both the simulation of SN core-collapses and the determination of the red-shift dependent SN rate.

Chapter 10

Conclusions

The present work is centered on the study of cosmic background in liquid-scintillator detectors (LSDs). On the one hand, this comprises imminent activity in the data analysis of the currently running BOREXINO solar neutrino experiment: Cosmic muons that cross the central volume of the detector and their cosmogenic byproducts pose a serious background for ν detection and have to be reliably identified and removed from the data. On the other hand, the next-generation large-volume detector LENA will be affected by the same backgrounds. In the present planning phase, a careful study of the influence of detector geometry and shielding is needed to ensure optimal background conditions for the widespread range of scientific objectives.

10.1 BOREXINO

The study of cosmic and cosmogenic events in BOREXINO provides valuable information: As muons and the induced spallation products represent a serious background not only for neutrino detection in BOREXINO but to all low background detectors, a detailed characterization is useful for various astroparticle experiments. Moreover, these events intrinsically offer a possibility for testing the performance of the muon veto and the muon tracking algorithms developed in the course of this thesis.

Muon Detection Performance

Both the liquid-scintillator Inner Detector (ID) and the water Čerenkov Outer Detector (OD) of BOREXINO provide the means for an identification of cosmic muons: While the ID tagging relies on pulse shape analysis, the OD registers the Čerenkov light cones of crossing muons. If both detectors are fully operational, the tagging inefficiency ranges from $(9\pm 3)\times 10^{-4}$ for muons near to the verge of the ID to below 4.9×10^{-6} for muons crossing the central Inner Vessel (IV) of the ID.

The present muon tracking algorithm consists of three submodules: For both ID and OD, a dedicated analysis of the light intensity and arrival time patterns provides two points reconstructed on the muon track. The independent information is combined by a three-dimensional linear fit to all available points, providing a global track. The performance of the track reconstruction was tested separately for each of the three modules by the use of cosmic muon and neutron data. OD and global tracking feature comparable efficiency levels similar uncertainties in the directional reconstruction $\Delta\theta < 5^\circ$

Tracking Module	Resolution		Efficiency	
	Angular	Lateral	Angular	Lateral
ID	16.2°	1.08 m	0.86	—
OD	4.7°	0.21 m	0.87	0.97
Global	3.7°	0.29 m	0.88	0.99

Table 10.1: Tracking Resolution and Efficiencies.

and lateral resolution $\Delta r=25\text{-}30$ cm (Tab. 10.1). The ID reconstruction on its own is up to now less accurate.

Cosmic Muons and Neutrons

Based on the studies of the muon tagging efficiency, the cosmic muon rate in the BOREXINO ID could be determined to $4307\pm 4\pm 4$ events per day. The corresponding cosmic muon flux is $(1.22\pm 0.4)\text{ m}^{-2}\text{ s}^{-1}$ according to expectation for the Gran Sasso underground laboratory (LNGS) at 3500 mwe. The muon tracking was used to determine the angular distribution of the incident muons that bears the imprint of the mountain topology (Figs. 6.4 and 6.5). Both absolute and angular-dependent flux agree well with the results of the already terminated MACRO experiment that was as well located at the LNGS [98].

The investigation of neutron production in muon spallation processes is of great interest for essentially all low-background underground experiments. The neutron capture time in PC of $(257.9\pm 1.7)\mu\text{s}$ that was obtained by isolating a clean sample of cosmogenic neutrons from other backgrounds has proven as a valuable tool in further analysis: Using this input, the average cosmogenic neutron production rate could be determined to $(211\pm 5)\text{ d}^{-1}$ in the BOREXINO IV. In more universal units, this corresponds to a production rate per areal density of $(1.98\pm 0.04)\times 10^{-4}\text{ g}^{-1}\text{ cm}^2$, comparable to the LVD result [101]. Also the frequency and volume extent of hadronic showers induced by cosmic muons in the ID could be studied using neutron multiplicity: The mean number of neutrons detected in the IV in the wake of a muon that produced at least one neutron could be determined to 3.0 ± 0.2 . About 40% of all neutrons are part of showers of more than 10 neutrons. The maximum multiplicity that was registered is close to 180 (Fig. 6.15). The lateral distance distribution of neutrons from the muon track shows a slight deviation from a simple exponential form due to the initial underlying neutron energy spectrum. An effective mean free path of (40 ± 2) cm could be found.

Background to Neutrino Analysis

The residual contamination of the BOREXINO neutrino data sample could be determined by combining results on the muon rate and tagging criteria: The high efficiency of the muon veto reduces this background in the relatively narrow ${}^7\text{Be}-\nu$ detection window to 1/500 of the neutrino signal. In the search for ${}^8\text{B}-\nu$'s, residual muons play a larger role: Due to the low ν rate and the large energy range of analysis, the signal to background ratio is merely 9:1. Without further-going reduction, the remaining muons will limit the accuracy of a ${}^8\text{B}$ flux measurement.

Concerning the upcoming analysis of solar *pep/CNO*- ν signals in BOREXINO, the results of the cosmic background analysis and especially the high average neutron mul-

tiplicity suggests to follow at the same time two complementary approaches in cosmogenic background suppression: ^{11}C β^- decay events pose the primary cosmogenic background to the detection of *pep/CNO* neutrinos. As the signal-to-background ratio is of the order of 1:10, an efficient event-by-event tagging of ^{11}C is indispensable. The main technique to achieve this is the threefold coincidence-veto: The TFC [100] uses the spacial information available on muons and neutrons to define detector subvolumes that are blinded-out from ν analysis for several ^{11}C half-lives. Here, an optimal radius of 1 m for the cylindrical muon cut and a 1.8 m radius for the spherical neutron cut could be determined; a veto of the intersection regions of 1.5 h would include 84 % of the ^{11}C events, reducing the live exposure by $\sim 30\%$. The veto efficiency is mainly limited by neutron-less ^{11}C production channels (5%), the veto duration (5%) and the current inefficiency of the neutron clustering algorithm (6%). At the same time, muons featuring very high luminosities (more than 90 000 hits) and neutron multiplicities larger than 20 should be followed by a 1 hour veto of the whole detector, corresponding to 10 % dead time. This measure would partially compensate the inefficiencies in neutron detection induced by the large light output of showering muons. At the same time, the neutron shower-induced production of ^{11}C at large distances from the muon track could be efficiently vetoed.

10.2 LENA

Regarding the recent success of the KAMLAND [25] and BOREXINO [81] experiments, the expansion of the now established technique of liquid-scintillator neutrino detectors to the 50 kt scale seems promising. While the large volume is demanding in terms of the scintillators optical transparency, it also offers the sensitivity necessary for the detection of very low neutrino fluxes.

Optical Parameters of Scintillator Samples

As one aspect of the optical transparency, scattering of scintillation light in several organic scintillator solvents was investigated as part of this thesis. In a laboratory experiment, intensity and polarization of scattered light were measured under several angles and for several wavelengths to determine the contributions of individual scattering processes: Both the intensities of Rayleigh scattering and absorption/reemission processes could be determined, while no relevant occurrence of Mie scattering was observed in any of the samples. The expected increase in scattering length with the wavelength of the incident light could be confirmed for the region from 415 to 442 nm. The values for 430 nm that are most interesting in terms of scintillation light transport over long distances are shown in Tab. 10.2.

Presently, the R&D activities on the LENA scintillator have identified the solvents PXE, LAB, and a 1:4 mixture of PXE/C12 (dodecane) as promising candidates. Based on the results of the present work and former experiments determining attenuation length and fluorescence decay time of the solvents [148, 126], a MC analysis was performed in order to determine the corresponding energy and time resolution in LENA: While LAB features the superior photoelectron yield and therefore a more accurate energy reconstruction, PXE offers a more precise time resolution due to its faster scintillation signal (Tab. 8.9). The addition of C12 to PXE has only minor influence on

Sample	ℓ_S [m]
PXE U	13.6 ± 1.2
PXE P	22.3 ± 3.2
C12	35.3 ± 3.7
LAB	25.0 ± 2.5
PC	7.8 ± 0.8

Table 10.2: Scattering length ℓ_S for the tested scintillator candidates. The incident wavelength of 430 nm corresponds to the spectrum of scintillation light. The suffixes P and U indicate purified and unpurified PXE. Further details are presented in Tabs. 8.7 and 8.8.

the overall performance. However, physics arguments, technical feasibility including a possible purification of the solvents and lastly costs must be considered as well for the final use in LENA.

Detection of the Diffuse Supernova Neutrino Background

Compared to water Čerenkov detectors that are presently merely able to provide limits on the cosmic Diffuse Supernova Neutrino Background (DSNB), the clear event signature of $\bar{\nu}_e$ detection in a liquid-scintillator detector is a central advantage in the search for the very rare neutrinos. It has been demonstrated in this work that – due to the efficient background discrimination – the only unremovable obstacles to DSNB observation in LENA are $\bar{\nu}_e$'s emitted by nuclear reactors and produced by cosmic rays in the Earth's atmosphere. The rate of cosmogenic ${}^9\text{Li}$ βn -decays and of fast neutrons events that might mimic $\bar{\nu}_e$ signals has been investigated, concluding that these backgrounds can either be safely identified or avoided. LENA will be able to detect about 10 DSNB events per year in a nearly background-free observation window from roughly 10 to 30 MeV. The exact energy limits depend on the $\bar{\nu}_e$ background fluxes at the detector site.

Providing the detection of about 100 DSNB $\bar{\nu}_e$'s in 10 years of data-taking, spectroscopy of these events allows in principle to obtain information on the input SN spectrum and the cosmic SN rate. Although an analysis premising no previous knowledge will not be able to constrain individual parameters [181], the steady progress in optical observations of the star formation and SN rate might soon provide accurate input values for the DSNB: MC simulations performed in the course of this thesis show that in this case the parameter space for the SN ν spectrum could be confined by a set of relations between the parameter values. Making in addition moderate assumptions ($\pm 50\%$) on the values of neutrino luminosity and spectral pinching, the mean energy of the SN spectrum could be determined on an uncertainty level of $\pm 10\%$ (1σ).

10.3 Outlook

BOREXINO will proceed to take data for a couple of years, as both *CNO/pep- ν* and geoneutrino analysis need a relatively large data set to provide the necessary statistics. For both, the muon tracking and the informations on neutrons are a central piece of background rejection. While the overall tracking right now is in a sufficiently good shape to be of real profit for data analysis, there are still possibilities to optimize its

performance. Both ID and OD track reconstruction will benefit from a simulation of the full detector which will be available in the second half of the year [182]. Another on-going project is the installation of an external muon sampler on top of the BOREXINO outer dome in collaboration with the University in Hamburg [183]. The independent high-resolution device would deliver a sample of tracks crossing both detectors that would provide the necessary means to determine and minimize systematical uncertainties.

While promising candidates have been found for the LENA scintillator and the most important optical parameters have been determined, further laboratory experiments at the TUM investigating scintillator properties are planned or on-going: A wavelength-dependent measurement of attenuation lengths will resolve remaining uncertainties in the characterization of LAB and C12. Further experiments aim at the determination of the quenching factors of γ and neutron visible event energies which will also have some impact on BOREXINO data analysis. On a more international scale, the LAGUNA site study which comprises the identification of an optimal underground laboratory for LENA will continue until 2010. In the follow-up, the efforts for LENA will be centered on technical design aspects of the detector hardware. Even now, a starting-up collaboration with French groups at the APC and LAL institutes aims at the development of PM readout systems, but also at an investigation of common cosmogenic background sources. Furthermore, a cooperative MC study of cosmic muons and track reconstruction in LENA and BOREXINO has been recently set up with Finnish Universities in Oulu and Jyväskylä. The involved groups have considerable experience in the analysis and operation of cosmic ray experiments. Finally, the output of BOREXINO on the various backgrounds to solar neutrino detection enters into the evaluation of LENA's detection potential: The next generation of liquid-scintillator detectors can be expected to provide interesting insights into a variety of astrophysical neutrino sources.

Bibliography

- [1] W. Pauli, *Collected Scientific Papers* (Vol. 2, p. 1313, Interscience, New York, 1964).
- [2] R. J. Davis *et al.*, *Astroph. J.* **496**, 505 (1998).
- [3] Gallex, W. Hampel and others, *Phys. Lett.* **B447**, 127 (1999).
- [4] GNO, M. Altmann and others, *Phys. Lett.* **B616**, 174 (2005), hep-ex/0504037.
- [5] J. N. Bahcall and H. A. Bethe, *Phys. Rev. Lett.* **65**, 2233 (1990).
- [6] S. M. Bilenky, *J. Phys.* **G32**, R127 (2006), hep-ph/0511227.
- [7] B. Kayser, *Phys. Lett.* **B667**, 163 (2008), hep-ph/0804.1497.
- [8] L. Oberauer, *Mod. Phys. Lett.* **A19**, 337 (2004), hep-ph/0402162.
- [9] ANTARES, T. Montaruli, (2008), astro-ph/0810.3933.
- [10] IceCube, S. R. Klein, *J. Phys. Conf. Ser.* **136**, 022050 (2008), astro-ph/0810.0573.
- [11] C. Spiering, (2008), astro-ph/0811.4747.
- [12] Borexino, G. Alimonti and others, (2008), physics/0806.2400.
- [13] T. Marrodan Undagoitia *et al.*, *Prog. Part. Nucl. Phys.* **57**, 283 (2006), hep-ph/0605229.
- [14] Particle Data Group, *Phys. Lett.* **B667**, 1 (2008).
- [15] Super-Kamiokande, Y. Fukuda *et al.*, *Phys. Rev. Lett.* **81**, 1562 (1998), hep-ex/9807003.
- [16] Super-Kamiokande, S. Fukuda *et al.*, *Phys. Lett.* **B539**, 179 (2002), hep-ex/0205075.
- [17] SNO, Q. R. Ahmad *et al.*, *Phys. Rev. Lett.* **89**, 011301 (2002), nucl-ex/0204008.
- [18] KamLAND, K. Eguchi *et al.*, *Phys. Rev. Lett.* **90**, 021802 (2003), hep-ex/0212021.
- [19] R. N. Mohapatra and A. Y. Smirnov, *Ann. Rev. Nucl. Part. Sci.* **56**, 569 (2006), hep-ph/0603118.
- [20] N. Schmitz, *Neutrino Physik* (Teubner, Stuttgart, 1997).

- [21] E. Fermi, *Z. Phys.* **88**, 161 (1934).
- [22] M. Chemarin, *Nucl. Phys. B* **85**, 67 (2000).
- [23] Super-Kamiokande, J. P. Cravens *et al.*, *Phys. Rev.* **D78**, 032002 (2008), hep-ex/0803.4312.
- [24] SNO, B. Aharmim *et al.*, *Phys. Rev. Lett.* **101**, 111301 (2008), nucl-ex/0806.0989.
- [25] KamLAND, S. Abe *et al.*, *Phys. Rev. Lett.* **100**, 221803 (2008), hep-ex/0801.4589.
- [26] Super-Kamiokande, J. Hosaka *et al.*, *Phys. Rev.* **D74**, 032002 (2006), hep-ex/0604011.
- [27] MINOS, P. Adamson *et al.*, *Phys. Rev. Lett.* **101**, 131802 (2008), hep-ex/0806.2237.
- [28] CHOOZ, M. Apollonio *et al.*, *Eur. Phys. J.* **C27**, 331 (2003), hep-ex/0301017.
- [29] M. C. Gonzalez-Garcia and M. Maltoni, *Phys. Rept.* **460**, 1 (2008), hep-ph/0704.1800.
- [30] M. Maltoni and T. Schwetz, (2008), hep-ph/0812.3161.
- [31] V. M. Lobashev *et al.*, *Phys. Lett.* **B460**, 227 (1999).
- [32] C. Weinheimer *et al.*, *Phys. Lett.* **B460**, 219 (1999).
- [33] S. Hannestad, A. Mirizzi, G. G. Raffelt, and Y. Y. Y. Wong, *JCAP* **0708**, 015 (2007), astro-ph/0706.4198.
- [34] L. Baudis *et al.*, *Phys. Rev. Lett.* **83**, 41 (1999), hep-ex/9902014.
- [35] Q. Y. Liu, B. L. Chen, J. Zhou, M. J. Luo, and S. C. Jing, *Commun. Theor. Phys.* **44**, 505 (2005), hep-ph/0509182.
- [36] M. Fukugita and T. Yanagida, *Physics of Neutrinos* (Springer, Berlin, 2003).
- [37] Borexino, G. Bellini and others, (2008), astro-ph/0808.2868.
- [38] C. Pena-Garay and A. Serenelli, (2008), astro-ph/0811.2424.
- [39] H. A. Bethe, *Phys. Rev.* **55**, 434 (1939).
- [40] J. N. Bahcall, M. C. Gonzalez-Garcia, and C. Peña Garay, *Phys. Rev. Lett.* **90**, 131301 (2003).
- [41] J. N. Bahcall, A. M. Serenelli, and S. Basu, *Astrophys. J. Suppl.* **165**, 400 (2006), astro-ph/0511337.
- [42] M. Asplund and others, *Cosmic Abundances as Records of Stellar Evolution and Nucleosynthesis* **336**, 25 (2005).
- [43] N. Grevesse and A. J. Sauval, *Space Sci. Rev.* **85**, 161 (1998).

- [44] K. Kotake, K. Sato, and K. Takahashi, Rept. Prog. Phys. **69**, 971 (2006), astro-ph/0509456.
- [45] M. Liebendörfer *et al.*, Astrophys. J. Suppl. **150**, 263 (2004), astro-ph/0207036.
- [46] T. Totani, K. Sato, H. E. Dalhed, and J. R. Wilson, Astrophys. J. **496**, 216 (1998), astro-ph/9710203.
- [47] T. A. Thompson, A. Burrows, and P. A. Pinto, Astrophys. J. **592**, 434 (2003), astro-ph/0211194.
- [48] M. T. Keil, G. G. Raffelt, and H.-T. Janka, Astrophys. J. **590**, 971 (2003), astro-ph/0208035.
- [49] S. Ando and K. Sato, New J. Phys. **6**, 170 (2004), astro-ph/0410061.
- [50] IMB, B. Bratton *et al.*, Phys. Rev. Lett. **58**, 1494 (1987).
- [51] KAMIOKANDE-II, K. Hirata *et al.*, Phys. Rev. Lett. **58**, 1490 (1987).
- [52] G. Sigl *et al.*, (2009), hep-ph/0901.0725.
- [53] G. S. Bisnovatyi-Kogan and S. F. Seidov, Ann. N.Y. Acad. Sci. **422**, 319 (1984).
- [54] Super-Kamiokande, M. Malek *et al.*, Phys. Rev. Lett. **90**, 061101 (2003), hep-ex/0209028.
- [55] C. Lunardini, Astropart. Phys. **26**, 190 (2006), astro-ph/0509233.
- [56] A. M. Hopkins and J. F. Beacom, Astrophys. J. **651**, 142 (2006), astro-ph/0601463.
- [57] E. Cappellaro, R. Evans, and M. Turatto, Astron. Astrophys. **351**, 459 (1999), astro-ph/9904225.
- [58] T. Dahlen *et al.*, Astrophys. J. **613**, 189 (2004), astro-ph/0406547.
- [59] S. Lilly *et al.*, Astrophys. J. **460**, L1 (1996).
- [60] P. Madau *et al.*, Mon. Not. R. Astron. Soc. **283**, 1288 (1996).
- [61] C. C. Steidel *et al.*, Astrophys. J. **519**, 1 (1999).
- [62] D. H. Hughes *et al.*, Nature **394**, 241 (1998).
- [63] H. Flores *et al.*, Astrophys. J. **517**, 148 (1999).
- [64] L. Strigari *et al.*, JCAP **0504**, 017 (2005), astro-ph/0502150.
- [65] J. M. Herndon, Proc. Nat. Acad. Sci. **100**, 3047 (2003).
- [66] KamLAND, T. Araki *et al.*, Nature **436**, 499 (2005).
- [67] S. Enomoto *et al.*, Earth Planet. Sci. Lett. **258**, 147 (2007).

- [68] G. Bertone, D. Hooper, and J. Silk, *Phys. Rept.* **405**, 279 (2005), hep-ph/0404175.
- [69] O. Adriani *et al.*, (2008), astro-ph/0810.4995.
- [70] ATIC, J. Chang *et al.*, *Nature* **456**, 362 (2008).
- [71] D. Hooper and K. Zurek, (2009), hep-ph/0902.0593.
- [72] F. Halzen and D. Hooper, *Phys. Rev.* **D73**, 123507 (2006), hep-ph/0510048.
- [73] F. Reines, *Rev. Mod. Phys.* **68**, 317 (1996).
- [74] R. J. Davis *et al.*, *Phys. Rev. Lett.* **20**, 1205 (1968).
- [75] SAGE, J. N. Abdurashitov *et al.*, *Nucl. Phys. Proc. Suppl.* **138**, 87 (2005).
- [76] Borexino, C. Arpesella, *Phys. Lett.* **B658**, 101 (2008), astro-ph/0708.2251.
- [77] J. D. Jackson, *Classical Electrodynamics* (Wiley, New York, 1962).
- [78] Super-Kamiokande, S. Fukuda *et al.*, *Phys. Rev. Lett.* **86**, 5651 (2001), hep-ex/0103032.
- [79] W. R. Leo, *Techniques for nuclear and particle physics experiments* (Springer Verlag, Berlin, 1994).
- [80] Borexino, H. O. Back *et al.*, (2004), physics/0408032.
- [81] Borexino, C. Arpesella and others, (2008), astro-ph/0805.3843.
- [82] J. G. Learned, (2009), hep-ex/0902.4009.
- [83] J. F. Beacom, W. M. Farr, and P. Vogel, *Phys. Rev.* **D66**, 033001 (2002), hep-ph/0205220.
- [84] A. Ianni, D. Montanino, and F. L. Villante, *Phys. Lett. B* **627**, 38 (2005), physics/0506171.
- [85] J. F. Beacom and M. R. Vagins, *Phys. Rev. Lett.* **93**, 171101 (2004), hep-ph/0309300.
- [86] Super-Kamiokande, H. Watanabe *et al.*, (2008), hep-ex/0811.0735.
- [87] Double-CHOOZ, F. Ardellier *et al.*, (2004), hep-ex/0405032.
- [88] K. A. Hochmuth *et al.*, *Astropart. Phys.* **27**, 21 (2007), hep-ph/0509136.
- [89] K. A. Hochmuth, M. Lindner, and G. G. Raffelt, *Phys. Rev.* **D76**, 073001 (2007), hep-ph/0704.3000.
- [90] R.B. Firestone and L.P. Ekström, LBNL Isotopes Project - LUNDS Universitet, ie.lbl.gov.
- [91] Pierre Auger, J. Abraham *et al.*, *Phys. Rev. Lett.* **101**, 061101 (2008), astro-ph/0806.4302.

- [92] T. Enqvist *et al.*, Nucl. Instrum. Meth. **A554**, 286 (2005), hep-ex/0506032.
- [93] LVD, M. Aglietta *et al.*, Phys. Atom. Nucl. **66**, 123 (2003), hep-ex/0202006.
- [94] T. K. Gaisser, *Cosmic rays and particle physics* (Cambridge Univ. Press, Cambridge, 1999).
- [95] V. A. Kudryavtsev, N. J. C. Spooner, and J. E. McMillan, Nucl. Instrum. Meth. **A505**, 688 (2003), hep-ex/0303007.
- [96] D. D'Angelo, Towards the detection of low energy solar neutrinos in Borexino: Data Readout, Data Reconstruction and Background Identification, PhD Thesis, Technische Universität München, Germany, 2005.
- [97] MACRO, S. Ahlen *et al.*, Astrophys. J. **412**, 301 (1993).
- [98] MACRO, M. Ambrosio *et al.*, Phys. Rev. D **52**, 3793 (1995).
- [99] T. Hagner *et al.*, Astropart. Phys. **14**, 33 (2000).
- [100] C. Galbiati *et al.*, Phys. Rev. **C71**, 055805 (2005), hep-ph/0411002.
- [101] LVD, M. Aglietta *et al.*, (1999), hep-ex/9905047.
- [102] S. R. Raghavan *et al.*, Phys. Rev. Lett. **57**, 1801 (1986).
- [103] O. Smirnov, private communication.
- [104] G. Fiorentini *et al.*, Phys. Rept. **453**, 117 (2007), physics/0707.3203.
- [105] Borexino, M. Balata *et al.*, Eur. Phys. J. **C47**, 21 (2006), hep-ex/0602027.
- [106] P. Antonioli *et al.*, New J. Phys. **6**, 114 (2004), astro-ph/0406214.
- [107] J. M. A. Winter, Phenomenology of Supernova Neutrinos, Spatial Event Reconstruction, and Scintillation Light Yield Measurements for the Liquid-Scintillator Detector LENA, PhD Thesis, Technische Universität München, Germany, 2007.
- [108] OPERA, R. Acquafredda *et al.*, New J. Phys. **8**, 303 (2006), hep-ex/0611023.
- [109] R. Zimmermann *et al.*, NIM A **555**, 445 (2008).
- [110] F. Rademakers and R. Brun, Linux Journal **51** (1998).
- [111] L. Ludhova, private communication.
- [112] T. Lewke, Calibration and Efficiency Determination of the Borexino Muon Veto Based on the First Realtime Measurements of ${}^7\text{Be}$ Solar Neutrinos, Diploma thesis, Technische Universität München, Germany, 2007.
- [113] W. Maneschg, private communication.
- [114] MACRO, M. Ambrosio *et al.*, Astropart. Phys. **7**, 109 (1997).

- [115] D. D'Angelo, private communication.
- [116] Q. Meindl, private communication.
- [117] H. M. Araujo *et al.*, *Astropart. Phys.* **29**, 471 (2008), hep-ex/0805.3110.
- [118] M. Göger-Neff, Development of a Liquid Scintillator and of Data Analysis Methods for BOREXINO, PhD Thesis, Technische Universität München, Germany, 2001.
- [119] Q. Meindl, Identification of Cosmogenic Background Signals in the Neutrino Experiment Borexino, Diploma thesis, Technische Universität München, Germany, 2008.
- [120] M. Wurm *et al.*, *AIP Conf. Proc.* **944**, 82 (2007).
- [121] T. Marrodan Undagoitia *et al.*, *J. Phys. Conf. Ser.* **120**, 052018 (2008).
- [122] S. Todor, Solar Neutrinos with LENA and a spectroscopical analysis of liquid scintillators, Diploma thesis, Technische Universität München, Germany, 2008.
- [123] S. Palomares-Ruiz and S. Pascoli, *Phys. Rev.* **D77**, 025025 (2008), astro-ph/0710.5420.
- [124] T. Marrodan Undagoitia *et al.*, *Phys. Rev.* **D72**, 075014 (2005), hep-ph/0511230.
- [125] S. T. Petcov and T. Schwetz, *Phys. Lett.* **B642**, 487 (2006), hep-ph/0607155.
- [126] T. Marrodán Undagoitia, Measurement of light emission in organic liquid scintillators and studies towards the search for proton decay in the future large-scale detector LENA, PhD Thesis, Technische Universität München, Germany, 2008.
- [127] A. S. Dighe, M. T. Keil, and G. G. Raffelt, *JCAP* **0306**, 006 (2003), hep-ph/0304150.
- [128] M. Wurm *et al.*, *Phys. Rev.* **D75**, 023007 (2007), astro-ph/0701305.
- [129] F. Halzen and A. D. Martin, *Quarks and Leptons: An Introductory Course in Modern Particle Physics* (Srpinger, New York, 1984).
- [130] Super-Kamiokande, K. Kobayashi *et al.*, *Phys. Rev.* **D72**, 052007 (2005), hep-ex/0502026.
- [131] C. Volpe, *J. Phys. G* **34**, R1 (2007).
- [132] D. Autiero *et al.*, *JCAP* **0711**, 011 (2007), hep-ph/0705.0116.
- [133] F. Suekane *et al.*, (2004), physics/0404071.
- [134] Borexino, G. Alimonti *et al.*, *Nucl. Inst. Meth.* **A440**, 360 (2000).
- [135] N. H. de V Heathcote, *Nobel prize winners in physics, 1901-1950* (H. Schuman, New York, 1953).

- [136] E. W. Otten, *Repetitorium Experimentalphysik für Vordiplom und Zwischenprüfung* (Springer Verlag, Berlin, 2002).
- [137] M. Born, *Optik* (Springer, Berlin, 1972).
- [138] H. C. van de Hulst, *Light scattering by small particles* (Dover, New York, 1981).
- [139] L. Henyey and J. Greenstein, *Astrophys. J.* **93**, 70 (1941).
- [140] W. Kaye and J. B. McDaniel, *Appl. Optics* **13**, 1934 (1974).
- [141] B. L. Sowers *et al.*, *J. Chem. Phys.* **57**, 167 (1972).
- [142] H. Wahid, *J. Optics* **26**, 109 (1995).
- [143] Dixie Chemical Co., POXE, www.dixiechemical.com.
- [144] Petresa Canada, Linear Alkylbenzene, www.petresa.ca.
- [145] Sigma-Aldrich, FLUKA 44020 Dodecane, www.sigmaaldrich.com.
- [146] Merck Group, 814505 1,2,4-Trimethylbenzene, www.merck-chemicals.com.
- [147] Merck Group, 102822 Cyclohexane Uvasol, www.merck-chemicals.com.
- [148] M. Wurm, Untersuchungen zu den optischen Eigenschaften eines auf PXE basierenden Flüssigszintillators und zum Nachweis von "Relic Supernova Neutrinos" in LENA, Diploma thesis, Technische Universität München, Germany, 2005.
- [149] Sarah Elizabeth Quirk, Purification of Liquid Scintillator and Monte Carlo Simulations of Relevant Internal Backgrounds in SNO+, PhD Thesis, Queens University Kingston, Canada, 2008.
- [150] Masato Shiozawa, Search for Proton Decay via $p \rightarrow e^+\pi^0$ in a Large Water Cherenkov Detector, PhD Thesis, University of Tokyo, Japan, 1999.
- [151] M. C. Johnson, Scintillator Purification and Light Propagation in a Large Liquid-Scintillator Detector, PhD Thesis, Princeton University, US, 1998.
- [152] C. Semmrich, private communication.
- [153] Sigma-Aldrich, D210404 2,5-Diphenyloxazole, www.sigmaaldrich.com.
- [154] Sigma-Aldrich, 222445 1,4-Bis(2-methylstyryl)benzene, www.sigmaaldrich.com.
- [155] H. Güsten *et al.*, *AIP Conf. Proc.* **82**, 459 (1978).
- [156] KARMEN, G. Drexlin, *Prog. Part. Nucl. Phys.* **48**, 89 (2002).
- [157] S. Agostinelli *et al.*, *Nucl. Instr. Meth. A* **506**, 250 (2003).
- [158] L. Pedrotti, *Prisms* (The Center for Occupational Research and Development, Waco TX, 1987).

- [159] C. Buck, private communication.
- [160] T. Marrodan Undagoitia *et al.*, *Rev. Sci. Instr.* **80**, 043301 (2009), physics/0904.4602.
- [161] T. Marrodan Undagoitia, private communication.
- [162] S. Horiuchi, J. F. Beacom, and E. Dwek, (2008), astro-ph/0812.3157.
- [163] A. Strumia and F. Vissani, *Phys. Lett.* **B564**, 42 (2003), astro-ph/0302055.
- [164] M. Fukugita *et al.*, *Phys. Lett.* **212**, 139 (1988).
- [165] G. Raffelt and T. Rashba, (2009), astro-ph/0902.4832.
- [166] Daya Bay, X. Guo *et al.*, (2007), hep-ex/0701029.
- [167] O. Tengblad *et al.*, *Nucl. Phys.* **A503**, 136 (1989).
- [168] A. Letourneau and D. Lhuillier, private communication.
- [169] V. Kopeikin, L. Mikaelyan, and V. Sinev, *Phys. Atom. Nucl.* **67**, 1892 (2004), hep-ph/0410100.
- [170] International Atomic Energy Agency, <http://www.iaea.org>.
- [171] International Nuclear Safety Center, <http://www.insc.anl.gov>.
- [172] L. K. Resvanis, *Nucl. Phys. B (Proc.suppl.)* **122**, 24 (2003).
- [173] J. G. Learned, S. T. Dye, and S. Pakvasa, (2008), hep-ex/0810.4975.
- [174] K. Loo, private communication.
- [175] KamLAND, T. Araki *et al.*, *Phys. Rev. Lett.* **94**, 081801 (2005).
- [176] T. K. Gaisser *et al.*, *Phys. Rev. D* **38**, 85 (1988).
- [177] G. Barr *et al.*, *Phys. Rev. D* **39**, 3532 (1989).
- [178] Y. Liu, L. Derome, and M. Buenerd, *Phys. Rev.* **D67**, 073022 (2003), astro-ph/0211632.
- [179] KamLAND, K. Eguchi *et al.*, *Phys. Rev. Lett.* **92**, 071301 (2004).
- [180] A. Tang, G. Horton-Smith, V. A. Kudryavtsev, and A. Tonazzo, *Phys. Rev.* **D74**, 053007 (2006), hep-ph/0604078.
- [181] K. A. Hochmuth, Low Energy Neutrinos as geological and astrophysical Messengers, PhD Thesis, Technische Universität München, Germany, 2001.
- [182] T. Lewke, private communication.
- [183] C. Hagner, private communication.

Acknowledgements

The presented analysis of BOREXINO data was performed within the framework of the European *echidna* data analysis group. Concerning the calibration, maintenance and hardware modifications of the BOREXINO Outer Detector and also most of the software coding required for the setup of the muon tracking, there was a close and very helpful collaboration with Davide D'Angelo (INFN Milano). Also most of the analysis on data selection, muon veto efficiencies and cosmic background presented here was done in parallel by the two of us with an extensive exchange of ideas and results. There was a close collaboration with Livia Ludhova (INFN Milano) concerning the ID muon identification flags and the muon run validation, and with Werner Maneschg (MPI-K Heidelberg) on the setup of the global track reconstruction. Quirin Meindl (TUM) and Davide Franco (INFN Milano) deserve some mentioning for their input on cosmogenic background (especially neutrons) and the ID tracking, respectively. Laura Perasso (INFN Milano) and Evgeny Litvinovich (Kurchatov Institute Moscow) provided the sample of CNGS beam events. Generally speaking, there was a brisk exchange of ideas between all the members of the *echidna* group.

Danksagung

An erster Stelle möchte ich Herrn von Feilitzsch und Lothar Oberauer danken, die mir die Mitarbeit an zwei sehr interessanten Projekten ermöglicht haben: In Bezug auf die Erfolgchancen von LENA hat der Chef glücklicherweise immer genug begründeten Optimismus übrig, wenn es an meinem einmal etwas mangelt. Und Lothar Oberauer hat immer Rat oder aufmunternde Worte für einen (wenn auch nicht sichtbar) gestressten Doktoranden, und seinen Erzählungen zu Folge viel mehr Kondition beim Radfahren.

Danken will ich natürlich auch allen, die Passagen meiner Doktorarbeit gelesen und korrigiert haben: Allen voran Marianne Göger-Neff, die sich klaglos durch mein Borexino-Gesamtwerk gekämpft hat. Aber natürlich auch der Wahlschweizerin Teresa Marrodán Undagoitia, die zwitzschen Xenon und Züri-Säcken noch immer Zeit für ihren alten Kollegen findet. Jürgen Winter, dem ich zu Klettverschlüssen rate. Quirin Meindl, der ein erklärter Experte für Neutronen und die Beschaffung von Kleinteilchenzoos ist. Und Patrick Pfahler, der ein bewundernswertes Talent zum Geldausgeben hat. Euch allen Danke, und nicht nur fürs Lesen! Ich revanchiere mich bei Gelegenheit!

Bei den Mitgliedern der Borexino Kollaboration muss ich mich für die freundliche Aufnahme, die viele Hilfe und Diskussionen bedanken. Vor allem natürlich bei Davide D'Angelo, der eh ein halber Münchner ist. Außerdem krieg ich in Mailand immer noch Cappuccino zum Frühstück, obwohl nie etwas aus Sky-Diving oder Schlittschuhlaufen geworden ist. Na, verstanden? Und Danke speziell der Münchner Borexino-Gruppe für die gute Zusammenarbeit, die neben Quirin, Jürgen und Randy auch Timo Lewke einfasst, der mit David Hasselhoff und schwarzem Tape viel für die Verschönerung unseres Büros getan hat.

Hier in Garching gilt mein Dank natürlich auch der LENA-Gruppe, vor allem dem kleinen Trüppchen von Selbstlosen, die sich an einem korsischen Gebirgsbach die Zeit genommen haben, mit mir über den DSNB zu diskutieren: Neben den bereits genannten ist da natürlich Walter Potzel, dessen Erfahrung und Hilfe beim Erstellen der dazugehörigen Veröffentlichung (und auch dieser Arbeit) ich sehr zu schätzen weiß.

Sowohl den alten als auch den neuen Bewohnern unserer beiden Sekretariate, Beatrice, Alexandra, Maria und Sonja, möchte ich danken für die viele Hilfe und Geduld. Das gleiche gilt für den Netzwerk-Admin Sebastian, der dafür, dass er keine nennenswerte Ahnung vom Ölpanschen hat, erstaunlich viel von Whisky versteht. Slainte!

Spezieller Dank auch noch mal an alle, die zum einen oder anderen Zeitpunkt als Werkstudenten, Diplomanden oder Doktoranden ohne mich (oder schlimmer: mit mir) am Computer saßen oder im Labor standen und damit am Entstehen dieser Arbeit mitgewirkt haben: Vor allem Sebastian Todor, der jetzt hoffentlich viel kürzere Wege ins Labor hat. Martin, der mir immer ein paar Kekse übrig lässt. Und Randy, der mich dank neuester Ergebnisse zu den Neutronenraten immer wieder schocken kann.

Dann noch ein großer Dank an alle anderen E15-Mitarbeiter! Ob in Garching oder am Gran Sasso, am Court oder im Kosch, die aufgeschlossene und nette Atmosphäre hilft einem über alltägliche Ärgernisse und Durststrecken in der Motivation hinweg. Mit Euch kann man Brautkränze stehlen!

Meiner Familie, fürs Dasein. Meiner Freundin, für so viel mehr als nur sauberes Wasser. Vielen Dank!